Computational micromechanics of matrix-inclusion composites

Vom Promotionsausschuss der
Technischen Universität Hamburg
zur Erlangung des akademischen Grades

Doktor-Ingenieur (Dr.-Ing.)

genehmigte Dissertation

von
Konrad Schneider

aus
Meerane

2019

Gutachter
Prof. Dr.-Ing. Christian J. Cyron
Prof. Dr.-Ing. Benjamin Klusemann

Vorsitzender des Prüfungsausschusses:
Prof. Dr.-Ing. Benedikt Kriegesmann

Tag der mündlichen Prüfung:
21.11.2019

Acknowledgement

This thesis resulted from my work during my time at the Institute of Continuum and Material Mechanics (ICM) at Hamburg University of Technology (TUHH). As anywhere else in life, preparing a dissertation isn't always fun and heavily depends on the external surroundings, the support of well-intentioned people and a little bit of luck or randomness, as the scientist would say. This section serves to acknowledge the first two aspects and simply gives a "thank you" to all the people that made this work possible, supported and encouraged me to never give up and in the end contributed in the one or the other way to a successful completion.

First I have to thank my spontaneously entered supervisor Prof. Dr.-Ing. Christian J. Cyron for taking over the supervision and reviewing process and initiating a fast and constructive endgame. Secondly, I am thankful to my second reviewer Prof. Dr.-Ing. Benjamin Klusemann who brought me to Hamburg. The smooth and instructive beginning made the introduction into the fascinating topic of computational micromechanics very pleasant and, with the granted scientific freedom, also very fruitful.

Besides my constantly shrinking workgroup at the ICM, I am very grateful for the friendliness and welcoming nature of all the colleagues at the Helmholtz-Zentrum Geesthacht (HZG). You always had the door open for me and offered an additional office space when ever it was necessary. It was very nice for me to visit all of you guys once in a while or on a regular basis, depending on the current situation at TUHH. Providing a certain kind of bureau asylum carried me over some lonely times. Besides the very friendly working environment there, I would like to give special thanks to Jana, Dirk, Ingo and, of course, to Jan for their willingness to discuss problems that are not their own, that they tried to think out of the box and made me always feel very welcome on the other side of the Elbe. Especially, Ingo and Jan contributed to the final state of the thesis by proof reading all the chapters and not at least putting all the commas for me ;)

Back at TUHH I need to express my gratitude to the entire Team of M-22 and M-26 who included me into their lunch routine. Special thanks goes to Lukas, Bene, Birthe, Mark, Manuel, Rainer, Gunnar, Manni, Guido and Dagmar. Introducing me into the secret art of foosball made my lunch break great again. The games nights, "Kicker"-tournaments and boulder evenings gave me the right stimulation to understand the matrix-inclusion composites from a different point of view.

In the private sector, first of all, I have to be very thankful to my parents. They encouraged and supported me during my entire life and career independent of the topic, situation or setting, which cannot be taken for granted. Furthermore, I would like to thank my friends who always offered an open door to discuss work and non-work related topics in person or via telephone. I am particular thankful to the friendship to Jan who grew from a visiting colleague to a friend for every situation in life. All of you carried me over the hard times and made the good times even better.

But the greatest thanks of all goes to my loving wife Julia. Her patients, forgivingness and encouraging attitude made the difficult parts of the journey easy and the easy parts more enjoyable. Without your willingness to almost unconditional support I would have never come so far.

Thank you so much!

Computational micromechanics of matrix-inclusion composites

Konrad Schneider

Abstract

This thesis is concerned with aspects of the computational retrievement of macroscopic material responses and investigations of the microscopic deformation behavior of random matrix-inclusion composites. To this end, the focus lies on the representative volume element (RVE) approach in the scope of finite element analyses and its applicability and integration into engineering practice.

The artificial random generation of the microstructural geometry, in a periodic and non-periodic manner, is established by studying and enhancing existing methods such as the random sequential adsorption method or collective rearrangement methods for cubic RVEs. Based on distance computations between two inclusions, the non-overlap requirement, which is characteristic for matrix-inclusion composites, is ensured for ellipsoidal, capsular, cylindrical and convex polyhedral inclusion shapes.

To comply with the state-of-the-art approach that utilizes fully periodic RVEs featuring a periodic topology, a periodic discretization and periodic boundary conditions (PBC), a new algorithm that automatically generates periodic meshes is developed. The algorithm systematically combines various meshing tools in an efficient and robust way. Special emphasis is placed on the discretization procedure to maintain a high quality mesh with as few elements as possible, thus, manageable for computer simulations applicable to high volume concentrations, high number of inclusions and complex inclusion geometries. Examples elucidate the ability of the proposed approach to efficiently generate large RVEs with a high number of anisotropic inclusions but still maintaining a high quality mesh and a low number of elements.

Since the generation of such a state-of-the-art RVE can significantly reduce the overall efficiency in multiscale finite element simulations, a benchmark study that investigates possible relaxations to this cumbersome task is performed. In particular, the RVE size, periodic and non-periodic RVE topologies, different discretization variants and various types of boundary conditions that either require periodicity or do not require periodicity of the underlying discretization are benchmarked. Approximate periodic boundary conditions are discussed in detail. The benchmark study proves that a fully periodic topology and mesh discretization with periodic boundary conditions is not necessary in order to identify effective macroscopic material parameters for technologically relevant composites.

Eventually, the gathered methodologies are applied to model a modern high-tech polymer nanocomposite. By utilizing a sophisticated material model for the polymeric matrix, the entropic and energetic deformation regime can be represented in a physically meaningful way. Furthermore, the explicit consideration of the matrix-inclusion interface failure via a cohesive zone model accounts for the non-negligible surface effects. Comparisons with experiments underline the predictive character of the modeling approach and allow for investigations of local deformation mechanisms.

Contents

Acronyms **vi**

1. Matrix-inclusion composites in the context of modern computational mechanics **1**
1.1. Challenges in computational modeling of matrix-inclusion composites 3
1.2. Structure of the thesis 4

2. Continuum Mechanics **7**
2.1. Notation 7
2.2. Kinematics 8
2.3. Kinetics and balance principles 9
2.4. Constitutive theory of damage and failure mechanics 11
2.5. Computational homogenization and localization 13
2.5.1. Micro-macro-link 17

3. Microstructure Generation **25**
3.1. Random sequential adsorption methods 31
3.1.1. Placement procedure 33
3.1.2. Distance computation of convex geometric primitives 36
3.1.3. Example microstructures 50
3.2. Collective rearrangement methods 53
3.3. Miscellaneous approaches: convex polyhedra 58
3.4. Statistics of microstructures 59

4. Microstructure Meshing **67**
4.1. Periodic meshing of matrix-inclusion RVEs 70
4.2. Examples and comparison 77
4.2.1. Mesh generation with the NETGEN software library 77
4.2.2. Mesh generation with the proposed algorithm 77
4.2.3. Comparison 78

5. Implementation of micromechanical boundary conditions **81**
5.1. Kinematic uniform boundary conditions (KUBC) 82
5.2. Static uniform boundary conditions (SUBC) 83
5.3. Periodic boundary conditions (PBC) 84
5.4. Approximate periodic boundary conditions (APBC) 87

6. Model setups of matrix-inclusion composites and their influences **93**
6.1. Benchmarking alternative model setups 95
6.1.1. Results and Discussion 99

7. Application to nanoparticulate composites **105**
7.1. Model setup 107
7.2. Material modeling 109
7.2.1. Nanoparticles 110
7.2.2. Polymeric matrix 110
7.2.3. Matrix-inclusion-interface 117

7.3. Results and discussion . . . 120
7.3.1. Uniaxial compression . . . 120
7.3.2. Uniaxial tension . . . 121
7.3.3. Discussion . . . 123

8. Summary and outlook 127
8.1. Conclusion . . . 127
8.2. Outlook . . . 128

A. Appendix 131
A.1. Linearization of hyperelasticity . . . 131
A.2. Computation of the two-point correlation function by FOURIER transforms . . 132
A.3. Kinematic and kinetic conclusions from averaging volume integrals over the RVE domain . . . 133
A.4. Diagrams of the Benchmark study . . . 138
A.5. Numerical treatment of the polymeric matrix material law . . . 143
A.6. Insertion of cohesive interfaces . . . 146

Bibliography 151

Acronyms

FCC	face-centered cubic
FE	finite element
FEA	finite element analysis
FEM	finite element method
KUBC	kinematic uniform boundary conditions
ids	identification numbers
RVE	representative volume element
PBC	periodic boundary conditions
PNC	polymer nanocomposites
SUBC	static uniform boundary conditions
UC	unit cell

1. Matrix-inclusion composites in the context of modern computational mechanics

The constant drive for progress and improvement of humanity steadily requires to spawn innovations, ideas and improvements from vague sketches on the drawing table up to the establishment in our everyday life. In that sense, the field of material science represents one fundamental basis that shaped civilizations up to the today's high technological standards. The development of new materials over the course of history can be seen as one of the most influential ingredients in modern human evolution. Already in the prehistory, technological leadership of tribes, nations or societies can be closely related to available materials and the knowledge of processing them. The ability of crafting tools, developing machinery or advance weaponry enabled humans to adopt to environmental circumstances, to increase productivity or to excel competitors. As depicted in Fig. 1.1, the relevance of different materials varied over time. This variation and its paramountcy to shape the individual eras is reflected in their naming. In the prehistorical Stone-Age the usage of materials was restricted to naturally occurring goods such as rocks, feathers, shells, animal skin and clay. Then, the ability to smelt and cast metals, and therefore directly manipulate the material's

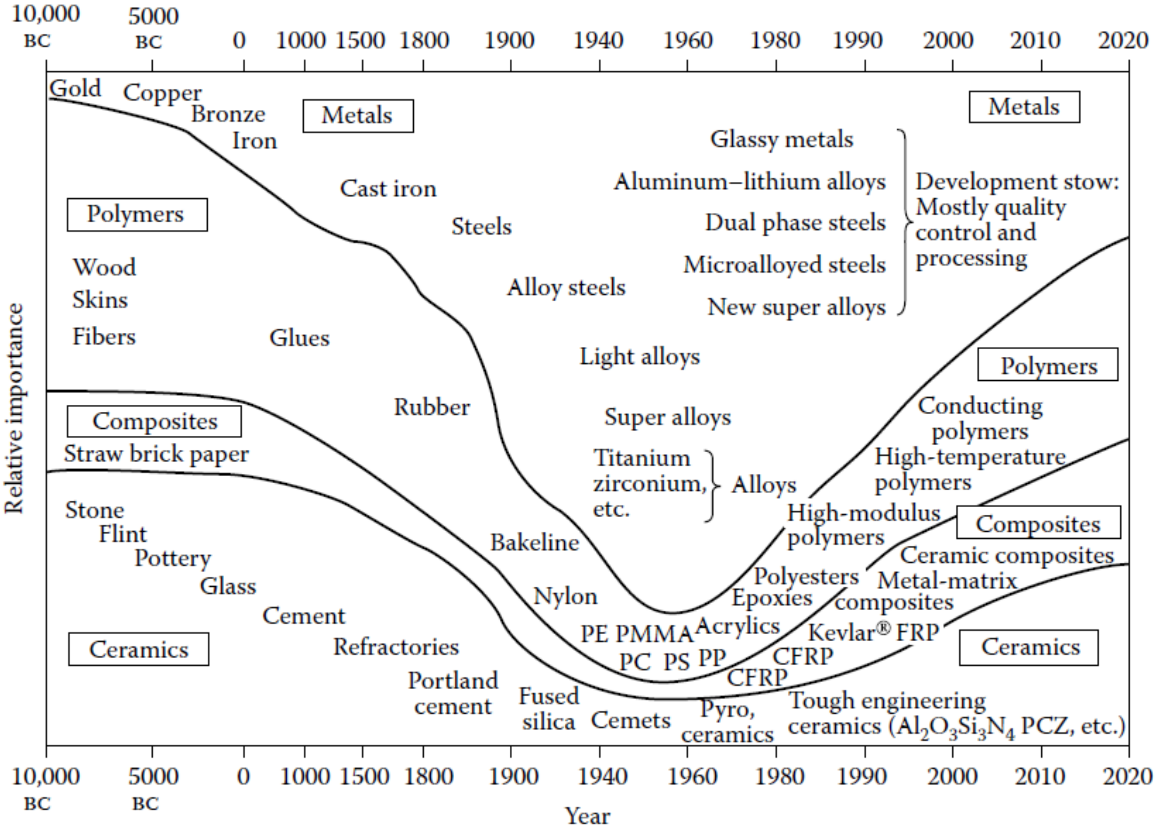

Figure 1.1.: Variation of the relative importance of materials in the course of history. Reprinted from [8] with permission from ROYAL SOCIETY.

composition, heralded the Metal-Age that lasted up to the early modern period (mid 20th century). Developing new alloys was driven by the constant drive to increase material's stiffness, strength and environmental resistance. However, the demands and requirements of increasingly more powerful machines in combination with the urge to increase their efficiency shifted the search to lighter but equally stiff, strong and resistant materials. Therefore, the leadership of metals weakened and alternative materials have been becoming more and more important in the modern industrial age.

One of the most successful and still promising material classes are composites, see the historical review article of Herakovich [97]. As the word composite implies, these materials are purposely or naturally composed of two or more continuum mechanically distinguishable constituents (exept of metallic alloys). The properties of the single constituents are beneficially combined to enhance the overall composite characteristics. Due to their outstanding specific stiffness and specific strength, see e.g. [9], composites represent one of the most important ingredients of our high-tech world today. Furthermore, these materials can show superior impact-resistance, corrosion-resistance, thermal stability and can be more appropriate for structures that rely on a lightweight design.

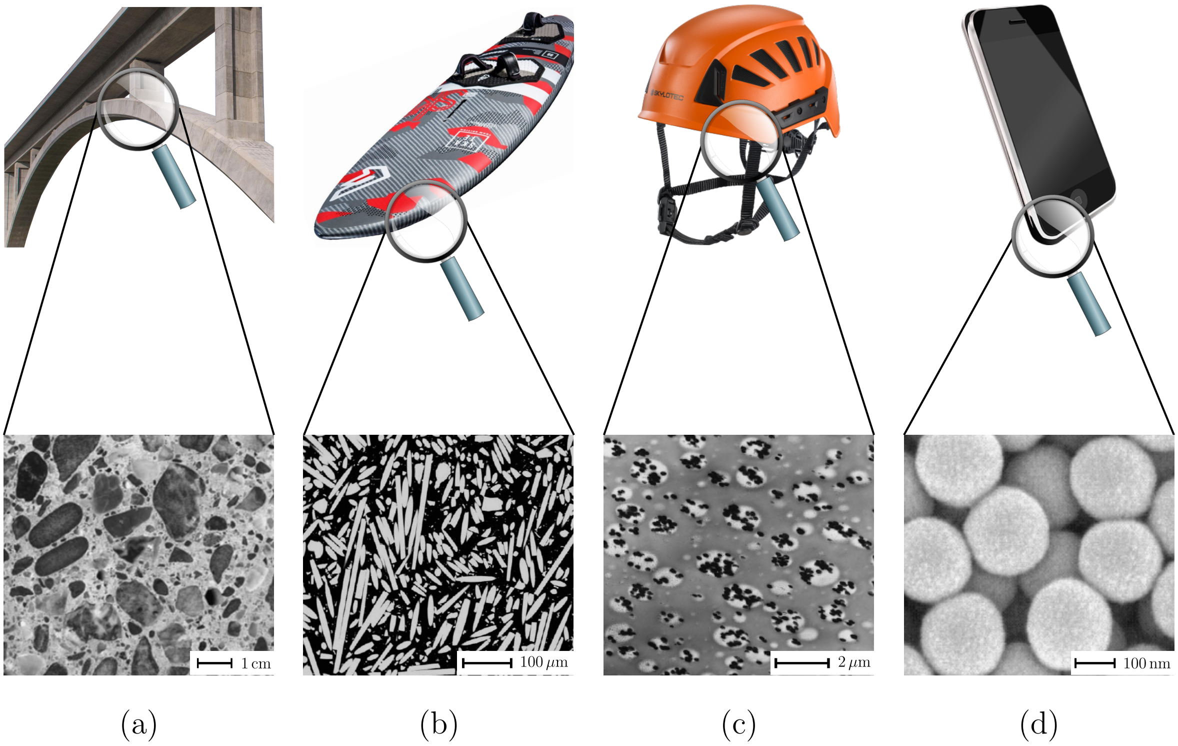

(a) (b) (c) (d)

Figure 1.2.: Different examples of matrix-inclusion composites: macroscopical (industrial) application and micrographs of the microstructure: (a) concrete utilized in bridges[a], (b) glass fiber reinforced composites utilized in surfboards[b], (c) polymer blends utilized in climbing helmets[c] and (d) polymer nanocomposite with possible future applications in phone covers[d].

---

[a] Micrograph image taken from [158] with permission to reprint from McGraw Hill Education. Bridge picture taken from `www.heidelbergcement.de` with permission to reprint HeidelbergCement AG.

[b] Micrograph image taken from [195] with permission to reprint from Elsevier. Windsurfboard image taken from `https://www.fanatic.com` with permission to reprint from Boards & More GmbH.

[c] Micrograph image taken from [243] with permission to reprint from Elsevier. Climbing helmet picture taken from `https://www.skylotec.com` with permission to reprint from Skylotec GmbH.

[d] Micrograph picture taken form [36] with permission to reprint from Elsevier. Smart phone picture taken from `www.pixapay.com`.

Composite materials occur in various forms in nature and industry, see [14]. Besides the ongoing success of long fiber reinforced materials, bicontinuous materials, agglomerates or fabrics, matrix-inclusion composites are of particular importance when it comes to the manufacturing of components of complex shapes (e.g. injection molding or additive manufacturing) and a high production volume. Distinctively differing from their related material classes in terms of micromechanical topology, matrix-inclusion composites are defined by their characteristic micromechanical morphology which is dominated by isolated, non-overlapping particles of arbitrary shape, embedded in a topologically interconnected matrix. Fig. 1.2 exemplarily shows an extract of the bandwidth of various forms of matrix-inclusion composites, which demonstrates their diversity and broad applicability as well as their already occurring integration in todays life.

Concrete, depicted in Fig. 1.2 (a), is characterized by polyhedral aggregates that are blended into a cement matrix. Due to its low production costs, convenient formability and high compressive strength, concrete is heavily utilized in civil engineering and, therefore, is the most widely used composite today. Particle or fiber reinforced composites, see Fig. 1.2 (b), combine very stiff and strong but brittle reinforcements, such as glass fibers or carbon fibers, with the ductile and more compliant properties of the matrix material to form a lightweight but still stiff and strong material that shows a reasonable ductility. By contrast, polymer blends, exemplarily depicted in Fig. 1.2 (c), possess softer inclusions. These are meant to increase the fracture toughness of the neat matrix material, predestinating the composite material for impact critical applications. In polymer nanocomposites, shown in Fig. 1.2 (d), the large inclusion surface area, emanating from the nano-sized nature of the particles, is used to retrieve beneficial mechanical properties. Associated surface effects entail outstanding stiffnesses, hardness and strength that outperform classic fiber reinforced materials.

Due to the diverse, frequent and indispensable occurrences of matrix-inclusions composites in industrial and personal applications today, they are highly relevant and it is of paramount importance to get a deep understanding of these materials.

1.1. Challenges in computational modeling of matrix-inclusion composites

Although the individual micromechanical deformation mechanisms can differ significantly, influences of the micromechanical morphology in terms of particle shapes, particle distributions or inclusion volume fractions is common to all matrix-inclusion composites. This allows to capture a variety of heterogeneous materials by standard simulation methods such as finite element analysis (FEA). FEA represents a valuable tool to grasp, explain and describe the micromechanical deformation behavior of composites and establish a link to macroscopic or effective material properties such as stiffness or strength. To this end, numerical simulations that are considering the microstructural nature of materials became indispensable for dimensioning machinery and components, investigating the mechanical behavior of composites in scenarios not accessible by experiments and analyze new material compositions to obtain so-called taylor-made materials. However, it still remains a major challenge to incorporate such methods from computational micromechanics into the practice of engineering because it remains controversial how to account for all relevant micromechanical features in the most efficient way.

In that sense, the state of the art is to only consider a small, but representative part of the microstructure, namely a representative volume element (RVE), featuring all relevant characteristics of the microstructure [28, 73, 122, 203, 222, 251]. Such an RVE should be of sufficiently large size to capture enough microstructural information while being significantly smaller than the macroscopic structure to hardly influence macroscopic gradients, see [28]. The formulation of a microscopical boundary value problem and the application of periodic boundary conditions (PBC) additionally requires the RVE to be periodic in its discretization, see [28, 87, 130, 165, 229].[1] The major challenges here are associated with the microstructure generation, discretization and the model setup procedure, and hence are related to the preprocessing in the context of FEA.

First, when dealing with randomized matrix-inclusion composites, a realistic representation of the random nature of particle shapes, distributions and arrangements in an RVE is very difficult, see [14]. The major challenge lies in achieving a high inclusion volume fraction while maintaining randomness and ensuring non-overlapping inclusions. Problems such as the attainment of jamming limits, pair-wise non-overlapping checks between inclusions that quickly evolve to a combinatorial exploding amount and the management of anisotropic inclusions need to be coped with. Only few authors employ large RVEs with more than 100 inclusions, see e.g. [45]. Furthermore, these RVEs often do not show periodic topologies nor are they generated by exact distance computations (typically approximative intersection test are conducted), and hence give only low to moderate inclusion volume fractions.

Secondly, the discretization of the RVE is an important step for subsequent simulations but non-trivial, especially if a periodic mesh topology is required for the application of PBC. Although there exist some software packages for a periodic mesh generation, e.g., NETGEN [204] or commercial meshing packages, e.g., ANSYS which allow mesh copying and constrained meshing, there is no straightforward way of generating such meshes reliably in an automated manner. Numerous methods are limited to very simple inclusion geometries, such as spheres. Unstable Boolean operations are a frequent obstacle. On the other hand, the mesh size can easily increase to a level too large for efficient simulations.

These examples highlight the problems and obstacles of a seamless integration of state of the art computational micromechanics into the engineering practices. Hence, there are demands for new ways to generate randomized matrix-inclusion RVEs featuring a periodic mesh topology that can be integrated easily in the engineering work flow.

On the other hand, the relevance of fully periodic computational models in the engineering practice might be questioned after all. Their construction can be very time consuming, even impossible to accomplish for certain microstructures. Therefore, many researchers introduced simplifications and approximations resulting in an inferior convergence of the effective material parameters obtained by computational homogenization. These simplifications affect the size of the RVE [45, 79], the periodicity of the RVE topology, the discretization in terms of voxelization [80, 120] instead of geometrically more exact tetrahedralization or the application of alternative boundary conditions such as kinematic uniform boundary conditions (KUBC), static uniform boundary conditions (SUBC) [112] or approximate PBC (APBC) [123, 251]. However, the impact of such simplifications is not fully understood. In general, the process of modeling advanced materials in engineering practice involves many assumptions, approximations and inaccuracies and the degree of diminishment of releasing the state-of-the-art approach might be in the order of these uncertainties.

1.2. Structure of the thesis

This thesis is concerned with the challenges illustrated in the previous section. The underlying hypothesis assumes a fully periodic RVE as ideal. The tremendous efforts necessary to setup a computational model in that sense will be illustrated. Furthermore, possibilities of relaxing these strict requirements will be highlighted, their effects investigated and recommendations that represent viable alternatives entailing reduced computational costs and ease modeling complications within a justifiable diminishment of accuracy will be given.

To this end, Ch. 2 introduces the micromechanical boundary value problem of micromechancis in the light of continuum mechanics. While covering the necessary notation and fundamental continuum mechanical equations in terms of kinematics and kinetics, the chapter

---

[1] The topology does not necessarily need to be periodic too. However, most of the authors also chose a periodic RVE topology when applying PBC.

focuses on the macrohomogeneity condition which forms the basis of subsequent micromechanical analyses. An overview of the nature of the effects and typical problems in the description of micromechanics is given and related to the state-of-the-art approach which utilizes representative volume elements (RVEs). Important experimental findings and established concepts from mechanical modeling are examined in detail. A critical analysis of existing approaches leads to the logical consequence of a computational micromechanics approach to model modern heterogeneous materials and address the problem of homogenization and localization. To this end, various micromechanical boundary conditions and their implications to the engineering practice are highlighted.

With the general micromechanical problem and resulting requirements to the RVE at hand, Ch. 3 focuses on the for this thesis mainly relevant matrix-inclusion composites. By reviewing experimental findings requirements to realistically model randomized RVEs are given. A classification of typical procedures to obtain the microstructural information allows the identification of approaches suitable for the engineering practice. To this end, artificially generated particle arrangements, in a periodic and non-periodic manner, are pursued. The standard random sequential adsorption scheme featuring geometric primitives such as sphere, ellipsoid, capsule, cylinder and convex polyhedra is examined. In particular, distance computations for each of the geometric primitives are formulated. The generation of high inclusion volume fraction RVEs is demonstrated via collective rearrangement methods. The chapter concludes by evaluating the randomness of the generated RVEs via orientation distributions and micromechanical descriptors.

Ch. 4 pursues the next logical step in the micromechanical modeling procedure that is the discretization. After a brief review of existing meshing strategies, a new meshing algorithm capable of generating a fully periodic mesh is introduced. The master-slave approach and the subsequent hierarchical discretization process is explained in detail. An analysis of the mesh quality together with a comparison to existing meshing softwares underlines the strength of the suggested algorithm.

Ch. 5 gives a detailed description of the algorithmic implementation of the most widely used micromechanical boundary conditions, namely: kinematic uniform boundary conditions (KUBC), periodic boundary conditions (PBC) and static uniform boundary conditions (SUBC). Furthermore, a highly feasible method of applying approximate periodic boundary conditions (APBC) is introduced and verified.

Ch. 6 compares various model setup strategies for the micromechanical boundary value problem by means of a benchmark study. By taking the fully periodic RVE featuring a periodic topology, mesh and PBC as a reference, the effect of relaxations to these conditions are highlighted. In particular, variations of the RVE size, RVE topology, RVE discretization and micromechanical boundary conditions are compared in the light of matrix-inclusion composites with different phase contrast for linear and non-linear material behavior of the constituents. A statistical evaluation of the findings supports a model setup which is a simpler alternative compared to the cumbersome state of the art approach and therefore appropriate in the engineering practice.

In Ch. 7, the gathered methodologies are applied to model a modern high-tech polymer nanocomposite. Via a brief literature review of recent contributions, the dominating micromechanical deformation mechanisms are identified. By utilizing a sophisticated material model for the polymeric matrix, the entropic and energetic deformation regime can be represented in a physically meaningful way. Furthermore, the explicit consideration of the matrix-inclusion interface failure via a cohesive zone model accounts for the non-negligible surface effects. Comparisons with experiments underline the accuracy of the modeling approach and allow for precise investigations of local deformation patterns.

Eventually, Ch. 8 summarizes the findings of this thesis and gives a brief outlook on possible future applications.

2. Continuum Mechanics

This chapter briefly introduces the theoretical concepts of nonlinear continuum mechanics in the light of solid mechanics to the extend necessary for this thesis. The field of continuum mechanics is well documented. More recent works are [44, 84, 103, 247] to name only a few. The basic concept of continuum mechanics manifests in a model description which is completely detached from the discrete nature of matter. In particular, depending on the length scale an atomic or molecular structure or the material's microstructure is not explicitly considered. Instead, an approximative smearing process is conducted. That process allows a spatially smooth and continuous description of bodies in the form of continuous fields and properties. With such an interpretation the powerful mathematical tools of differential geometry are applied to derive analytically exact kinematic relations. Kinetic relations are introduced to provide the causal link between loads and stresses. Furthermore, continuous generalizations of the empirical laws of nature in terms of partial differential equations such as: balance of mass, balance of linear momentum, balance of angular momentum, balance of energy and balance of entropy, are introduced. These balance laws induce the initial and boundary value problem of the investigated body. The kinematic relations are then set into relation with kinetic quantities by constitutive relations to fulfill the continuum mechanical closing problem (i.e. too many unknowns / not enough equations). Finally, this chapter lays special emphasis on the aspect on micromechanics in the light of computational homogenization.

2.1. Notation

Herein all continuum mechanical descriptions are restricted to Cartesian coordinate systems with orthonormal base vectors $\vec{e}_i$ or $\vec{e}_K$ with $i, K \in \{1, 2, 3\}$ in the euclidean space $\mathbb{R}^3$. If not stated otherwise, the EINSTEIN summation convention, which takes the sum over all indices that appear twice in a term, applies. Tensors, understood as physical quantities with directional references, are utilized in various forms:

$$\begin{array}{rl} 0^{\text{th}} \text{ order Tensor:} & \alpha = \alpha \\ 1^{\text{st}} \text{ order Tensor:} & \vec{a} = a_i \vec{e}_i \\ 2^{\text{nd}} \text{ order Tensor:} & \boldsymbol{a} = a_{ij} \vec{e}_i \otimes \vec{e}_j \\ 3^{\text{rd}} \text{ order Tensor:} & \vec{e}^{\,3} = e_{ijk} \vec{e}_i \otimes \vec{e}_j \otimes \vec{e}_k \\ 4^{\text{th}} \text{ order Tensor:} & \mathbb{c} = c_{ijkl} \vec{e}_i \otimes \vec{e}_j \otimes \vec{e}_k \otimes \vec{e}_l \\ & \dots \end{array} \tag{2.1}$$

with the tensor product operator $\otimes$. A single contraction is introduced via the $\cdot$ operator and entails $\vec{a} \cdot \vec{b} = a_i b_i$ for first order tensors and $\boldsymbol{A} \cdot \boldsymbol{B} = A_{ik} B_{kj} \vec{e}_i \otimes \vec{e}_j$ for second order tensors Double contractions are referenced by the : operator and result in $\boldsymbol{A} : \boldsymbol{B} = A_{ij} B_{ij}$ for second order tensors or $\mathbb{c} : \boldsymbol{A} = c_{ijkl} A_{kl} \vec{e}_i \otimes \vec{e}_j$. Additionally to the tensor product the box operator is introduced via $\boldsymbol{A} \,\square\, \boldsymbol{B} : \boldsymbol{C} = \boldsymbol{A} \cdot \boldsymbol{C} \cdot \boldsymbol{B}$. For second order tensors the transpose of a tensor is introduced via $\boldsymbol{A}^{\mathrm{T}} = \left(A_{ij} \vec{e}_i \otimes \vec{e}_j\right)^{\mathrm{T}} = A_{ij} \vec{e}_j \otimes \vec{e}_i$. For fourth order tensors three transpositions are possible: the left subtransposition $\mathbb{c}^{\mathrm{T_L}} = \left(c_{ijkl} \vec{e}_i \otimes \vec{e}_j \otimes \vec{e}_k \otimes \vec{e}_l\right)^{\mathrm{T_L}} = c_{ijkl} \vec{e}_j \otimes \vec{e}_i \otimes \vec{e}_k \otimes \vec{e}_l$, the right subtransposition $\mathbb{c}^{\mathrm{T_R}} = \left(c_{ijkl} \vec{e}_i \otimes \vec{e}_j \otimes \vec{e}_k \otimes \vec{e}_l\right)^{\mathrm{T_R}} = c_{ijkl} \vec{e}_i \otimes \vec{e}_j \otimes \vec{e}_l \otimes \vec{e}_k$ and the major transposition $\mathbb{c}^{\mathrm{T_H}} = \left(c_{ijkl} \vec{e}_i \otimes \vec{e}_j \otimes \vec{e}_k \otimes \vec{e}_l\right)^{\mathrm{T_H}} = c_{ijkl} \vec{e}_k \otimes \vec{e}_l \otimes \vec{e}_i \otimes \vec{e}_j$. With the transpose operators tensors are decomposable into their symmetric part $\boldsymbol{A}^{\text{sym}} = \frac{1}{2}\left[\boldsymbol{A} + \boldsymbol{A}^{\text{T}}\right]$ and antisymmetric part $\boldsymbol{A}^{\text{asym}} = \frac{1}{2}\left[\boldsymbol{A} - \boldsymbol{A}^{\text{T}}\right]$. For fourth order tensors $\mathbb{C}^{\text{sym}_\text{R}} = \frac{1}{2}\left[\mathbb{C} + \mathbb{C}^{\text{T}_\text{R}}\right]$, $\mathbb{C}^{\text{sym}_\text{L}} = \frac{1}{2}\left[\mathbb{C} + \mathbb{C}^{\text{T}_\text{L}}\right]$ and $\mathbb{C}^{\text{sym}_\text{H}} = \frac{1}{2}\left[\mathbb{C} + \mathbb{C}^{\text{T}_\text{H}}\right]$ their antisymmetric counterparts are $\mathbb{C}^{\text{asym}_\text{R}} = \frac{1}{2}\left[\mathbb{C} - \mathbb{C}^{\text{T}_\text{R}}\right]$, $\mathbb{C}^{\text{asym}_\text{L}} = \frac{1}{2}\left[\mathbb{C} - \mathbb{C}^{\text{T}_\text{L}}\right]$ and $\mathbb{C}^{\text{asym}_\text{H}} = \frac{1}{2}\left[\mathbb{C} - \mathbb{C}^{\text{T}_\text{H}}\right]$. The three invariants of a tensor $\boldsymbol{A}$ are denoted by $I_A = \boldsymbol{A} : \boldsymbol{1}$, $II_A = \frac{1}{2}\left[\left[\boldsymbol{A} : \boldsymbol{1}\right]^2 - \boldsymbol{1} : \boldsymbol{A}^2\right]$ and $III_A = \det(\boldsymbol{A})$ with $\boldsymbol{1}$ being the identity tensor. Deviatoric operator $(\dots)'$ of a second order tensor $\boldsymbol{A}$ is defined by

$$\boldsymbol{A}' = \boldsymbol{A} - \frac{I_A}{3}\boldsymbol{1} \ . \tag{2.2}$$

For completeness the gradient operator w.r.t. a spatial position $\vec{x}$ is denoted by $\vec{\nabla}(\dots) = \frac{\partial(\dots)}{\partial \vec{x}} = \frac{\partial(\dots)}{\partial x_i} \otimes \vec{e}_i = (\dots)_{,i} \otimes \vec{e}_i$ and the divergence operator via $\vec{\nabla} \cdot (\dots) = \frac{\partial(\dots)}{\partial x_i} \cdot \vec{e}_i$. Counterparts w.r.t. to a referential position $\vec{X}$ are similarly denoted by $\vec{\nabla}_X$.

2.2. Kinematics

The field of kinematics denotes the general geometrical description of a body's motion regardless of its cause. A material body $\mathcal{B}$ is defined as a compact set of material particles. $\partial\mathcal{B}$ denotes the set of material particles on the body's boundary. The assignment of all positions of these material particles in the physical space $\mathcal{B} \to \mathbb{R}^3$ at time t is called configuration. Now, motion is understood as a continuous sequence of different configurations. Typically, one distinguishes two configurations: the initial or reference configuration $\mathcal{B}_0$ at time $t_0 = 0$ and the current configuration of the body $\mathcal{B}_t$ at time t.[2] The motion function then describes this motion via the mapping

$$\vec{\varphi} : \begin{cases} \mathbb{R}^3 & \to \quad \mathbb{R}^3 \\ \vec{X} & \to \quad \vec{x} = \vec{\varphi}(\vec{X}, t) \end{cases} \tag{2.3}$$

with the position $\vec{x}$ in the current configuration and $\vec{X}$ in the initial configuration. A dependency of functions of $\vec{X}$ is also referenced as material description and favorably utilized in solid mechanics. To describe a compatible deformation, $\vec{\varphi}$ must be bijective. The displacement field is the difference between current and refference configuration

$$\vec{u}(\vec{X}, t) = \vec{x}(\vec{X}, t) - \vec{X} \ . \tag{2.4}$$

With the material time derivative $\dot{(\dots)} = \left.\frac{\partial(\dots)}{\partial t}\right|_{\vec{X}=\text{const.}}$ the motion's velocity is introduced by

$$\vec{v}(\vec{X}, t) = \dot{\vec{u}}(\vec{X}, t) = \frac{\partial \vec{u}(\vec{X}, t)}{\partial t} \ . \tag{2.5}$$

The deformation gradient

$$\boldsymbol{F} = \vec{\nabla}_X(\vec{x}) = \frac{\partial \vec{x}}{\partial \vec{X}} = \vec{\nabla}_X(\vec{u}) + \boldsymbol{1} \quad \text{with} \quad J = \det(\boldsymbol{F}) > 0 \tag{2.6}$$

is a crucial deformation measure. It maps differential line elements $d\vec{X}$ from the reference configuration into the current configuration $d\vec{x}$. To eliminate rotational contributions from $\boldsymbol{F}$, the symmetric left and right stretch tensors $\boldsymbol{U}$ and $\boldsymbol{v}$ are introduced via the polar decomposition

$$\boldsymbol{F} = \boldsymbol{R} \cdot \boldsymbol{U} = \boldsymbol{v} \cdot \boldsymbol{R} \ . \tag{2.7}$$

---

[2] Taking into account only two configurations is the most simple and for this thesis sufficient case. For complex materials so-called intermediate configurations are introduced to consider plasticity, thermal effects etc..

$\boldsymbol{R} \in \mathrm{SO}(3)$ denotes a rotational tensor. In the following the right and left CAUCHY-GREEN stretch tensors $\boldsymbol{C}$ and $\boldsymbol{b}$

$$\boldsymbol{C} = \boldsymbol{F}^{\mathrm{T}} \cdot \boldsymbol{F} \quad \text{and} \quad \boldsymbol{b} = \boldsymbol{F} \cdot \boldsymbol{F}^{\mathrm{T}} \tag{2.8}$$

are of importance. With these stretch tensors the SETH-HILL-family, cf. [99, 208], of strain measures is introduced by

$$\boldsymbol{E}_{(m)} = \frac{1}{m}\left[\boldsymbol{U}^m - \boldsymbol{1}\right] \qquad \text{and} \qquad \boldsymbol{e}_{(m)} = \frac{1}{m}\left[\boldsymbol{1} - \boldsymbol{v}^m\right] \ . \tag{2.9}$$

For $m \to 0$ the strains of Eq. (2.9) become logarithmic (or HENCKY) strains through

$$\boldsymbol{E}^H = \ln(\boldsymbol{U}) \qquad \text{and} \qquad \boldsymbol{e}^H = \ln(\boldsymbol{v}) \ . \tag{2.10}$$

In the case of infinitesimal small displacement gradients $|\vec{\nabla}_X(\vec{u})| \ll 1$, the referential and current configurations fall together and linearizations are permissible. The strain tensors then transform to the infinitesimal strain tensor

$$\boldsymbol{\varepsilon} = \frac{1}{2}\left[\vec{\nabla}(\vec{u}) + \vec{\nabla}(\vec{u})^{\mathrm{T}}\right] \ . \tag{2.11}$$

Besides the state formulations, relying solely on stretches and strains, an alternative formulation via the velocity gradient $\boldsymbol{l} = \vec{\nabla}(\vec{v})$ is possible via

$$\dot{\boldsymbol{F}} = \boldsymbol{l} \cdot \boldsymbol{F} \ . \tag{2.12}$$

Contributions of angular velocities are separated from deformation velocities via a split into the symmetric deformation velocity tensor $\boldsymbol{d}$ and the antisymmetric material spin tensor $\boldsymbol{w}$ by

$$\boldsymbol{d} = \boldsymbol{l}^{\mathrm{sym}} = \frac{1}{2}\left[\boldsymbol{l} + \boldsymbol{l}^{\mathrm{T}}\right] \qquad \text{and} \qquad \boldsymbol{w} = \boldsymbol{l}^{\mathrm{asym}} = \frac{1}{2}\left[\boldsymbol{l} - \boldsymbol{l}^{\mathrm{T}}\right] \ . \tag{2.13}$$

2.3. Kinetics and balance principles

The field of kinetics introduces physical quantities that cause the body's motion by internal and external loadings. All kinds of loadings from all fields of physics are conceivable, e.g. mechanical, thermal, chemical, electrical etc.. In this work, solely mechanical loadings in the scope of a CAUCHY-continuum (neglecting volume moment densities) assumption are considered, which implies loads being forces and tractions only. Therefore, a body might be loaded in form of point, line or surface distributed forces that induce internal forces. To cope with these internal forces the concept of free body diagrams reveals forces $\Delta\vec{F}$ connected with surface area elements Δa in any cut surface, e.g. in the current configuration $\mathcal{B}_t$. The traction vector $\vec{t}$ is then defined as

$$\vec{t} = \lim_{\Delta a \to 0} \frac{\Delta \vec{F}}{\Delta a} \ . \tag{2.14}$$

CAUCHY's fundamental theorem states that $\vec{t}$ depends only linearly on the normal vector $\vec{n}$ of the cut surface through

$$\vec{t} = \boldsymbol{\sigma}^{\mathrm{T}} \cdot \vec{n} \ ,^3 \tag{2.15}$$

which introduces the CAUCHY-stress tensor $\boldsymbol{\sigma}$, defined in the current configuration. $\boldsymbol{\sigma}$ acts as a stress measure and relates to stress measures defined in other configurations via

$$\boldsymbol{\sigma} = \frac{1}{J}\boldsymbol{\tau} = \frac{1}{J}\boldsymbol{F} \cdot \boldsymbol{P} = \frac{1}{J}\boldsymbol{F} \cdot \boldsymbol{S} \cdot \boldsymbol{F}^{\mathrm{T}} \ . \tag{2.16}$$

---

[3] The transposition $(\dots)^T$ is due to the interpretation of the indices of $\boldsymbol{\sigma}$, with the first index referencing the surface and the second index referring to the force.

Here $\boldsymbol{\tau}$ denotes the KIRCHHOFF stress tensor, $\boldsymbol{P}$ the 1st PIOLA-KIRCHHOFF stress tensor (1. PK) and $\boldsymbol{S}$ the 2nd PIOLA-KIRCHHOFF stress tensor (2. PK). In the case of infinitesimal displacement gradients, all stress tensors coincide:

$$\boldsymbol{\sigma} \approx \boldsymbol{\tau} \approx \boldsymbol{P} \approx \boldsymbol{T} \ . \tag{2.17}$$

In the following, the mechanical balance laws that originate from empirical principles are given. All balance laws must be satisfied for the body at all times. They are presented in their local form as typically utilized in solid mechanics (i.e. material description) w.r.t. the current configuration.

Balance of mass

The mass balance states, that in a closed system the mass of a body remains constant. The local form, also known as continuity equation, in material descriptions is given by the equation

$$\dot{\varrho}_0 = \dot{(\varrho J)} = 0 \tag{2.18}$$

with the density of the material body in the reference configuration ϱ_0 and the density of the material body in the current configuration ϱ. The overall statements comes down to the trivial fact that the density of the reference configuration does not change over time.

Balance of linear momentum

The balance of linear momentum is the central balance relation for isothermal solid mechanics, as it acts as the defining field equation of the majority of problems. It states that the change of linear momentum ($\varrho\vec{v}$) over time equals all forces acting on the body, also known as NEWTON's second law of motion. The local form is given by

$$\varrho\dot{\vec{v}} = \vec{\nabla} \cdot \boldsymbol{\sigma}^{\mathrm{T}} + \varrho\vec{f} \tag{2.19}$$

with the specific body force $\vec{f}$. For quasi-static problems the inertia term $\varrho\dot{\vec{v}}$ gets irrelevant and Eq.(2.19) becomes the describing field equation. This is a system of partial differential equations. Associated boundary conditions are formulated via

$$\begin{aligned} \vec{u}(\vec{X}) - \vec{u}_0(\vec{X}) \quad &= 0 \ \forall \ \vec{X} \in \partial\mathcal{B}_0^D \\ \vec{t}(\vec{X}) - \vec{t}_0(\vec{X}) \quad &= 0 \ \forall \ \vec{X} \in \partial\mathcal{B}_0^N \end{aligned} \quad \forall \quad t \in [t_0, t_E] \tag{2.20}$$

with $\vec{u}_0$ being the prescribed displacements on the DIRICHLET boundary $\partial\mathcal{B}_0^D$ and $\vec{t}_0$ the prescribed tractions on the NEUMANN boundary $\partial\mathcal{B}_0^N$ with $\partial\mathcal{B} = \partial\mathcal{B}^D \cup \partial\mathcal{B}^N$. Eq. (2.19) and Eq. (2.20) together with the initial conditions

$$\begin{aligned} \vec{u}(\vec{X}, t_0) &= \vec{u}_0 \\ \vec{v}(\vec{X}, t_0) &= \vec{v}_0 \end{aligned} \tag{2.21}$$

form the initial and boundary value problem of solid mechanics, where $\vec{v}_0$ are the initially prescribed velocities.

Balance of angular momentum

The balance of angular momentum states that the change over time of the moment of momentum ($\vec{x} \times \varrho\vec{v}$) equals the sum of all moments and all moments of all forces acting on the body w.r.t. an arbitrary but fixed point. This balance principle was introduced by EULER and is given in its local form by

$$\boldsymbol{\sigma} = \boldsymbol{\sigma}^{\mathrm{T}} \ , \tag{2.22}$$

which states the symmetry of the CAUCHY stress tensor.

Balance of energy

The balance of energy is also known as the first law of thermodynamics. It equals the change over time of the total energy (internal energy (ϱu) and kinetic energy ($\frac{1}{2}\varrho\vec{v}\cdot\vec{v}$)) to the flux and supply of heat and power. The typical local form is given by

$$\varrho\dot{u} = -\vec{\nabla}\cdot\vec{q} + \boldsymbol{\sigma}^{\mathrm{T}} : \boldsymbol{d} + \varrho r \tag{2.23}$$

with the specific internal energy u, the heat flux vector $\vec{q}$ and the specific heat supply r. $\boldsymbol{\sigma}^{\mathrm{T}} : \boldsymbol{d}$ is known as stress power.

Balance of entropy

To handle the second law of thermodynamics in the scope of continuum mechanics, the balance of entropy s in its local form is introduced via

$$\varrho\dot{s} = -\vec{\nabla}\cdot\vec{h} + \varrho z^s + \varrho p^s \ . \tag{2.24}$$

Here, $\vec{h}$ denotes the flux of entropy, z^s the supply of entropy and p^s the entropy production. The requirement $p^s \geq 0$ then constitutes the second law of thermodynamics. For the practical evaluation of Eq.(2.24), typically the constitutive assumptions w.r.t. $\vec{h} = \frac{\vec{q}}{T}$ and $z^s = \frac{r}{T}$ are made, while introducing the absolute temperature $T > 0$. Employing these assumptions together with Eq.(2.23) yields the Clausius-Duhem- inequality

$$\underbrace{\varrho\left[\dot{s}T - \dot{u}\right] + \boldsymbol{\sigma}^{\mathrm{T}} : \boldsymbol{d}}_{\mathcal{D}^{\mathrm{loc}}}\underbrace{-\vec{q}\cdot\vec{\nabla}\left(\ln(T)\right)}_{\mathcal{D}^{\mathrm{con}}} \geq 0. \tag{2.25}$$

The total dissipation assembles by the local dissipation $\mathcal{D}^{\mathrm{loc}}$ and the conductive dissipation $\mathcal{D}^{\mathrm{con}}$. Satisfying Eq.(2.25) might be cumbersome and the weaker requirement of $\mathcal{D}^{\mathrm{loc}} \geq 0$ and $\mathcal{D}^{\mathrm{con}} \geq 0$ is often postulated.[4] In purely mechanical problems (isothermal) $\mathcal{D}^{\mathrm{con}}$ is immaterial and only the Clausius-Planck- inequality

$$\varrho\left[\dot{s}T - \dot{u}\right] + \boldsymbol{\sigma}^{\mathrm{T}} : \boldsymbol{d} \geq 0 \tag{2.26}$$

must hold. A further alteration of Eq.(2.26) by multiplying J and introducing the free energy $\psi = u - sT$ via the Legendre-transformation gives the final form

$$\boldsymbol{\tau}^{\mathrm{T}} : \boldsymbol{d} - \varrho_0[\dot{\psi} + s\dot{T}] \overset{\text{isothermal}}{=} \boldsymbol{\tau}^{\mathrm{T}} : \boldsymbol{d} - \varrho_0\dot{\psi} \geq 0 \ . \tag{2.27}$$

2.4. Constitutive theory of damage and failure mechanics

The unknown field variables and introduced relations in the previous sections are not sufficient to solve the initial and boundary value problem of solid mechanics. In particular the number of unknown field variables (kinematics and kinetics) does not match the number of given balance relations. This problem is addressed as the continuum mechanical closing problem. Additional equations need to be formulated: the constitutive relations or material laws. These equations relate kinematical to kinetic quantities. They account for the individual properties of the materials a continuum might consist of. In isothermal solid mechanical problems the displacement field $\vec{u}$ is chosen as the primal field variable all other fields depend on.

With regard to a systematic classification and verification of material laws, so called principles of material theory have been introduced in the course of the last century. These principles are deduced to ensure physical plausibility. Some of the more prominent candidates are

---

[4] $\mathcal{D}^{\mathrm{con}} = -\vec{q}\cdot\vec{\nabla}\left(\ln(T)\right) \geq 0$ in combination with the constitutive assumption $\vec{q} = -\boldsymbol{\kappa}\cdot\nabla(T)$, where $\boldsymbol{\kappa}$ denotes the positive tensor of heat conductivity, is also known as Fouriers law.

1. the principle of determinism,
2. the principle of local action,
3. the principle of material objectivity,
4. the principle of thermodynamical admissibility,
5. the principle of equipresence.

The practical formulation of a constitutive law might be conducted in the form of functionals. These functionals can be written explicitly in the form of integrals over the course of the entire deformation or implicitly via differential equations, also called evolution equations. The latter approach is also known as the theory of internal variables which experienced tremendous success in the past decades. The internal variables can generally be denoted as a tensor of order n via $\vec{\alpha}_i^n$. The stress-deformation relation can then be given as

$$\boldsymbol{\tau}(\boldsymbol{F}, \vec{\alpha}_i^n) = \boldsymbol{\tau}(\boldsymbol{b}, \vec{\alpha}_i^n) \ . \tag{2.28}$$

Of particular importance is the fulfillment of the fourth principle in terms of equation Eq. (2.27) which becomes

$$[\boldsymbol{\tau} - 2\frac{\partial \varrho_0 \psi(\boldsymbol{b}, \vec{\alpha}_i^n)}{\partial \boldsymbol{b}} \cdot \boldsymbol{b}] : \boldsymbol{d} - \sum_i \frac{\partial \varrho_0 \psi(\boldsymbol{b}, \vec{\alpha}_i^n)}{\partial \vec{\alpha}_i^n} \odot \dot{\vec{\alpha}}_i^n \geq 0 \ . \tag{2.29}$$

Here $\odot$ denotes the to $\vec{\alpha}_i^n$ appropriate contraction. Since $\boldsymbol{d}$ directly derives from the primal variable of the field equations, any value is adjustable, such that the first term in (2.29) must vanish and the hyperelastic stress deformation relation becomes

$$\boldsymbol{\tau} = 2\frac{\partial \varrho_0 \psi(\boldsymbol{b})}{\partial \boldsymbol{b}} \cdot \boldsymbol{b} \ . \tag{2.30}$$

The local dissipation further reduces to

$$\mathcal{D}^{\text{loc}} = -\sum_i \frac{\partial \varrho_0 \psi(\boldsymbol{b}, \vec{\alpha}_i^n)}{\partial \vec{\alpha}_i^n} \odot \dot{\vec{\alpha}}_i^n \geq 0 \tag{2.31}$$

where $\dot{\vec{\alpha}}_i^n$ are often interpreted as thermodynamical fluxes which the thermodynamical driving forces $\frac{\partial \varrho_0 \psi(\boldsymbol{b}, \vec{\alpha}_i^n)}{\partial \vec{\alpha}_i^n}$ are energy conjugated to. Thermodynamically consistent modeling is ensured by choosing an appropriate free energy function and driving forces.

Hyperelasticity

Elastic materials are defined via their vanishing local dissipation $\mathcal{D}^{\text{loc}}$. Every stress state of the material is a one-to-one mapping from the deformation state. Specifying the free energy ψ ensures this condition. For isotropic materials ψ must only depend on the invariants of $\boldsymbol{b}$ namely I_b, II_b, III_b. For a further simplification in the formulation of ψ the split of the deformation gradient into its isochoric part $\bar{\boldsymbol{F}}$ and volumetric part $\boldsymbol{F}^{\text{vol}}$ is introduced by

$$\boldsymbol{F} = \boldsymbol{F}^{\text{vol}} \cdot \bar{\boldsymbol{F}} = J^{1/3}\mathbf{1} \cdot J^{-1/3}\boldsymbol{F} \ . \tag{2.32}$$

Consequently the isochoric Cauchy-Green stretch tensor is given by $\bar{\boldsymbol{b}} = J^{-2/3}\boldsymbol{b}$. This decoupling allows to better distinguish the contributions of the free energy. By assuming an additive split into isochoric and volumetric parts, the free energy becomes

$$\varrho_0 \psi = \varrho_0 \psi^{\text{iso}}(I_{\bar{b}}, II_{\bar{b}}) + \varrho_0 \psi^{\text{vol}}(J) \ . \tag{2.33}$$

For simplicity often no dependence on the second invariant $II_{\bar{b}}$ is assumed and then the stress deformation relation reads

$$\boldsymbol{\tau} = 2\frac{\partial \varrho_0 \psi}{\partial I_{\bar{b}}} \cdot \bar{\boldsymbol{b}}' + \frac{\partial \varrho_0 \psi}{\partial J} J \mathbf{1} \tag{2.34}$$

with the deviatoric part of the isochoric left Cauchy-Green tensor $\bar{\boldsymbol{b}}' = J^{-2/3}\boldsymbol{b}'$. In Eq. (2.34), the pressure $p(J) = \frac{\partial \varrho_0 \psi}{\partial J}$ and the tangent shear modulus $\mu(\boldsymbol{b}) = 2\left[\frac{\partial \varrho_0 \psi}{\partial I_{\bar{b}}}\right]$ can be identified.[5] In the case of incompressible materials ($J = 1$) the volumetric distribution of the free energy takes the form

$$\varrho_0 \psi^{\mathrm{vol}} = p(J-1) \tag{2.35}$$

with the undetermined pressure p which can be interpreted as a Lagrange multiplier. For small deformations, the stress deformation relation linearizes to the general form of Hookes law

$$\boldsymbol{\tau} \approx \boldsymbol{\sigma} = \mathbb{C} : \boldsymbol{\varepsilon} \tag{2.36}$$

with the elasticity tensor $\mathbb{C}$. $\mathbb{C}$ incorporates 81 unknown tensor coordinates which can be reduced to two independent material parameters for isotropic materials. The stiffness tensor then reads

$$\mathbb{C} = K_0 \mathbf{1} \otimes \mathbf{1} + 2\mu_0 \left[\mathbb{1}^s - \frac{1}{3}\mathbf{1} \otimes \mathbf{1}\right] \tag{2.37}$$

with the initial bulk modulus K_0 and the initial shear modulus μ_0 and the forth oder symmetric identity tensor $\mathbb{1}^s = \frac{1}{2}\left[\mathbf{1} \,\square\, \mathbf{1} + (\mathbf{1} \,\square\, \mathbf{1})^{\mathrm{T_L}}\right]$.

2.5. Computational homogenization and localization

The methods to describe materials, which are presented in the previous section, can be categorized as general heuristic approaches. In particular the majority of established material laws is heuristically based on observations of the macroscopical material behavior such as elasticity e.g. Hookes law Eq. (2.36), plastic yielding, viscous behavior or failure, without any attempts of considering the microstructural nature of materials. More sophisticated models motivate the stress-deformation relation by microscopical considerations, e.g. for polymeric materials considering entropic effects of molecular chain behavior, see the review [26], crystal plasticity models including slip-systems connected to atomic structures, see the review [190] or damage models smearing out microvoid formations, see the review [22]. However, these approaches are often only justified in the case of a homogeneous or single-phased material. In reality, almost all materials exhibit some inhomogeneities at a certain length scale. Inhomogeneities are understood as distinguishable material phases that classify the material as heterogeneous. Prominent examples are composites[6], wood, concrete, solid foams, soils or polycrystals to name only a few. It is well accepted in the literature that the microscopic morphology, that is, the geometric arrangement of distinguishable phases, constitutes the most influential factor for the macroscopic material behavior [28, 105]. The main goal of micromechanical considerations is connecting the different length scales in both directions. Individual constituents are treated as a continuum since the microscopic length scale is assumed to be much larger then the molecular dimensions.

On the one hand, it is of major importance to understand the macroscopical material behavior such as effective material properties, anisotropies etc. based on the microstructural information. This process will be addressed as homogenization or upscaling. The material, which is inhomogeneous on a lower length scale, is described as homogeneous on a larger

---

[5] The reader is referred to Appendix A.1 for a detailed derivation of the deformation tangent shear modulus.

[6] A composite is a man-made material manufactured from two or more constituent materials with significantly different physical or chemical properties. The combination of the raw constituents forms a material with characteristics different from the individual components.

length scale, and one can establish a relationship between the microstructure and the effective mechanical properties on the macroscale (where the material appears homogeneous). In contrast, the so-called localizing or downscaling is understood as the examination of microscopic consequences such as stress distributions, damage initiations and deformation patterns due to macroscopical loading states. Emerging local fields at the length scale of the inhomogeneities are of interest to understand the material's distinctive behavior on the microscopical level.

Either way, the crucial link between the micro- and macroscale is a proper description of the geometric morphology of the phase arrangements on the microscale in combination with a meaningful continuum mechanical transition between the length scales. Fig. 2.1 illustrates this process by introducing macroscopical quantities denoted by $^{\mathrm{M}}(\dots)$. The microstructural description is realized via introducing an representative volume element (RVE). Following this concept, the following questions arise: How to establish a continuum mechanically sound connection between the micro- and macroscale? What properties are required to yield an RVE? How is an RVE defined? The state of the art to answer these question will be given in the following.

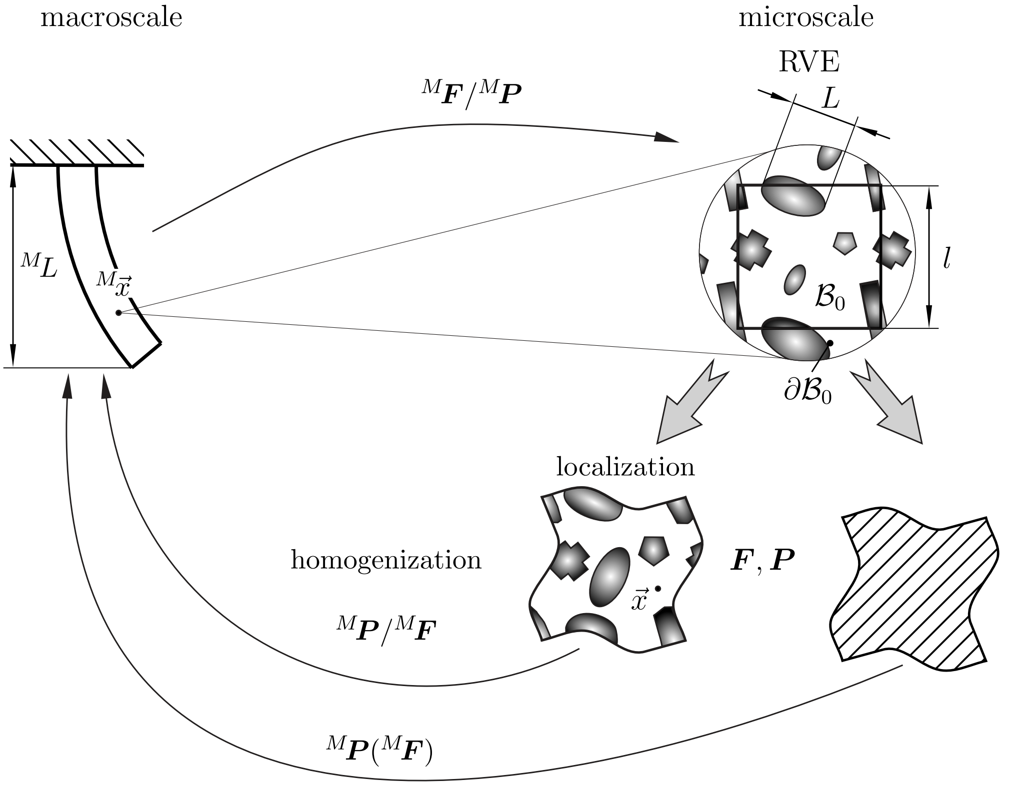

Figure 2.1.: Homogenization and localization in computational micromechanics with characgteristic length scales: macroscopic dimension $^{\mathrm{M}}L$, characteristic dimension of microstructural entities L and characteristic dimension of a representative volume element (RVE) l. Either $^{\mathrm{M}}\boldsymbol{F}$ or $^{\mathrm{M}}\boldsymbol{P}$ act as the macroscopical input to the microscopical analysis. Output are $^{\mathrm{M}}\boldsymbol{P}$ or $^{\mathrm{M}}\boldsymbol{F}$ in a homogeniation analysis or the distribution of field variables for localization purposes.

In the last decades, many researchers contributed to the field of micromechanics which led to a considerable amount of review papers [73, 78, 104, 105, 127, 145, 165, 172, 193, 203] or textbooks [2, 16, 28, 31, 62, 70, 72, 85, 170, 222, 224, 229] and references therein. The research area of micromechancis might be divided into classical analytical methods and computational approaches.

In the early stages of micromechanics as a research area, with the absence of today's computational resources, analytical methods were developed, especially for linear elasticity. Results of these considerations give an effective elasticity tensor $\mathbb{C}^M$. Well-established examples are the VOIGT and REUSS bounds associated with infinitesimal deformations or their finite deformation equivalents, the TAYLOR and SACHS bounds. These approaches neglect any geometrical information by assuming uniform (stress or strain) fields on the microscale and only depend on the volume fraction as the geometric parameter on the micro level. So-called bounds of second order, are suggested by HASHIN-SHTRIKMAN. These bounds are typically very wide and give only rough estimates.

More involved approaches consider geometric properties of the microstructure. The most famous approach is the dilute defect distribution. Assuming non-interacting behavior of the inhomogeneities in form of an infinite dilute distribution of inclusions, so-called single inclusion problems are formulated. The inclusions, as an approximative representation of the microstructure, are embedded in an infinite matrix and the microscopic fields are analyzed. Results of this method rely on the ESHELBY-solution of ellipsoidal inclusions. More advanced methods attempt to consider interactions between the inhomogeneities. Famous examples are the MORI-TANAKA method, the (generalized) self-consistent scheme, the differential method or LIELENS method. However, these methods are only coarse approximations due to the use of simplified geometries and constitutive behaviors, which are necessary for the analytical solutions. As soon as the situation becomes nonlinear (geometrically / physically) or the morphology of the microstructure is rather complex, these methods only give poor results.

To overcome this limitation, modern computational micromechanics, relies on much more detailed representations of the material microstructure. The basic idea is describing the entire material's small length scale morphology by only a finite region, containing sufficient microstructural information, namely the RVE. It is worth noticing that there are several specifications in the literature on the definition of this region or its existence, see [79]. This ambiguity results from the requirement of the *sufficiency* of information.

Clearly, in the situation of a periodic arrangement of microstructural entities a repeating unit cell (UC) exists and therefore the RVE is well defined as stated in [171]. Materials of such structure are also known as periodic media. However, the majority of engineering materials is non-periodic. Typical phase arrangements of heterogeneous media show very complex morphologies. Ideally, a mathematically infinite set of microstructural entities is necessary to capture all information, which results in the sample volume to be infinitely large. Assumptions and approximations are necessary to proceed with a finite sized region.

A fundamental assumption and necessary condition for the existence of an RVE is the ergodicity and statistically homogeneity of the heterogeneous media, see [171]. In particular, this statement allows to extract RVEs at different positions of the material, while maintaining similar morphologies in a statistical sense and equal averaged macroscopic properties, which is indispensable for a statistically valid macroscopic response. For the first time HILL suggests in [98] that an RVE should be typical for the whole mixture on average and contains a sufficient number of entities for the apparent overall moduli. These overall moduli are required to be independent of surface values of tractions and displacements on the RVEs boundary i.e. from the microscopical boundary conditions in general. In particular, the fluctuation of these tractions and displacements about a mean should become insignificant within a short distance of the surface compared to the RVEs dimension. The surface layer contribution to any average needs to be negligible, which is accomplished by a large enough sample. Similarly, the authors in [234] require the RVE to contain statistically enough mechanisms of deformation processes. In addition, an increase of the RVE size should not alter the material's response. In [48], the RVE is linked to the smallest material volume element of the composite for which the usual spatially constant overall macroscopic modulus is a sufficiently accurate model. Furthermore, the RVE needs to be small enough to still be regarded as a material point in a continuum mechanical description on the macroscale and does not disguise any macroscopic heterogeneities, see [57, 238]. GITMAN et al. summarize in [79] that the RVE should include information of the microstructure but simultaneously be sufficiently smaller than dominating macroscopic dimensions. Hence, the opposing requirements of the adverse positions of an RVE being small enough regarding the macroscopic setting and large enough w.r.t. the microstructural features follows. The associated principle is known as the separation of scales

$$^{\mathrm{M}}L \gg l \gg L \ , \tag{2.38}$$

which was first suggested by Hashin in [92]. As depicted in Fig. 2.1, Eq. (2.38) relates the characteristic length of the macroscopic setting $^{\mathrm{M}}L$ to the dimension of the RVE l and the characteristic dimension of the material's microstructure L. Finally, the conclusion, a sample of a material must be large enough to reflect statistical fluctuations on the level of observation, see [254], is drawn. This raises the key questions on how to properly choose $^{\mathrm{M}}L$, l and L or what is the minimum size of an RVE and how to determine the RVE?

As a non-dimensional microstructural control parameter

$$\delta = \frac{l}{L} \tag{2.39}$$

is introduced (ideally $\delta \to \infty$.). The ratio δ is assessable via experiments using stereological and image analyzing techniques such as digital image correlation or X-ray tomography to capture geometrical dispersions. Statistical investigations then lead to quantitative statements. In [189], the authors considered the material class of asphalt concrete, which they regard as a particle matrix composite. The comparison of global properties w.r.t. the specimen size reveals an RVE length of $l = 150\,\mathrm{mm}$ and an aggregate size of $L = 25\,\mathrm{mm}$ or smaller, which gives $\delta = 6.00$. In [209], the authors investigate ceramic matrix composites with reinforcing fibers. Experimental findings in combination with numerical simulations of statistically similar RVEs result in an approximative RVE length scale of $d = 100\,\mu\mathrm{m}$ and a fiber diameter of $14\,\mu\mathrm{m}$ leading to $\delta = 7.14$. While the previous contributions considered isotropic distributions of the inhomogeneities, in [227] unidirectional carbon fiber reinforced composites with a high fiber volume and anisotropic fiber distributions are analyzed and compared to their isotropic counterparts. Congruously, different RVE sizes are necessary due to the anisotropy. While the averaged fiber diameter as the characteristic micro length scale is given with $l = 8\,\mu\mathrm{m}$, they report a minimum RVE size of $l_{\mathrm{iso}} = 473\,\mu\mathrm{m}$ for an anisotropic fiber arrangement and $l_{\mathrm{iso}} = 130\,\mu\mathrm{m}$ for an isotropic fiber arrangement, which leads to $\delta_{\mathrm{aniso}} = 59.13$ and $\delta_{\mathrm{iso}} = 16.25$. In [144], the author analyzes a matrix inclusion composite with granular aggregates (PBS 9501, a highly explosive simulant material). With an average grain sizes of $L = 100\,\mu\mathrm{m}$ the RVE size reveals to be $l = 1.5\,\mathrm{mm}$ which gives $\delta = 15$. A polycrystalline low carbon steel with an average grain size of $20\,\mu\mathrm{m}$ is considered in [186]. The authors report a minimum RVE length of $l = 177\,\mu\mathrm{m}$ which agrees with numerically computed values and corresponds to $\delta = 8.85$. [129] analyzes orthogonal plain woven composites. Experimental full-field deformation measurements reveal an RVE length of ten times the fiber tow widths, which gives $\delta = 10$.

Thus, experimentally, a strong dependence of $\delta \in [6..60]$ on various characteristics of the composite such as the geometry of inhomogeneities, the phase contrast and material classes is observed. The quantitative determination of δ via experiments is possible but very resource consuming.

On the other hand, far more contributions exist in the field of computationally determining the RVE size, see the review section of [193]. Numerical simulations allow to investigate a much richer selection of criteria to quantify and qualify an RVE at much smaller costs. For linear properties, the highly cited contributions [87, 120] need to be highlighted. These studies report that a relatively small number of inhomogeneities is required to form an RVE. Furthermore, quantities such as the physical properties, the contrast of properties, the volume fractions of components, the relative precision for the estimation of the effective property and the number of realizations of the RVE are identified as additional triggering parameters. For non-linear material behavior, the contribution [178] indicates an increased RVE size w.r.t. to linear material behavior. [126] shows that more ensembles are possible as a remedy to utilize smaller RVEs and, thus, a decreased δ. It it worth mentioning that the existence of an RVE in the case of localization phenomena might not be ensured [79, 165].

In summary, it can be concluded that for non-localizing material behavior of microstructural materials truly RVEs exists. Estimating the size of an RVE, quantified by δ, however is a delicate task.

2.5.1. Micro-macro-link

Assuming a proper RVE is found, the continuum mechanical link between the length scales must be established. In particular, the continuum mechanical boundary value problem of the microscale (similar to Sec. 2.2-2.4) needs to be formulated.

On the microscale, all kinematic, kinetic and balance relations as given in the previous sections hold and are properly defined. In the framework of solid mechanics, it proves convenient to conduct the averaging process in the initial configuration of the RVE since the initial setting is known a priori. In particular, the balance equations are formulated in terms of $\boldsymbol{P}$ and $\boldsymbol{F}$. Assuming, the RVE is in a state of quasi-static equilibrium with zero volume forces ($\vec{f} = \vec{0}$) such that the material form of Eq. (2.19) becomes

$$\vec{0} = \vec{\nabla}_X \cdot \boldsymbol{P}^{\mathrm{T}} \ . \tag{2.40}$$

Eq. (2.40) is the central field equation for the microscale. Solely, the boundary conditions remain ambiguous. Likewise, on the macroscale, where continuum mechanical quantities are referenced via ${}^{\mathrm{M}}(\dots)$, the same relations must hold. Here, boundary conditions are given by the specific macro-problem. The key idea for linking both scales manifests in the application of spatial averaging. Spatial averages of quantities defined at RVE level are linked to their macroscopic counter parts. For an arbitrary field variable ${}^{\mathrm{M}}\phi$ on the macroscopic scale, the relation to its microscale counterpart ϕ is defined via

$${}^{\mathrm{M}}\phi = \lim_{V_{\mathrm{RVE}} \to \infty} \frac{1}{V_{\mathrm{RVE}}} \int_{\mathcal{B}_0} \phi(\vec{X}) dV_0 \approx \frac{1}{V_{\mathrm{RVE}}} \int_{\mathcal{B}_0} \phi(\vec{X}) dV_0 \tag{2.41}$$

with the volume of the RVE V_{RVE} and the set of all material points of the RVE $\mathcal{B}_0$. In particular the relation

$$V_{\mathrm{RVE}} = \int_{\mathcal{B}_0} dV_0 \tag{2.42}$$

holds. Eq. (2.41) implicitly makes use of the ergodic hypothesis that states the equality of spatial averages and ensemble averages, see [229] for a detailed discussion. The averaging idea is also based on the fact that gradients on the macro field are not noticeable or applicable to the lower length scale. The macroscopic gradients appear locally constant and are seen by the RVE as uniform fields or far fields, which motivates the omission of body forces $\vec{f}$ in Eq. (2.40). This approach is also known as first order theory.[7] In particular, the connection between both deformation gradients is defined by

$${}^{\mathrm{M}}\boldsymbol{F} = \frac{1}{V_{\mathrm{RVE}}} \int_{\mathcal{B}_0} \boldsymbol{F}\, dV_0 = \frac{1}{V_{\mathrm{RVE}}} \int_{\partial\mathcal{B}_0} \vec{x} \otimes \vec{N}\, dA_0 \ .^{8} \tag{2.43}$$

Applying the divergence theorem, volume integrals are transformed into surface integrals with the RVEs boundary's normal vector in the reference configuration $\vec{N}$ and the differential area element of the reference configuration dA_0. As stated in [131], the averaging concept does not uniquely define the macro-variables by the micro variables. Exemplarily, the definition of the

---

[7] Extensions in form of second-order schemes are given in [131].

[8] A detailed derivation of the transition from volume to surface integrals is given in Appendix A.3.

determinant of the deformation gradient is not straightforward. This is due to the disparity of the average integral and the determinant operation as shown in the following relation

$$\det({}^{\mathrm{M}}\boldsymbol{F}) = \det\left(\frac{1}{V_{\mathrm{RVE}}}\int_{\mathcal{B}_0} \boldsymbol{F}\, dV_0\right) \neq \frac{1}{V_{\mathrm{RVE}}}\int_{\mathcal{B}_0} \det(\boldsymbol{F})\, dV_0 \ . \tag{2.44}$$

Therefore, the definition of the determinant is arbitrarily introduced through[9]

$${}^{\mathrm{M}}J = \frac{1}{V_{\mathrm{RVE}}}\int_{\mathcal{B}_0} J\, dV_0 = \frac{1}{V_{\mathrm{RVE}}}\int_{\mathcal{B}} dv = \frac{v_{\mathrm{RVE}}}{V_{\mathrm{RVE}}} \tag{2.45}$$

with v_{RVE} being the RVE volume in the current configuration. This approximation assumes ${}^{\mathrm{M}}J \approx \det({}^{\mathrm{M}}\boldsymbol{F})$ which is valid for moderate volume changes (${}^{\mathrm{M}}J < 1.5$). The macroscopic 1. PK stress, defined via the volume average of the microscopic 1. PK stress tensor for the quasi-static case, computes to

$${}^{\mathrm{M}}\boldsymbol{P} = \frac{1}{V_{\mathrm{RVE}}}\int_{\mathcal{B}_0} \boldsymbol{P} dV_0 = \frac{1}{V_{\mathrm{RVE}}}\int_{\partial\mathcal{B}_0} \vec{X} \otimes \vec{p}\, dA_0 \ .^{10} \tag{2.46}$$

Here $\vec{p}$ is the stress vector referred to an infinitesimal surface element of the reference configuration and the corresponding force acting on the current configuration.[11] Similar to the determinant of the deformation gradient, the CAUCHY stress tensor can be defined in two ways via the direct volume average or Eq. (2.16), that is

$${}^{\mathrm{M}}\boldsymbol{\sigma}^{*} = \frac{1}{v_{\mathrm{RVE}}}\int_{\mathcal{B}} \sigma dv = \frac{1}{v_{\mathrm{RVE}}}\int_{\partial\mathcal{B}} \frac{1}{2}\left[\vec{t} \otimes \vec{x} + \vec{x} \otimes \vec{t}\,\right] da \neq \frac{1}{{}^{\mathrm{M}}J}{}^{\mathrm{M}}\boldsymbol{F} \cdot {}^{\mathrm{M}}\boldsymbol{P} \quad . \tag{2.47}$$

The CAUCHY stress tensor is then again not uniquely defined due to the multiplicative character of its definition in terms of $\boldsymbol{P}$ and $\boldsymbol{F}$. To circumvent a cumbersome evaluation of volume or surface integrals,

$${}^{\mathrm{M}}\boldsymbol{\sigma} = \frac{1}{{}^{\mathrm{M}}J}{}^{\mathrm{M}}\boldsymbol{F} \cdot {}^{\mathrm{M}}\boldsymbol{P} \tag{2.48}$$

is taken as the definition of ${}^{\mathrm{M}}\boldsymbol{\sigma}$.[12]

Besides kinematic and kinetic quantities, the balance laws must be linked between the micro- and macroscale. It is straightforward to establish this connection for the balance of mass, the balance of linear momentum, the balance of angular momentum and the entropy balance by usage of Eq. (2.41). However, the energy balance incorporates scalar products between thermodynamical conjugated quantities, namely the stress power $\boldsymbol{P}^{\mathrm{T}} : \dot{\boldsymbol{F}}$. Because the power contributions in the energy balance should be deducible from these power conjugated kinematic and kinetic quantities, there is no natural need to define the stress power by some averaging definition. However, a correct mapping between the micro- and the macroscale should hold. This results in the requirement of the equality of the stress power deduced by the macroscopic quantities and the stress power calculated by its microscopically averaged counterparts via

$${}^{\mathrm{M}}\boldsymbol{P}^{\mathrm{T}} : {}^{\mathrm{M}}\dot{\boldsymbol{F}} = \frac{1}{V_{\mathrm{RVE}}}\int_{\mathcal{B}_0} \boldsymbol{P}^{\mathrm{T}} : \dot{\boldsymbol{F}} dV_0 \ . \tag{2.49}$$

---

[9] Eq. (2.45) naturally relates to the well known continuum mechanical relation between infinitesimal volume elements of the reference and current configuration $dv = JdV$.

[10] A detailed derivation of the transition from volume to surface integrals is given in Appendix A.3.

[11] The surface integral form is conceived by applying GAUSS integral theorem and respecting the quasi-static balance of linear momentum $\vec{\nabla}_X \cdot \boldsymbol{P}^{\mathrm{T}} = \vec{0}$ with vanishing body forces $\vec{f} = \vec{0}$. The traction vector $\vec{p}$ relates to $\vec{t}$ via $\vec{t}da = \vec{p}dA_0$.

[12] The contribution [132] points out that the choice of deformation and stress measures and their relation to the microscopic quantities is arbitrary to a certain extend. Typically the macroscopic key quantities (${}^{\mathrm{M}}\boldsymbol{P}$ and ${}^{\mathrm{M}}\boldsymbol{F}$) are derived from the volume averages over the RVE in the reference configuration due to the convenience of computations.

Eq. (2.49) is known as the macro-homogeneity condition or Hill-Mandel condition [98]. It represents the central relation in isothermal micromechanics and acts as an additional equation, which must be satisfied.[13] In practice, Eq. (2.49) dictates the boundary conditions on the microscale, which have yet to be formulated. Fig. 2.1 illustrates the micro-to-macro link by the input and output labeled arrows.

However, the form of Eq. (2.49) is of no practical use. Therefore, the stress and deformation fields are rewritten via their fluctuations, denoted by $\widetilde{(\dots)}$, to

$$\boldsymbol{P} = {}^{\mathrm{M}}\boldsymbol{P} + \widetilde{\boldsymbol{P}} \quad \text{and} \quad \dot{\boldsymbol{F}} = {}^{\mathrm{M}}\dot{\boldsymbol{F}} + \dot{\widetilde{\boldsymbol{F}}} \ . \tag{2.50}$$

These fluctuations, vary around the constant mean (macroscopic) values. Insertion into Eq. (2.49) and rearranging yields

$$0 = \frac{1}{V_{\mathrm{RVE}}} \int_{\mathcal{B}_0} \widetilde{\boldsymbol{P}}^{\mathrm{T}} : \dot{\widetilde{\boldsymbol{F}}} \, dV_0 = \frac{1}{V_{\mathrm{RVE}}} \int_{\mathcal{B}_0} \left[\boldsymbol{P} - {}^{\mathrm{M}}\boldsymbol{P}\right]^{\mathrm{T}} : \left[\dot{\boldsymbol{F}} - {}^{\mathrm{M}}\dot{\boldsymbol{F}}\right] \, dV_0 \ . \tag{2.51}$$

The stress power of the fluctuation fields must vanish.

A simple solution to Eq. (2.51) outlines the approach of setting one of the bracket terms to zero. The prescription of a constant 1. PK stress tensor (Sachs condition) or a constant material time derivative of the deformation gradient (Taylor condition) via

$$\boldsymbol{P} = {}^{\mathrm{M}}\boldsymbol{P} \quad \forall \vec{X} \in \mathcal{B}_0 \qquad \text{or} \qquad \dot{\boldsymbol{F}} = {}^{\mathrm{M}}\dot{\boldsymbol{F}} \quad \forall \vec{X} \in \mathcal{B}_0 \ {}^{14} \tag{2.52}$$

yields two conditions. Both conditions do not require a solution of the boundary value problem on the microscale. For the Taylor a homogeneous deformation is assumed such that a volume averaged evaluation of the constitutive relations of the constituents is done. Similarly, the Sachs condition requires the volume averaged evaluation of the inverse constitutive relations. Congruously, these conditions represent very strong restrictions and are known to form upper and lower bounds for the composite's stiffness and compliance in a finite strain formulation.

Transforming the volume integrals of Eq. (2.51) to surface integrals and respecting Eq. (2.40) results in

$$0 = \frac{1}{V_{\mathrm{RVE}}} \int_{\partial\mathcal{B}_0} \left[\vec{p} - {}^{\mathrm{M}}\boldsymbol{P}^{\mathrm{T}} \cdot \vec{N}\right] \cdot \left[\vec{v} - {}^{\mathrm{M}}\dot{\boldsymbol{F}} \cdot \vec{X}\right] \, dA_0 . \tag{2.53}$$

Eq. (2.53) is a requirement for the boundary values of $\vec{p}$ or $\vec{v}$ on the boundary of the RVE. Thus, the restrictions of Eq. (2.52) are relaxed. Again, the bracket terms are set to zero to receive two opposing conditions. Firstly, the condition

$$\vec{p} = {}^{\mathrm{M}}\boldsymbol{P}^{\mathrm{T}} \cdot \vec{N} \quad \forall \vec{X} \in \partial\mathcal{B}_0 \tag{2.54}$$

is known as static uniform boundary conditions (SUBC) or Neumann boundary conditions. Only the stress vectors are prescribed on the RVEs boundary. Obviously, a potential rigid body motion must be prevented additionally to yield a well posed boundary value problem. Contrary, setting the right bracket term in Eq. (2.53) to zero, restricts the material velocity by

$$\vec{v} = {}^{\mathrm{M}}\dot{\boldsymbol{F}} \cdot \vec{X} \quad \forall \vec{X} \in \partial\mathcal{B}_0 \ . \tag{2.55}$$

This condition goes along with the prescription of the boundary motion through

$$\vec{x} = {}^{\mathrm{M}}\boldsymbol{F} \cdot \vec{X} \qquad \forall \vec{X} \in \partial\mathcal{B}_0 \ , \tag{2.56}$$

---

[13] If thermal behavior is to be considered, an additional macrohomogeneity conditions needs to be fulfilled. By requiring ${}^{\mathrm{M}}\mathcal{D}^{\mathrm{cond}} = -{}^{\mathrm{M}}Q \cdot {}^{\mathrm{M}}\vec{\nabla}_X(T) = \frac{1}{V_{\mathrm{RVE}}} \int_{\mathcal{B}_0} -\vec{Q} \cdot \vec{\nabla}_X(T) dV_0 = \frac{1}{V_{\mathrm{RVE}}} \int_{\mathcal{B}_0} \mathcal{D}^{\mathrm{cond}} dV_0$, which claims the equality of the conductive dissipation computed via averaging on the micro or directly with the macroscale quantities. Here $\vec{Q}$ represents the Lagrangian heat flux vector.

[14] Since the time derivative of the deformation gradient is constant, it is possible to write $\boldsymbol{F} = \boldsymbol{1} + t^{\mathrm{M}}\dot{\boldsymbol{F}}$ which implies $\vec{x} = \vec{X} + t^{\mathrm{M}}\dot{\boldsymbol{F}} \cdot \vec{X} = {}^{\mathrm{M}}\boldsymbol{F} \cdot \vec{X}$, with ${}^{\mathrm{M}}\boldsymbol{F} = t^{\mathrm{M}}\dot{\boldsymbol{F}}$.

assuming a vanishing initial rigid body motion.[15] The boundary conditions of Eq. (2.56) are referred to as kinematic uniform boundary conditions (KUBC) or Dirichlet boundary conditions. Again two opposing cases are introduced by the KUBC or SUBC, which result in upper and lower bounds of the composite's stiffness and compliance.

The third and most sophisticated method accounting for Eq. (2.49) is the application of so-called periodic boundary conditions (PBC). This form can be regarded as a combination of the conditions (2.54) and (2.56) and is state of the art.[16] The key idea is to combine both bracket terms of the integrand in Eq. (2.53) such that the surface integral vanishes. Therefore, the boundary of the RVE is split into two associated parts by

$$\partial\mathcal{B}_0 = \partial\mathcal{B}_0^+ \cup \partial\mathcal{B}_0^- \tag{2.57}$$

as depicted in Fig. 2.2. Every point $\vec{X}^+ \in \partial\mathcal{B}_0^+$ with the normal vector $\vec{N}^+$ possess a correlated point $\vec{X}^- \in \partial\mathcal{B}_0^-$ with a normal vector $\vec{N}^-$. For the normal vectors, the condition

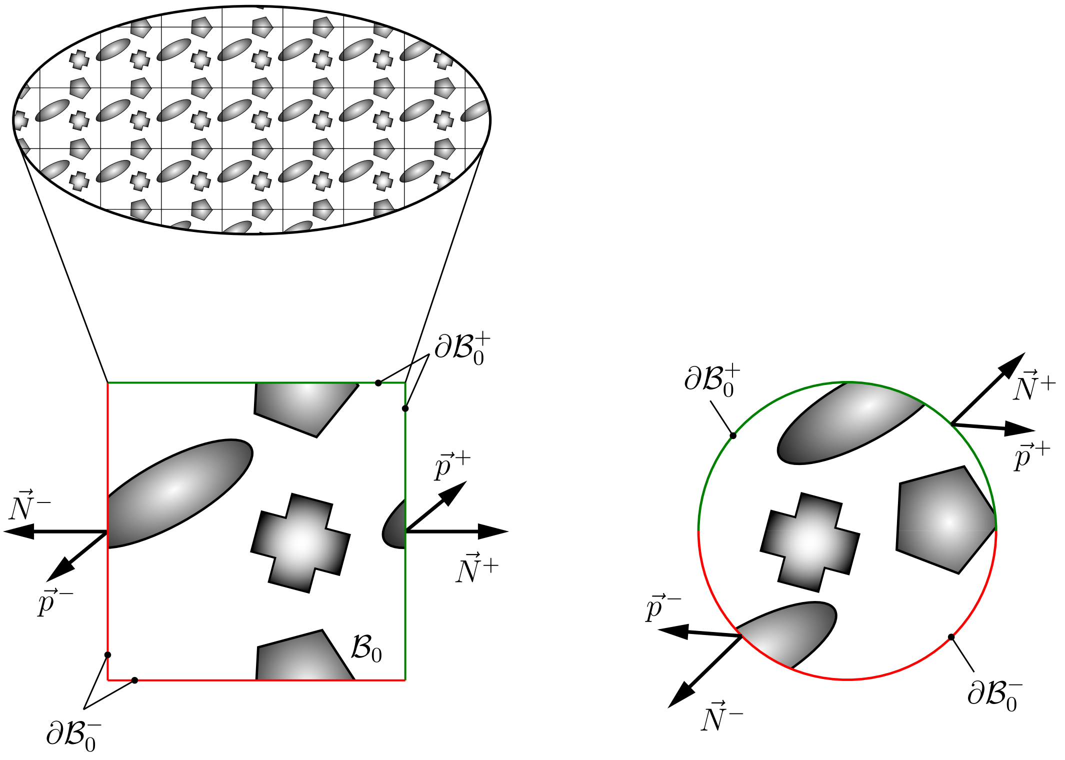

(a) (b)

Figure 2.2.: Different RVE forms featuring a periodic surface split for the application of PBC: (a) cuboidal RVE inherited from periodic media and (b) spherical RVE.

$$\vec{N}^+ = -\vec{N}^- \; \forall \vec{X}^+ \in \partial\mathcal{B}_0^+ \text{ and } \forall \vec{X}^- \in \partial\mathcal{B}_0^- \tag{2.58}$$

must hold. The RVE boundary then reveals a periodic surface topology. Additionally, a fluctuation field $\tilde{\vec{u}}$ of the displacement field $\vec{u}(\vec{X})$ is introduced via

$$\vec{x} = {}^{\mathrm{M}}\boldsymbol{F} \cdot \vec{X} + \tilde{\vec{u}}(\vec{X}) \qquad \text{and} \qquad \vec{v} = {}^{\mathrm{M}}\dot{\boldsymbol{F}} \cdot \vec{X} + \dot{\tilde{\vec{u}}}(\vec{X}) \; . \tag{2.59}$$

---

[15] Since $\vec{v} = {}^{\mathrm{M}}\dot{\boldsymbol{F}} \cdot \vec{X}$ holds, a time integration results in $\vec{x} = t\,{}^{\mathrm{M}}\dot{\boldsymbol{F}} \cdot \vec{X} + \vec{c}_0$ with the constant integration vector $\vec{c}_0$ that is linked to an initial rigid body motion.

[16] Due to the combination of KUBC and SUBC some authors refer to PBC as mixed boundary conditions, see [80].

The constraint

$$\vec{\tilde{u}}^{+} = \vec{\tilde{u}}(\vec{X}^{+}) = \vec{\tilde{u}}(\vec{X}^{-}) = \vec{\tilde{u}}^{-} \ \forall \vec{X}^{+} \in \partial\mathcal{B}_0^{+} \text{ and } \forall \vec{X}^{-} \in \partial\mathcal{B}_0^{-} \tag{2.60}$$

ensures the periodicity of the displacement field. The separation of the RVE's boundary does not alter the average relation between $\boldsymbol{F}^{M}$ and $\boldsymbol{F}$ since

$$\begin{aligned}
\frac{1}{V_{\mathrm{RVE}}}\int_{\mathcal{B}_0} \boldsymbol{F}\, dV_0 &= \frac{1}{V_{\mathrm{RVE}}}\int_{\mathcal{B}_0} {}^{\mathrm{M}}\boldsymbol{F} + \vec{\nabla}_X(\vec{\tilde{u}})\, dV_0 \\
&= {}^{\mathrm{M}}\boldsymbol{F}\frac{1}{V_0}\int_{\mathcal{B}_0} 1\, dV_0 + \int_{\mathcal{B}_0} \frac{\partial \vec{\tilde{w}}}{\partial \vec{X}}\, dV_0 = {}^{\mathrm{M}}\boldsymbol{F} + \int_{\partial\mathcal{B}_0} \vec{\tilde{w}} \otimes \vec{N}\, dA_0 \\
&= {}^{\mathrm{M}}\boldsymbol{F} + \frac{1}{V_{\mathrm{RVE}}}\left[\int_{\partial\mathcal{B}_0^{+}} \vec{\tilde{u}}^{+} \otimes \vec{N}^{+}\, dA_0 + \int_{\partial\mathcal{B}_0^{-}} \vec{\tilde{u}}^{-} \otimes \vec{N}^{-}\, dA_0\right] \\
&= {}^{\mathrm{M}}\boldsymbol{F} + \frac{1}{V_{\mathrm{RVE}}}\underbrace{\left[\int_{\partial\mathcal{B}_0^{+}} \vec{\tilde{u}}^{+} \otimes \vec{N}^{+} - \vec{\tilde{u}}^{+} \otimes \vec{N}^{+}\, dA_0\right]}_{=0} = {}^{\mathrm{M}}\boldsymbol{F}\ .
\end{aligned}$$

Here, the boundary integral of Eq. (2.43) if beneficially divided into its two opposing parts employing Eq. (2.58). The KUBC, defined in Eq. (2.56), are henceforth fulfilled in an average sense, since the boundary contributions of the displacement fluctuations to the deformation gradient vanish only in an integral manner. Therefore, the constraint Eq. (2.56) is relaxed. Employing the same procedure to Eq. (2.53) yields

$$\begin{aligned}
0 &= \frac{1}{V_{\mathrm{RVE}}}\int_{\partial\mathcal{B}_0} [\vec{p} - {}^{\mathrm{M}}\boldsymbol{P}^{\mathrm{T}} \cdot \vec{N}] \cdot [\dot{\vec{u}} - {}^{\mathrm{M}}\boldsymbol{F} \cdot \vec{X}]\, dA_0 = \frac{1}{V_{\mathrm{RVE}}}\int_{\partial\mathcal{B}_0} [\vec{p} - {}^{\mathrm{M}}\boldsymbol{P}^{\mathrm{T}} \cdot \vec{N}] \cdot \dot{\vec{\tilde{u}}}\, dA_0 \\
&= \frac{1}{V_{\mathrm{RVE}}}\left[\int_{\partial\mathcal{B}_0^{+}} [\vec{p}^{\,+} - {}^{\mathrm{M}}\boldsymbol{P}^{\mathrm{T}} \cdot \vec{N}^{+}] \cdot \dot{\vec{\tilde{u}}}^{\,+}\, dA_0 + \int_{\partial\mathcal{B}_0^{-}} [\vec{p}^{\,-} - {}^{\mathrm{M}}\boldsymbol{P}^{\mathrm{T}} \cdot \vec{N}^{-}] \cdot \dot{\vec{\tilde{u}}}^{\,-}\, dA_0\right] \\
&= \frac{1}{V_{\mathrm{RVE}}}\int_{\partial\mathcal{B}_0^{+}} [\vec{p}^{\,+} - {}^{\mathrm{M}}\boldsymbol{P}^{\mathrm{T}} \cdot \vec{N}^{+}] \cdot \dot{\vec{\tilde{u}}}^{\,+} + [\vec{p}^{\,+} + {}^{\mathrm{M}}\boldsymbol{P}^{\mathrm{T}}\vec{N}^{+}] \cdot \dot{\vec{\tilde{u}}}^{\,+} dA_0 \\
&= \frac{1}{V_{\mathrm{RVE}}}\int_{\partial\mathcal{B}_0^{+}} [\vec{p}^{\,+} + \vec{p}^{\,-}] \cdot \dot{\vec{\tilde{u}}}^{\,+} dA_0\ .
\end{aligned} \tag{2.61}$$

Eq. (2.61) is only fulfilled for antiperiodic traction vectors

$$\vec{p}^{\,+}(\vec{X}^{+}) = -\vec{p}^{\,-}(\vec{X}^{-}) \ \forall \vec{X}^{+} \in \partial\mathcal{B}_0^{+} \text{ and } \forall \vec{X}^{-} \in \partial\mathcal{B}_0^{-}\,. \tag{2.62}$$

The set of Eq. (2.58), (2.60) and (2.62) forms the definition of the PBC. A combination of the requirements (2.60) and (2.62) might appear somewhat contradictory, since it is not possible to prescribe DIRICHLET and NEUMANN boundary conditions at the same set of boundary points. However, due to the kinematic constraints, namely the enforced periodic fluctuations of the boundary displacement, antiperiodic traction naturally result, see [81]. The reason for this circumstance lies in the fact that constraints do not contribute to the internal power. Contributions from coupled material points on the RVEs boundary to the internal power read

$$\begin{aligned}
P_P &= \vec{v}^{\,+} \cdot \vec{p}^{\,+} + \vec{v}^{\,-} \cdot \vec{p}^{\,-} = \left[{}^{\mathrm{M}}\dot{\boldsymbol{F}} \cdot \vec{X}^{+} + \dot{\vec{\tilde{u}}}^{+}\right] \cdot \vec{p}^{\,+} + \left[{}^{\mathrm{M}}\dot{\boldsymbol{F}} \cdot \vec{X}^{-} + \dot{\vec{\tilde{u}}}^{-}\right] \cdot \vec{p}^{\,-} \\
&= \underbrace{\left[{}^{\mathrm{M}}\dot{\boldsymbol{F}} \cdot \vec{X}^{+}\right] \cdot \vec{p}^{\,+} + \left[{}^{\mathrm{M}}\dot{\boldsymbol{F}} \cdot \vec{X}^{-}\right] \cdot \vec{p}^{\,-}}_{p_{\mathrm{external}}} + \underbrace{\dot{\vec{\tilde{u}}}^{+} \cdot \left[\vec{p}^{\,+} + \vec{p}^{\,-}\right]}_{p_{\mathrm{constraint}} \overset{!}{=} 0} \\
&= {}^{\mathrm{M}}\dot{\boldsymbol{F}} \cdot \left[\vec{X}^{\,+} - \vec{X}^{\,-}\right] \cdot \vec{p}^{\,+}\ .
\end{aligned} \tag{2.63}$$

Eq. (2.62) is the only choice that ensures a vanishing $p_{\text{constraint}}$.[17] PBC are known to give intermediate results w.r.t. the stiffness and compliance compared to the KUBC and SUBC. This fact entails a quicker convergence to the composite's macroscopic by means of an increasing RVE size for PBC, and hence typically qualifying PBC over the other alternatives.

Tab. 2.1 summarizes all requirements for a continuum mechanical sound link between the micro- and macroscale. Fig. 2.3 illustrates these conditions for a two-dimensional RVE with a soft inclusion and a stiff matrix under shear loading (simple shear or applied shear tractions) for all variants. The TAYLOR conditions results in a homogeneous deformation state where every material point experience the same deformation gradient. KUBC result in flat boundary deformations, PBC show a flat boundary deformation superimposed with periodic displacement fluctuations and SUBC show constant tractions at the boundary which result in a non-periodic deformation pattern of the RVE. The SACHS condition results in a non-admissible deformation state with constant stress over the entire domain. All cases comply with the macro-homogeneity condition (2.49) such that microscopic boundary value problem with its kernel, namely the balance of linear momentum Eq. (2.40), is fulfilled. Inputs from the macroscopic scale which are $\boldsymbol{F}^M$ or $\boldsymbol{P}^M$ yield their energetically conjugated counterparts by solving this microscopic boundary value problem. To utilize this information, typically two variants can be found in the literature. Firstly, the RVE might be subjected to specific macroscopic loading cases (uniaxial tension, shear loading etc.). In homogenization, the computed response is interpreted to identify and calibrate macroscopical continuum mechanical material laws, e.g. the stiffness tensor of an elastic constitutive relation. Otherwise, in the case of localization, prominent deformation mechanisms and modes are investigated to get more

Table 2.1.: Micromechanical settings to fulfill the macro-homogeneity condition Eq. (2.49).

conditions	requirements	
SACHS	$\boldsymbol{P}(\vec X) = {}^{\mathrm{M}}\boldsymbol{P}$	$\forall \vec X \in \mathcal{B}_0$
TAYLOR	$\boldsymbol{F}(\vec X) = {}^{\mathrm{M}}\boldsymbol{F}$	$\forall \vec X \in \mathcal{B}_0$
KUBC	$\vec x(\vec X) = {}^{\mathrm{M}}\boldsymbol{F} \cdot \vec X$	$\forall \vec X \in \partial\mathcal{B}_0$
SUBC	$\vec p(\vec X) = {}^{\mathrm{M}}\boldsymbol{P}^{\mathrm{T}} \cdot \vec N(\vec X)$	$\forall \vec X \in \partial\mathcal{B}_0$
PBC	$\vec x = {}^{\mathrm{M}}\boldsymbol{F} \cdot \vec X + \vec{\tilde{u}}(\vec X)$ $\vec{\tilde{u}}^+(\vec X^+) = \vec{\tilde{u}}^-(\vec X^-)$ $\vec N^+(\vec X^+) = -\vec N^-(\vec X^-)$ $\vec p^+(\vec X^+) = -\vec p^-(\vec X^-)$	$\forall \vec X^+ \in \partial\mathcal{B}_0^+$ and $\forall \vec X^- \in \partial\mathcal{B}_0^-$

---

[17] Furthermore, the quasi-static balance of linear and angular momentum are fulfilled via

$$\begin{aligned} \vec 0 &= \int_{\partial\mathcal{B}_t} \vec t da \overset{\vec t da = \vec p dA_0}{=} \int_{\partial\mathcal{B}_0} \vec p dA_0 = \int_{\partial\mathcal{B}_0^+} \vec p^{\,+} dA_0 + \int_{\partial\mathcal{B}_0^-} \vec p^{\,-} dA_0 \\ &\overset{A_0^+ = A_0^-}{=} \int_{\partial\mathcal{B}_0^+} \vec p^{\,+} + \vec p^{\,-} dA_0 \overset{\vec p^{\,+} = -\vec p^{\,-}}{=} \vec 0 \end{aligned} \tag{2.64}$$

and

$$\begin{aligned} \vec 0 &= \int_{\partial\mathcal{B}_t} \vec x \times \vec t da = \int_{\partial\mathcal{B}_0} \vec x \times \vec p dA_0 = \int_{\partial\mathcal{B}_0} \frac{1}{2} \left[\vec x \times \vec p + \vec x \times \vec p\right] dA_0 \\ &= \frac{1}{2}\left[\int_{\partial\mathcal{B}_0^+} \vec x \times \vec p^{\,+} dA_0 - \int_{\partial\mathcal{B}_0^-} \vec p^{\,-} \times \vec x dA_0\right] \\ &= \frac{1}{2}\left[\int_{\partial\mathcal{B}_0^+} \vec x \times \vec p^{\,+} dA_0 - \int_{\partial\mathcal{B}_0^+} \vec x \times \vec p^{\,+} dA_0\right] \overset{\vec p^{\,+} = -\vec p^{\,-}}{=} \vec 0\,. \end{aligned} \tag{2.65}$$

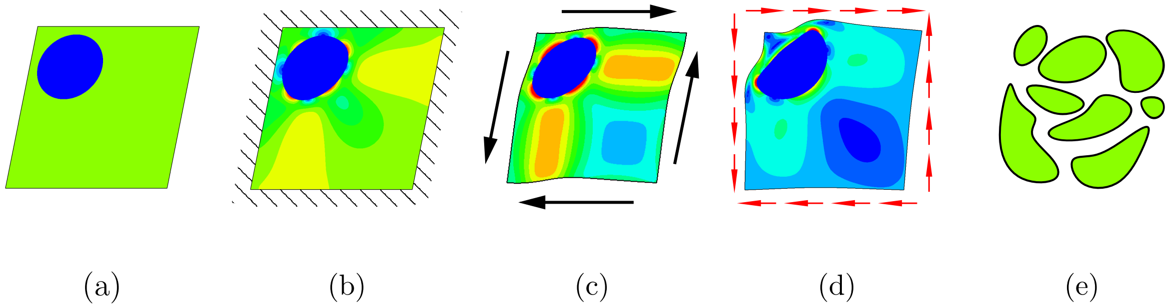
(a) (b) (c) (d) (e)

Figure 2.3.: Different conditions to fulfill the macro-homogeneity condition on the example of an RVE with a soft inclusion and a stiff matrix subjected to macroscopically applied simple shear or shear tractions: (a) TAYLOR conditions, (b) KUBC, (c) PBC, (d) SUBC and (e) SACHS conditions. Contour plots of the VON MISES equivalent stress are shown.

insight in the material's micromechanics. These approaches are very effective and often only require a manageable amount of simulations. On the other hand, it is possible to couple the micro- and macroscale directly, see [61, 75, 132, 226]. The constitutive law (2.28) is replaced by the solution of the microscopic boundary value problem. If the FEM is applied to solve the macroscopic and microscopic boundary value problem, this scheme is referred to as FE^2. The drawback of this approach is its extreme computational costs since every constitutive law evaluation requires the solution of an entire FE problem.

Up to this point, the actual RVE shape has not be specified. In fact, the entire procedure is completely independent of a specific choice of shape. The solution of the microscopic boundary value problem might be seen as a "black box" with its inputs (${}^{\mathrm{M}}\boldsymbol{F}$ or ${}^{\mathrm{M}}\boldsymbol{P}$) and outputs (${}^{\mathrm{M}}\boldsymbol{P}$ or ${}^{\mathrm{M}}\boldsymbol{F}$). The only requirement lies in the realizability of the various settings of Tab. 2.1. In this sense, the most restrictive fact manifests in the requirement of periodic topologies for the application of PBC. As reported in [80–82], the most beneficial shape turns out to be a spherical RVE for two reasons, see Fig 2.2 (b). Firstly, the dependence on the specific choice of boundary conditions is weakened due to the smallest possible surface-to-volume ratio that is provided by a sphere. In particular, the surface integral evaluation in terms of Eq. (2.53) encompasses the largest possible volume. Furthermore, these kinds of RVEs circumvent a material-independent anisotropy like cubical RVEs in combination with PBC. However, spherical RVEs are rarely utilized. A major drawback is a required periodic discretization in the case of PBC. Furthermore, spherical RVEs do not allow further interpretations of the micro-to-macro link since a kinematical admissibility is not given. Most noticeably, spheres are not space filling.

By contrast, cuboidal RVEs are arrangeable in a space filling way, especially under the assumption of periodic media, see Fig 2.2 (a). In a small vicinity around a macroscopical point, RVEs are repeated to form the continuum. It is also possible to associate different macroscopic points with different morphologies representing a locally periodic microstructure. Since the model setup utilizing cuboidal RVEs is more seamlessly integrable in the engineering practice, this kind of RVE is dominating the field of computational micromechanics.

3. Microstructure Generation of matrix inclusion composites[18]

This chapter reviews and substantiates generation methods of RVEs featuring a matrix-inclusion microstructure. After reviewing the literature and state of the art approaches, standard methods are introduced, namely the random sequential adsorption procedure (RSA), molecular dynamic (MD) inspired methods and collective rearrangement methods, which are categorisable as geometrical or artificial RVE generation approaches. These methods generate so-called randomized microstructures, while special emphasis is layed on a periodic and non-periodic generation of randomized microstructural geometry information. All approaches are elaborated for convex inclusions such as spheres, ellipsoids, capsules and cylinders. The crux is represented by distance computations between these geometric primitives. Finally, a statistical quantification of the generated microstructures in terms of orientation distributions and two-point correlation functions is conducted.

The most basic and fundamental characteristic of matrix-inclusion composites relates to the microscopic phase topology. Matrix-inclusion materials define themselves via inclusions, particles, short fibers, voids or aggregates that are distinctively distinguishable from the surrounding matrix material. The matrix embeds these particles in a topologically interconnected manner, whereas the particles are separated. Therefore, solely considering the particle arrangement suffices to describe the entire microstructural geometry information. In [28], BÖHM refers to such kind of materials as *solid suspensions.* They can be found in typical composite materials, porous materials and in closed-cell foams. Typically, the inclusions are meant to improve mechanical properties such as the specific strength in lightweight construction (e.g. short fiber reinforced materials) or fracture toughness (e.g. polymer blends). Additionally, unwanted inclusions like cavities or defects are possible.[19] These might emerge from the manufacturing processes (e.g. injection molding or sintered metals). Materials with distinctive inclusion shapes may exhibit overlapping inclusions, e.g. void coalescence. In that sense, STOYAN suggests in [220] that matrix-inclusion material systems can be divided into

1. systems with isolates particles, which are not in contact and
2. systems with packed particles that are in contact.

In this respect, the particle arrangements are also referred to as packings or particle packings. In the following, only isolated non-overlapping particles are considered, since particles in contact might entail degenerated volumes with infinitely sharp angles (e.g. two spheres in contact).[20] This kind of particle arrangements are also known as hard-core arrangements or non-overlapping inclusions.

A very basic parameter to characterize the particles of matrix-inclusion composites constitutes the aspect ratio α. This aspect ratio is defined via the ratio of the largest over the smallest inclusion dimension (e.g. the length over the diameter of a cylinder). Experimental

---

[18] This chapter is based on the publication "Automatic three-dimensional geometry and mesh generation of periodic representative volume elements of" [199] and "Generation of 3D representative volume elements for heterogeneous materials: A review" [14].

[19] The case of cavities is also referred to as porous material. However, the consideration of these materials in the scope of matrix-inclusion composites is straightforward.

[20] Degenerated volumes often lead to unfavorable discretizations or make it even impossible to conduct a meaningful discretization.

observations indicate various geometries of inclusions from aspect ratios around unity up to several orders of magnitude. In [14], the authors refer to fibers with $\alpha > 100$ as long fibers. Long fibers will not be considered in the following.

An essential but difficult task is the generation of microstructural geometry information, which can be used for building an RVE and discretizing it to obtain a computational model. Ideally, the geometrical information is present in terms of position, orientation and shape of every single inclusion of the microstructure. This information may be given in the form of statistical distributions and microstructural descriptors of all kinds, see [229]. An important and very accessible quantity in this regard is the inclusion volume fraction v_f, which is known to be most influential to the effective (elastic) material behavior. Artificial methods that generate matrix-inclusion composites are often benchmarked against the attainable maximum v_f.

The most natural approach to gain microstructural geometry information are experimental investigations. These indicate various forms and geometric formations of particles, depending on the specific composite. Since matrix-inclusion composites are made of very different materials, ranging from rather soft polymers to hard crystalline ceramics, it is highly complex to find appropriate techniques for investigating the individual composites. Basically, two methods can be found in the literature: destructive and non-destructive methods. In either way, imaging techniques must be employed to collect and process the raw data. Typically, the data is then utilized to completely reconstruct the microstructure or to extract statistical and stereological information such as particle size distributions, orientation distributions, covariance or pair correlation functions etc., see [171, 229].

The most widely applied destructive experimental approaches are cutting and mechanical serial sectioning methods, see the review [236]. In principle, many slices or layers are removed from the material. The generated surfaces of each individual layer are further investigated via imaging techniques. Distinguishable phases need to be present for the data collection, which often requires a surface treatment. Many sequential layers then yield the targeted three-dimensional data. A crucial limitation is that the employed cutting technology and imaging methods must be applicable to all constituents of the composite.

The cutting techniques are dividable into *traditional* macroscopic cutting of slices in the range of μm up to mm. The simplest way of visually investigating the surfaces is based on optical microscopy, which allows large specimen sizes, a fast data collection and is applicable to almost all materials. Exemplarily, in [34, 218] or [118] the authors employed a serial sectioning three-dimensional reconstruction method to a metal matrix composite with an aluminum matrix and silicon carbid (SiC) particles with a particle size in the range of several μm. The surface treatment is conducted by a combination of grinding and polishing.

If the chemical structure of the matrix and particles is very similar or the atomic number differs between the constituents only a little (e.g. co-polymers), the contrast visible with optical microscopy might not be sufficient. Furthermore, optical microscopy has a lower bound to the resolution not allowing the investigation of microstructured materials on the nanoscale. In such cases microtome or ultramicrotome cutting, ion milling or consecutive polishing steps prove to offer viable remedies, see [253].

Atomic-force microscopy is a sophisticated method to investigate nanostructured surfaces, see [50]. This method scans the specimen's surface with a very sub-micron sized tip of only a few nanometers in size. Images with resolutions of fractions of a nanometer are feasible. Exemplarily, [54] investigates biopolymeric and polymeric materials of several nm. Alternatively, [210, 233] employed scanning electron microscopy to conduct the imaging.

If the material removal is unfeasible, non-destructive methods characterize the microstructure by tomography via transmissive radiation, such as X-rays or electrons. By collecting a series of two-dimensional projection images of the microstructures under a variety of angles (tilt series), which are then further processed in reconstruction software, the three-dimensional information of the composites microstructure is obtained. The number of projections in the tilt series and the range of the tilt angles dictates the resolution. Ideally, projections over a range of 360° would be used. The contrast in the projections results from different degrees of X-ray absorption in different material regions. Most commonly, the X-ray tomography, also known as μCT, is employed to metal matrix composites [154], ceramic composites [107], fiber-reinforced materials [55, 133] or woven-fibrous materials [152]. Typically, specimen sizes are in the range of some μm. For nanostructured materials, synchrotron X-ray sources employing parallel beams allow finer resolutions down to the range of some nm. But again, materials with a hardly distinguishable chemical structure are difficult to characterize, since the contrast of the projections is governed to the atomic numbers.

An alternative, is electron tomography, which is based on scanning transmission electron microscopy, see [156]. These methods are often used for biological materials and polymers and rely on the interaction between electrons and matter, which are more intensive than X-rays and matter. Resolutions lay in the range of several 100 nm to 1 nm.

Generally speaking, experimental acquisition of microstructural geometry information to generate RVEs is very labor intensive and costly due to the complex experimental setups. Furthermore, all methods require non-trivial post-processing procedures to identify different constituents and transfer the information in a manageable way. These facts cause experimental methods to be not feasible in the engineering practice and alternatives are necessary. A viable solution are computer-aided simulation methods generating inclusions located in a bounded region of three-dimensional space, namely the RVE. One class of methods is the physics-based microstructure generation approaches.

These approaches simulate real physical processes, which are causative for the final microstructure. Typical for matrix-inclusion microstructures are so-called bulk or mixing processes that occur during the manufacturing process. However, these processes are very complex and labor intensive, such that the simulation time and expenses outrange the gains of finding the desired particle distribution. Therefore, many methods exist that are inspired by the actual physical processes like shakedown, motion of particles, growth simulations or molecular dynamics, but do not exactly model the underlying physical problem.

A prominent simulation method in this regard is the discrete element method, which considers particle movement and interaction, also known as granular flow, see the fundamental work [42]. The core of this method is an explicit calculation scheme for multibody dynamics (rigid bodies). The contact between the particles acts as the fundamental interaction mechanism. Incorporation of gravity establishes a physics-based densification of the particles, which finally leads to the desired microstructure. If all particles are put into a container before the simulation starts, this method is referred to as sedimentation algorithm or mechanical contraction algorithm, see [220]. The densified particles in the container then form the desired RVE. Alternatively, drop-and-roll approaches place particles randomly one by one into a container with gravity present, see [239]. In contrast to sedimentation algorithms, the drop-and-roll approaches are capable of generating RVEs closer to true packings with inclusion volume fractions up to 58% for monodisperse spheres. However, weak anisotropies are always present due to the stacking direction (parallel to the direction of gravity). Since particles are in contact at the final stage, a shrinkage is necessary to yield an isolated matrix-inclusion microstructure. Typically, this approaches is realized with spheres or capsules as the interactions modeling (bouncing) is straightforward, see [244]. In [67, 68], the authors utilize cylinders, which results in a much higher effort.

Another method of generating the microstructural geometry information based on a physical phenomenon, namely growth, is suggested in [17, 59, 140]. Based on the advancing front approach, an initial configuration of three particles forms a front. New particles of different size are randomly attached to enlarge the front until the desired region, i.e. the RVE, is filled. In addition to these packing algorithms, rheological models often are utilized for fiber reinforced composites. The combination of mold filling flow simulations with hydrodynamic models of the fiber movement yields distinctive fiber distributions. These fiber distributions are comparable to the ones gained from common processing techniques such as injection molding. In such particle-based simulations, fibers are represented by chains of spheres [198] or rods [248] and interactions between fibers as well as fibers and the fluid matrix are modeled.

However, the most widely employed classes of methods to generate microstructural geometry information are geometrical methods. Such kind of algorithms operate completely detached from any physical processes, and, hence artificially generate the microstructural geometry information. Only the imitation of an artificial particle setting as closely related as possible to the real microstructure is of importance. With a distinctly reduced effort, these methods are meant to be more accessible than the afore mentioned.

The artificial generation of particle systems has a long history with countless scientific contributions. Crucial to this approach are the mathematical sound description of the employed primitive shapes. Manipulation of these geometric objects in connection with numerical tools for the RVE generation, requires the utilization of computational geometry and can get quite involved. However, all generation methods require a control mechanism to avoid overlapping which necessitates a geometric parameterization of the bodies. Typically, inclusions are approximated via convex bodies namely spheres, ellipsoids, capsules, cylinders or polyhedra, due to their operational ease. Every shape is characterized by its center point $\vec{x}_c$ and shape specific parameters defining their dimensions. For anisotropic bodies, the orientation is described via the normalized direction vector $\vec{d}$ and an angle of rotation γ around this vector. The discussed shapes are then parameterizable through:

$$
\begin{aligned}
&\text{sphere:} && \mathcal{S}(\vec{x}_c, r) && : \{ && [\vec{x}-\vec{x}_c]\cdot[\vec{x}-\vec{x}_c]-r^2 \leq \} \\
&\text{ellipsoid:} && \mathcal{E}(\vec{x}_c, \vec{d}, \gamma, a, b, c) && : \{ && \vec{x}\cdot\boldsymbol{A}\cdot\vec{x}+\vec{b}\cdot\vec{x}+c \leq 0\}^{21} \\
&\text{cylinder:} && \mathcal{C}(\vec{x}_c, \vec{d}, r, l) && : \{ && [\vec{x}-\vec{x}_c]^T\cdot\left[\boldsymbol{1}-\vec{d}\otimes\vec{d}\right]\cdot[\vec{x}-\vec{x}_c]-r^2 \leq 0 \\
& && && && \cap\,[\vec{x}-\vec{x}_c]\cdot\vec{d}-\frac{l}{2} \leq 0 \cap -[\vec{x}-\vec{x}_c]\cdot\vec{d}-\frac{l}{2} \leq 0\} \\
&\text{capsule:} && \mathcal{C}a(\vec{x}_c, \vec{d}, r, l) && : \{ && [\vec{x}-\vec{x}_c]^T\cdot\left[\boldsymbol{1}-\vec{d}\otimes\vec{d}\right]\cdot[\vec{x}-\vec{x}_c]-r^2 \leq 0 \\
& && && && \cap\,[\vec{x}-\vec{x}_c]\cdot\vec{d}-\frac{l}{2} \leq 0 \cap -[\vec{x}-\vec{x}_c]\cdot\vec{d}-\frac{l}{2} \leq 0 \\
& && && && \cup\left[\vec{x}-\vec{x}_c+\frac{l}{2}\vec{d}\right]^T\left[\vec{x}-\vec{x}_c+\frac{l}{2}\vec{d}\right]-r^2 \leq 0 \\
& && && && \cup\left[\vec{x}-\vec{x}_c-\frac{l}{2}\vec{d}\right]^T\left[\vec{x}-\vec{x}_c-\frac{l}{2}\vec{d}\right]-r^2 \leq 0\} \\
&\text{polyhedra:} && \mathcal{P}(\vec{n}_i, d_i) && : \{ && \bigcap_i^m \vec{x}\cdot\vec{n}_i-d_i \leq 0\}.
\end{aligned}
\tag{3.1}
$$

All the geometric primitives and the interpretation of the individual parameters are depicted in Fig. 3.1. By varying inclusion specific parameters, stochastic distributions can be utilized w.r.t. position, orientation and individual shape parameters in a random manner to mimic experimental findings. The shapes then need to be put in a containing region to form an RVE.

As stated in Sec. 2.5.1, different RVE forms are possible. Fig. 3.2 depicts the chosen form in this work, which is also the most widely employed approach, namely a cubical RVE with dimensions l_x, l_y and l_z. One corner of the RVE is located at the origin of the global coordinate system with edges aligned parallel to the coordinate axes as shown in Fig. 3.2. The faces of the RVE are interpreted as subsets of planes $\mathcal{P}_i$. These planes are described by

---

[21] Ellipsoids are described by the parameters $\boldsymbol{A} = \boldsymbol{Q}^T\cdot\tilde{\boldsymbol{A}}\cdot\boldsymbol{Q}, \vec{b} = -2\boldsymbol{A}\cdot\vec{x}_c, c = \vec{x}_c\cdot\boldsymbol{A}\cdot\vec{x}_c - 1, \tilde{\boldsymbol{A}} = \operatorname{diag}\left(1/a^2, 1/b^2, 1/c^2\right)$ and the rotation matrix (here given by Rodrigues' rotation formula) $\boldsymbol{Q} = \vec{d}\otimes\vec{d} + \cos(\gamma)\left(\boldsymbol{1}-\vec{d}\otimes\vec{d}\right) - \sin(\gamma)\vec{\epsilon}^{\,3}\cdot\vec{d}$, see also Sec. 3.1.2..

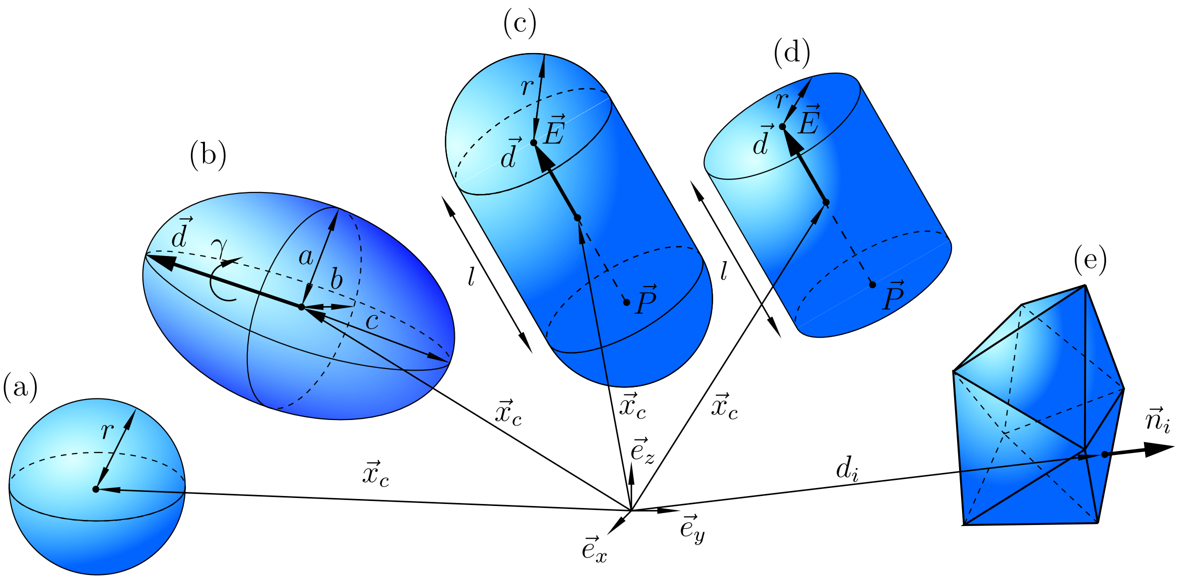

Figure 3.1.: Geometric primitives: (a) sphere, (b) ellipsoid, (c) capsule, (d) cylinder and (e) convex polyhedra. Spheres are isotropic and are only described via their center $\vec{x}_c$ and radius r. Capsules and cylinders are transversal-isotropic bodies and require the orientation $\vec{d}$ to be specified. Ellipsoids are anisotropic, which necessitates the consideration of the rotation angle γ as a third orientation parameter. For ellipsoids the three half-axis are described via the three parameters a, b, c. Capsules and cylinders are defined by two parameters, namely the radius r and length l. Finally convex polyhedra are described by the intersection of n half-spaces where each half-space is defined by the unit normal vector $\vec{n}_i$ and the distance to the coordinate system origin d_i ($3n$ parameter).

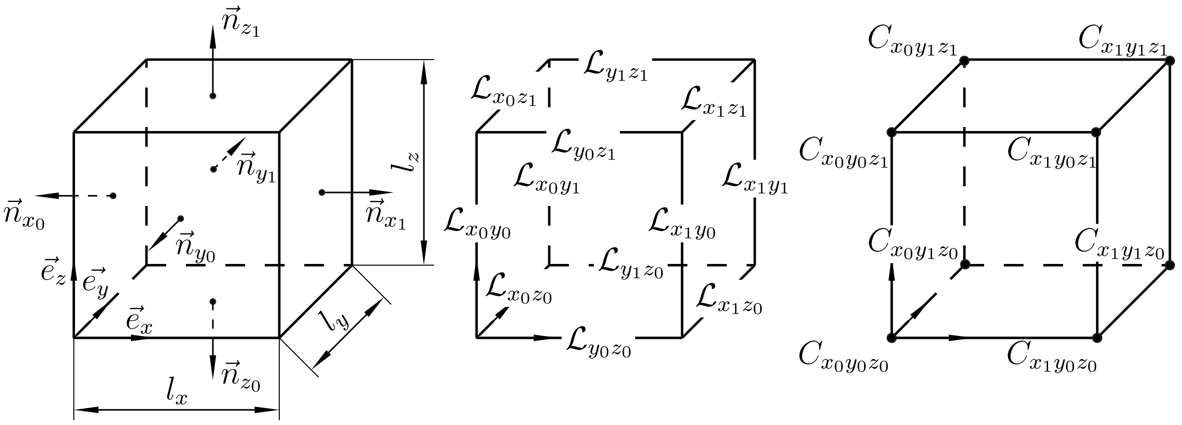

Figure 3.2.: Description of the cube: (a) normal vectors $\vec{n}$ defining faces $\mathcal{P}_i$ and the dimensions l_x, l_y and l_z (see Eq. (3.3)) , (b) edges $\mathcal{L}_i$ (see Eq. (3.5)) and (c) corners C_i (see Eq. (3.6)). Figure reprinted from [199] with permission from Elsevier.

the Hessian normal form

$$\mathcal{P}_i = \{\vec{x} \in \mathbb{R}^3 \,|\, \vec{x} \cdot \vec{n}_p + d = 0\}, \tag{3.2}$$

with the outward normal vector $\vec{n}_p$ and the signed distance of the plane from the origin d.

With this description, the six faces of the cube are defined by

$$\begin{aligned} \mathcal{P}_{x_0} &= \{\vec{n}_{x_0} = [-1,\ 0,\ 0]^{\mathrm{T}}; d = 0\}, & \mathcal{P}_{x_1} &= \{\vec{n}_{x_1} = [1,0,0]^{\mathrm{T}}; d = -l_x\}, \\ \mathcal{P}_{y_0} &= \{\vec{n}_{y_0} = [\ 0,-1,\ 0]^{\mathrm{T}}; d = 0\}, & \mathcal{P}_{y_1} &= \{\vec{n}_{y_1} = [0,1,0]^{\mathrm{T}}; d = -l_y\}, \\ \mathcal{P}_{z_0} &= \{\vec{n}_{z_0} = [\ 0,\ 0,-1]^{\mathrm{T}}; d = 0\}, & \mathcal{P}_{z_1} &= \{\vec{n}_{z_1} = [0,0,1]^{\mathrm{T}}; d = -l_z\}\ . \end{aligned} \tag{3.3}$$

The edges of the cube are defined by subsets of lines $\mathcal{L}_i$

$$\mathcal{L}_i = \{\vec{l} + \lambda\, \vec{n}_L \mid \lambda \in \mathbb{R}\}, \tag{3.4}$$

where $\vec{l}$ is a point on the line and $\vec{n}_L$ its unit direction vector. These 12 subsets are defined via the intersection of two planes as

$$\begin{aligned} &\left.\begin{aligned} \mathcal{L}_{y_0 z_0} &= \{\mathcal{P}_{y_0} \wedge \mathcal{P}_{z_0}\}, & \mathcal{L}_{y_0 z_1} &= \{\mathcal{P}_{y_0} \wedge \mathcal{P}_{z_1}\}, \\ \mathcal{L}_{y_1 z_1} &= \{\mathcal{P}_{y_1} \wedge \mathcal{P}_{z_1}\}, & \mathcal{L}_{y_1 z_0} &= \{\mathcal{P}_{y_1} \wedge \mathcal{P}_{z_0}\} \end{aligned}\right\} \quad \text{with} \quad \vec{n}_L = [1,0,0]^{\mathrm{T}}, \\ &\left.\begin{aligned} \mathcal{L}_{x_0 z_0} &= \{\mathcal{P}_{x_0} \wedge \mathcal{P}_{z_0}\}, & \mathcal{L}_{x_0 z_1} &= \{\mathcal{P}_{x_0} \wedge \mathcal{P}_{z_1}\}, \\ \mathcal{L}_{x_1 z_1} &= \{\mathcal{P}_{x_1} \wedge \mathcal{P}_{z_1}\}, & \mathcal{L}_{x_1 z_0} &= \{\mathcal{P}_{x_1} \wedge \mathcal{P}_{z_0}\} \end{aligned}\right\} \quad \text{with} \quad \vec{n}_L = [0,1,0]^{\mathrm{T}}, \\ &\left.\begin{aligned} \mathcal{L}_{x_0 y_0} &= \{\mathcal{P}_{x_0} \wedge \mathcal{P}_{y_0}\}, & \mathcal{L}_{x_0 y_1} &= \{\mathcal{P}_{x_0} \wedge \mathcal{P}_{y_1}\}, \\ \mathcal{L}_{x_1 y_1} &= \{\mathcal{P}_{x_1} \wedge \mathcal{P}_{y_1}\}, & \mathcal{L}_{x_1 y_0} &= \{\mathcal{P}_{x_1} \wedge \mathcal{P}_{y_0}\} \end{aligned}\right\} \quad \text{with} \quad \vec{n}_L = [0,0,1]^{\mathrm{T}}. \end{aligned} \tag{3.5}$$

The eight corners C_i of the cube are described as the intersection of three planes by

$$\begin{aligned} C_{x_0 y_0 z_0} &= \{\mathcal{P}_{x_0} \wedge \mathcal{P}_{y_0} \wedge \mathcal{P}_{z_0}\}, & C_{x_0 y_1 z_0} &= \{\mathcal{P}_{x_0} \wedge \mathcal{P}_{y_1} \wedge \mathcal{P}_{z_0}\}, \\ C_{x_1 y_1 z_0} &= \{\mathcal{P}_{x_1} \wedge \mathcal{P}_{y_1} \wedge \mathcal{P}_{z_0}\}, & C_{x_1 y_0 z_0} &= \{\mathcal{P}_{x_1} \wedge \mathcal{P}_{y_0} \wedge \mathcal{P}_{z_0}\}, \\ C_{x_0 y_0 z_1} &= \{\mathcal{P}_{x_0} \wedge \mathcal{P}_{y_0} \wedge \mathcal{P}_{z_1}\}, & C_{x_0 y_1 z_1} &= \{\mathcal{P}_{x_0} \wedge \mathcal{P}_{y_1} \wedge \mathcal{P}_{z_1}\}, \\ C_{x_1 y_1 z_1} &= \{\mathcal{P}_{x_1} \wedge \mathcal{P}_{y_1} \wedge \mathcal{P}_{z_1}\}, & C_{x_1 y_0 z_1} &= \{\mathcal{P}_{x_1} \wedge \mathcal{P}_{y_0} \wedge \mathcal{P}_{z_1}\}\,. \end{aligned} \tag{3.6}$$

Various methods exist to artificially generate particle systems embedded in cubical RVEs defined by Eq. (3.2)-(3.6). The main objective is to mimic statistical information from experiments such as location and orientation distributions of particles. As stated above, the most crucial parameter in this regard is the inclusion volume fraction v_f. It may be very difficult to meet the high inclusion volume fractions of real microstructures. This is due to the non-overlapping constraint, which is usually satisfied via pairwise checks of the inclusions in the geometry generation process. These tests are either distance calculations, intersection tests or contact algorithms closely related to computational geometry, see [53, 202].

The simplest geometric inclusion form is a sphere. For spheres, the non-overlapping check reduces to distance calculations between their centers $\vec{x}_c$. Arrangement of spheres, or their two-dimensional counterpart, namely disks, have a wide field of application. For regular arrangements of mono-sized disks, GAUSS proved that the highest possible inclusion volume fraction of $v_f = {}^{\pi}\!/_{2\sqrt{3}} \approx 0.91$ results from a hexagonal positioning of the discs centers (each disc is surrounded by 6 other discs) [40]. The three-dimensional counterpart, incorporating spheres, is known as the KEPLER-conjecture from 1611, which suspects that the maximum possible inclusion volume fraction needs to be a cubic closed packing arrangement (i.e. face-centered cubic structure) or the hexagonally closed-packed structure. As late as in 1998, HALES and FERGUSON verified KEPLERs conjecture in [89] and proved that the maximal attainable inclusion volume fraction is $v_f = {}^{\pi}\!/_{\sqrt{18}} \approx 0.74$. However, for real microstructures a random particle arrangement is more meaningful and the highest possible inclusion volume fraction for the regular arrangement acts as a reference value. In this regard, a random arrangement of particles is referred to as a state of particles, where no structure or pattern is recognizable. In contrast to the previous situation the random closed packing problem of spheres is not well defined, see [230]. Therefore, various generation algorithms can be found in the literature. Several authors report an asymptotic value of $v_f \approx 0.85\%$ [46, 148] for disks and $v_f \approx 0.64$ for spheres [21, 111]. For the highest attainable inclusion volume fraction, the particles are in a seized state, also known as jamming limit. No further movement or repositioning without overlapping is possible anymore. In contrast, arbitrarily large inclusion volume fractions are attainable for spheres of different size.

If shapes more complicated than spheres are considered or high inclusion volume fractions are required, microstructure generation algorithms quickly become very complex [220]. In the following, some of the most widely utilized approaches are presented. Only monodisperse particles are considered, although the presented algorithms are not limited to that constraint. Besides non-periodical RVEs, special emphasis is layed on a randomized periodic microstructure generation, which proves beneficial for a direct application of PBC, see Sec. 2.5. The artificial random microstructures are then interpretable as statistical realizations of stochastic identically distributed processes. All considerations are based on the assumption of statistically homogeneous microstructures that is, properties of the microstructure are not dependent on the position in the macroscopic body.[22] In particular, the generation process should not depend on the local position in order to make the RVE truly representative, see [229]. For statistically homogeneous microstructures, it is common to assume ergodicity. Ergodicity states the equivalence of ensemble averaging (averaging over all realizations of microstructures) and volume averaging w.r.t. an infinite volume of one particular microstructure.[23]

3.1. Random sequential adsorption methods

The random sequential adsorption method (RSA) is the most intuitive and most widely used algorithm to generate non-overlapping matrix-inclusion RVEs and was introduced by WIDOM [242] for spherical particles. Alg. 1 depicts a four step scheme of the RSA. Core is the approval based sequential and random placement of inclusions into the RVE. Before a new inclusion is approved, it has to fulfill the admissibility requirements e.g. non-overlapping. The to-be-placed inclusion has to be checked versus all already accepted inclusions not to intersect or violate a distance larger than a specified threshold. The consideration of additional constraints, such as a minimal distance of the inclusion w.r.t. the RVE boundary or the avoidance of the RVE boundary penetration at all is straightforward. Statistical distributions of inclusion centers (e.g. to mimic cluster effects), orientation distributions, shape variations or periodic positioning of particles resulting in periodic RVE topologies are realizable via an adjustment of the placement procedure. A stopping criteria such as reaching the desired inclusion volume fraction v_f or the attainment of the systems jamming limit such that further placing attempts fail, see [220], stops the algorithm Although the algorithm possesses a tremendous simplicity, its implementation can get very tricky due to a precise formulation and computation of the admissibility checks.

Algorithm 1: Random sequential absorption process.

```
while STOP CRITERION NOT MET (E.G. INCLUSION VOLUME FRACTION $v_f$) do
    randomly place inclusion $i$
    if ADMISSIBILITY CHECK==FALSE then
        reject inclusion $i$
    end
end
```

The simplicity of the algorithm additionally comes with the drawback that RSA methods are only capable of generating packings with low to moderate inclusion volume fractions.

---

[22] In contrast, graded microstructures with, for example, directionally increasing pores are per se not statistically homogeneous. Another counterexample are clustered particle arrangements.

[23] In practice, this infinite volume average is conducted by either assuming a periodic RVE or approximating the infinite volume average by a finite one.

When reaching the jamming limit, the number of rejections increases dramatically. Consequently, generating high inclusion volume fractions gets very time consuming or may be even impossible. FEDER et al. [58] numerically demonstrate an asymptotical jamming limit of $v_f = 54.7\%$ for two-dimensional disks, see also [100, 188]. For three-dimensional spherical inclusions, COOPER [41] reports a maximal attainable limit of $v_f = 38.5\%$ incorporating a total of $9 \cdot 10^6$ placement attempts.

If non-spherical inclusions are considered, this effect aggravates even more. Originating from the anisotropic nature, maximal attainable inclusion volume fractions drastically decrease with an increasing particle aspect ratio α. Inclusions with high aspect ratios and isotropic orientation distributions, very quickly lead to increasingly high number of placement attempts. Experiments, computer simulations and theoretical arguments [180] indicate that the inclusion volume fraction tends towards zero for long straight fibers. Exemplarily, for fibers with an aspect ratio of $\alpha = 20$ these models predict a maximum inclusion volume fraction of 20% [56], 30% [176] or 27% [244]. NARDIN [164] introduced an approximative asymptotic scaling law

$$v_f^{\infty} = \frac{\bar{c}}{\alpha} \tag{3.7}$$

with the constant $\bar{c} \in [4, 5.6]$, see also [244]. In fact, Eq. (3.7) reveals to be independent of the actual anisotropic inclusion shape. Exemplarily, fibers with an aspect ratio of $\alpha = 100$ would result in a maximum attainable inclusion volume fraction of $v_f = 5.6\%$ for an optimistic value of $\bar{c} = 5.6$.

Despite theses limitations RSA methods are popular due to their operational ease. They are applied to various shapes in micromechanical investigations by utilizing mostly statistically uniform distributions for particle positions and orientations. For moderate aspect ratios in the range of $\alpha \in [1, 10]$, typical inclusion volume fractions in the range of 10% to some 20% are observable. In [29] and [30] BÖHM et al. investigate metal-matrix composites. Periodic RVEs with 20 spheres or 15 randomly oriented ellipsoids of revolution or cylinders either with an aspect ratio of $\alpha = 5$ are utilized. They reach inclusion volume fractions of $v_f = 20\%$ for spheres and $v_f = 15\%$ for ellipsoids or cylinders. The non-overlapping constraint is governed by a minimum distance of 0.0075 times the RVE edge length. However, the authors give very little detail on the employed algorithm to compute theses distances. STROEVEN et al. [221] use an RSA approach to generate RVEs with multidisperse spheres in combination with a densification approach to reach inclusion volume fractions up to 70%. These high inclusion volume fractions are reached due to the varying sphere radii. In their method, the inclusions are not allowed to penetrate the RVE boundary. In the same manner, the contribution [235] presents inclusions in the form of cylinders and spheres that do not penetrate the RVE's boundary. With an aspect ratio of up to $\alpha = 7$ and 50 inclusions, volume fractions up to 30% are reached. Again, no details are given concerning the non-overlapping checks w.r.t. the cylinders. KARI et al. [122] utilize RSA approaches to generate periodic RVEs with an inclusion volume fraction of 60% incorporating multidisperse spheres and short chopped fibers approximated by cylinders with an aspect ratio of $\alpha = 5$. Inclusion volume fraction of 25% are reached, see [121]. All RVEs show a moderate amount of inclusions. In particular, the RVE with cylinders feature a low number of inclusions. The non-overlapping check is realized via distance computation between the axis of the cylinders while treating the cylinders as infinite lines or line segments. The authors also reach higher inclusion volume fractions for multidisperse aligned cylinders by successively adding cylinders of equal radii until the jamming limit is reached. Their algorithm proceeds by inserting cylinders with the next lower radius. Here, inclusions do not intersect with the RVEs corners or edges, probably for a more stable subsequent discretization which is necessary for computational modeling. The contributions [174] and [173] present periodic RVEs with 70 cylindrical inclusions featuring an aspect ratio of $\alpha = 10$ and an inclusion volume fraction of 13.5%. The non-overlapping check is realized by intersection test via projections onto linear subsets reducing the problem to line intersections. For convex bodies, like cylinders, it is then sufficient to conduct the intersection test on these subsets. Based on the investigated fiber reinforced composite, only in plane orientation distributions are considered. To reach higher volume fractions up to 35.1%, the authors introduce modifications that feature fiber bending. Galli et al. [69] apply the RSA method to a cubic RVE which is discretized by an unstructured tetrahedral mesh. Sequentially, random vertices from the mesh are chosen as nucleation points for connecting four points to tetrahedra which are taken as particles. Thereby, rejections may occur in the case of overlapping. Eventually, inclusion volume fraction up to 25% are reached. Contrary to the hitherto mentioned contributions featuring small to moderate RVE sizes, Dirrenberger et al. [45] introduce gigantic RVEs with up to 800 cylindrical fibers. The cylinders are modeled as infinitely long. Therefore the RVEs end up to be non-periodic and only an approximate inclusion volume fraction of up to 15% is reached. However, due to the finite length of the RVE and the cylinders radius, the inclusions possess finite aspect ratios. Reasoned by the infinite nature of the inclusions, non-overlapping checks reduce to infinite line distances. In [163], RVEs with a large number of cylindrical inclusions of different aspect ratios and a seemingly low inclusion volume fraction are presented. Unfortunately, the authors give little detail on the implementation. Tian et al. [228] approximate cylinders by capsules and employ corresponding distance computations for capsules. Via a growth inspired procedure, where fibers grow from zero length capsules until the non-overlap criteria is reached, volume fractions of 22.5% are achievable. Salnikov et al. [194] combined 30 spheres and 30 cylinders with an aspect ratio of $\alpha = 5$ to generate RVEs featuring inclusion volume fractions of 20%. Again no distance calculations but intersection tests between the inclusions are conducted to perform the non-overlap checks.

Reviewing all these contributions reveals the following discrepancies:

- If non-spherical particles are considered, often no distance computations but intersection test are conducted to perform the non-overlap check. This approach is prone to generate infinitely small distances between inclusions and thus may result in degenerated volumes. Furthermore, detailed descriptions of distance computations between the inclusions are missing.
- For non-periodic RVEs with inclusions penetrating the RVE boundary, it is unclear how the inclusion volume fractions inside the RVE are obtained. These partial volumes are essential to enter the RVE generation procedure to match a given inclusion volume fraction.
- Only vague elaborations on non-periodic RVEs, periodic RVEs and RVEs featuring inclusions that are penetrating the RVE boundary, are given. Especially, the avoidance of intersections between inclusions and the RVE boundary can deteriorate a desired statistical distribution of particles.

These ambiguities motivate a proper description of the placement procedure and non-overlap checks, which will follow in the subsequent sections. All presented approaches are implemented using the interpreted programming language `Python` (`https://www.python.org/`).

3.1.1. Placement procedure

The placement procedure can be interpreted as a stochastical process to achieve a random RVE. The essence of randomly placing inclusions inside the RVE, described via Eq. (3.2) - (3.6), lies in utilizing statistical distributions for defining parameters of the inclusions. Random positions and orientations are generated, thus, leading to six stochastic parameters in the most general case: three coordinates of the inclusion center $\vec{x}_c$, two angles describing inclusion's orientation vector $\vec{d}(\varphi, \theta)$ and a rotation angle γ around $\vec{d}$. Four random generator functions $\mathcal{R}(\Omega), \mathcal{V}(\Omega), \mathcal{W}(\Omega), \mathcal{T}(\Omega)$, with $\Omega \in [0, 1]$ being the probability space, can be arbitrarily chosen to match experimental findings. They are employed to the stochastic parameters via

$$\begin{aligned}\vec{x}_c &\propto [l_x\,\mathcal{R}(\Omega), l_y\,\mathcal{R}(\Omega), l_z\,\mathcal{R}(\Omega)]\ ,\\ \varphi &\propto 2\pi\,\mathcal{V}(\Omega) - \pi\ ,\\ \theta &\propto \pi\,\mathcal{W}(\Omega)\ ,\\ \gamma &\propto 2\pi\,\mathcal{T}(\Omega)\ .\end{aligned} \tag{3.8}$$

The orientation vector $\vec{d}$ is given by

$$\vec{d} = [\sin(\theta)\cos(\varphi), \sin(\theta)\sin(\varphi), \cos(\theta)]^{\mathrm{T}} \tag{3.9}$$

where φ and θ are the azimuth angle and polar angle in a spherical coordinate system. In the following, only generator functions that produce uniform distributions will be considered. This results in $\mathcal{R}(\Omega) = \mathcal{V}(\Omega) = \mathcal{T}(\Omega) = \mathcal{U}(\Omega)$ with $\mathcal{U}(\Omega)$ being the random uniform generator function. To achieve a truly uniform orientation distribution, the polar angle θ must be chosen according to

$$\theta \propto \arccos(2\mathcal{U}(\Omega) - 1)\ .^{24} \tag{3.10}$$

Fig. 3.3 depicts this random placing exemplarily for an ellipsoid of revolution. Starting from the template inclusion, placed and oriented in the tilde-coordinate system where the orientation vector $\vec{d}$ is aligned with $\vec{e}_{\tilde{z}}$, the placement into the RVE is divided into a rotation and a translation.[25] For the rotation operation it proves convenient to generate the proper orthogonal rotation matrix $\boldsymbol{Q} \in \mathrm{SO}(3)$ using Rodrigues' rotation formula

$$\boldsymbol{R}(\beta, \vec{v}\,) = \vec{v} \otimes \vec{v} + \cos(\beta)[\mathbf{1} - \vec{v} \otimes \vec{v}] - \sin(\beta)\vec{\varepsilon}^{\,3} \cdot \vec{v} \quad \text{with} \quad ||\vec{v}||_2 = 1 \tag{3.11}$$

that rotates any vector by an angle β around the vector $\vec{v}$. Here, $\vec{\varepsilon}^{\,3}$ denotes the Ricci tensor that is defined by

$$\varepsilon_{ijk} = \begin{cases} 1 & \text{if} \quad i,j,k = \{(1,2,3),(2,3,1),(3,1,2)\} \\ -1 & \text{if} \quad i,j,k = \{(2,1,3),(1,3,2),(3,2,1)\} \\ 0 & \text{else} \end{cases}\ . \tag{3.12}$$

Transversely isotropic shapes, like ellipsoids of revolution, cylinders or capsules, require a $\boldsymbol{Q}$ only defined by the orientation vector $\vec{d}$ via

$$\boldsymbol{Q}^{\text{trans}}(\vec{d}) = \boldsymbol{R}(\pi, \vec{v}) = 2\vec{v} \otimes \vec{v} - \mathbf{1} \quad \text{with} \quad \vec{v} = \frac{\vec{d} + \vec{e}_{\tilde{z}}}{||\vec{d} + \vec{e}_{\tilde{z}}||_2}\ . \tag{3.13}$$

Then, $\boldsymbol{Q}$ transforms the orientation vector in the tilde coordinate system to the desired orientation via

$$\vec{d} = \boldsymbol{Q}^{\text{trans}} \cdot \vec{e}_{\tilde{3}}\ . \tag{3.14}$$

If the inclusions of consideration are fully anisotropic, a subsequent rotation around $\vec{d}$ must follow and $\boldsymbol{Q}$ is given by

$$\boldsymbol{Q} = \boldsymbol{R}(\gamma, \vec{d}) \cdot \boldsymbol{Q}^{\text{trans}}(\vec{d})\ , \tag{3.15}$$

which is a sequence of rotations that first generate the orientation $\vec{d}$ and then rotate the shape around that $\vec{d}$ by a given angle γ. In the following, only transversely isotropic shapes are considered and $\boldsymbol{Q} = \boldsymbol{Q}^{\text{trans}}(\vec{d})$. Eventually, the rotated inclusion is translated inside the RVE to its final center $\vec{x}_c$.

---

[24] The infinitessimal surface element in spherical coordinates is defined by $dA = \sin(\theta)d\theta d\varphi = -d(\cos(\theta))d\varphi$. A uniform distribution of orientations is analog to a uniform size of infinitessimal surface elements over the unit sphere. To obtain this uniform size, a proper angle distribution needs to be given. Since $d(\cos(\theta))$ and $d\varphi$ are linear in the formular for dA, $\varphi \propto \mathcal{U}(\Omega)$ and $\cos(\theta) \propto \mathcal{U}(\Omega)$ must hold for utilizing uniform sized infinitessimal surface elements. With the adjustment to the entire range of $\varphi \in [-\pi, \pi]$ and $\arccos(\theta) \in [-1, 1]$, the formula (3.10) is received.

[25] This placement directly relates to rigid body kinematics in the scope of continuum mechanics with $\boldsymbol{U} = \mathbf{1}$.

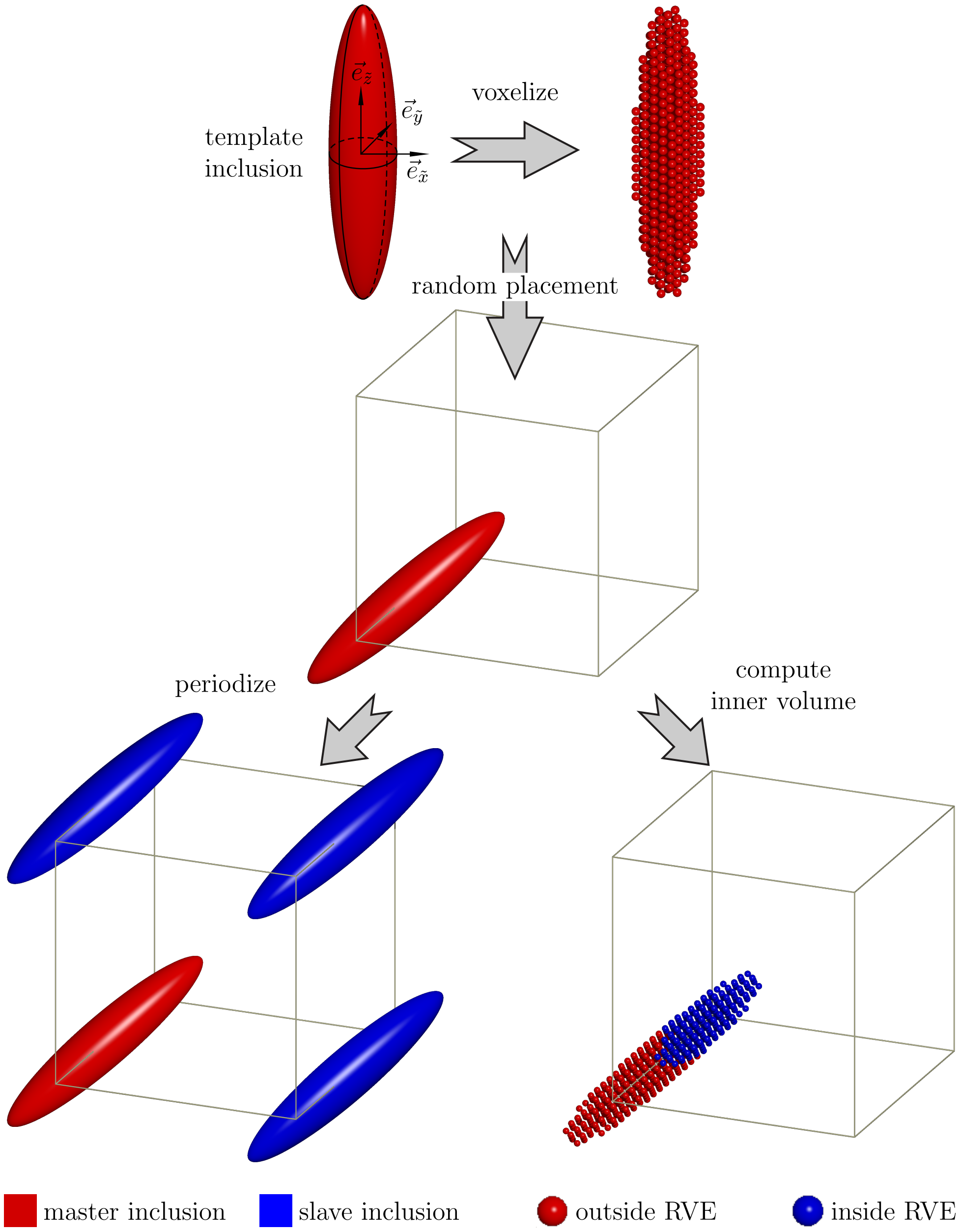

Figure 3.3.: Randomized placement procedure of an inclusion (exemplarily demonstrated with an ellipsoid of revolution) into a periodic or non-periodic setting. Starting from the template state of the inclusion described in the local tilde-coordinate system, the inclusion is voxelized for the non-periodic case. By utilizing random positions and orientations, the inclusion is put in the RVE described in the global coordinate system. For the periodic case, intersections with the RVE boundary faces require periodic continuations. For the non-periodic case, the voxelized image of the inclusions allows a simple approximation of the inner volume of the inclusion.

If the goal is to generate periodic RVEs, periodic counterparts of the inclusion are necessary. An intersection with one of the RVE's boundary faces requires adequate periodic continuations. The intersection information is collected by computing the sign based distances between an inclusion $\mathcal{I}$ and the RVE faces. The distance computation between RVE faces and the inclusion is conducted by solving the constraint optimization problem

$$\min_{\vec{x}\in\mathbb{R}^3} \ \vec{x}\cdot\vec{n}_p + d \quad \text{s.t.} \quad \vec{x}\in\mathcal{I} \ . \tag{3.16}$$

Here, the objective function represents the Hessian normal form of the planes $\mathcal{P}_i : \{\vec{x} \in \mathbb{R}^3 | \vec{x}^{\mathrm{T}} \cdot \vec{n}_p + d = 0\}$, corresponding to the definition of the RVE faces, see Fig. 3.2 and Eq. (3.3). Computing all stationary points of Eq. (3.16) and their corresponding objective function values gives the distances. If the distances possess different signs, the inclusion intersects the RVE face and periodic copies translated to opposing faces need to be generated.

In the example of Fig. 3.3, two RVE boundary face intersections occur such that three additional copies are necessary. If multiple plane intersections are simultaneously present, multiple copies of the inclusions are required to establish periodicity. In particular, edge intersections require three copies and corner intersections require seven copies of the inclusion. It proves convenient to divide the inclusion into master and slave inclusions for a later periodic discretization. Master inclusions intersect with at least one of the faces $\mathcal{P}_{x_0}, \mathcal{P}_{y_0}$ and $\mathcal{P}_{y_0}$ or do not intersect with the RVE boundary at all (inclusion completely inside the RVE). After a successful placement the complete inclusion volume adds to the inclusion volume fraction of the entire RVE.

Contrary, only the intersection volume between the inclusion and the RVE must be considered for the non-periodic case. An analytic computation of intersection volumes between cubes and convex bodies is a non-trivial task and requires numerical strategies even for spheres, see [115]. Therefore, a voxelized inclusion is generated in its template version, see Fig. 3.3 (coarse voxelization with 1000 voxels). This voxel arrangement is then transformed analog to the inclusion itself. Counting the voxel centers inside the RVE and multiplying this number with the voxel volume gives an approximation of the intersection volume that adds to the inclusion volume fraction of the entire RVE. For all considered microstructures in this work $n_{\text{voxel}} = 10^6$ voxels show acceptable accuracy.

3.1.2. Distance computation of convex geometric primitives

The core part of every RSA method is the admissibility constraint, which typically reveals to be the non-overlap check between particles. Categorizable as a pure geometric problem, methods closely connected to computational geometry or computer graphics are used here, see [53, 202]. Since the generated RVEs are intended to be discretized in the scope of computational simulations, degenerated volumes with infinitely sharp corners must be avoided to decrease or even prevent degenerated elements and, thus, guarantee a high discretization quality. Enforcing a large enough threshold distance between inclusions can ensure this request such that very small and badly shaped volumes are almost completely avoidable. Therefore, distance calculations instead of much simpler intersection tests are considered in the following.

The distance computation between two arbitrary objects is a delicate task and plays an important role in many applications such as robotics, computer aided design or computer aided modeling and computer graphics. Within the scope of distance computations, it suffices to describe objects via their bounding surfaces. The distance computations between two objects $\mathcal{I}_0$ and $\mathcal{I}_1$ reveals to be a constraint optimization problem which reads

$$\min_{\vec{x}\in\mathbb{R}^3,\vec{y}\in\mathbb{R}^3} ||\vec{x}-\vec{y}||_2 = \sqrt{[\vec{x}-\vec{y}]\cdot[\vec{x}-\vec{y}]} \ \text{ s.t. } \ \vec{x}\in\mathcal{I}_0 \ , \ \vec{y}\in\mathcal{I}_1 \ . \tag{3.17}$$

The optimal values $\vec{x}^*$ and $\vec{y}^*$ solve problem (3.17) and denote the locations of the two points of minimal distance between the two objects. To circumvent the root in the objective function and associated difficulties concerning the continuity, it is beneficial to optimize the square of the distance, yielding identical optimal values. Unfortunately, problem (3.17) generally reveals to be a non-convex optimization problem, which can be solved analytically only for special cases (e.g. spheres or capsules). Therefore, numerical techniques must be used. For arbitrary shapes, the bounding surfaces can be described via implicit functions or discretized surfaces [35, 217]. As stated in [139], already the distance computation between quadratic surfaces is in general a difficult task since roots of high degree polynomials must be found. The authors suggest a generic algorithm incorporating the idea of decomposing the inclusion boundaries in multiple simpler surfaces resulting in pairwise distance computations between these smaller surfaces. However, those general methods entail much effort and are not feasible to be used in RSA approaches where a large amount of distance computations needs to be conducted. For an efficient RSA distance computations must be computationally very fast. For the convex geometric primitives of Fig. 3.1, efficient iterative schemes exist.

Furthermore, the admissibility check of the RSA must be extended to distance computations between inclusion and RVE boundaries, namely faces and corners, to circumvent the formation of degenerated volumes and ensure a subsequent high discretization quality. With these distance computations, problematic clearances or intersections between inclusions and the RVE boundary can be reduced or even circumvented. To this end, the extremal points of the underlying distance problem, namely face-inclusion distance and point-inclusion distance, are computed. Unfortunately, distance computations w.r.t. the RVE edges are not reasonable since an RVE edge penetrating an inclusion need not necessarily lead to a degenerated volume although the RVE edge inclusion distance is zero. However, sharp angles between RVE edges and inclusion boundaries might occur and can not be circumvented. To minimize the restrictions on the randomness of the placement procedure, and, hence facilitating the representativeness of the generated microstructure, no threshold distance between inclusions and edges is set.

The general problem of distance calculations w.r.t. faces and corners is realized by substituting $\mathcal{I}_1$ in problem (3.17) by either a planar surface that holds an RVE face or by a point representing an RVE corner. This leads to the following three checks constituting the admissibility inspection that needs to be done for every placed inclusion against a threshold distance $d_{\min} > 0$:

(a) inclusion-inclusion distance computation,

(b) inclusion-face distance computation,

(c) inclusion-corner distance computation.

For spheres, the cases (a) and (c) simplify to distance computations between points and (b) reduces to the distance computation between a point and a plane. In the following these three distance computation will be presented for ellipsoids, capsules and cylinders.

Ellipsoids

Ellipsoids can be regarded as scaled spheres and show a smooth surface. As depicted in Fig. 3.1, the half axes a, b and c act as the shape defining parameters. A mathematically sound description of an arbitrary placed ellipsoid is established via an implicit function of the form

$$\mathcal{E} : \left\{ \vec{x} \cdot \boldsymbol{A} \cdot \vec{x} + \vec{b} \cdot \vec{x} + c \leq 0 \right\} \tag{3.18}$$

where the positive definite matrix $\boldsymbol{A}$, the vector $\vec{b}$ and scalar c are given via

$$\boldsymbol{A} = \boldsymbol{Q}^T \cdot \tilde{\boldsymbol{A}} \cdot \boldsymbol{Q} \ , \ \vec{b} = -2\boldsymbol{A} \cdot \vec{x}_c \ , \ c = \vec{x}_c \cdot \boldsymbol{A} \cdot \vec{x}_c - 1 \ , \ \tilde{\boldsymbol{A}} = \operatorname{diag}\left(\frac{1}{a}, \frac{1}{b}, \frac{1}{c}\right) \ . \tag{3.19}$$

The ellipsoid's center $\vec{x}_c$ and the rotation tensor $\boldsymbol{Q}$ arise from the random placement procedure.[26]

Lin et al. [143] suggest a numerically efficient iterative algorithm for solving the ellipsoid-ellipsoid distance problem. Fig. 3.4 (a) illustrates the fundamental idea of their method. Initially, spheres are inserted into $\mathcal{E}_0$ and $\mathcal{E}_1$ such that they are inside their corresponding ellipsoid and tangential to the respective boundaries. The sphere radii choice of $r = \frac{1}{\sqrt{\boldsymbol{A}:\boldsymbol{A}}}$ and the initial sphere position at the ellipsoids centers ensures these conditions. The iterative process starts by computing the connecting line between both sphere centers and its penetration points of $\mathcal{E}_0$ and $\mathcal{E}_1$. Inserting the line equation $\vec{x} = \vec{c}_0 + t[\vec{c}_1 - \vec{c}_0]$ with the sphere centers $\vec{c}_0$ and $\vec{c}_1$ into the equal sign version of Eq. (3.18) for both ellipsoids results in a quadratic equation for t, which determines the penetration points. For numerical stability, the quadratic equation is solved in accordance to the solution method given in [184]. The penetration points act as the new tangential location for the spheres inside the ellipsoids. By using the ellipsoids gradients at the penetration points (which are parallel to the ellipsoids normal vector $\vec{n}$), the new sphere centers are computed. The entire process is repeated until the direction of the connection line $\vec{c}_1 - \vec{c}_0$ is parallel with $\vec{n}$ at the actual penetration points. The resulting connection line between the penetration points then represents the shortest connection path between the two ellipsoids with its magnitude being the desired distance.

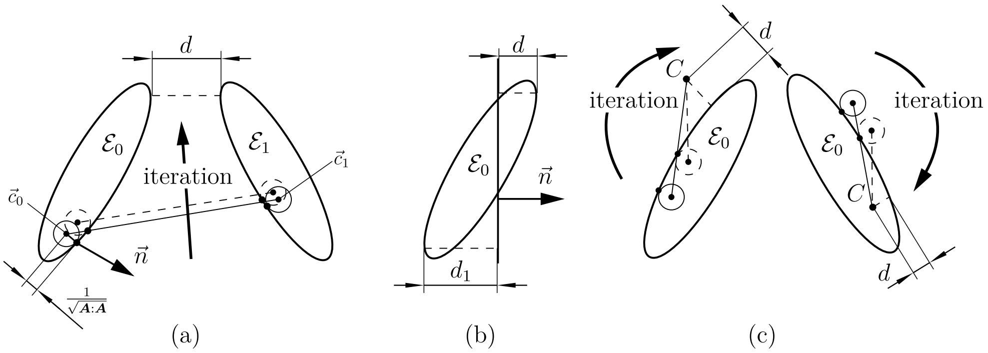

(a) (b) (c)

Figure 3.4.: Schematic two-dimensional representation of distance computation d between an ellipsoid $\mathcal{E}_0$ and: (a) a point (e.g. a corner inside or outside of $\mathcal{E}_0$), (b) a plane $\mathcal{P}_0$ and (c) an ellipsoid E_1. Figure adopted from [199] with permission to reprint from Elsevier.

This intuitive method has an excellent convergence behavior and is straightforward to implement. For the utilized ellipsoids with an aspect ratio of $\alpha = [5..10]$, typically 20 iterations are necessary for the algorithm to successfully terminate. As proven in [143], convergence to the unique solution of the problem is guaranteed after a finite number of iterations.

Distances to the RVE faces are computed by substituting the inclusion $\mathcal{I}$ by the ellipsoid $\mathcal{E}$ in (3.16) such that the problem

$$\min_{\vec{x}\in\mathbb{R}^3} \ \vec{x}\cdot\vec{n} + d \quad \text{s.t.} \quad \vec{x}\cdot\boldsymbol{A}\cdot\vec{x} + \vec{b}\cdot\vec{x} + c = 0 \tag{3.20}$$

results. The analytical solution to the problem (3.20) is obtained by the Lagrange multiplier method with the two Lagrange multipliers

$$\tilde{\lambda}_{0,1} = \pm\sqrt{\frac{\vec{n}\cdot\boldsymbol{A}\cdot\vec{n}}{\vec{b}\cdot\boldsymbol{A}^{-1}\cdot\vec{b} - 4c}} = \pm\frac{\sqrt{\vec{n}\cdot\boldsymbol{A}\cdot\vec{n}}}{2} \tag{3.21}$$

---

[26] In the tilde coordinate system, see Fig. 3.3, $\vec{b}$ vanishes, $c = 1$ and $\boldsymbol{A}$ becomes $\tilde{\boldsymbol{A}}$.

and the two optimal values

$$\vec{x}^*_{0,1} = -\frac{1}{2}\boldsymbol{A}^{-1} \cdot \left[\vec{b} + \frac{1}{\tilde{\lambda}_{0,1}}\vec{n}\right] \ . \tag{3.22}$$

Since $\boldsymbol{A}$ is positive definite and $||\vec{n}||_2 \neq \vec{0}$ by definition, there are always two distinct solutions, see Fig. 3.4 (b). The two extremal distances denoted by d and d_1 with $|d| < |d_1|$ are determined with $\vec{x}^*_0$ and $\vec{x}^*_1$.

For the ellipsoid-corner distance calculation, a modification of the ellipsoid-ellipsoid distance algorithm reveals practical. Instead of changing the position of both spheres, only one sphere evolves whereas the center of the other sphere coincides with the considered corner throughout the iteration process, see Fig. 3.4 (c). However, a distinction between the two cases of the corner being inside or outside the ellipsoid is necessary. If the corner lies inside the ellipsoid, the advancing sphere is positioned outside the ellipsoid. The space surrounding the sphere is non-convex (complement of three-dimensional space and ellipsoid) and, thus, convergence problems possibly occur. Therefore, we compute the penetration points of the line defined by the ellipsoid midpoint and the corner. The penetration point with the shortest distance to the corner then acts as the initial guess, which always results in a convergence of the algorithm.

Resulting exemplary periodic and non-periodic RVEs are shown in Fig. 3.16 (i) and Fig. 3.17 (i).

Capsules

Capsules can be regarded as cylinders with hemispheric caps and posses a smooth surface, see Fig. 3.1 (c). Often they are utilized as an approximation to cylinders, since analytic expressions for the capsule-capsule distance problem exist, see [52, 149, 202]. For cylinders with high aspect ratios, capsules are suited very well as a substitute, since the error made by the extra caps becomes negligible. The radius r and length l act as the shape defining parameters and, thus, capsules reveal transversely isotropic shape properties. A practical description of capsules is given by a line segment with starting point $\vec{P}$ and end point $\vec{E}$, also referred to as on-points.[27] All points having a distance smaller than r from this line segment define the capsule.

The randomized placement parameters $\vec{x}_c$ and $\vec{d}$ are related to the on-points via

$$\vec{d} = \frac{\vec{E} - \vec{P}}{||\vec{E} - \vec{P}||_2} \quad \text{and} \quad \frac{1}{2}[\vec{P} + \vec{E}] = \vec{x}_c \ . \tag{3.23}$$

Two line segments $\mathcal{L}_i$ with $i \in \{0, 1\}$ are described through

$$\begin{aligned} \mathcal{L}_0(\lambda_0) &: \left\{\vec{x}_{\mathcal{L}} = \vec{P}_0 + \lambda_0\vec{s}_0, \quad \lambda_0 \in [0,1]\right\} \quad \text{with } \vec{s}_0 = \left[\vec{E}_0 - \vec{P}_0\right] \\ \mathcal{L}_1(\lambda_1) &: \left\{\vec{x}_{\mathcal{L}} = \vec{P}_1 + \lambda_1\vec{s}_1, \quad \lambda_1 \in [0,1]\right\} \quad \text{with } \vec{s}_1 = \left[\vec{E}_1 - \vec{P}_1\right] \end{aligned} \tag{3.24}$$

with the line vector $\vec{s}_i$ and the line parameter λ_i. $\vec{x}_{\mathcal{L}}$ represents any point on the line $\mathcal{L}_i$. Analogously to ellipsoids, a substitution of the inclusions $\mathcal{I}_i$ in the squared version of Eq. (3.17) by the line segments $\mathcal{L}_i$ results in

$$\min_{\lambda_0 \in \mathbb{R}, \lambda_1 \in \mathbb{R}} d^2(\lambda_0, \lambda_1) = \min_{\lambda_0 \in \mathbb{R}, \lambda_1 \in \mathbb{R}} \left|\left|\vec{P}_0 + \lambda_0\vec{s}_0 - \left[\vec{P}_1 + \lambda_1\vec{s}_1\right]\right|\right|_2^2 \quad \text{s.t.} \quad \lambda_0, \lambda_1 \in [0,1] \ . \tag{3.25}$$

Evaluating the necessary condition of the unconstrained version of problem (3.25) leads to

$$\begin{bmatrix} \frac{\partial d^2(\lambda_0,\lambda_1)}{\partial \lambda_0} \\ \frac{\partial d^2(\lambda_0,\lambda_1)}{\partial \lambda_1} \end{bmatrix} = \begin{bmatrix} 2\frac{\partial \mathcal{L}_1(\lambda_0)}{\partial \lambda_1}[\mathcal{L}_0(\lambda_0) - \mathcal{L}_1(\lambda_1)] \\ -2\frac{\partial \mathcal{L}_2(\lambda_1)}{\partial \lambda_2}[\mathcal{L}_0(\lambda_0) - \mathcal{L}_1(\lambda_1)] \end{bmatrix} \overset{!}{=} \vec{0} \ , \tag{3.26}$$

---

[27] A line segment is always a subset of an infinite line. Points that are a subset of the infinite line but not of the line segment are referred to as off-points. Contrary, on-points are points that are a subset of the line segment.

which is a linear system of equations in λ_0 and λ_1. It gives the optimal points of the distance problem between two infinite lines. Since the resulting pair (λ_0, λ_1) must be evaluated in the scope of a case distinction to respect the constraints, the $\lambda_0 - \lambda_1-$plane is separated in nine regions, see Fig. 3.5 (a). These nine regions represent the nine possible relative positions of the line segments and are illustrated in Fig. 3.5 (b). The blue colored sector of Fig. 3.5 (a) represents the admissible range of λ_0 and λ_1. If $\lambda_0, \lambda_1 \in [0, 1]$, Eq. (3.26) can be solved directly. For all other cases, depending on whether $\lambda_i < 0$ or $1 < \lambda_i$, the λ_i have to be set to 0 or 1. This procedure represents the evaluation of the KARUSH-KUHN-TUCKER conditions of the underlying constrained optimization problem.[28] The optimal points $\vec{x}_i^*$ are determined by inserting the computed λ_i into Eq. (3.24). Eventually, the capsule distance is by

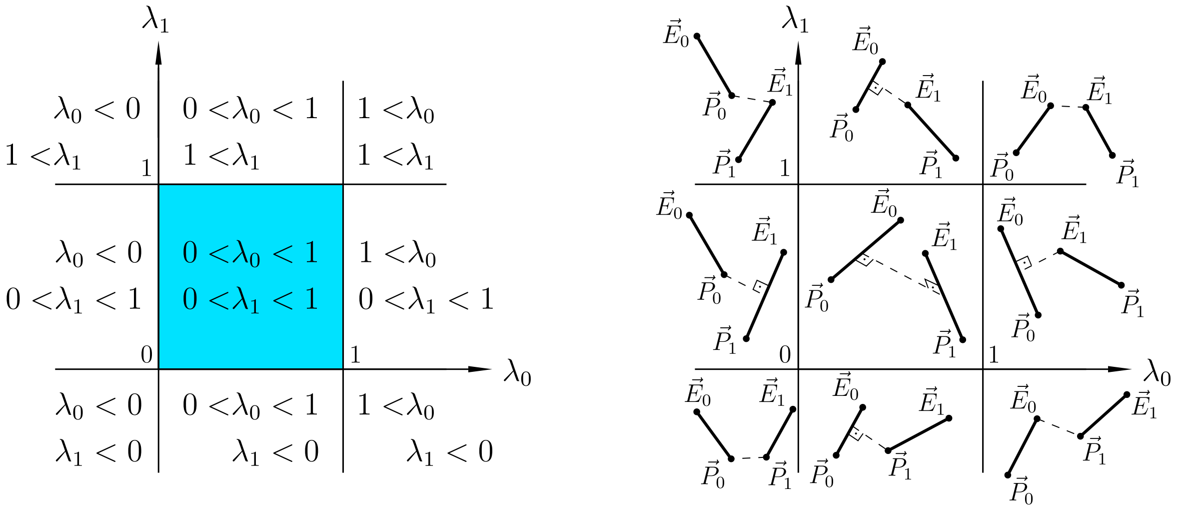

(a) (b)

Figure 3.5.: Distance computations between two line segments: (a) partition of the $\lambda_1 - \lambda_1$-plane into nine regions with the admissible blue region and (b) corresponding scenarios of relative positions between the line segments.

$$d = ||\vec{x}_0^* - \vec{x}_1^*||_2 - 2r \ . \tag{3.27}$$

For completeness, the special case of the two line segments being parallel needs to be considered. If

$$\vec{s}_0 \parallel \vec{s}_1 \ , \tag{3.28}$$

the coefficient matrix in Eq. (3.26) becomes singular.[29] Therefore, the point-line segment distance is evaluated for the two on-points of one line segment w.r.t. the other line segment. Fig. (3.6) shows the three cases that need to be considered. The minimum distance of all three cases then gives the desired distance. Similarly to problem (3.25), the point-line segment distance is a constrained optimization problem with only $\lambda_1 \in [0, 1]$. The distance between the capsules is then computed utilizing Eq. (3.27).

For the plane-line segment distance, only the distances between the on-points and the investigated plane is computed. This operation breaks down to obtaining the signed point-plane distance. If the signs of these distances are different, surely an intersection occurs.

---

[28] The LAGRANGIAN multipliers do not play an important role in this problem and are not necessary to be computed.

[29] EBERLY [52] mentions robustness issues of the presented algorithm. This stability problem emanates from deciding whether two line segments are truly parallel or not. The determinant of the coefficient matrix of Eq. (3.26) or the norm of the cross product between the vectors $[\vec{E}_0 - \vec{P}_0]$ and $[\vec{E}_0 - \vec{P}_0]$ is checked against a numerical threshold. Due to rounding errors and subtractive cancellation, which are unavoidable in finite precision computations, wrong results may occur. However, in the scope of the randomized orientation generation no problems were experienced here. If necessary, the suggested, but far more involved, algorithm in [52] should be used.

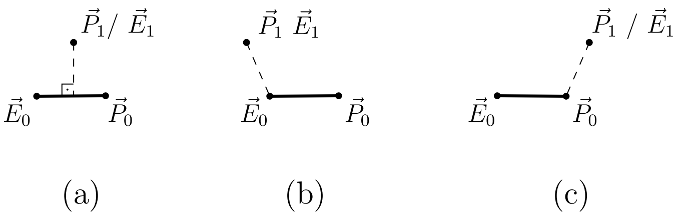

Figure 3.6.: Three potential cases for the distance computation between a point and a line segment: (a) the projection of $\vec{P}_1$ or $\vec{E}_1$ onto the line lie on the line segment, (b) and (c) the projection of $\vec{P}_1$ or $\vec{E}_1$ onto the line do not lie on the line segment

Otherwise the minimal absolute value and the radius are used to compute the minimum distance between the capsule and the plane.

For checking distances between the RVE corners and line segments, a point-line segment problem analogously to the already described procedure of the preceding paragraphs is utilized.

Resulting exemplarily periodic and non-periodic RVEs are shown in Fig. 3.16 (ii) and Fig. 3.17 (ii).

Cylinders

Contrary to capsules or ellipsoids, distance computations between cylinders are far more complicated. The increased complexity emanates from the non-smooth character of cylinders. Cylinders exhibit a discontinuity at the joining of the cylindrical shell and the circular top and bottom disks.

Due to its complexity, the early works of KETCHEL and LAROCHELLE [124, 125] only consider cylinder collision and intersection, which they employ to trajectory planning of industrial robots. Their approach is based on line geometric considerations, since a cylinder always carries a line segment to which an infinite line is associated. They inspect the infinite line-infinite line problem w.r.t. the optimal points, which could either lie on or off the cylinder line segments. The normal between the two infinite lines then determines various collisions possibilities. Eventually, seven possible collision cases need to be captured in a hierarchical manner, which leads to a heavily branching algorithm. Unfortunately, their approach does not cover the scenarios of interpenetrating cylinders, as well as one cylinder being completely inside another. EBERLY [51] reports a separating axis approach to determine if two cylinders intersect. Core of the algorithm is a cylinder axes projection onto a line or plane where the projections of two cylinders do not intersect. Unfortunately, the algorithm lacks of a contact criterion encompassing all surface combinations and is not capable of handling a cylinder shell-cylinder edge contact. In [128], the authors fixed that issue by employing explicit formulations for every contact scenario between the different cylinder boundary elements, such as top and bottom edges, top and bottom faces and the cylindrical surfaces. Similar to KETCHEL and LAROCHELLE, they end up with seven contact cases. In [37] the authors suggest an improved analytical methodology for collision detection by the use of dual number algebra. By taking advantage of the axisymmetric properties of cylinders, they show that five separate contact cases arranged in a logical sequence suffice to solve the collision problem.

As suggested by the mentioned contributions, it makes sense to divide the cylinder $\mathcal{C}$ in its geometric primitives. Fig. 3.7 depicts this decomposition into an infinite cylinder around the line segment $\mathcal{L}$ with its on-points $\vec{P}$ and $\vec{E}$ and two disks $\mathcal{D}_E$ and $\mathcal{D}_P$ at the cylinder's top and bottom. Here, a disk $\mathcal{D}$ is defined by

$$\vec{x}_{\mathcal{D}} = \vec{C} + \tilde{r}\left[\vec{u}\cos(\varphi) + \vec{v}\sin(\varphi)\right] \quad \text{with} \quad \tilde{r} \in [0, r]\ ,\ \varphi \in [0, 2\pi)\ ,\ \vec{n}\cdot\vec{u} = 0 \text{ and } \vec{n}\cdot\vec{v} = 0 \quad (3.29)$$

where $\tilde{r}$ and φ are the polar control variables, $\vec{C}$ is the center, $\vec{n}$ the unit normal vector, r the

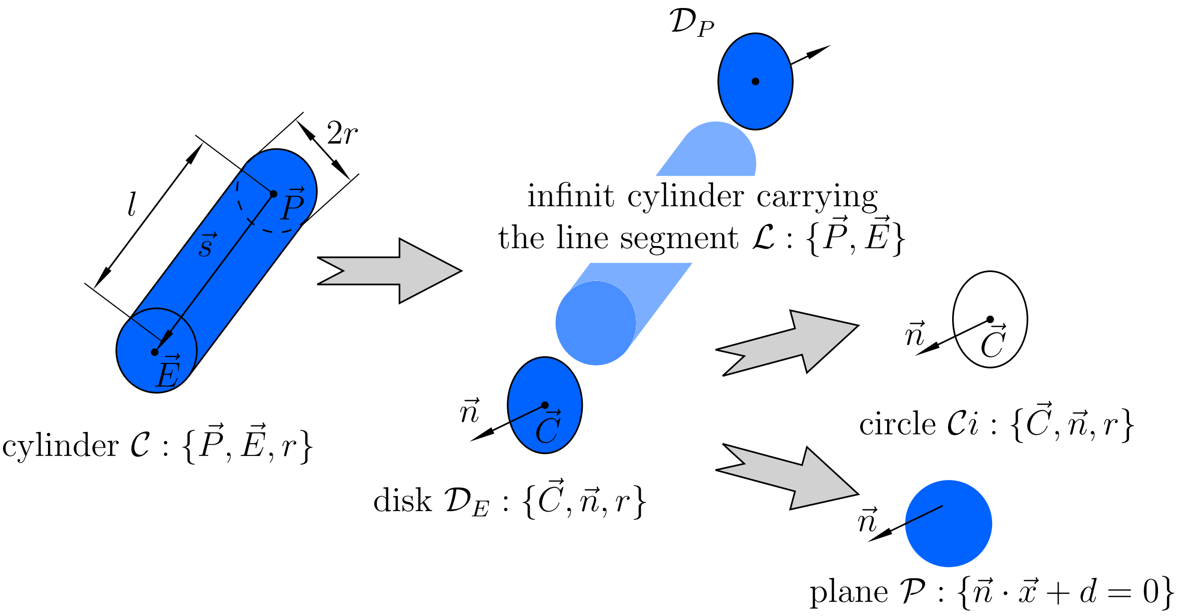

Figure 3.7.: Decomposition of a cylinder in its geometric primitives.

radius and $\vec{x}_{\mathcal{D}}$ any point on the disk. A disk assembles via a plane $\mathcal{P}$ with its normal vector $\vec{n}$ and scalar d and a circle $\mathcal{C}i$. Circles are given by Eq. (3.29) with the constant radius $\tilde{r} = r$.

Naturally, the mentioned approaches for collision testing between cylinders can be extended to distance computations by exploiting all cases of the relative positions of two cylinders, see Fig. 3.8.

Biermann et al. [23] use a divide and conquer strategy that successively walks through distance checks between all the geometric primitives of cylinders to find the appropriate distance problem that defines the relevant relative position case between the two cylinders. The distance computation between a pair of cylinders is split into the computation of the proximity of various pairs: one between cylindrical surfaces (infinite lines), eight between circles and disks, four between circles and line segments and four between pairs of circles. Some of the combinations are logically redundant, which diminishes the algorithms efficiency. Within all these distance computations, the line-circle and circle-circle problems represent the bottleneck of the algorithm, since these computations are the most involved ones. They require the computation of the roots of a fourth order univariate polynomial and an eighth order univariate polynomial conducted via the iterative method suggested in [240].

A more efficient approach of distance computations between cylinders is suggested by Agarwal et al. [3] and Srivatsan et al. [219]. The distance computation between geometric primitives are reduced to a minimum by an intelligent branching strategy and utilizing the axis-symmetric shape properties of cylinders. A heavy use of symbolic precomputations enables the formulation of very general analytical expressions that assist to solve the non-trivial cases of disk-line, disk-circle and circle-circle distance problems. They result in expressions for polynomial coefficients for the fourth and eighth order polynomials. However, these polynomial coefficients grow dramatically with the polynomial order. To capture the coefficients for the eighths order polynomial, a file of 740 kB in size is necessary. Hence, the approach becomes less efficient and prone for errors associated with finite precision computations.[30]

Therefore, an algorithm inspired by the contributions [3, 219] combined with the branching ideas of [23, 124, 125] is presented in the following. The focus is layed on utilizing simple geometric routines, lacking of generality but providing computational efficiency and operational

---

[30] For computations in the field of computational geometry, numerical robustness and stability is of paramount importance. Often, case distinction based on precomputations, e.g. parallel or non-parallel, need to be carried out. If numerical unstable algorithms are utilized, wrong results are likely to occur.

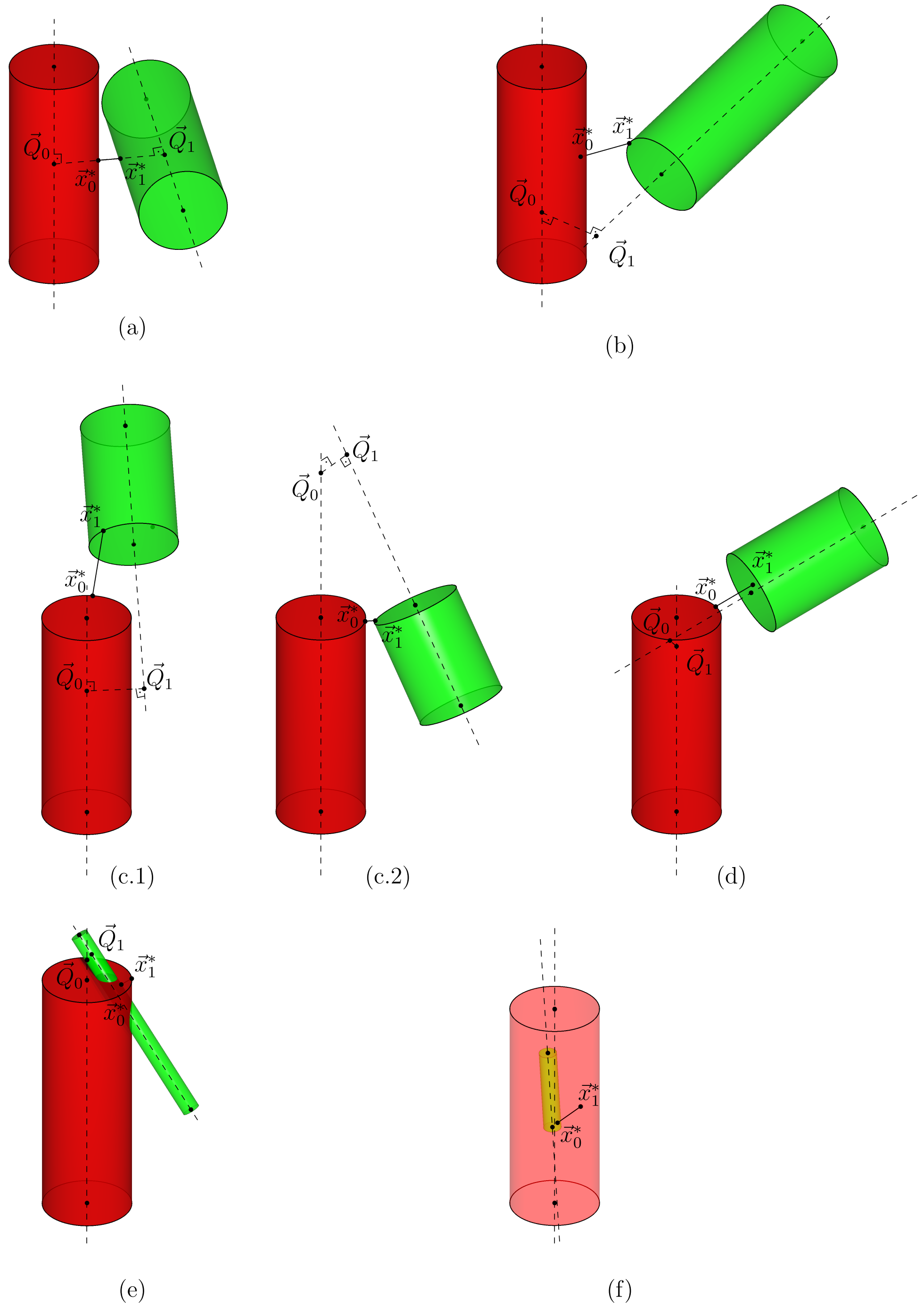

(a)

(b)

(c.1)

(c.2)

(d)

(e)

(f)

Figure 3.8.: All cases of relative positions of two cylinders for distance computation: (a) infinite cylinder-infinite cylinder on-on-case, (b) circle-cylinder on-case, (c.1) circle-circle on-case, (c.2) circle-circle off-case, (d) disk-circle on-case, (f) intersection case and (g) one cylinder inside the other. For all scenarios, the optimal points of the underlying distance problem are depicted via $\vec{x}_0^*$ and $\vec{x}_1^*$. The location of the points $\vec{Q}_0$ and $\vec{Q}_1$, which are the optimal points of the infinite line-infinite line distance problem, determine between on-on, on- or off-case.

ease. The combination of the former approaches from the literature results in an moderate branching covering all special cases, which makes the algorithm very robust and simultaneously very efficient. A flowchart of the algorithm is shown in Fig. 3.9. Input are the two

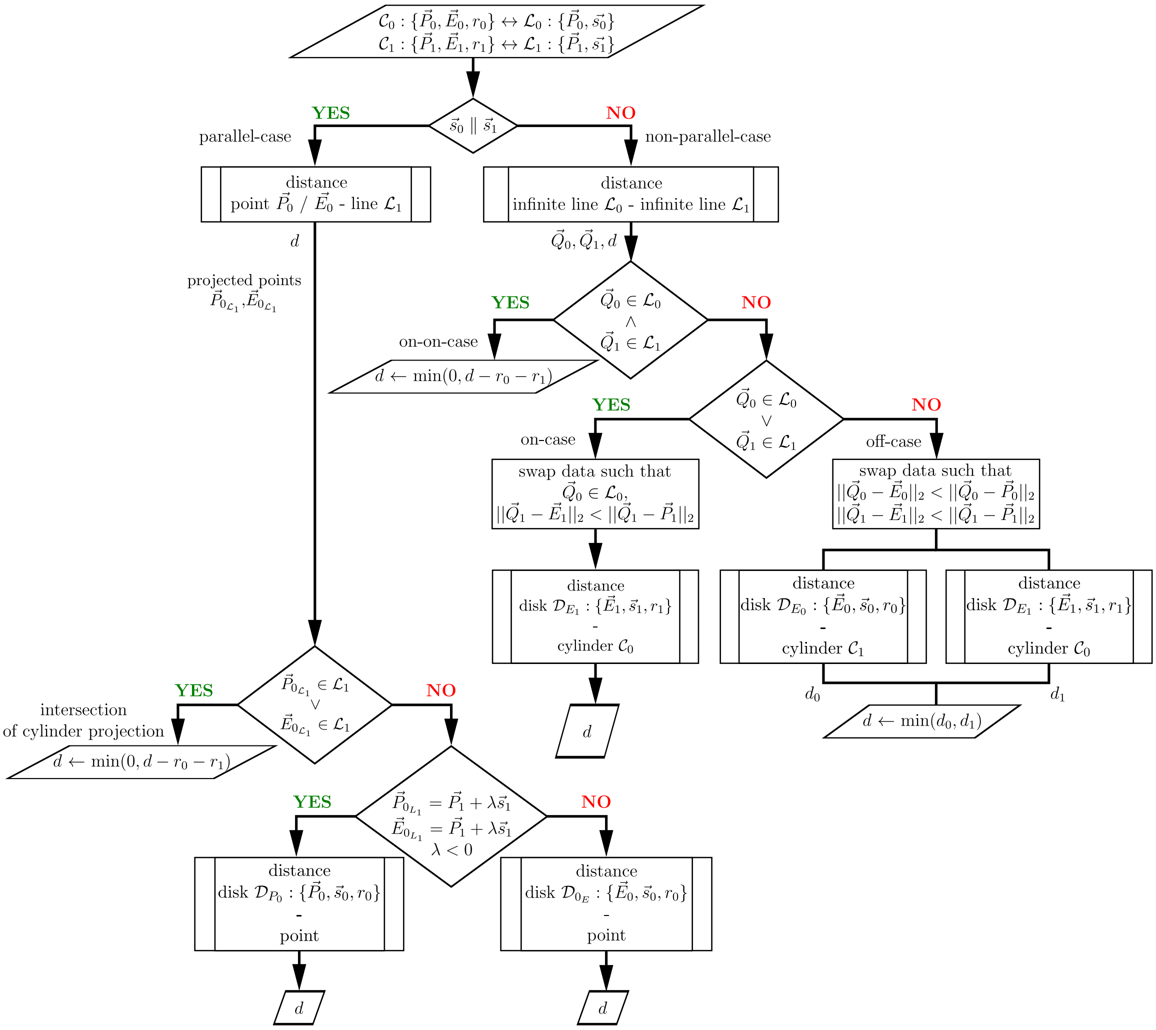

Figure 3.9.: Flowchart of the distance computation between the cylinder $\mathcal{C}_0$ with the on-points $\vec{P}_0$, $\vec{E}_0$ and radius r_0 and the cylinder $\mathcal{C}_1$ with the on-points $\vec{P}_1$, $\vec{E}_1$ and radius r_1. The cylinders carry the line segments $\mathcal{L}_0$ with the line vector $\vec{s}_0 = \vec{E}_0 - \vec{P}_0$ and $\mathcal{L}_1$ with the line vector $\vec{s}_1 = \vec{E}_1 - \vec{P}_1$. The algorithm branches into two cases, namely parallel and non-parallel. For the parallel case, a distinction between intersecting projected line segments and non-intersecting projected line segments is necessary. This distinction is evaluated via point-line distances and the projection points $\vec{P}_{0_{\mathcal{L}_1}}$ and $\vec{E}_{0_{\mathcal{L}_1}}$, which are the points $\vec{P}_0$ and $\vec{E}_0$ projected onto line $\mathcal{L}_1$. The non-parallel scenario branches into three different cases based on the computation of the optimal point of the distance problem between the infinite lines carrying $\mathcal{L}_0$ and $\mathcal{L}_1$: on-on-case, on-case and off-case. These cases refer to the optimal points $\vec{Q}_0$ and $\vec{Q}_1$ which can lie on the line segments or not. The algorithm requires the non-trivial distance computations disk-point and disk-cylinder, which involves the circle-line and circle-circle distance.

cylinders $\mathcal{C}_0$ and $\mathcal{C}_1$ that carry the line segments $\mathcal{L}_0$ and $\mathcal{L}_1$. Output is the distance d between the two cylinders and the optimal points $\vec{x}_0^*$ and $\vec{x}_1^*$ on the cylinder boundaries, see Fig. 3.8.

First, the algorithm checks in a numerically stable way, circumventing numeric cancellation, if the two cylinders are parallel or non-parallel, see [119]. To this end, the angle θ between the line vectors $\vec{s}_0$ and $\vec{s}_1$ is analyzed via

$$\left|\frac{||\vec{s}_0||_2\cdot\vec{s}_1-||\vec{s}_1||_2\cdot\vec{s}_0}{||\vec{s}_0||_2\cdot\vec{s}_1+||\vec{s}_1||_2\cdot\vec{s}_0}\right|=\tan\left(\frac{\theta}{2}\right)<0\ . \tag{3.30}$$

The parallel case is very similar to the scenario of parallel capsules, depicted in Fig. 3.6. The computation of the optimal points $\vec{P}_{0_{\mathcal{L}_1}}$ and $\vec{E}_{0_{\mathcal{L}_1}}$ of the point-line distances between $\vec{P}_0$ and $\vec{E}_0$ and $\mathcal{L}_1$ results in a further case distinction. If one of the projected points lies on the line segment, the distance computation is straight-forward. Alternatively, the projected points can be off the line segment $\mathcal{L}_1$ in direction of $\vec{P}_1$ or $\vec{E}_1$. This case leads to a disk-point distance calculation between the disk around $\vec{P}_1$ or $\vec{E}_1$ and the corresponding extremal points on the cylinder $\mathcal{C}_0$. These extremal points on $\mathcal{C}_0$ are determined by the fact that for parallel cylinders, the two line segments $\mathcal{L}_0$ and $\mathcal{L}_1$ lie in the same plane. Likewise, the extremal points have to lie in this very plane. Eventually, the analytical solution of a point-disk distance problem remains.

This point-disk distance problem between a point $\vec{P}$ and a disk $\mathcal{D}:\{\vec{C},\vec{n},r\}$ is shown in Fig. 3.10. Two cases need to be distinguished. First, the projection $\vec{P}_P$ with

$$\vec{P}_P=\vec{P}-\vec{n}\cdot[\vec{P}-\vec{C}]\vec{n} \tag{3.31}$$

of $\vec{P}$ onto the disk's plane is computed. If the projection $\vec{P}_P$ lies inside the disk, the optimal point $\vec{x}^*=\vec{P}_P$ and $d=0$. If $\vec{P}_P\notin\mathcal{D}$, a circle-point distance problem needs to be solved. Then, $\vec{x}^*=r\vec{w}$ with $\vec{w}=\frac{\vec{P}_P-\vec{C}}{||\vec{P}_P-\vec{C}||_2}$, see Fig. 3.10 (b).

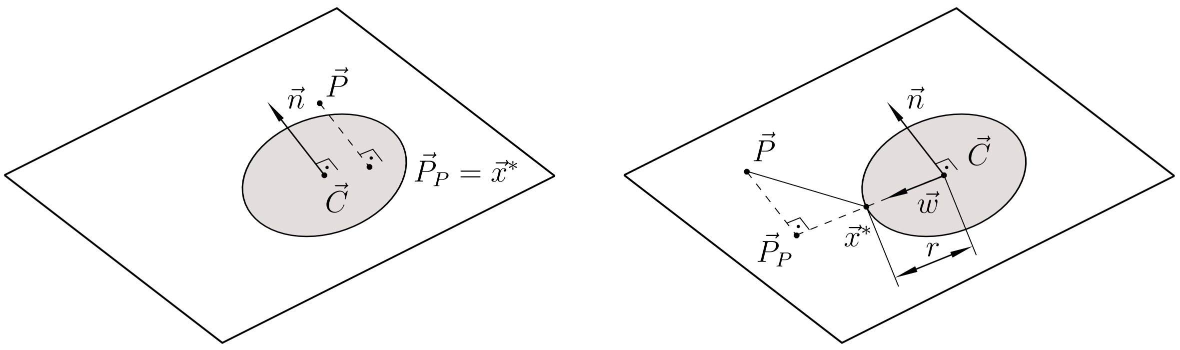

(a) (b)

Figure 3.10.: Distance computation between a point $\vec{P}$, the disk $\mathcal{D}$: (a) the projection $\vec{P}_P$ lies within the disk such that $d=0$ and (b) $d>0$.

For non-parallel cylinders the distance computation is much more difficult due to the increased number of possible relative cylinder positions resulting in a more complex branching of the algorithm. Basis of the first branching is the solution of the infinite line-infinite line distance problem with the optimal points $\vec{Q}_0$ and $\vec{Q}_1$ and the distance d. These points can either lie on or off the associated line segments, which indicates branching.

Fig. 3.8 (a) depicts the on-on-case. $\vec{Q}_0$ and $\vec{Q}_1$ lie within both cylinders and the cylinder-cylinder distance computation is given by the infinite line-infinite line solution.

If only one optimal point of the infinite line-infinite line problem is inside a cylinder, three relative positions are possible, see Fig. 3.8 (b), (c.1) and (d). For generalization purposes, the geometric data is swapped such that $\vec{Q}_0$ lies always in cylinder $\mathcal{C}_0$ and $\vec{Q}_1$ lies always outside of cylinder $\mathcal{C}_1$ in direction of $\vec{s}_1$ (outside the disk $\mathcal{D}_{E_1}$ around $\vec{E}_1$). Then, all cases are covered by the distance computation between the cylinder $\mathcal{C}_0$ and the disk $\mathcal{D}_{E_1}$. The flowchart of the solution to this cylinder-disk distance problem is depicted in Fig. 3.11.

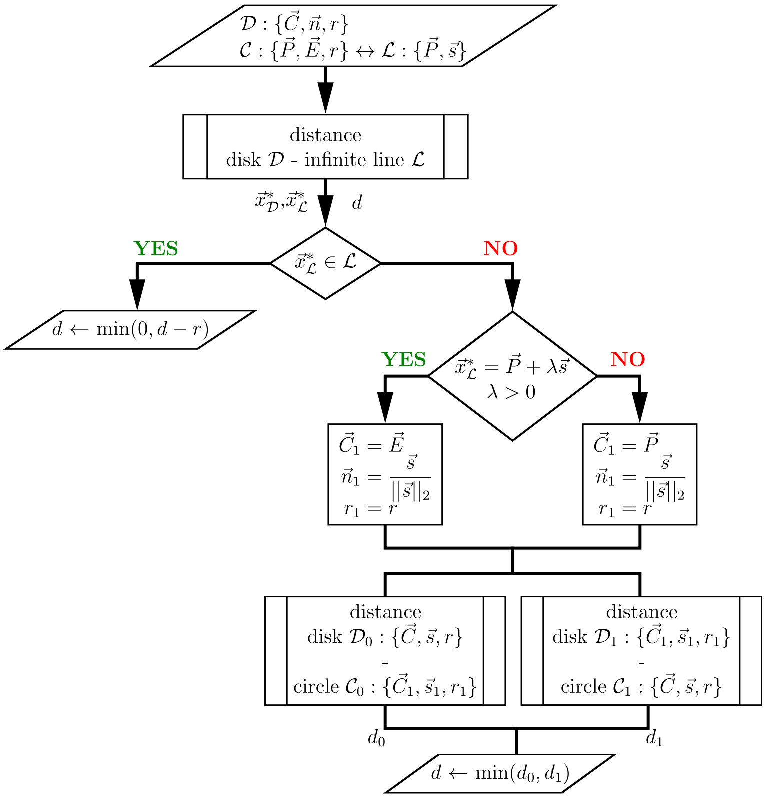

Figure 3.11.: Flowchart of the solution to the cylinder-disk distance problem with the cylinder $\mathcal{C}$ and the disk $\mathcal{D}$.

First, a disk-line distance problem is solved to yield the optimal point $\vec{x}^*_{\mathcal{D}}$ on the disk $\mathcal{D}$ and the optimal point $\vec{x}^*_{\mathcal{L}}$ on the line $\mathcal{L}$ and the distance d. To this end, two cases need to be distinguished. On the one hand, the line could penetrate the disk such that $\vec{x}^*_{\mathcal{D}} = \vec{x}^*_{\mathcal{L}}$ and $d = 0$, which is verified by a plane-line intersection test. On the other hand, the line may not intersect with the disk. Here, only the disk's boundary in form of a circle needs to be considered and a reduction to a circle-line distance problem follows. By replacing $\mathcal{I}_0 = \mathcal{C}i$ and $\mathcal{I}_1 = \mathcal{L}$ in the squared version of Eq. (3.17) by means of Eq. (3.29) with $\tilde{r} = r$ and Eq. (3.24) with $\lambda \in \mathbb{R}$, the objective (squared distance) function becomes

$$\begin{aligned} d^2 &= [\vec{C} + r[\vec{u}\cos(\theta) + \vec{v}\sin(\theta)] - \vec{x}_{\mathcal{L}}]^2 \\ &= [\vec{C} - \vec{x}_{\mathcal{L}} + r\vec{w}]^2 \\ &= [\vec{C} - \vec{x}_{\mathcal{L}}]^2 + r^2 - 2r[\vec{x}_{\mathcal{L}} - \vec{C}] \cdot \vec{w} \end{aligned} \tag{3.32}$$

with $\vec{x}_{\mathcal{L}} = \vec{P} + \lambda \vec{s}$ and the unit circle vector $\vec{w} = \vec{u}\cos(\theta) + \vec{v}\sin(\theta)$. Eq. (3.32) needs to be minimized w.r.t. λ and θ. Considering the situation depicted in Fig. 3.10 (b) with $\vec{P} = \vec{x}_{\mathcal{L}}$, $\vec{w}$ can be expressed via

$$\vec{w} = \frac{\vec{x}_{\mathcal{L}_P} - \vec{C}}{\|\vec{x}_{\mathcal{L}_P} - \vec{C}\|_2} , \tag{3.33}$$

with $\vec{x}_{\mathcal{L}_P}$ being the projection of $\vec{x}_{\mathcal{L}}$ onto the disk plane, and, hence eliminating the dependency of d on θ. Substituting $\vec{x}_{\mathcal{L}_P} = \vec{x}_{\mathcal{L}} - \vec{n} \cdot [\vec{x}_{\mathcal{L}} - \vec{C}]\vec{n}$ in Eq. (3.32) results in

$$\begin{aligned} d^2 &= [\vec{C} - \vec{x}_{\mathcal{L}}]^2 + r^2 - 2r[\vec{x}_{\mathcal{L}} - \vec{C}] \cdot \vec{w} \\ &= [\vec{C} - \vec{x}_{\mathcal{L}}]^2 + r^2 - 2r\frac{[\vec{x}_{\mathcal{L}} - \vec{C}]^2 - [\vec{n} \cdot [\vec{x}_{\mathcal{L}} - \vec{C}]]^2}{\sqrt{[\vec{x}_{\mathcal{L}} - \vec{C}]^2 - 2[\vec{n} \cdot [\vec{x}_{\mathcal{L}} - \vec{C}]]^2 + [\vec{n} \cdot [\vec{x}_{\mathcal{L}} - \vec{C}]]^2}} \\ &= [\vec{C} - \vec{x}_{\mathcal{L}}]^2 + r^2 - 2r\sqrt{[\vec{x}_{\mathcal{L}} - \vec{C}]^2 - 2[\vec{n} \cdot [\vec{x}_{\mathcal{L}} - \vec{C}]]^2 + [\vec{n} \cdot [\vec{x}_{\mathcal{L}} - \vec{C}]]^2} \; . \end{aligned} \tag{3.34}$$

With the abbreviations

$$\begin{aligned}
a_6 &= \vec{s}\cdot\vec{s}\ , \\
a_5 &= 2[\vec{P}-\vec{C}]\cdot\vec{s}\ , \\
a_4 &= [\vec{P}-\vec{C}]\cdot[\vec{P}-\vec{C}]+r^2\ , \\
a_3 &= -2r\ , \\
a_2 &= [\vec{s}-[\vec{n}\cdot\vec{s}]\vec{n}]\cdot[\vec{s}-[\vec{n}\cdot\vec{s}]\vec{n}]\ , \\
a_1 &= 2[\vec{s}-[\vec{n}\cdot\vec{s}]\vec{n}]\cdot[\vec{P}-\vec{C}-[\vec{n}\cdot[\vec{P}-\vec{C}]]\vec{n}]\ , \\
a_0 &= [\vec{P}-\vec{C}-[\vec{n}\cdot[\vec{P}-\vec{C}]]\vec{n}]\cdot[\vec{P}-\vec{C}-[\vec{n}\cdot[\vec{P}-\vec{C}]]\vec{n}]
\end{aligned} \tag{3.35}$$

the final form of the squared distance function is given by

$$d^2(\lambda) = a_6\lambda^2 + a_5\lambda + a_4 + a_3\sqrt{a_2\lambda^2 + a_1\lambda + a_0}\ . \tag{3.36}$$

Eq. (3.36) solely depends on the line parameter λ and needs to be minimized, such that the necessary condition

$$0 \overset{!}{=} \frac{\partial d^2(\lambda)}{\partial\lambda} = 2a_6\lambda + a_5 + \frac{1}{2}\frac{a_3[2a_2\lambda + a_1]}{\sqrt{a_2\lambda^2 + a_1\lambda + a_0}} \tag{3.37}$$

holds. By multiplication with the denominator and utilizing the third binomial formula Eq. (3.37) is recast into a fourth order polynomial. The analytic solution, see [114], eventually brings $\vec{x}^*_{\mathcal{L}}$ and $\vec{x}^*_{\mathcal{D}}$.

If $\vec{x}^*_{\mathcal{L}} \in \mathcal{L}$, the scenario depicted in Fig. 3.8 (b) is present (the optimal point $\vec{x}^*_0$ lies on the cylindrical surface of $\mathcal{C}_0$). Alternatively, $\vec{x}^*_{\mathcal{L}}$ can be located outside of $\mathcal{L}$. With regard to the original cylinder-cylinder distance problem, the optimal points must lie on the disks of the two cylinders, see Fig. 3.8 (c.1), (c.2) and (d).

For $\vec{x}^*_{\mathcal{L}} \notin \mathcal{L}$ a disk-disk distance problem needs to solved. The position of $\vec{x}^*_{\mathcal{L}}$ w.r.t. the on-points $\vec{P}$ and $\vec{E}$ of the cylinder $\mathcal{C}$ determines the disks. For a disk-disk distance problem, one of the optimal points is always located on one of the disk's boundary. Therefore, it suffices to consider two disk-circle problems only. Fig. 3.12 depicts the flowchart of the solution algorithm of such a disk-circle distance problem. First, the optimal points of the circle-plane distance problem are obtained. Again, two cases need to be distinguished, see Fig. 3.13. On the one hand, the circle can penetrate the plane, see Fig. 3.13 (a). In this case, the optimal

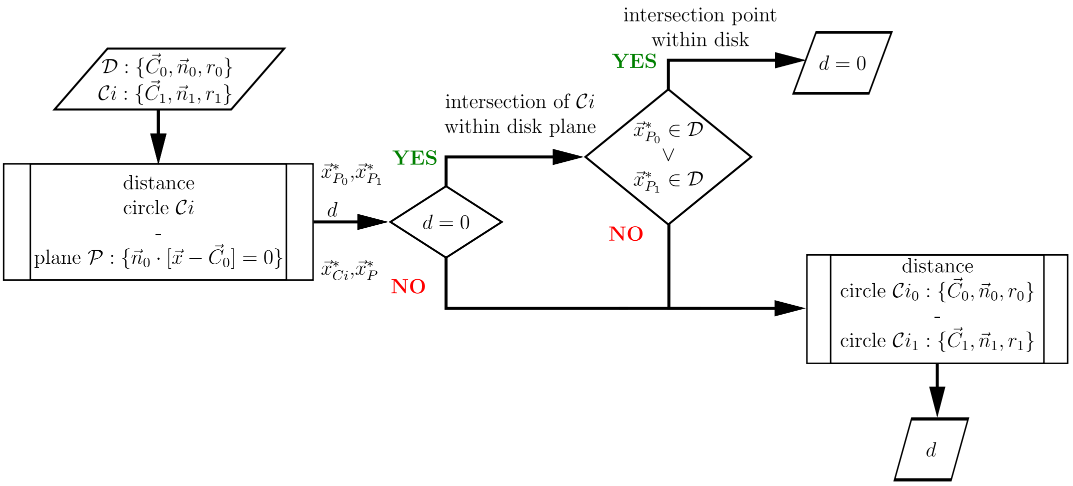

Figure 3.12.: Flowchart of the solution of the disk-circle distance problem with the disk $\mathcal{D}$ and the circle $\mathcal{C}i$.

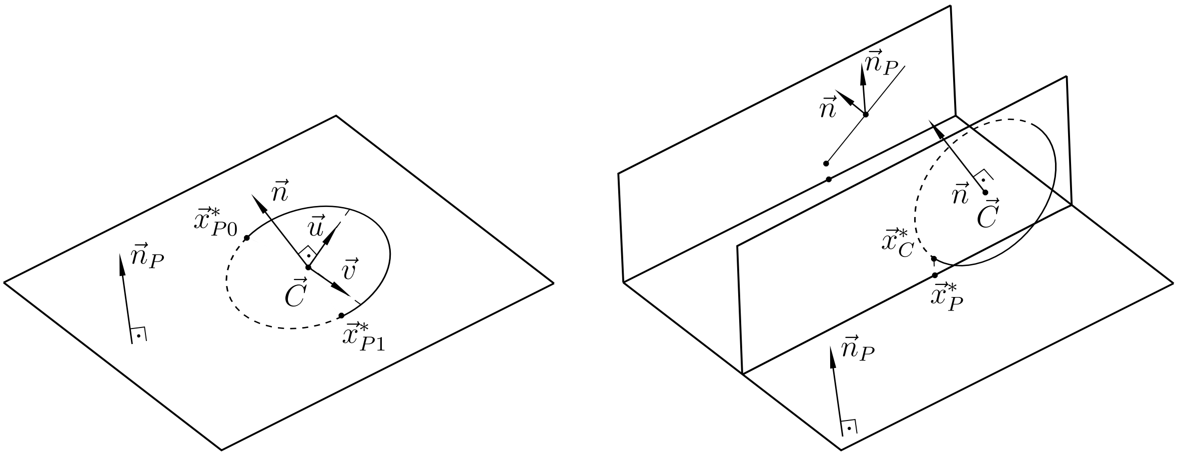

(a) (b)

Figure 3.13.: Circle-plane extremal point computation: (a) circle-plane intersection (b) no circle-plane intersection.

points are the penetration points. They are computed by inserting Eq. (3.29) with $\tilde{r} = r$ into the plane equation by

$$0 = \vec{n}_0 \cdot [\vec{C}_1 - \vec{C}_0] + r\,[\vec{n}_0 \cdot \vec{u}\cos(\theta) + \vec{n}_0 \cdot \vec{v}\sin(\theta)] \ . \tag{3.38}$$

Substituting $\sin\theta = \frac{2\tan(\frac{\theta}{2})}{1+\tan^2(\frac{\theta}{2})}$, $\cos\theta = \frac{1-\tan^2(\frac{\theta}{2})}{1+\tan^2(\frac{\theta}{2})}$ and multiplication with the denominator results in a quadratic polynomial for $\tan(\frac{\theta}{2})$, which can be solved analytically. If the two penetration points $\vec{x}^*_{P_0} \in \mathcal{D}$ or $\vec{x}^*_{P_1} \in \mathcal{D}$, the disk-circle distance $d = 0$. Alternatively, the circle does not penetrate the disk and a circle-circle distance problem must be solved. Similarly to the circle-line distance problem one could insert the two circle equations (3.29) into Eq. (3.17), see [3, 23]. This would lead to an eight order polynomial, which is typically solved numerically by polynomial-root-finding algorithms. However, ALMOHAMAD et al. [5] suggest an iterative algorithm with linear convergence properties which will be used here. Fig. 3.14 illustrates the iteration procedure w.r.t. the two circles $\mathcal{C}i_0$ and $\mathcal{C}i_1$. The core of the algorithm

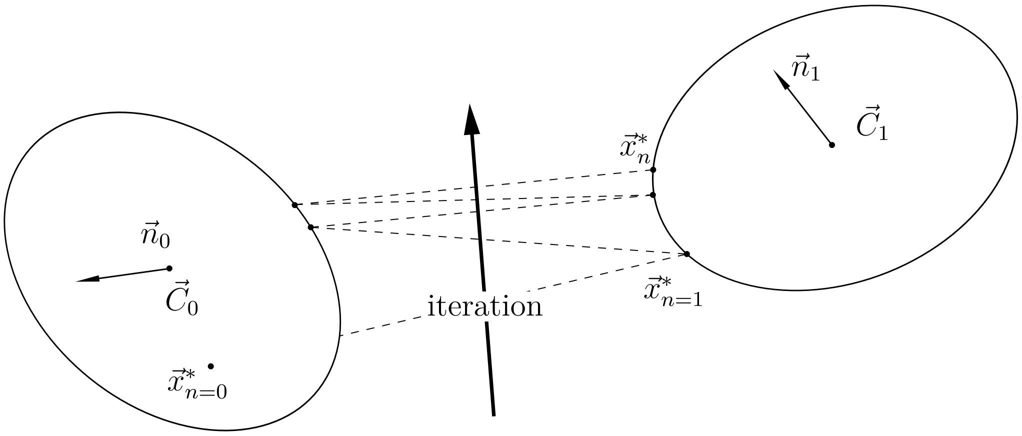

Figure 3.14.: Iterative scheme to compute the optimal points of the circle-circle distance problem.

is a repeatedly executed circle-point distance computation. Iteration starts with a random point $\vec{x}^*_{n=0} \in \mathcal{C}i_0$. Next, the optimal point $\vec{x}^*_{n=1}$ of the circle-point distance problem with the circle $\mathcal{C}i_0$ and the point $\vec{x}^*_{n=0}$ is computed. Vice versa, the optimal point $\vec{x}^*_{n=2}$ of the circle-point distance problem with the circle $\mathcal{C}i_1$ and the point $\vec{x}^*_{n=1}$ is obtained. The algorithm proceeds until the difference of the iterated distances $|d_n - d_{n-1}|$ becomes smaller than a threshold. Very fast convergence is observable for circles far away from each other. Contrary, for circles close to each other, many iterations are necessary to yield the final distance.[31] Since only two circle-point computations are necessary per iteration, this algorithms shows a high computational effectiveness and robustness, while simultaneously being very easy to implement. In contrast to the solution of the analytically exact eight order polynomial, with the evaluation of the coefficients being the bottle neck of the algorithm in [3], the presented algorithms proves advantageous. In fact, the solution of an eight order polynomial is ultimately retrieved iteratively as well.

The remaining third case of the cylinder-cylinder distance problem represents the off-case. The reference points $\vec{Q}_0$ and $\vec{Q}_1$ lie both outside the two cylinders, see Fig. 3.8 (c.2), so that, similarly to the on-case, disk-cylinder problems need to be solved. However, mutual cases between the disks $\mathcal{D}_{E_0}$ and $\mathcal{D}_{E_1}$ and the other cylinder have to be considered, since it is not clear which disk-cylinder combination defines the overall distance between the cylinders. With the help of the detailed cylinder-disk algorithm, the two distances of both possibilities are compared to eventually give the final result. Exemplarily, Fig. 3.8 (c.2) depicts a case that is ultimately defined by a circle-circle distance problem. Due to the utilization of two cylinder-disk distance computations, the off-branch is computationally most expensive.

Finally, the case of one cylinder being completely inside the other, see Fig. 3.8 (f), is checked by examining if one of the optimal points $\vec{x}^*_0$ or $\vec{x}^*_1$ is inside the other cylinder. The case of one cylinder penetrating the other is naturally considered in the described routines. In the case of Fig. 3.8 (e), the line segment $\mathcal{L}_1$ penetrates the disk $\mathcal{D}_{E_0}$, and hence $d = 0$.

The performance of the suggested cylinder-cylinder distance algorithm is evaluated by repeatedly generating two random cylinders

$$\mathcal{C}_i : \{r, \vec{d}, l\} \qquad r \in (0..0.1] \qquad l \in (0..1] \tag{3.39}$$

which randomly placed in a unit cube for 10^6 times. Fig. 3.15 depicts the frequencies of iterations for all conducted circle-circle tests, which is the bottleneck of the algorithm and dominates its numerical effectiveness. Mean and median iteration numbers are very small such that an overall numeric efficiency can be assessed, although very high iteration numbers may occur. However, these high iteration cases occur very seldom and fade in regard to the gross of distance computations. The percentage distribution of the different cases indicates the absence of the parallel case. To further verify the algorithm's favorability, Tab. 3.1.2 shows the normalized mean time of the results given in [3] in comparison with the suggested modified algorithm here. The different cases for 10^5 randomized trials per case are listed. Since the on-on-case represents the most simple one, all times are normalized to that case.

Table 3.1.: Comparison of cylinder distance algorithms w.r.t. the required normalized mean time per cylinder-cylinder case.

Case	Alg. of [3]	Alg. of Fig. 3.9
on-on-case	1.00	1.00
on-case (disk-line)	6.25	2.44
on-case (disk-disk)	72.60	16.00
off-case	96.37	23.10

It is observable that the suggested algorithm brings a speed up of roughly factor four that can be tracked to the efficient iterative procedures employed within the circle-circle distance problem.

---

[31] Here, two circles being close to each other means $\frac{||\vec{C}_0 - \vec{C}_1||_2}{2(r_0+r_1)} < 1$.

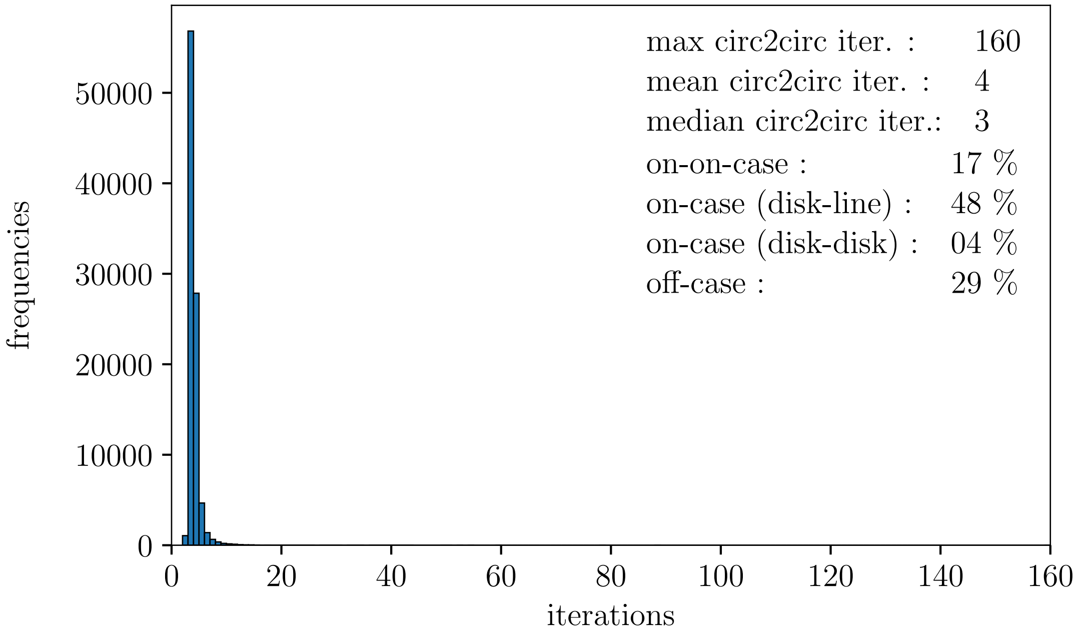

Figure 3.15.: Frequencies of iterations for the circle-circle test for 10^5 random placements of random cylinders into the unit cells.

Similar to capsules and ellipsoids, the prevention of degenerated volumes in the RVE generation process requires cylinder-plane distances. These are obtained by solving disk-plane distance problems. Computing two extremal points for each of the two disks of the cylinder gives four candidates. Comparing four plane-point distances eventually gives the desired minimal distance.

Finally, cylinder-point distances result from solving line segment-point distance problems between a cylinder's line segment and an RVE corner. If the projection of the corner onto the line lies within the line segment, the required distance computation is straightforward. If the line projection of the corner lies outside the line segment, a disk-point distance computation is necessary.

Resulting exemplarily periodic and non-periodic RVEs featuring cylindrical inclusions are shown in Fig. 3.16 (ii) and Fig. 3.17 (ii).

3.1.3. Example microstructures

Fig. 3.16 and Fig. 3.17 depict a variety of periodic and non-periodic randomized RVEs featuring 10, 50 and 150 ellipsoidal, cylindrical and capsular inclusions all generated with the described algorithms. The RVEs possess an inclusion volume fraction of $v_f = 20\%$. A clearance distance of $d_{\text{min}} = 0.001$ is chosen between inclusions as well as between inclusions and RVE faces and between inclusions and corners. It impedes the generation of high inclusion volume fractions and can be interpreted as an extra layer around every inclusions entailing a virtual inclusion volume fraction. For demonstration purposes, the clearance distance is set as an absolute value which implies an increase of the virtual inclusion volume fraction for an increasing inclusion count. More sophisticated choice of d_{min} are correlated to the inclusion dimensions. However, the absolute value option ensures a clearance more accessible for subsequent discretizations. The inclusion's aspect ratios vary from $\alpha = 5$ for ellipsoids over $\alpha = 10$ for cylinders to $\alpha = 20$ for capsules. An increasing inclusion number entails a drastic increase in placement attempts. For non-periodic RVEs an increased number of inclusions is necessary to match the desired inclusion volume fraction. As can be seen by the naked eye, RVEs with a small number of inclusions but a high aspect ratio, cf. Fig. 3.16 and Fig. 3.17, exhibit more aligned inclusions. Here, long inclusions that have been

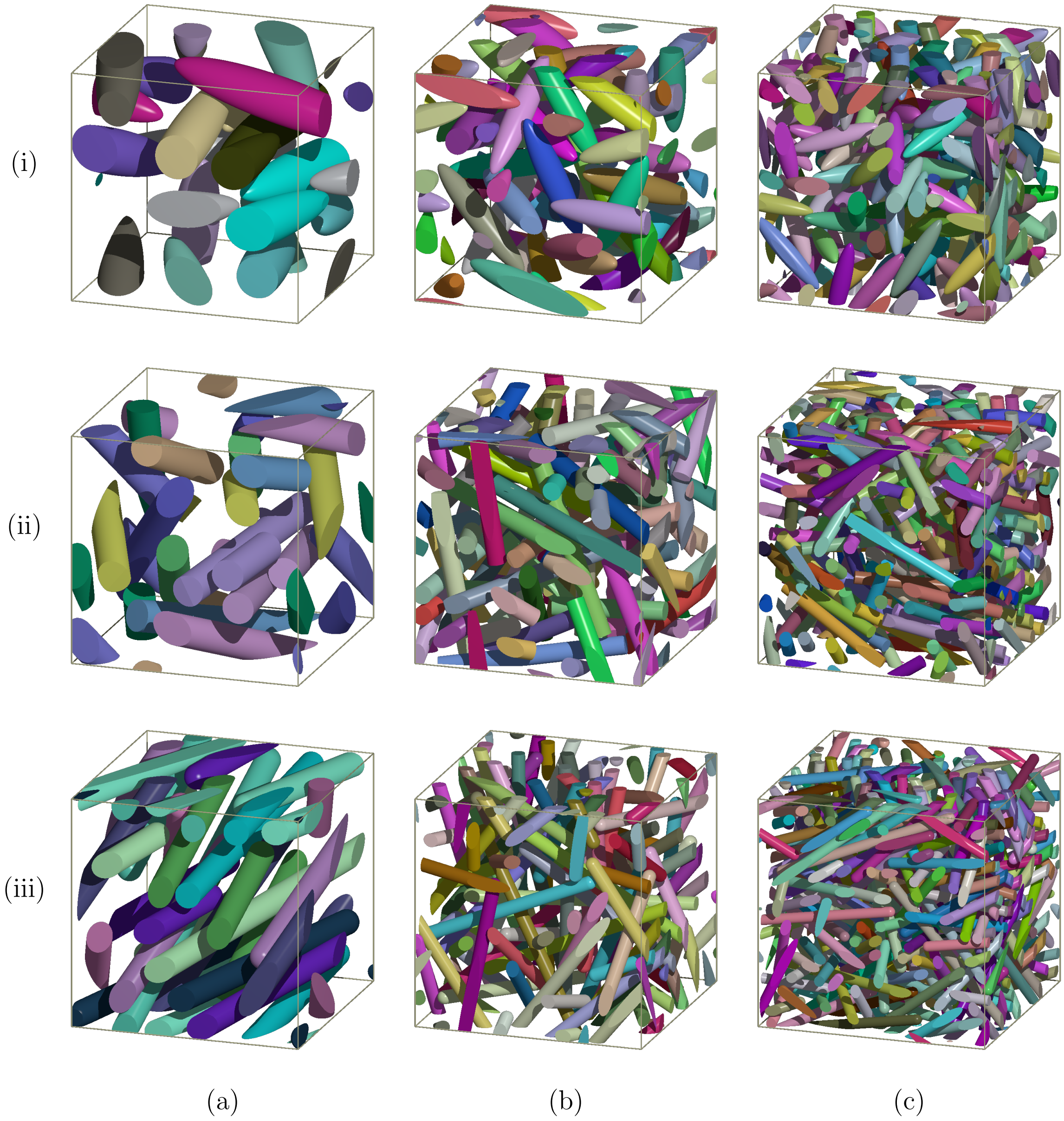

Figure 3.16.: Randomized periodic RVEs generated with the RSA method with (a) 10, (b) 50 and (c) 150 inclusions of different types: (i) ellipsoids of revolution with an aspect ratio of $\alpha = 5$ and $v_f = 0.2$, (ii) cylinders with an aspect ratio of $\alpha = 10$ and $v_f = 0.2$ and (iii) capsules with an aspect ratio $\alpha = 20$ and $v_f = 0.2$. The periodically continued parts of inclusions intersecting the RVE boundary possess identical colors.

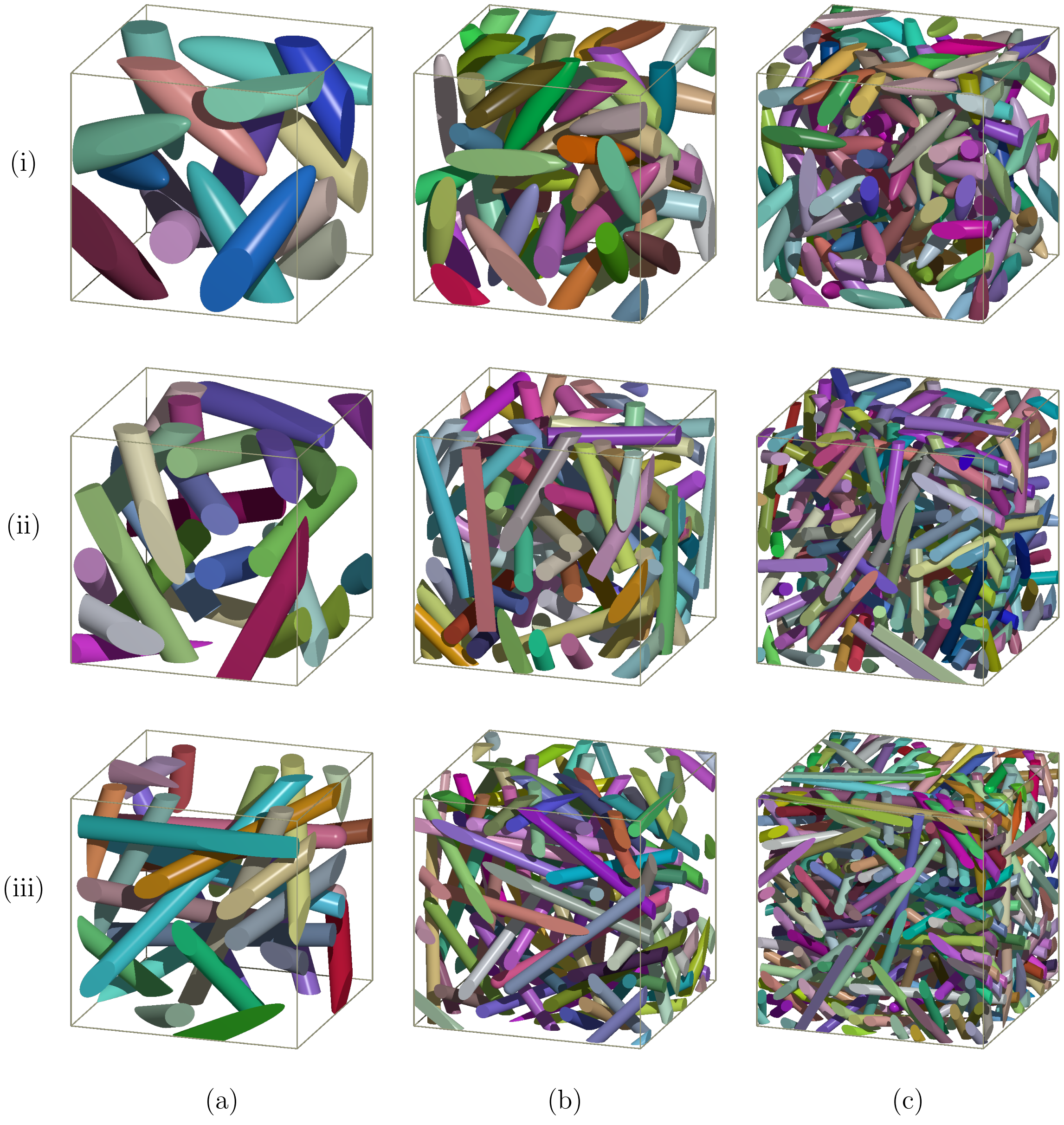

Figure 3.17.: Randomized non-periodic RVEs generated with the RSA method with (a) 10, (b) 50 and (c) 150 intended inclusions of different types: (i) ellipsoids of revolution with an aspect ratio of $\alpha = 5$ and $v_f = 0.2$, (ii) cylinders with an aspect ratio of $\alpha = 10$ and $v_f = 0.2$ and (iii) capsules with an aspect ratio $\alpha = 20$ and $v_f = 0.2$. Since no periodic continuations of inclusions intersecting the RVE boundary exist, the intended inclusion numbers correlate to the periodic versions of the RVE.

placed already tend to block available positions for the upcoming to-be-placed inclusions. As a result, the randomized nature of the generated microstructures fades and the intended random distributions, especially w.r.t. orientations, is hard to achieve. However, with such a small amount of inclusions, it is difficult to identify a certain statistical distribution anyway. Larger RVEs with higher inclusion numbers appear qualitatively more random. A quantitative study of the RVE's randomness follows in Sec. 3.4.

3.2. Collective rearrangement methods

The drawback of RSA algorithms lies in the low to moderate achievable inclusion volume fraction. It is not possible to generate dense particle arrangements up to the theoretical jamming limit. To this end, collective rearrangement methods represent a powerful remedy to this problem. Typically, these approaches are utilized in combination with RSA or sedimentation methods that generate an initial configuration. Thereafter, a better (i.e. denser) packing is achieved by repositioning or shrinking some or all particles. This densification processes is inspired by modifications of the original RSA approach, Monte Carlo methods, molecular dynamics or artificial repositioning schemes driven by heuristics. The differentiation between the various methods is not sharp and one particular algorithm may not be clearly categorizable. However, the benefits of denser particle arrangements come along with more involved and more complex algorithms and higher computational costs. Furthermore, it is noticeable that a certain bias w.r.t. the employed algorithm is always present and a ideally random microstructure is not attainable [230].

Most intuitively are modifications to RSA algorithms that incorporate modifications of the rejection decision or subsequent modifications of a RSA based initial configuration. Jullien [117] et al. generate a two-dimensional setting of randomized disks. Their algorithm firstly drops particles sequentially onto a plane by utilizing a random initial trajectory. If a collision with already placed particles occurs, the path of steepest decent is followed until the plane is reached. Inclusion volume fractions up to $v_f = 61\%$ are achievable. Zhou et al. [255] describe an altered placement scheme for line segments mimicking cylindrical fibers. By a complicated algorithm, randomly placed line segments are repositioned, based on distances and directions to other already placed line segments. Here, the reduced space, diminished by already placed inclusion, is taken into account for the generation of new fibers. Bailakanavar et al. [11] go one step further by changing the inclusion shape. First cylinders are randomly placed one after another. If a newly placed cylinder intersects with already placed inclusions, intersection points are determined, and the to-be-placed cylinder is bent around the obstacular cylinders. Schneider [201] combines a RSA process with a migration and reposition of fibers. Fed by a given orientation distribution, the fibers are iteratively moved. This movement is driven by the iterative solution of a minimization problem in terms of the steepest gradient. Large aspect rations as well as high volume fractions up to 50% are achieved. However, the randomness of the generated RVEs is deteriorated since large regions of similarly oriented fibers emanate. Similarly, Pathan et al. [177] employ an iterative method to solve a constrained optimization problem for reaching an inclusion volume fraction of $v_f = 80\%$ for unidirectional cylinders (arrangement of two-dimensional disks on a plane) and for spheres up to 40%. The contribution [187] describes the generation of RVEs with polydisperse spheres that are placed in an descending order, starting with the largest radii. To achieve denser arrangements, the particles are slightly translated towards their nearest neighbor.

Reviewing these modified RSA approaches reveals that denser particle arrangements based on modified RSA methods are traded against the randomness of the arrangement. A viable alternative are Monte Carlo methods. These methods are interpretable as a repeated squashing and shaking of particles within the RVE. Densities close to the jamming limit are attainable. Gusev et al. [88] generate periodic RVEs of polydisperse unidirectional fibers (two-dimensional disk arrangement). Starting from multiple initial configurations with regularly arranged disks of different radii successive Monte Carlo steps are conducted to match the intended radii distribution. One Monte Carlo step alters the coordinates of randomly selected fibers and shrinks the initial box size. New configurations are only accepted if no overlaps between fibers are detected. Eventually, inclusion volume fractions of 54% are achieved. He et al. [95] start from a random, multidisperse and overlapping sphere arrangement. By repeating many Monte Carlo steps, overlapping particles are rearranged via a relaxation procedure that is comparable to a "vibration" process. Han et al. [90] apply gravitational forces and contact interactions to an initial arrangement of monodisperse spheres in enclosing shapes like boxes or cylinders. A combination of global compression, random (local) compression as well as shaking further densifies the microstructure to inclusion volume fractions of up to 52%. Yu et al. [250] suggest a compacting algorithm applicable to ellipsoids. First, the ellipsoids are put layer wise into a box followed by compression and selection process, which is not detailed in depth. More recent contributions are addressed to fiber reinforced RVEs modeled by cylinders. Starting with experimental data as input of a fibrous microstructure, Gaiselmann et al. [68] compress the fibrous network of cylinders. The cylinders are modeled as concatenated spheres that also allows bending of the fibers. Harper et al. [91] and Islam et al. [110] used FE-simulations to conduct the compression to achieve inclusion volume fractions of up to 50%. Contrary to the mentioned shapes, Sheng et al. [211] modeled concrete-like particle reinforced composites with polyhedral inclusions. The RVEs are generated by free fall acceleration simulations incorporating gravity and contact in the scope of FE-simulations.

In contrast to the modified RSA algorithms, Monte Carlo methods are more powerful resulting in increased inclusion volume fraction while maintaining randomness. However, due to the immense number of Monte Carlo steps or complex compression simulations the computational effectiveness is questionable.

Therefore, here the choice for generating RVEs featuring moderate inclusion volume fractions falls on molecular dynamics inspired methods. In contrast to the aforementioned approaches, inclusions are treated as physical bodies inside the RVE. Each inclusion possesses a velocity, an inertia and interacts with other inclusions based on physical phenomena (e.g. conservation of momentum). The particles move and change until the desired configuration is attained. Two approaches are reported in the literature, denoted as "time driven" and "event driven". The "time driven" approach explicitly solves the equation of motion by some time integration scheme, see the fundamental work of Alder et al. [4]. All parameters of all particles (coordinates, velocities, angular velocities, sizes...) are updated at each time step, independent of whether or not particles interact with each other.

Contrary, "event driven" algorithms neglect the dynamics of the system. They focus on the computation of the particle arrangement whenever an event occurs. Typically, events are defined by collisions between two particles or the collision of a particle and the RVE boundary. Only in the case of an event, all parameters are updated. The updates are repeated until particle arrange into the desired configuration. The crux of "event driven" simulations is to find an efficient way to compute the events. If such a scheme exists, "event driven" approaches outreach the "time driven" methods by far in computational efficiency. For two-dimensional disks, Lubachevsky and Stillinger [148] published their famous algorithm that is straightforward to be extended to spheres. This algorithm will be presented in the following and is adopted from Ghossein et al. [76, 77], who implemented the Lubachevsky-Stillinger-algorithm for spheres and ellipsoids. For monodisperse spheres, the algorithm is capable of producing RVEs with an inclusion volume fractions up to the jamming limit of $v_f = 65\%$ while maintaining randomness.

Initially the intended number of spheres is generated by assigning a normalized mass of $m = 1$, random positions, random velocities and zero radii as well as a growth rate, e.g. $g_{\text{fact}} = 0.1$. The key idea of the algorithm is to let the particles grow by the growth rate and simultaneously move while interacting with each other and the RVE boundary. The growing particles entail an increasing inclusion volume fraction up to the desired value. Collision times are computed repeatedly for all particles. Due to the isotropic nature of spheres, these computations are straightforward. Analogously, interaction times between all particles and the RVE boundary are obtained. Then the global minimum time is the event time which is utilized to move all particles and update positions and radii. If the event time is due to particle collision, the velocities of the according (two) particles need to be updated as well. Here, the conversation of momentum defines the new velocities. If the event time is due to a particle interacting with the RVE boundary, two scenarios are possible. On the one hand, a particle may intersect with the RVE boundary. In that case, periodic copies of the particle are distributed around the RVE boundaries, similar to the placement procedure described in Sec. 3.1.1. On the other hand, a particle which already intersects with the RVE boundary may exit the RVE boundary. By deleting all periodic particle only a single particle inside the RVE remains. Computing the current inclusion volume fraction determines if the algorithm terminates or not. After termination the radii of all particles are shrunk such that the required inclusion volume fraction is received. Therefore, a small gap between the particles is always current. However, this gap can be infinitely small.

The growing radii entails the (pseudo) kinetic energy in the system to continuously increase. This entails a dramatically decreasing time increment down to the computer precision entailing a stagnation of the algorithm. Francqueville et al. [43] suggest a remedy to this problem by uniformly decreasing the particle velocities after a given number of events. Furthermore, it is worth noticing that the randomness of the entire microstructure heavily depends on the randomness of the particles' initial positions and velocities. The initial positions can be computed by a standard random number generator. However, the initial velocity of every particle $\vec{v}$ need to be assigned according to a Maxwell-Boltzmann distribution to ensure randomness, see [43]. The distribution is given by

$$f(\vec{v}) = \left[\frac{m}{2\pi k_B T}\right]^{\frac{3}{2}} \exp\left(-m\frac{\vec{v}\cdot\vec{v}}{2k_B T}\right) \tag{3.40}$$

with the normalized mass $m = 1\,\mathrm{kg}$, the Boltzmann constant k_B and the (artificial) temperature T. Fig. 3.18 depicts corresponding periodic RVEs generated with the Lubachevsky-Stillinger-algorithm for different inclusion volume fractions and an artificial temperature of $T = 100.1\,\mathrm{K}$.

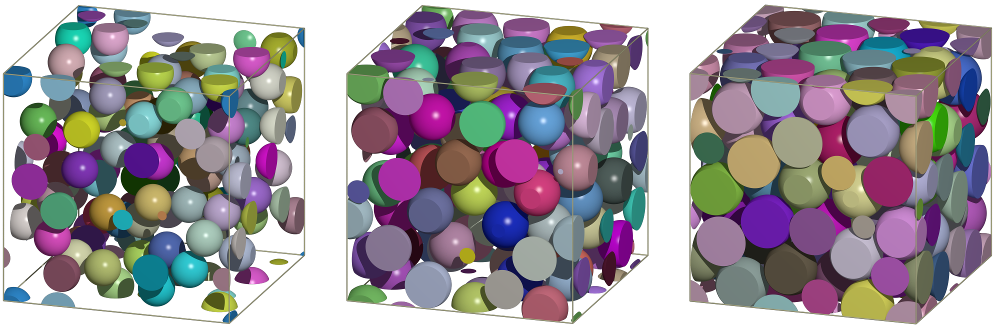

(a) (b) (c)

Figure 3.18.: Randomized periodic microstructures with 100 spherical particles generated by the Lubachevsky-Stillinger-algorithm with an inclusion volume fraction of (a) 20%, (b) 40% and (c) 60%.

In [77], the authors give an extension to ellipsoids. In [194], a combination of spheres and cylinders is suggested. Both approaches result in RVEs with a maximal inclusion volume fraction of up to 40% while maintaining an aspect ratio of roughly $\alpha = 3$. Since the involved shapes are not isotropic anymore, rotations and therefore the conservation of angular momentum needs to be additionally considered.

If inclusion volume fractions larger than the jamming limit in combination with a certain randomness are required, only few methods for disks and spheres are reported in the literature. Since jamming limits are exceeded, at least short range patterns are unavoidable, and, hence the randomness fades. Mościński et al. [162] employed a force bias algorithm to generate particle arrangements with $v_f = 67\%$. Starting with a random, overlapping sphere arrangement artificial forces are introduced that rearrange all particles. The forces are intelligently chosen and act only on overlapping particles such that the overlaps decrease. Maggi et al. [153] suggest complex modifications to the original Lubachevsky-Stillinger-algorithm to inclusion volume fractions up to $v_f = 70\%$. However, these approaches are quite involved in terms of implementation and consumption of computational resources while the outcome in terms of a fading randomness might not be worth the effort.

Catalanotti [33] suggests a more accessible approach for spherical particles. Due to its operational ease, this algorithm is chosen for the generation of dense RVEs with inclusion volume fractions up to the theoretical limit. Contrary to afore mentioned approaches, the algorithm starts with a regular face-centered cubic (FCC) arrangement of the particles. The unit cell of an FCC structure consists of four spheres. In Fig. 3.19 (a) the spheres of the unit cell are colored yellow. These four spheres possess the centers

$$\vec{x}_{c_0} = \begin{bmatrix} 0 \\ 0 \\ 0 \end{bmatrix} \ , \ \vec{x}_{c_1} = \begin{bmatrix} 1 \\ 0 \\ 1 \end{bmatrix} \sqrt{2} r_{\text{dens}} \ , \ \vec{x}_{c_2} = \begin{bmatrix} 0 \\ 1 \\ 1 \end{bmatrix} \sqrt{2} r_{\text{dens}} \ , \ \vec{x}_{c_3} = \begin{bmatrix} 1 \\ 1 \\ 2 \end{bmatrix} \sqrt{2} r_{\text{dens}} \ . \tag{3.41}$$

Here, r_{dens} denotes the sphere radius associated with the densest packing and is defined through

$$r_{\text{dens}} = \frac{1}{2\sqrt{2}M} \ .^{32} \tag{3.42}$$

Due to the initial FCC-arrangement, the number of inclusions is given via $n_{\text{incl}} = 4M^3$ with $M \in \mathbb{N}$. M represents the amount of repeating FCC unit cells in all three space directions. In Fig. 3.19 $M = 2$ for demonstration purposes which results in an RVE with 32 inclusions. To account for periodicity, periodic copies of the initial particles need to be generated. In the next step, all particles are shrunk to match the desired inclusion volume fraction, see Fig. 3.19 (b). Eventually, all particles are repeatedly, sequentially, randomly rearranged by a

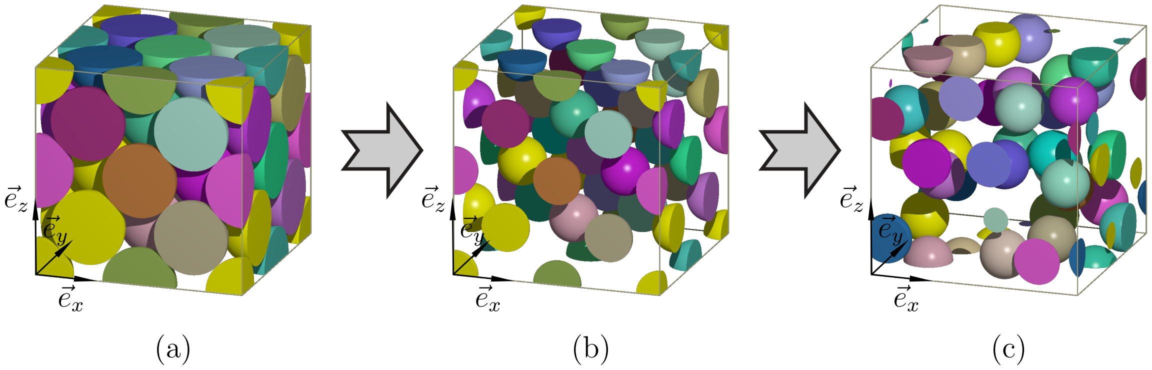

Figure 3.19.: Periodic RVE generation algorithm of [33] with 32 spherical particles and an inclusion volume fraction of $v_f = 20\%$: (a) initializing FCC structure by repeating the FCC unit cell of four spheres (yellow) $M = 2$ times along the three coordinate axis directions; (b) shrinking the spheres such that the desired inclusion volume fraction is reached and (c) randomly translating every inclusion 50 times to yield the final randomized RVE.

---

[32] Here, the RVE edge dimensions are of unit length such that $l_x = l_y = l_z = 1$.

random translation in a random direction $\vec{n}_L$. However, the translation must not violate the non-overlapping constraint. Therefore, a maximal translative distance ρ (contact distance) between the to-be-rearranged particle with center $\vec{x}_{c_m}$ and all other particles with centers $\vec{x}_{c_i}$ is computed. In [33], the author employs an iterative procedure to prevent a collision. Here, this is substituted by the analytical computation of ρ which enhances the algorithm, see Fig. 3.20.

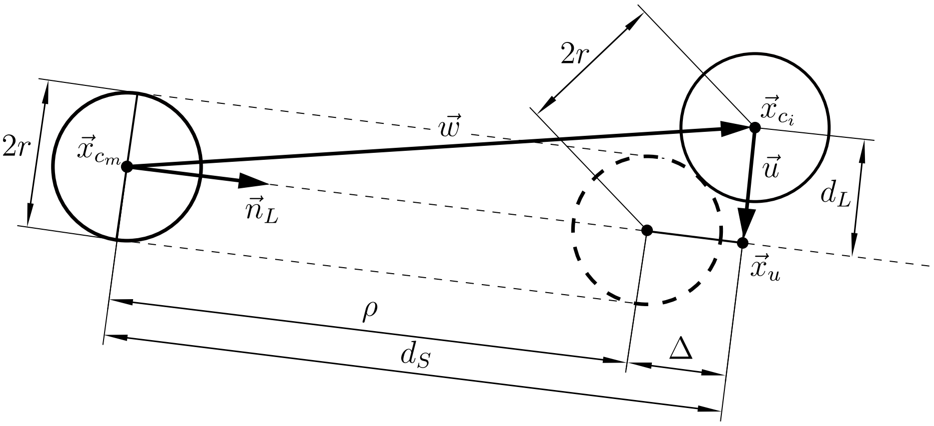

Figure 3.20.: Analytical computation of the contact distance between two spheres in translative direction $\vec{n}_L$.

To check if the two spheres touch, the square of the distance d between the line $\vec{x} = \vec{x}_{c_m} + \lambda \vec{n}_L$ and $\vec{x}_{c_i}$ is computed via

$$d_L^2 = |\vec{w} \times \vec{n}_L|^2 = \sin^2(\alpha)\vec{w} \cdot \vec{w} = [\vec{w} - \vec{w} \cdot \vec{n}_L \, \vec{n}_L] \cdot [\vec{w} - \vec{w} \cdot \vec{n}_L \, \vec{n}_L] \quad \text{with} \quad \vec{w} = \vec{x}_{c_i} - \vec{x}_{c_m} \; . \tag{3.43}$$

For a potential contact

$$d_L^2 \leq 4r^2 \tag{3.44}$$

must be fulfilled. If Eq. (3.44) is true, one has to check if the sphere with index i intersects with the translative corridor defined by $\vec{n}_L$ via

$$\vec{w} \cdot \vec{n}_L = d_S \geq 0 \; . \tag{3.45}$$

If the conditions (3.44) and (3.45) are fulfilled, ρ evaluates to

$$\rho = d_S - \Delta = \vec{w} \cdot \vec{n}_L - \sqrt{4r^2 - d_L^2} \; . \tag{3.46}$$

Fig. 3.21 exemplarily depicts periodic RVEs with 108 inclusions and various inclusion volume fractions. Clearly visible is the lacking randomness for all variants. Due to the translation of spheres with the consideration of potential contact interactions to other spheres, particles may not get past each other, and, hence the initial FCC pattern is conserved. Nevertheless, a certain kind of randomness distinguishing the generated microstructures from a perfect FCC is present, and, hence justifying the algorithm's relevance for high inclusion volume fractions. Beneficial to this algorithm is its feature to always succed with the desired volume fraction. Catalanotti [33] numerically shows that rearranging each particle 20 times suffices to yield a satisfactory grade of randomness, at least for low inclusion volume fractions. A minimum clearance distance d_{min} is straightforward to incorporate by increasing the radius of the sphere with the center $\vec{x}_{c_i}$ by d_{min}.

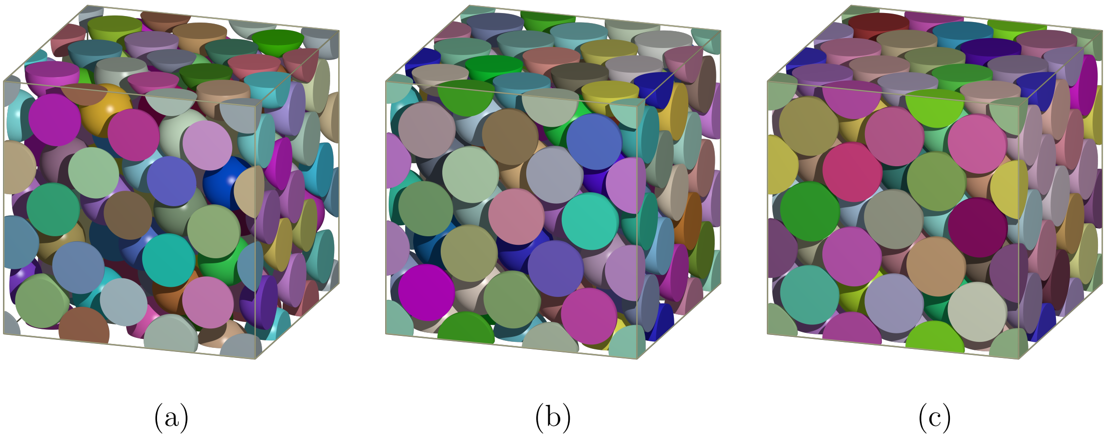
(a) (b) (c)

Figure 3.21.: Periodic RVEs with 108 spherical inclusions generated by the collective rearrangement algorithm suggested in [33]: (a) $v_f = 50\%$, (b) $v_f = 60\%$ and (c) $v_f = 70\%$.

3.3. Miscellaneous approaches: convex polyhedra

For completeness, a short review of random matrix-inclusion composites with convex polyhedra is given in the following. Convex polyhedra can be described in two ways: via their vertices or via the intersection of halfspaces, see Eq. (3.1) and Fig. 3.1.[33] Distance computations between two convex polyhedral break down to point-plane distance computations between the vertices and the polyhedra defining halfspaces. The generation of each individual polyhedron is possible by randomly locating the vertices in a predefined space and computing the convex hull. Software packages like `QHull` [13] offer a fast and robust way of conducting these computations.

However, more common approaches to generate polyhedral inclusions rely on shrinking Voronoi tesselations, see [65, 205]. Voronoi-tessellations have a wide range of applications originating from computational geometry. A good overviews are given by Aurenhammer [10], Preparata [183] or Okabe et al. [169]. Mathematically speaking, a Voronoi-tessellation is a partitioning of a plane of arbitrary dimension n into convex, polygonal regions based on distance to points.[34] The generation points are often called germs, seeds or nucleation points and are specified before the generation process starts. They are combined in the set

$$\mathcal{G} = \{\vec{x}_{g_1}, ..., \vec{x}_{g_m}\} \quad \vec{x}_{g_i} \in \mathbb{R}^n. \tag{3.47}$$

Every point in space $\vec{x} \in \mathbb{R}^n$ is associated with the nearest germ to which it has the minimal distance. All points within one Voronoi-region or Voronoi-cells are closer to the associated germ than to any other germ. Analogously to the convex polyhedra, a description of Voronoi-cell via the vertices or by the intersection of halfspaces is possible.[35] Because of its convexity and space filling properties, Voronoi-tessellations are suitable to mimic polycrystals. Computationally advantageous are the facts that Voronoi-tessellations are analytically well-defined, a generation process will always terminate and very stable and fast software packages are available. Some of the most popular ones are `QHull` from Barber et al. [13], `voro++` by Rycroft et al. [192] or `Neper` by Quey et al. [185].

Voronoi-cells' shape is governed by the germ positions. A Poisson-Voronoi-tessellation is defined by random uniformly generated germs. However, these unconstrained germ lo-

---

[33] Due to the convex nature of halfspaces and the fact that intersections of convex regions also result in convex regions, halfspaces state a viable alternative for the description of convex polyhedra.

[34] For the generation of RVEs only $n = \{2, 3\}$ is of interest.

[35] Dual to a Voronoi-tessellation is the Delaunay-triangulation. The edges of the triangulation define the normals of the halfspaces that form the Voronoi-cells.

cations often result in degenerated Voronoi-cells with extreme aspect ratios not suitable for micromechanical investigations. A remedy is the hardcore Voronoi-tessellation. Germs are generated via the random placement of non-overlapping spheres [66, 185] where as the germs coincide with the sphere centers. Any of the afore mentioned algorithm can be used to generated the sphere arrangement featuring a periodic or non-periodic setting. Fig. 3.22 (a) exemplarily depicts a hardcore Voronoi-tessellation with 100 germs and therefore 100 convex polyhedral Voronoi-cells inside a cuboidal RVE with $n = 3$. The resulting Voronoi-cells

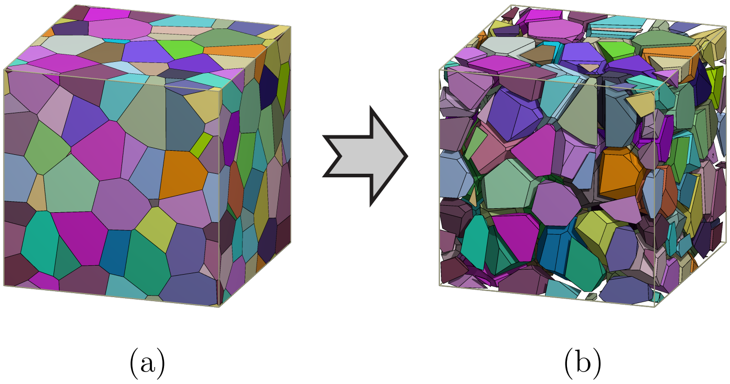

Figure 3.22.: Generation of a periodic RVE with 100 convex polyhedra inclusions based on Voronoi-tessellation: (a) initial hardcore Voronoi-diagram and (b) eroded microstructure.

are regular with no extreme or degenerated grains. Another widely used approach is the centroidal Voronoi-tessellation. Here, the centers and geometrical midpoints (center of mass) of the Voronoi-cells must coincide, see [49]. To this end, either regular germ patterns (honeycomb) or iterative algorithms are utilized. The iterations often start with randomly placed germs and successively repositioning the germs to the midpoints of the successively computed Voronoi-cells. The resulting tesselations possess more regular Voronoi-cells compared to the hardcore tessellation. The most involved germ generation method is the Laguerre-Voronoi-tessellation [101, 109]. Here different radii and weights are assigned to each germ allowing a lot of possibility to mimic experimental findings. Therefore, the information of assigning different weights and radii to the germs can be fed by experimental measurements.

The key idea to generate a matrix-inclusion microstructure from a Voronoi-tessellation is suggested by Fritzen et al. [65]. By isotropically shrinking all Voronoi-cells simultaneously, an interconnecting matrix phase emerges. Fig. 3.22 (b) depicts the eroded Voronoi-tessellation. Due to the space filling property of Voronoi-tesselations and the isotropic shrinking, arbitrary inclusion volume fractions are possible. This fact makes the Voronoi based generation approach very valuable for microstructures with an extremely high inclusion volume fraction.

3.4. Statistics of microstructures

It is important to evaluate the generated microstructures in terms of their randomness to get meaningful statements concerning the representativeness of the microstructures and benefits or limits of the employed microstructure generation algorithm.

To this end, statistical distributions associated with the actual geometric shape can be inspected to quantify the microstructures. Exemplarily, Fig. 3.23 and Fig. 3.24 depict the amplitude normalized orientation distributions in terms of $\cos(\theta)$ with the polar angle θ and the azimuthal angle φ of all microstructures of Fig. 3.16 and Fig. 3.17. Since the generation algorithms are fed with statistically uniform distributions, ideally these uniform distributions should be recovered. Comparing periodic against non-periodic RVEs, it is clearly

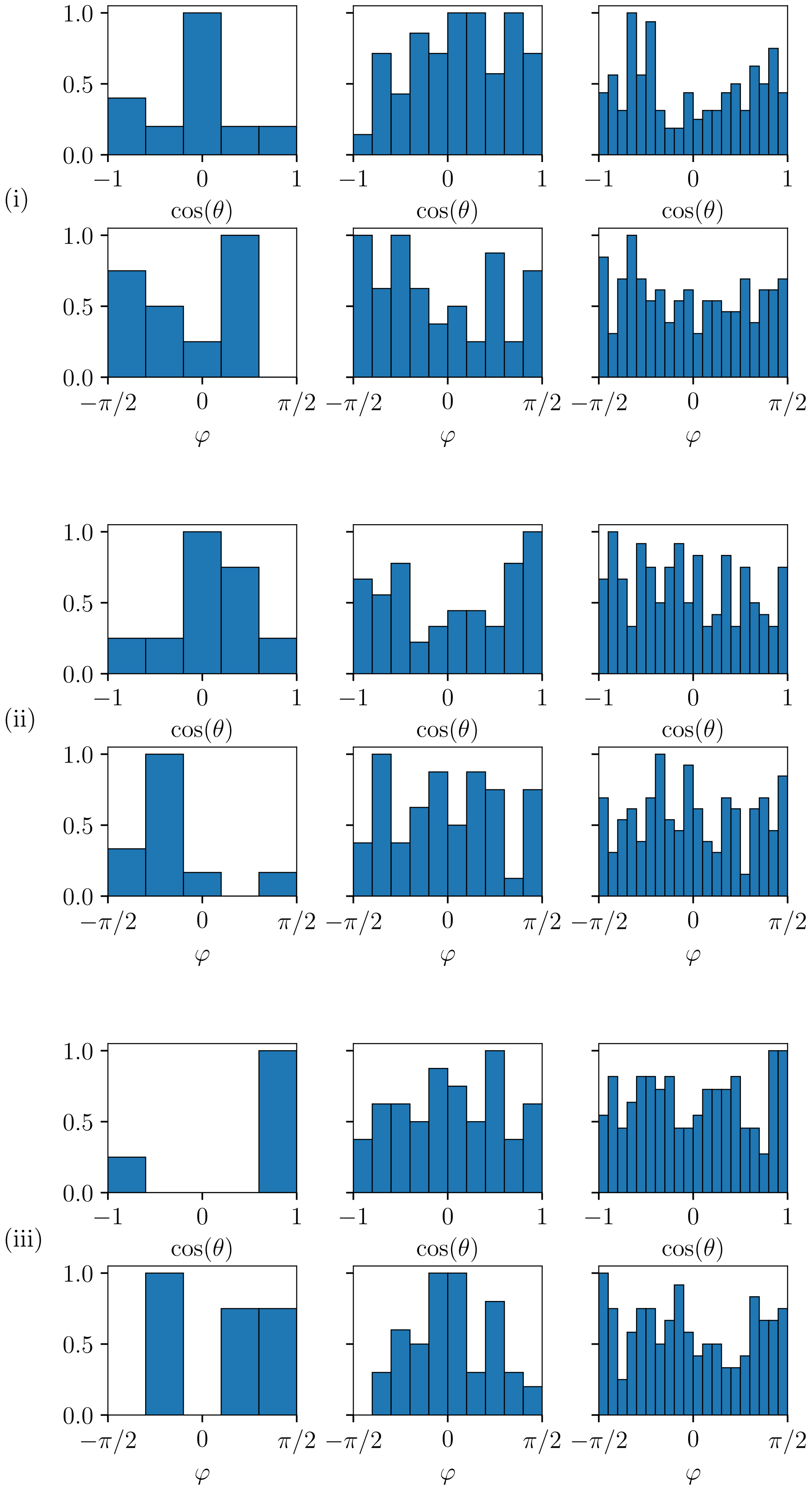

(a) (b) (c)

Figure 3.23.: Orientation distributions normalized to the maximum amplitude of the periodic RVEs of Fig. 3.23: (i) ellipsoidal inclusions; (ii) cylindrical inclusions; (iii) capsular inclusions; (a) 10 inclusions; (b) 50 inclusions and (c) 150 inclusions.

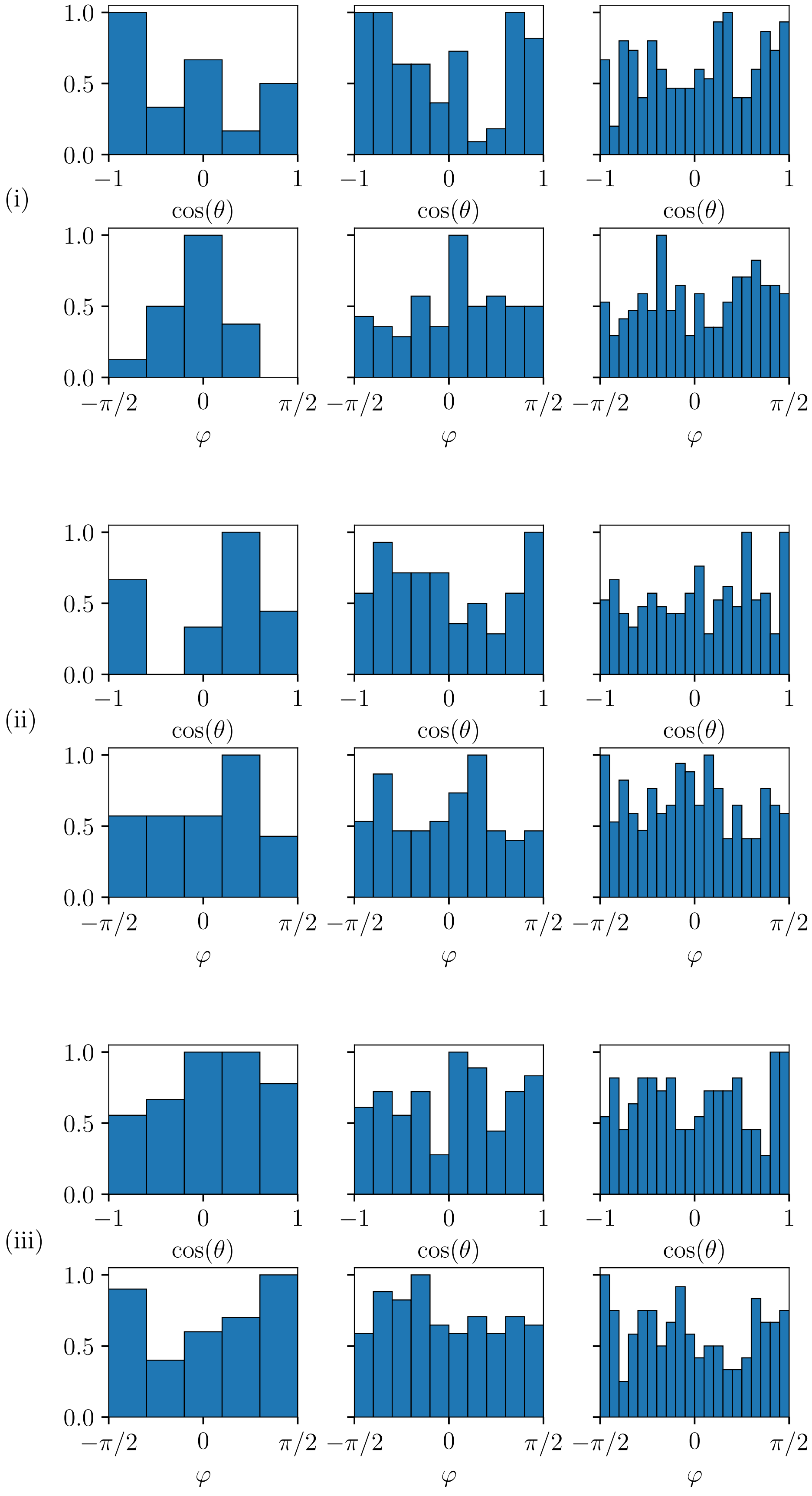

(a) (b) (c)

Figure 3.24.: Orientation distributions normalized to the maximum amplitude of the periodic RVEs of Fig. 3.24: (i) ellipsoidal inclusions; (ii) cylindrical inclusions; (iii) capsular inclusions; (a) 10 intended inclusions; (b) 50 intended inclusions and (c) 150 intended inclusions.

visible that non-periodic RVEs show a broader and more uniform spread of orientations w.r.t. all investigated aspect ratios and inclusion shapes. Causative for this fact are the more restrictive generation criteria for periodic RVEs. The periodicity constraint requires periodic continuations of inclusions intersecting with the RVE boundary. The total occupied space for a single inclusion is then associated with one orientation. For the non-periodic case, such effects are not observable since multiple inclusions with multiple orientations can occupy the same amount of space and hence resulting in a broader variety of orientations. Especially for low inclusion numbers and high particle aspect ratios (e.g. capsules with $\alpha = 20$), the number of inclusions intersecting the RVE's boundary is significantly increased and the uniformity of the orientation distributions increases with the aspect ratio. This is not true for periodic RVEs. For both RVE variants the uniformity of orientation distributions increases with an increasing inclusion number such that differences in the orientation distributions between periodic and non-periodic variants fade. Overall, the periodic RVE with 10 capsules featuring an aspect ratio of $\alpha = 10$, see Fig. 3.23 (iii)(a), represents the worst RVE in terms of uniformness of the orientation distributions. Due to the high aspect ratio and the periodicity constraint, the randomness of all inclusions is dominated by the inclusion placed first. The visual inspection of all inclusions having similar orientations is confirmed by the diagram of Fig. 3.23 (iii)(a). Nevertheless, the orientation distributions of RVEs featuring 50 inclusions or more show acceptable spreads.

Another approach to abstractly describe random media can be done by the use of so-called microstructural descriptors or microstructural correlation functions, see [229]. These descriptors are detached from specific information of the inclusion itself. Important representatives are

- n-point probability functions,
- surface correlation functions,
- lineal-path function,
- chord-length density function,
- pore-size functions,
- percolation and cluster functions,
- nearest-neighbor functions.

One of the most popular descriptors, which will be solely considered in the following, is the n-point probability function. To this end, the indicator function of the phase i is introduced via

$$I^{(i)}(\vec{X}) = \begin{cases} 1 & \text{if } \vec{X} \in \mathcal{B}_0^{(i)} \\ 0 & \text{else} \end{cases} \tag{3.48}$$

to fully describe the microstructure incorporating the entire geometrical information. The indicator function has the idempotent properties

$$I^{(i)}(\vec{X}) I^{(i)}(\vec{X}) = I^{(i)}(\vec{X}) \quad \text{and} \quad I^{(i)}(\vec{X}) I^{(j)}(\vec{X}) = 0 \quad \text{with} \quad i \neq j \; . \tag{3.49}$$

In the case of matrix-inclusion composites with only two constituents,

$$I^{(1)}(\vec{X}) + I^{(2)}(\vec{X}) = 1 \tag{3.50}$$

must hold such that it suffices to consider the indicator function of only one phase. With the ergodicity assumption, the n-point correlation function of phase i is defined via

$$S_n^{(i)}(\vec{r}_j) = \lim_{V_0 \to \infty} \frac{1}{V_0} \int_{\mathcal{B}_0} \prod_{j=0}^{n} I^{(i)}(\vec{X} + \vec{r}_j) dV \tag{3.51}$$

whereby $\vec{r}_j$ depicts a position vector. $S_n^{(i)}$ is a measure of the probability of finding the same phase i at n points that are apart by $\vec{r}_j$ with $j \in 1, 2, \ldots$ at a random point $\vec{X}$ and at all points $\vec{X} + \vec{r}_j$. Due to the assumed statistically homogeneity, $S_n^{(i)}(\vec{r}_j)$ must be independent of $\vec{r}_1$ which is beneficially chosen with $\vec{r}_1 = \vec{0}$.[36] Of particular importance is the two-point-correlation function or auto-correlation function since results are visualizable by an affordable effort. For the two-point-correlation function Eq. (3.51) becomes

$$S_2^{(1)}(\vec{r}) = \lim_{V_0 \to \infty} \frac{1}{V_0} \int_{\mathcal{B}_0} I^{(1)}(\vec{X}) I^{1}(\vec{X} + \vec{r}) dV. \tag{3.52}$$

$S_2^{(1)}$ solely depends on the position vector $\vec{r}$. When exploring the limiting cases of $\vec{r} = \vec{0}$, the two-point correlation functions reduces to

$$S_2^{(1)}(\vec{0}) = \lim_{V_0 \to \infty} \frac{1}{V_0} \int_{\mathcal{B}_0} I^{(i)}(\vec{X}) I^{(i)}(\vec{X}) dV = \lim_{V_0 \to \infty} \frac{1}{V_0} \int_{\mathcal{B}_0} I^{(i)}(\vec{X}) dV = v_f^i \tag{3.53}$$

which is the volume fraction of phase i.

In practice, the generated microstructures are not infinite nor could the infinite limit w.r.t. the microstructure's volume be evaluated. However, in the case of periodic media Eq. (3.52) becomes

$$S_2(\vec{r}) = \frac{1}{V_{\text{RVE}}} \int_{\mathcal{B}_0} I(\vec{X}) I(\vec{X} + \vec{r}) dV \tag{3.54}$$

exactly for the inclusion phase. However, a precise definition of the indicator function has yet not been given. Evaluating Eq. (3.54) analytically is only possible in very special cases, e.g. spherical particles, see [64]. Therefore, the microstructure is transformed into a binarized voxel representation in terms of a regular grid of dimension $N \times N \times N$. Fig. 3.25 (a) depicts such a binarization of the microstructure of Fig. 3.18 (b) with $N = 101$. Only grid points inside particles are assigned with the value one to give a discretized version of the particle indicator function. The underlying field of dimension $N \times N \times N$ is then subjected to a discrete FOURIER-transformation. In the FOURIER-space, the power spectrum is calculated. The inverse discrete FOURIER-transformation eventually yields the discrete version of $S_2(\vec{r})$,

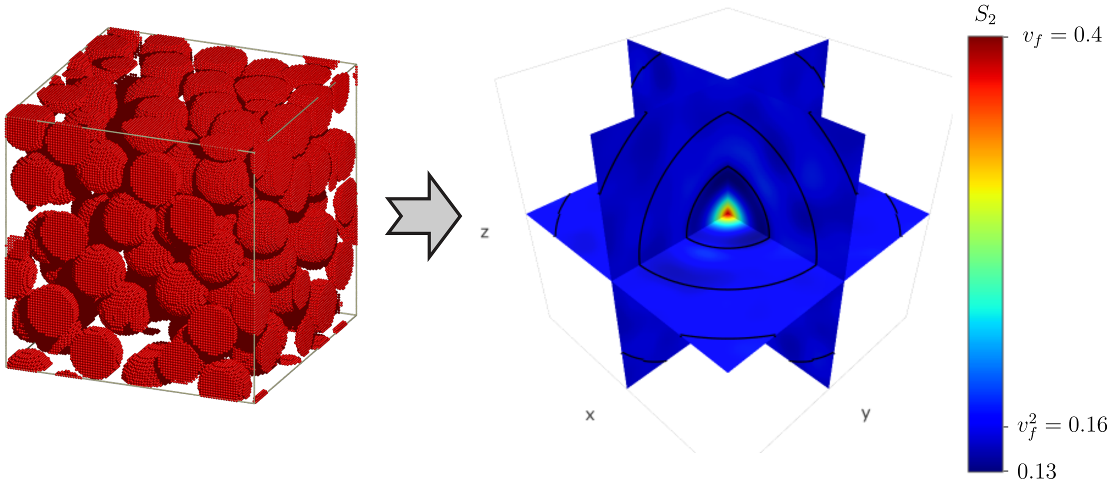

Figure 3.25.: Generation of the two-point correlation function from the microstructure of Fig. 3.18 (b): (a) binarized microstructure; (b) slice plot of the two-point correlation function.

---

[36] If the microstructure is isotropic, the directional properties of $\vec{r}_j$ drops and it suffices to the solely consider the distances r_j.

which is shown in Fig. 3.25 (b) in an interpolated manner for slices equivalent to the coordinate system planes.[37] Additionally to the colored slice plots, black circles indicate multiples of the characteristic microstructural length, namely the diameter of the spherical particles in the case of Fig. 3.25. If no long order ranges are present, the two-point correlation function decays to the value v_f^2. A statistically isotropic microstructure shows an S_2 with spherical symmetry. Since this decay from v_f to v_f^2 occurs relatively fast, the representation of Fig. 3.25 (b) is not practical for the evaluation of the microstructural randomness. It is more meaningful to utilize a reduced color scale centered around the asymptotic value v_f^2, see [43]. Since the decay range is given by $[v_f..v_f^2]$ and S_2 rapidly decays, it is practical to normalize the contour plot colors to 10% of that decay range.

To evaluate the randomness of the RSA method of the previous sections, Fig. 3.26 depicts the two-point correlation functions for all microstructures of Fig. 3.16. Clearly visible are the slowly decaying S_2 values for small RVEs (10 inclusions). In that sense, RVE (i)(a) shows very poor random properties. This is due to the relatively large characteristic microstructural length (only one black circle is visible in the plot) and the present periodicity which results in a long range order. For RVEs with elongated particles, see Fig. 3.26 (ii)(a) and (iii)(a), significant anisotropic patterns are visible. These results correlate well with the findings from the orientation distributions. However, for larger RVEs no long range patterns or dominating anisotropies are observable anymore.

Fig. 3.27 depicts the two-point correlation functions of the RVEs of Fig. 3.18 generated with the LUBACHEVSKY-STILLINGER algorithm. The characteristic spherical symmetric drop of S_2 in the region of $r < |\vec{r}|_2 < 2r$ is clearly visible. This drop can be related to the non-overlapping constraint of the particles. Reviewing the three RVEs of different inclusion volume fraction, it is noticeable that the randomness decreases with an increasing inclusion volume fraction. However, this effect correlates with difference of only some percent in the S_2 values, and, hence a good randomness can be assessed.

Finally, Fig. 3.28 depicts the two-point correlation functions of RVEs of Fig. 3.21 generated with the method suggested by CATALANOTTI. The FCC pattern inherited from initial particle arrangement dominates the plots. Hence, the generated RVEs show long range ordered particles. However, small differences in the patterns that indicate a certain kind of randomness, are observable. Smaller inclusion volume fractions lead to a slightly larger drop of S_2 between the peaks. Therefore, again the randomness decreases with an increasing inclusion volume fraction.

---

[37] Appendix A.2 presents a derivation of the interrelation between FOURIER transforms and the two-point correlation function.

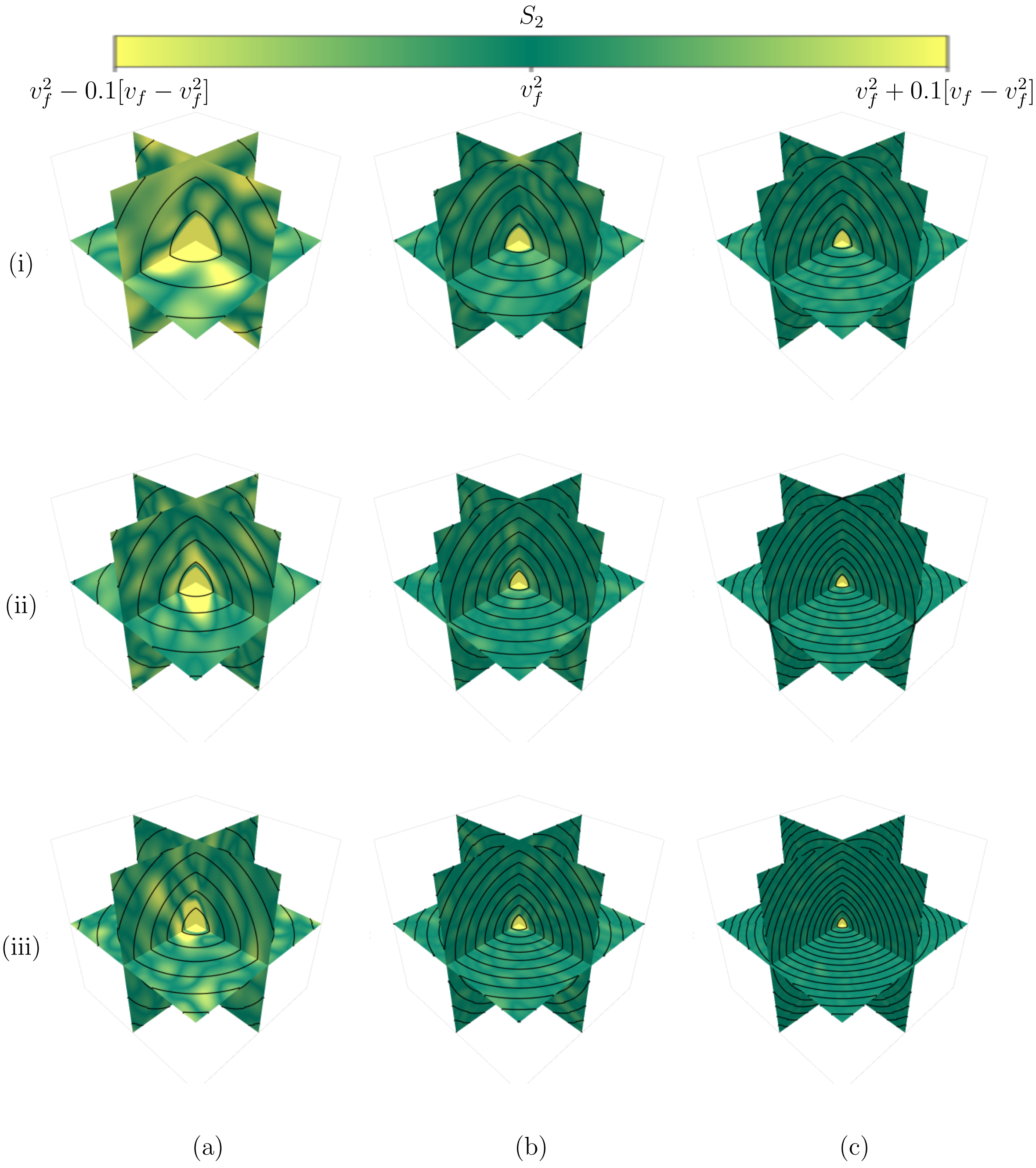

Figure 3.26.: Two-point correlation functions of the periodic RVEs of Fig. 3.23 with an inclusion volume fraction of $v_f = 0.2$: (i) ellipsoidal inclusions; (ii) cylindrical inclusions; (iii) capsular inclusions; (a) 10 inclusions; (b) 50 inclusions and (c) 150 inclusions.

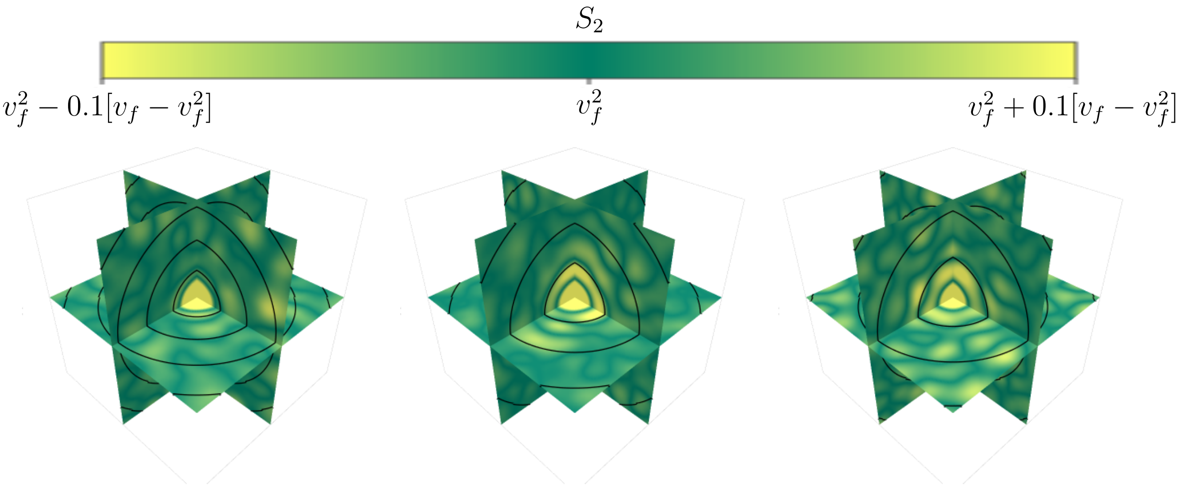

(a) (b) (c)

Figure 3.27.: Two-point correlation functions of the periodic RVEs of Fig. 3.18 with 100 spherical inclusions and inclusion volume fractions of: (a) 20%, (b) 40% and (c) 60%.

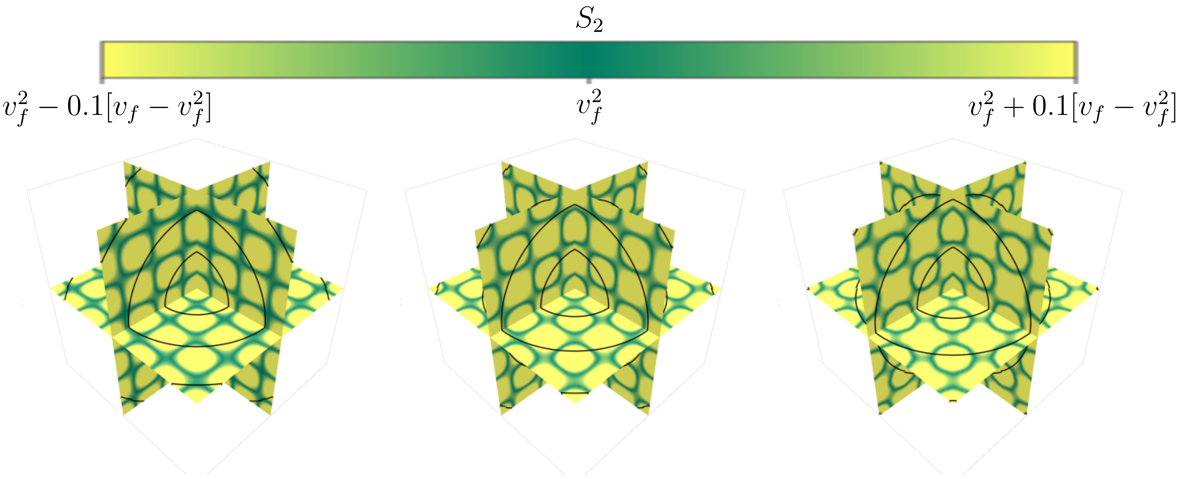

(a) (b) (c)

Figure 3.28.: Two-point correlation functions of the periodic RVEs of Fig. 3.21 with 108 spherical inclusions and inclusion volume fractions of: (a) 50%, (b) 60% and (c) 70%.

4. Microstructure Meshing[38]

This chapter covers the coherently next step in reaching the ultimate goal of solving the microscopic boundary value problem, namely discretizing the RVEs generated in Ch. 3. With the FEM as the solution strategy of choice in mind, special emphasis is layed on generating a periodic mesh topology for the direct application of periodic boundary conditions. To this end, a new meshing algorithm is introduced. Via a hierarchical meshing procedure utilizing constrained line splittings, constrained two-dimensional triangulations and constrained three-dimensional tetrahedralizations, fully periodic and high-quality meshes are generated. Available meshing tools are combined in a highly automizable manner. The focus on maintaining a manageable amount of elements takes limited computational resources into account. Capabilities of the proposed approach are quantitatively compared to existing strategies to demonstrate its beneficial properties.

To solve the microstructural boundary value problem, emerging from Eq. (2.40), typically approximative solution techniques are utilized. Accordingly, the continuous problem is replaced by a solvable discrete problem. As the solution method of choice, this work focuses on the FEM which requires a discretization of the underlying microstructural information.The idea is to construct a mesh of the computational domain that replaces the continuous regions by finite regions, namely finite elements (FE). This procedure outlines a major part in the so-called preprocessing procedure to set up a simulation. Constructing a veritable discretization featuring a high element quality can be very cumbersome and often takes a fair amount of time and manual work. Methods of generating FE meshes are summarized in the excellent review of Ho-Le [102] or can be found in the textbooks of Frey [63] or Lo [146].

Generally, FE meshes are categorizable into two types: structured meshes and unstructured meshes. Structured meshes are generated over smooth regular domains that can be mapped to cartesian regions based on some deterministic procedures. For these meshes, elements exhibit beneficial properties in terms of quality and size, such that the amount of elements needed to discretize, stays in a manageable range. Contrary, unstructured meshes are geometrically more flexible such that it is possible to discretize complex, irregular domains such as randomized matrix-inclusion composites.

For unstructured meshes two major generation methods exist: the advancing front approach and Delaunay triangulations. The advancing front method starts by distributing seeding points on the domain's boundary. Starting from this discretized boundary successive layers of elements that form new closed boundaries are generated. The procedure terminates when the entire domain is filled with elements. A mesh smoothing concludes the advancing front approach. On the other hand, a Delaunay triangulation starts from a given point cloud where all points lie either inside the domain or on the domain's boundary. Next, a Delaunay triangulation of the point cloud is formed. By successively inserting more points and refining the triangulation in combination with smoothening and swapping operations, the final mesh is conceived. While the advancing front approach is more straightforward to implement, multiple solutions in terms of final discretizations exist. Furthermore, the algorithm can be unstable and mesh islands are more likely to occur. Contrary, a Delaunay triangulation only possesses one optimal solution which is computed.

If the considered domains show badly shaped or degenerated geometric features, the amount

---

[38] This chapter is based on the publication "Automatic three-dimensional geometry and mesh generation of periodic representative volume elements for matrix-inclusion composites" [199].

of distorted, bad quality elements increases. Additionally, elements can become arbitrarily small in size or extremely large in number. Due to the diversity of the to-be discretized regions, automatization is only rarely possible making mesh generation a delicate research topic. BAKER [12] stresses this problem in trying to find the answer to the question: *"Is mesh generation an art or science?"* He concludes: *"Some of the advances* [in mesh generation] *were based on a sound theoretical understanding; many others were heuristic in nature, guided by an intuitive feel for what seemed like the right approach."*. This statement expresses the difficulty of generating a good FE mesh, qualifying mesh generation as a highly non-trivial task. Although there are systematic optimization procedures that try to improve the mesh quality in a deterministic manner, in some cases a proper solution of how to discretize a domain may not exist. The freedom of choosing element types, using different number and sizes of elements, utilizing various node seeding strategies at the boundary or in the domain etc. makes it difficult to put mesh generation in a deterministic and theoretical sound framework. Boundary and internal constraints or optimal mesh quality requirements further entail additional difficulties in a theoretical closed form approach to the meshing problem. Most often, the experience of the engineer plays a crucial role for success or failure.

However, automatization is an essential requirement especially within the scope of seeking statistical statements of randomized microstructures which requires many RVEs to be discretized. It is highly unfeasible to manually adjust every discretization. In the following, an algorithm is presented that solves these issues. A meshing procedure for matrix-inclusion RVEs featuring a high capability of automatization is suggested.

In context of computational micromechanics PBCs are favorable. However, they inevitably require a periodic mesh topology. Nodes on opposing RVE faces must possess the exact same coordinates w.r.t. the underlying in-plane positions such that node pairs for applying PBC are present. It is obvious that the requirement of a periodic mesh represents a very strong and cumbersome constraint within the mesh generation algorithm which is the first premiss of the proposed method.

Typically, FE meshes consist of hexahedral elements (most likely in structured meshes) or tetrahedral elements.[39] Due to the complexity of the matrix-inclusion RVEs, hexahedral elements are only applicable for simple grid based (voxelized) meshes. By dividing the cubic RVE into a regular grid consisting of repeating hexaedra of equal size and assigning their midpoints to the different constituents the discretization is generated. Fig. 4.1 exemplarily shows three RVEs featuring ellipsoidal inclusion with 125000 hexahedral elements (50 elements per edge). No geometric representations of the inclusions in the sense of a computer model are necessary. It suffices to implement a routine that determines whether a voxel midpoint is inside or outside of an inclusion, see Eq. (3.1). The grid structure of the mesh intrinsically exhibits a periodic mesh topology, allowing the direct application of PBC. However, the major drawback of this approach lies in the poor approximation of the RVE's geometric features. Staircaselike element arrangements introduce artificial sharp transitions resulting in, at least locally, unphysical gradients of field variables. Tiny regions of inclusions intersecting with the RVE boundary may not be covered at all.

A veritable alternative to hexahedral elements are the geometrically more versatile tetrahedral elements in combination with an unstructured meshing approach. To this end, a geometric representation of matrix and inclusion domains needs to be provided. By the use of constructive solid geometry which utilizes boolean operations on geometric primitives, namely the cubic RVE and the inclusions, a computer model of the complex microstructural geometry is established. These procedures are closely connected to computer aided design (CAD) methods which are integrated in almost all commercial and non-commercial preprocessors or full FE software packages such as ABAQUS, ANSYS, COMSOL, HYPERMESH, GMESH, NET-

---

[39] Besides these dominating element types, there are other element variants like wedge elements, pyramid elements etc. or special purpose elements such as cohesive elements, crack tip elements etc. which are adapted to the actual problem under consideration.

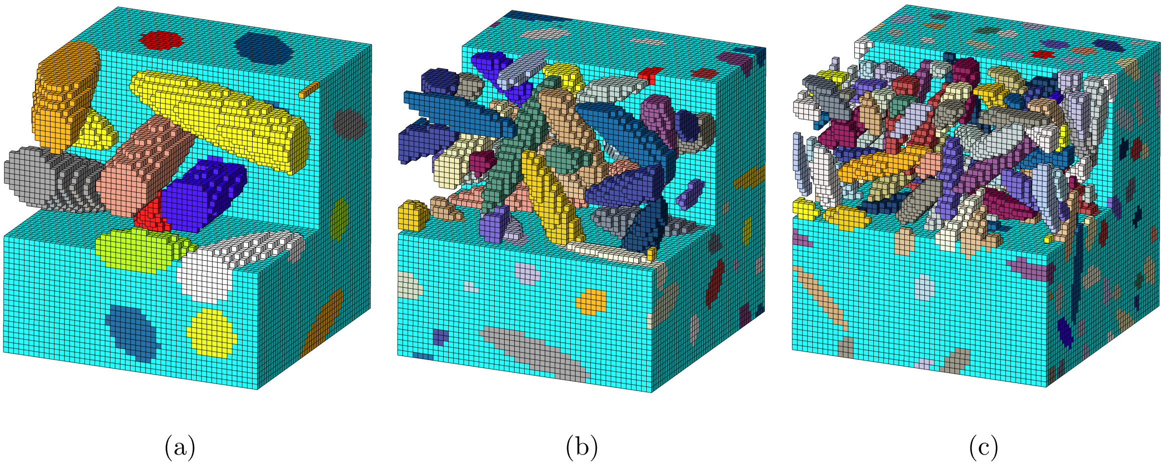
(a) (b) (c)

Figure 4.1.: Voxel discretization with 125000 hexahedral elements (50 elements per edge) of the three RVEs from Fig. 3.16 (i) (a) - (c).

GEN etc.. The majority of available software packages represents the geometric domains by a combination of some interpolative functions such as splines. However, due to the arbitrary positions of the inclusions in combination with the vast amount of particles, unstable behavior in the generation process of most software packages is likely. Very tiny regions or small angles between surfaces, emanating from intersections of inclusions with the RVE boundary lead to unstable boolean operations which are likely to fail in the process of constructing the geometry and, thus, are an inevitable obstacle.

Additionally, only very few software packages provide the feature of a periodic mesh generation. Böhm et al. [29, 30] and Brassart et al. [27] investigate random RVEs with different types of inclusions using Netgen, which is a non-commerical software written by Schöberl [204]. Netgen innately offers the possibility to generate a periodic mesh topology. However, all authors report that for a small number of inclusions very large number of elements are generated (e.g. 15 inclusions yield 100000 elements). The mesh size seems to increase easily, resulting in finite element models too large for efficient simulations. To circumvent this problem Pierard et al. [181] solely considered aligned ellipsoids of revolution with aspect ratios smaller than three. In fact, they report that *"serious difficulties were found to discretize microstructures with ellipsoids with an aspect ratio larger than 3"*. Besides the direct imposition of a periodic mesh, some software packages allow mesh copying and constrained meshing which represents a viable possibility to produce a periodic mesh manually. In that sense, Berger et al. [19] used Ansys to periodically mesh RVEs with cylinders. However, their inclusions do not intersect the RVE edges or corners, which indicates problematic issues. To circumvent the cumbersome mesh constraining and copying, Trias et al. [231, 232] embed the RVE into a larger cubic domain with no inclusions intersecting its boundary. A straightforward structured boundary mesh then ensures the required mesh periodicity. However, this approach has major drawbacks concerning the maximum attainable inclusion volume fraction and restricts the microstructural morphology itself. Generally speaking, there is no straightforward way of generating periodic meshes by utilizing a single software package.

The recent work of Dirrenberger et al. [45] shows an approach featuring a large number of inclusions with infinite length. A combination of multiple software packages is applied to circumvent the drawback of using boolean operations. However, neither the generated microstructure nor the mesh feature a periodic topology. In this regard, the publication of Sohn et al. [216] reveals the most promising approach. By successively treating each inclusion individually a periodic mesh is obtained. Hereby, the individual treatment encompasses a partitioning of the inclusions by the RVE boundary and a subsequent individual mesh generation. However, their method is restricted to spherical inclusions and requires the utilization of polyhedral finite elements, which requires non-standard software.

4.1. Periodic meshing of matrix-inclusion RVEs

The examples of the former section highlight the demand for a proper method to generate discretizations of randomized matrix-inclusion RVEs in a periodic manner. Additionally, discretizations featuring a high element element shape factor quality and a manageable amount of elements is of major importance. To address the demand for a meshing method that provides such features, in the following a new and comprehensive algorithm for discretizing RVEs of matrix-inclusion composites is proposed.

Fig. 4.2 depicts the flow chart of the proposed algorithm. With the findings of Ch. 3 as an input to the algorithm, the core is to process the inclusions successively. One by one, surface meshes of each individual inclusion are generated. Respecting potential intersections between inclusions and the RVE boundary, surface meshes of the inclusions are split and distributed (translated) around the RVE to ensure periodicity. A hierarchical meshing procedure, similar to the method suggested by Fritzen et al. [66], is pursued. Within this process, master edge meshes and master face meshes are generated and copied. They serve as constraints for the triangulations (master face meshes) and final tetrahedralization (volume mesh). By utilizing individual source meshes emanating from the individual inclusions, mesh periodicity is intrinsically incorporated. The algorithm is implemented using Python (`https://www.python.org/`), allowing a straightforward incorporation of third party libraries via scripts, which ensures a high efficiency. Throughout the whole algorithm, mesh information is split into the geometric information of nodal positions and topology information in terms of element connectivity tables which significantly increasing numerical stability.[40]

A detailed description of the new meshing algorithm, based on the exemplary periodic RVE of Fig. 3.3, is given in the following. The RVE features one ellipsoidal inclusion with its three periodic copies. Key feature of the entire meshing procedure is a division of geometric objects into master and slave objects. This classification, which is reasoned by the periodicity requirement, allows the identification of periodic counterparts. $\mathcal{P}_{x_0}$, $\mathcal{P}_{y_0}$ and $\mathcal{P}_{z_0}$ are master faces and $\mathcal{L}_{x_0y_0}$, $\mathcal{L}_{y_0z_0}$ and $\mathcal{L}_{x_0z_0}$ are master edges of the RVE. Accordingly, master inclusions are the inclusions that show the highest number of intersections with master entities (master edges or master faces) of the RVE or do not intersect with the RVE boundary at all. In that sense, Fig. 4.3 (a) depicts the detected master inclusion of the example RVE. Its center is located at $\vec{x}_c = [0,\ 0.5,\ 0]^{\mathrm{T}}$ such that intersections with $\mathcal{P}_{x_0}$, $\mathcal{P}_{z_0}$ and $\mathcal{L}_{x_0z_0}$ are present. This qualifies the inclusion as a master inclusion. The three slave inclusion possess centers $\vec{x}_{c_i} = \vec{x}_c + \vec{v}_i$ for $i \in \{1, 2, 3\}$ with the shift vectors

$$\vec{v}_1 = [l_x\ 0\ 0]^{\mathrm{T}}, \quad \vec{v}_2 = [0\ 0\ l_z]^{\mathrm{T}}, \quad \vec{v}_3 = [l_x\ 0\ l_z]^{\mathrm{T}} \tag{4.1}$$

w.r.t. the master inclusion center.

Next, the master inclusion is split by the master faces which yields a quadripartite ellipsoid, see Fig. 4.3 (b). All four pieces are partial volumes of the combined set of master and slave inclusions inside the RVE. The resulting periodic boundary mesh of the RVE mandatorily requires a compatibility of the mesh's leading edges. Due to the partitioning of the inclusion, nodes are generated at geometric intersections. Accordingly, Fig. 4.3 (c) shows the resulting unstructured surface triangulation with nodes and leading mesh edges on the master faces $\mathcal{P}_{x_0}$ and $\mathcal{P}_{z_0}$ emanating from the fragmented structure of the partitioned master inclusion.

---

[40] Queries and manipulations on the geometric data are critical in terms of the finite precisions of a computer. By splitting the mesh information those operations are reduced to a minimum.

[7] For demonstration purpose the three periodic copies are not displayed.

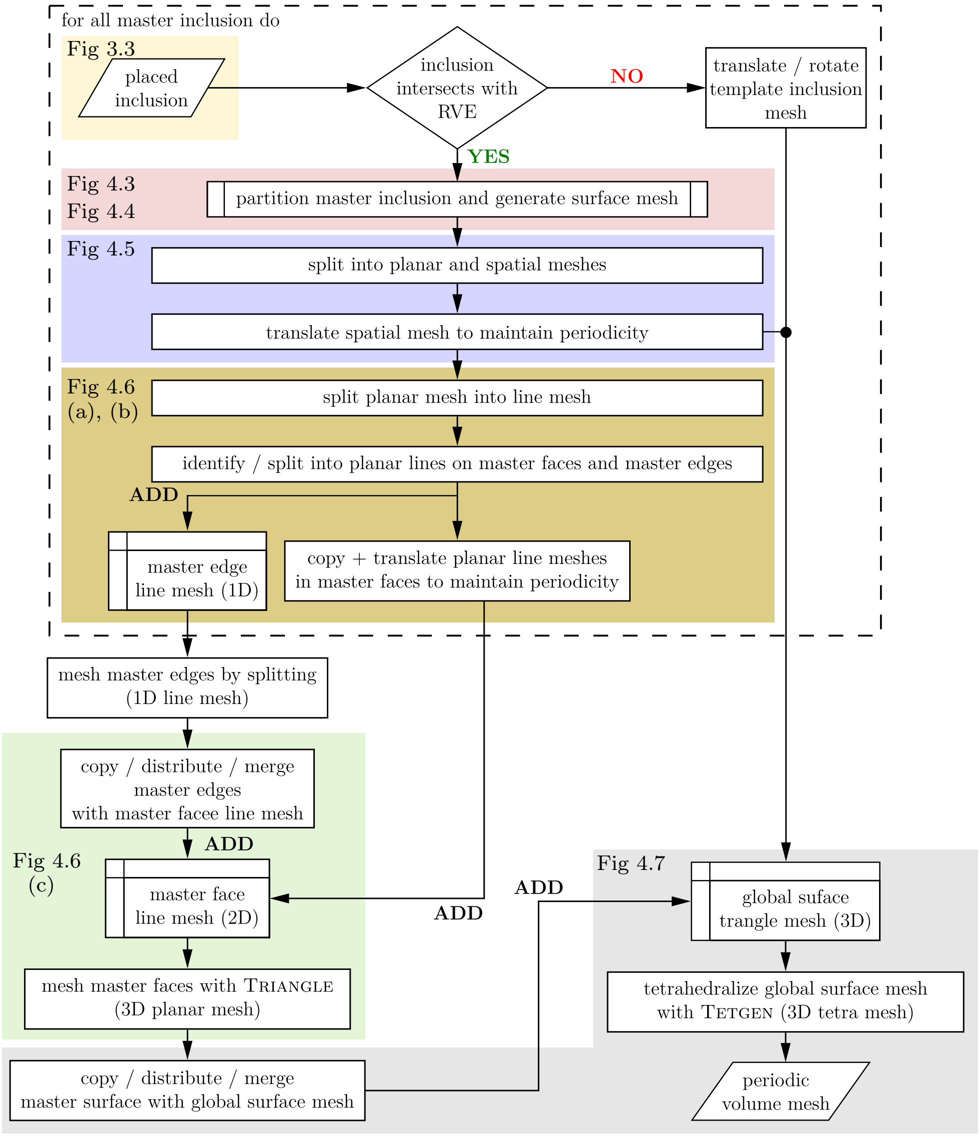

Figure 4.2.: Automatic generation of a high quality periodic mesh with a small number of elements. Figure adopted from [199] with permisson from Elsevier.

Additionally, the triangulation must feature planar mesh sections within the master faces and nodes at the penetration points of the inclusion-master edge $\mathcal{L}_{x_0 z_0}$ intersection, cf. Fig. 4.5.

The generation of such a partition and a subsequent triangulation is not a trivial task. Intersection curves and intersection areas of the inclusion-master plane overlap can only be expressed analytically for simple geometries (e.g. spheres or polyhedra).[8] Therefore, third party meshing software is utilized.

By means of boolean operations in the scope of constructive solid geometry, the partitioning is realized and followed by a preferably homogeneous surface triangulation. However,

---

[8] Even for a simple geometry like a spheroid the intersection edges and intersection surface w.r.t. planes are complex and must be computed numerically [204].

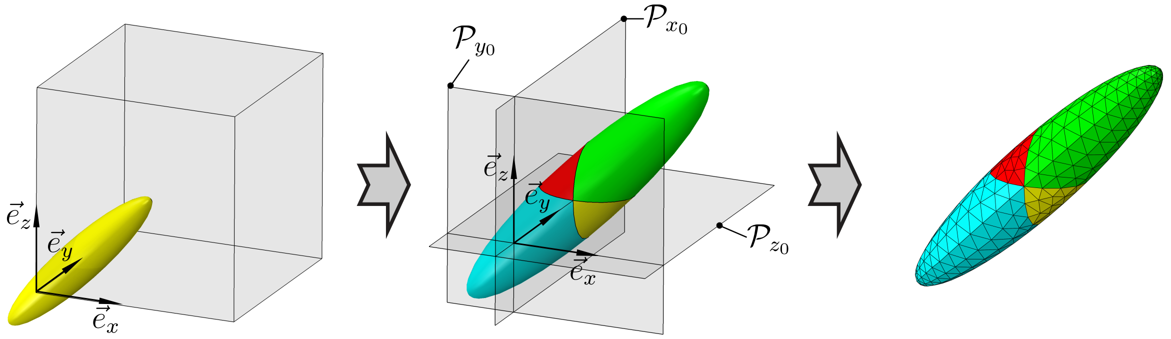

(a) (b) (c)

Figure 4.3.: Procedure of placement and meshing of the master inclusion: a) random placement of the master inclusion, b) partitioning by boolean operations and c) resulting surface mesh.[7] Figure reproduced from [199] with permission to reprint from Elsevier.

the partitioning produces small volumes or sharp angles for some cases. These unwanted features emanate from unfavorable relative positions between inclusion and RVE boundary. Degenerated surface meshes which are highly inhomogeneous, possess self-intersections or are non-waterproof (open faces) can result, depending on the chosen software and underlying meshing algorithm. To capture possible errors, a mesh integrity check follows each surface triangulation. The flowchart of this integrity check is shown in Fig. 4.4. Multiple tests are

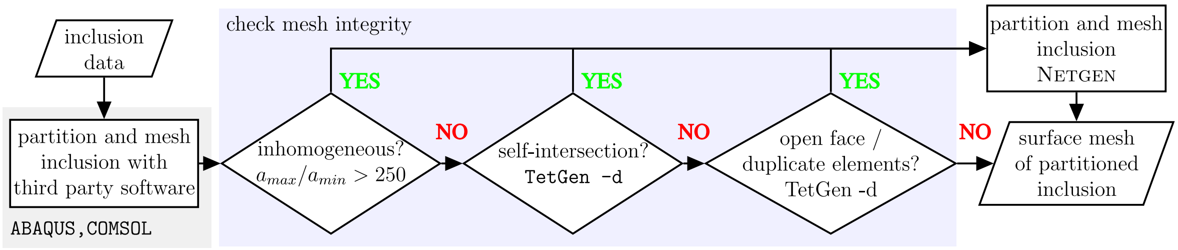

Figure 4.4.: Flowchart of the algorithm to ensure mesh integrity. Figure reproduce from [199] with permission to reprint from Elsevier.

sequentially conducted. First, the mesh inhomogeneity is checked by a heuristic threshold of the ratio of the maximum to minimum element area of the surfaces mesh. By utilizing the non-commercial software TetGen [214, 215] self-intersection tests (options `-d`) and open face checks (option `-V`) are conducted. Only if all the three checks evaluate negative, the mesh is accepted. If one of the requirements is violated, the inclusion is partitioned and meshed by Netgen [204]. It is found that Netgen provides the most robust mesh generator.[9] However, due to the employed advancing front algorithm, generated meshes are very dense and therefore, under the viewpoint of obtaining a manageable amount of elements, Netgen is not the first choice. Commercial software like Comsol or Abaqus represents the geometry in a different way which is more prone to the above described errors. These errors result from degenerated partitions that produce very small volumes or sharp angles, resulting in nodes treated as coincident due to the finite precision of computers. On the other hand, these software packages employ more sophisticated meshing methodologies resulting in meshes that are more homogeneous, show higher element quality and keep the amount of elements manageable, and, hence qualifying them as first choice. Hence, first a commercial software, e.g.

---

[9] Netgen uses an implicit function representation of geometric primitives resulting in accurate and robust boolean operations.

Comsol, is used to create a reasonably dense mesh and Netgen is used to ensure mesh quality in case that TetGen reveals substantial deficiencies of the mesh.

If the master inclusion lies completely inside the RVE, no partitioning is required. Instead, a template surface mesh of the inclusion that is initially generated once, is copied and located according to the geometric information of the master inclusion similar to the placement procedure of Sec. 3.1.1.

In conclusion, it can be noted that master inclusions exclusively act as the source for the further meshing process. Here, and in the following the term mesh set is understood as a subset of a once generated mesh, consisting of nodes and elements. In that sense, slave inclusions are only considered via their shift vectors for the mesh set distribution in the next step. The exclusiveness of the master inclusions, meaning only one inclusion of the master-slave group is meshed, represents the key component to a periodic mesh topology.

Next, the surface mesh is split into planar and spatial mesh sets, see Fig. 4.5 (a), and distributed across the RVE, see Fig. 4.5 (b) and (c). The resulting four planar mesh sets

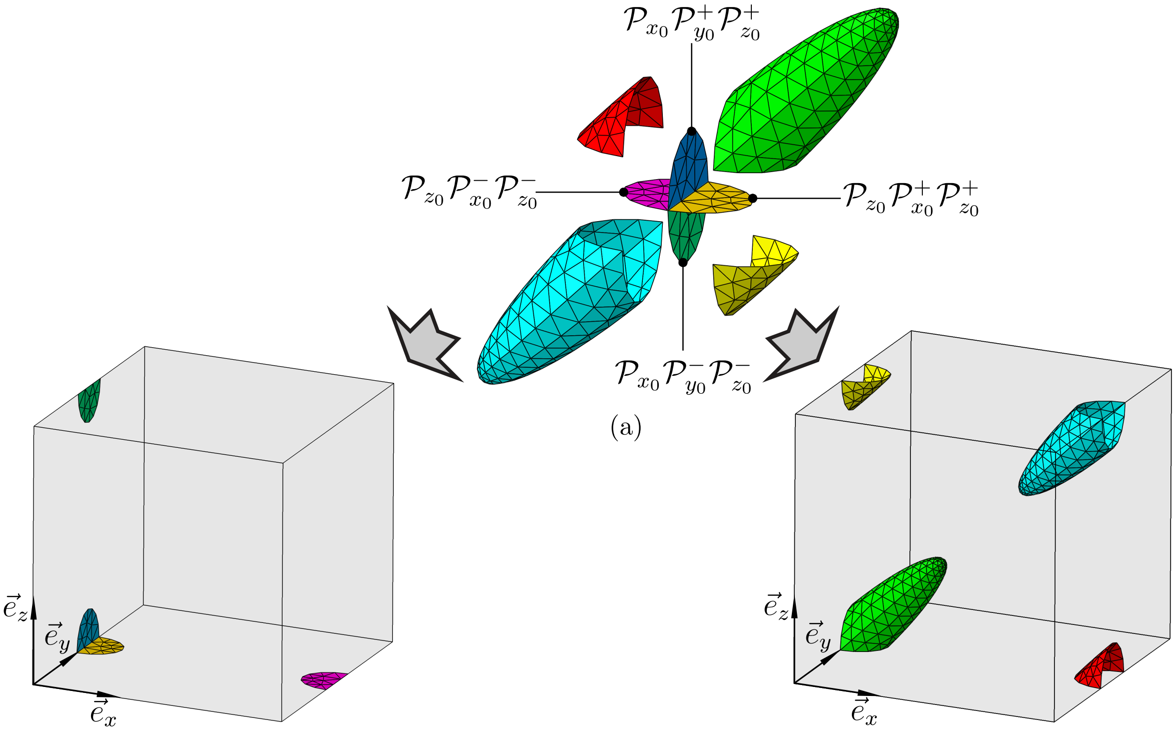

(b) (c)

Figure 4.5.: Splitting and distribution process of partitioned master inclusion surface mesh: (a) split surface mesh, (b) partitioned master face mesh and (c) distribute interior surface mesh. Fig. reproduced from [199] with permission from Elsevier.

lie within the master faces and the resulting four spatial mesh sets lie within the octants of the cartesian coordinate system. Vital to this step is the differentiation between spatial and planar parts of the non-manifold surface mesh. To identify the planar triangle elements on the master planes computational operations on the geometric information of the nodes are necessary. A numerical tolerance δ_N is utilized to decide whether or not nodes and accordingly elements are located on the faces. Every master plane and, accordingly, every planar mesh set is assigned to a positive and a negative region, according to the octants of cartesian coordinate systems. Hence, the four mesh sets consisting of nodes and elements

$$\begin{aligned}
&\mathcal{P}_{x_0}\mathcal{P}^{+}_{y_0}\mathcal{P}^{+}_{z_0}: && |\overrightarrow{node}_i \cdot \vec{n}_{x_0}| \leq \delta_N && \wedge && \overrightarrow{node}_i \cdot \vec{n}_{y_0} \leq \delta_N && \wedge && \overrightarrow{node}_i \cdot \vec{n}_{z_0} \leq \delta_N \ , \\
&\mathcal{P}_{x_0}\mathcal{P}^{-}_{y_0}\mathcal{P}^{-}_{z_0}: && |\overrightarrow{node}_i \cdot \vec{n}_{x_0}| \leq \delta_N && \wedge && \overrightarrow{node}_i \cdot \vec{n}_{y_0} \geq \delta_N && \wedge && \overrightarrow{node}_i \cdot \vec{n}_{z_0} \geq \delta_N \ , \\
&\mathcal{P}_{z_0}\mathcal{P}^{+}_{x_0}\mathcal{P}^{+}_{z_0}: && |\overrightarrow{node}_i \cdot \vec{n}_{z_0}| \leq \delta_N && \wedge && \overrightarrow{node}_i \cdot \vec{n}_{x_0} \leq \delta_N && \wedge && \overrightarrow{node}_i \cdot \vec{n}_{y_0} \leq \delta_N \ , \\
&\mathcal{P}_{z_0}\mathcal{P}^{-}_{x_0}\mathcal{P}^{-}_{y_0}: && |\overrightarrow{node}_i \cdot \vec{n}_{z_0}| \leq \delta_N && \wedge && \overrightarrow{node}_i \cdot \vec{n}_{x_0} \geq \delta_N && \wedge && \overrightarrow{node}_i \cdot \vec{n}_{y_0} \geq \delta_N
\end{aligned} \tag{4.2}$$

are present in the elaborated example. Here, $\overrightarrow{node}_i$ is a node of a mesh set with $i \in \{1..\, n_{nodes}\}$ where n_{nodes} represents the total number of nodes of the same mesh set. Choosing the right δ_N is challenging due to the finite precision in computers. For the purpose of this work, $\delta_N = 10^{-9}$ was found to be an adequate choice.

Since periodicity of the mesh topology is the ultimate objective, surface triangulations of opposing RVE faces must coincide. Therefore, the element sets $\mathcal{P}_{x_0}\mathcal{P}^{+}_{y_0}\mathcal{P}^{+}_{z_0}$, $\mathcal{P}_{x_0}\mathcal{P}^{-}_{y_0}\mathcal{P}^{-}_{z_0}$, $\mathcal{P}_{z_0}\mathcal{P}^{+}_{x_0}\mathcal{P}^{+}_{z_0}$ and $\mathcal{P}_{z_0}\mathcal{P}^{-}_{x_0}\mathcal{P}^{-}_{y_0}$ impose constraints on the later generated master face meshes and are translated accordingly, see Fig. 4.5 (b). Analogously to the slave inclusions and their shift vectors of Eq. (4.1), the appropriate regions of spatial mesh sets are translatively distributed across the RVE, see Fig. 4.5 (c). These spatial mesh sets are going to contribute to the interior of the global surface mesh in a later step.

Prior to the hierarchical meshing procedure, the algorithm transforms all planar element sets on all master faces into a line mesh of the exterior edges, see Fig. 4.6 (a).[10] The resulting two-dimensional skeleton line mesh on the individual master faces is inherited from the inclusions and, thus, conforms with the spatial triangulation shown in Fig. 4.5 (c). Congruently, intersection points between the inclusions and the master edges are incorporated into the master edge mesh. An identification of these points is followed by an approach similar to Eq. (4.2) via a threshold δ_N through

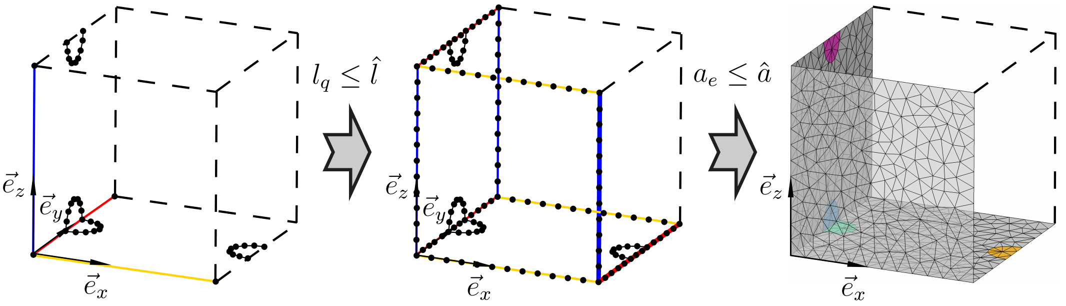

(a) (b) (c)

Figure 4.6.: Meshing of master edges and faces: (a) finding master inclusion-master edge intersection points and generating master face line mesh, (b) mesh master edges and copy them around master faces and (c) mesh master faces. The meshing process is triggered by a maximum line length $\hat{l}$ and a maximum element area $\hat{a}$. Fig. reproduced from [199] with permission from Elsevier.

$$\begin{aligned}
&\mathcal{L}_{x_0y_0}: && |\overrightarrow{node}_i \cdot \vec{n}_{x_0}| \leq \delta_N && \wedge && |\overrightarrow{node}_i \cdot \vec{n}_{y_0}| \leq \delta_N \ , \\
&\mathcal{L}_{y_0z_0}: && |\overrightarrow{node}_i \cdot \vec{n}_{y_0}| \leq \delta_N && \wedge && |\overrightarrow{node}_i \cdot \vec{n}_{z_0}| \leq \delta_N \ , \\
&\mathcal{L}_{x_0z_0}: && |\overrightarrow{node}_i \cdot \vec{n}_{x_0}| \leq \delta_N && \wedge && |\overrightarrow{node}_i \cdot \vec{n}_{z_0}| \leq \delta_N \ .
\end{aligned} \tag{4.3}$$

In the example RVE, the master edge $\mathcal{L}_{x_0z_0}$ (red) is divided into three partitions by the inclusion.

---

[10] This operation is conducted by working on the element connectivity information.

The hitherto described subprocess is repeated for all inclusions.

Next, the hierarchical meshing procedure starts by dividing all master edges via a line splitting algorithm which splits all line segments on the master edges with a length larger than a predefined maximum length $\hat{l}$. These line segments originate from potential inclusion intersections. To obtain the desired periodic mesh, opposite edges of master faces must have identical discretizations. Therefore, the generated line meshes of the master edges $\mathcal{L}_{x_0y_0}$ (blue), $\mathcal{L}_{y_0z_0}$ (yellow) and $L_{x_0z_0}$ (red) are copied (two copies per edge) to the slave edges on the master faces, see Fig. 4.6 (b).

The subsequent meshing of all master faces requires a fully enclosing line mesh (waterproof) that originates from the described inclusion-master face intersections and the edges of the master faces. This is certainly not the case, since line meshes have been copied without altering the element connectivity information and duplicated nodes at corners and inclusion-master edge intersections are present. All duplicate nodes of the entire line mesh (the combination of skeleton line meshes of the inclusions and master edge meshes) must be merged by joining all nodal pairs that possess a distance smaller than δ_N. Finding all these pairs in a numerically stable and efficient way is a non-trivial task and belongs to the research branch of nearest-neighbor-lookup algorithms. Here, incorporating a `k-d` tree via the `scipy.spatial.cKDTree` class from the `scipy` library [116], proved to be a very robust and fast method to conduct these point queries.[11] Identification, removal and reindexing of the nodes and their corresponding element connectivity entries, eventually results in the desired enclosing, waterproof line mesh which serves as input for the master face triangulations.

Crucial to this master face triangulation is the retention of enclosing line meshes. This requirement demands the utilization of so-called constrained triangulations where the input line mesh is not altered. The very robust and fast `Triangle` library from SHEWCHUK [213] offers such capabilities in form of constrained DELAUNAY triangulations. To receive high quality triangulations, the triangulation process is separated into two stages. First, a coarse constrained triangulation is executed (`Triangle` option `-pYYVa`). The resulting mesh serves as input for the second triangulation which then gives a high quality mesh (`Triangle` option `-pqrjYYVa`). By defining a maximum triangle area $\hat{a}$, it is possible to control the mesh size and promote a homogeneous mesh. Fig. 4.6 (c) depicts the resulting discretized master faces of the example microstructure.

The final step of the algorithm of Fig. 4.2 encompasses the three-dimensional mesh generation. To this end, meshed master faces are copied to their opposing counterparts $\mathcal{P}_{x_1}$, $\mathcal{P}_{y_1}$ and $\mathcal{P}_{z_1}$. Fig. 4.7 (a) depicts a corresponding exploded view. In addition, the stored interior surface triangles of the inclusions, see Fig. 4.5 (c), are added to the process. Together, the sets of meshed master faces and spatially triangulated inclusions act as input to the final three-dimensional tetrahedralization. Again, duplicated nodes are merged via a `k-d` tree routine, resulting in a waterproof surface mesh, cf. Fig. 4.7 (b). This surface mesh exhibits a periodic mesh topology which need not be altered in the following. Therefore, in analogy to the two-dimensional constrained meshing procedure, a constrained DELAUNAY tetrahedralization is conducted utilizing the very robust and fast software `TetGen` [214, 215]. Similar to the two-dimensional triangulation, the three-dimensional tetrahedralization is separated into two stages to yield better results, see [66].[12] Fixing all bounding triangles during the meshing process via a constrained tetrahedralization eventually results in the desired mesh periodicity, cf. Fig. 4.7 (c). The mesh density can be specified via the maximum element volume $\hat{v}$. Based on the cavities, formed by the inclusion in the initial surfaces triangulation, element sets are automatically generated by `TetGen`. This way further post-processing is not needed and an assignment of the element sets to the inclusions is straightforward.

Depending on the considered problem, it is necessary to adjust the element size to yield

---

[11] The `cKDTree.query_pairs` function is used for the pair search. `k-d` tree lookups show a complexity of $\mathcal{O}(n \log n)$ in contrast to the brute force approach with a complexity of $\mathcal{O}(n^2)$.

[12] The corresponding `TetGen` options are `-pYQA` and `-pqYQArao2`.

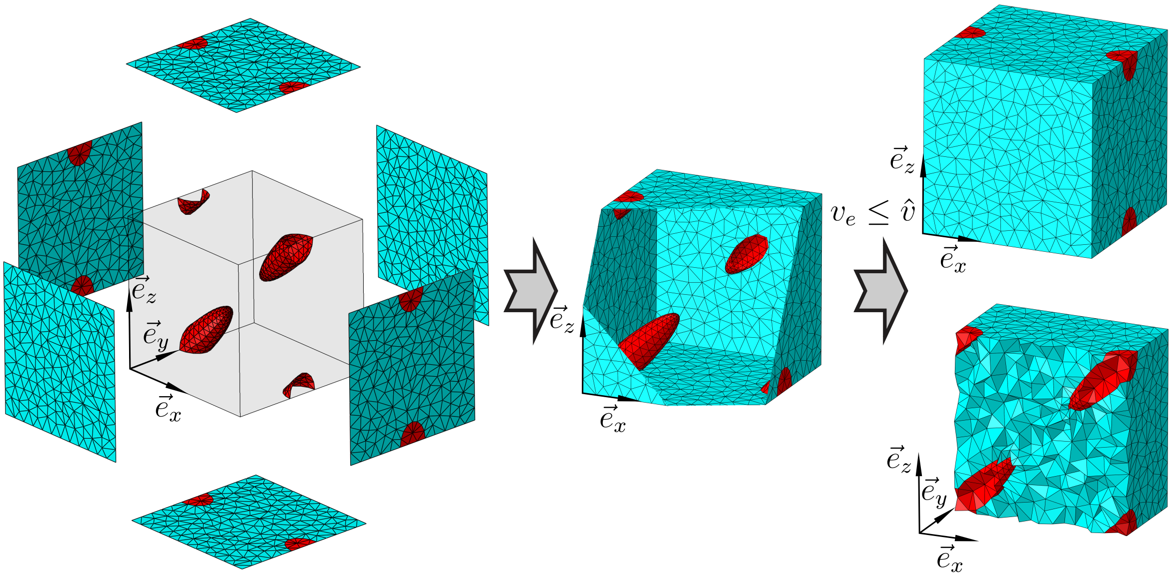

(a) (b) (c)

Figure 4.7.: Merging surface meshes and generating three-dimensional constrained tetrahedralization: (a) assembly and merge of master faces and interior mesh, (b) closed (waterproof) three-dimensional surface mesh and (c) final three-dimensional tetrahedral mesh as well as a cut through the unit cell. Volume meshing is controlled by specifying a maximum element volume $\hat{v}$. Fig. reproduced from [199] with permission from Elsevier.

a coarse or fine discretization. To this end, a sound relationship between the maximum line element length $\hat{l}$, the maximum triangle element area $\hat{a}$ and the maximum tetrahedral element volume $\hat{v}$ and the intended total number of elements n_{el} based on the edge length, area and volume of equilateral triangles and tetrahedrons is suggested by Fritzen [66] via

$$\hat{v} = \frac{V_{\mathrm{RVE}}}{n_{\mathrm{el}}} \ , \quad \hat{l} = \sqrt[3]{\frac{12}{\sqrt{2}}\hat{v}} \ , \quad \hat{a} = \frac{\sqrt{3}}{4}\hat{l}^2 \tag{4.4}$$

to form homogeneous meshes. However, in some cases it may be of importance to refine the discretization in regions where high stress or strain gradients would be anticipated, e.g. at interfaces of inclusions. By utilizing a finer surface triangulation of the inclusion surfaces, the algorithm allows to realize this refinement. In particular, only the maximum triangle element area of every inclusion surface mesh needs to be altered. The subsequent constrained Delaunay tetrahedralization via `TetGen` is altered by a larger intended tetrahedron volume. This assures a smooth transition from fine surface meshes to coarser mesh regions of the bulk volume. Exemplarily, Fig. 4.8 depicts an RVE with a mesh refinement around the inclusion.

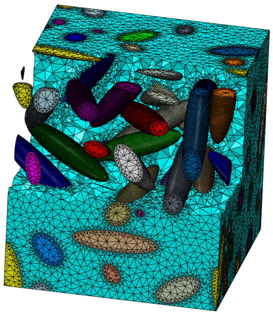

Figure 4.8.: Periodic RVE with 50 ellipsoidal inclusion featuring a refined mesh around the inclusion surfaces.

4.2. Examples and comparison

This section examines the effectiveness and applicability of the proposed meshing algorithm. Du to the limited capabilities of computers, the total number of elements cannot be arbitrarily large. Contrary, a fine discretization captures the geometry more precisely and highly distorted elements, which may lead to error-prone numerical simulations, can be avioded. Therefore, the trade-off between quality demands and computation time is always difficult. From that perspective, it is of major importance quantify the mesh quality. Among many element quality criteria and the general uncertainty of the most meaningful one [212], the shape factor $\eta = v/v_{opt}$, relating the element volume v to the optimal volume v_{opt} of an equilateral tetrahedron with the same circumradius, is used to evaluate discretizations.

In the following, example meshes generated via Netgen, a software library which is capable of producing periodic meshes automatically and, therefore, considered state of the art, and the proposed algorithm are analyzed and compared. All meshes are created under the premises of achieving a small amount of elements but maintaining a high overall mesh quality. To this end, the mesh is considered to be sufficiently good if an average element shape factor of $\overline{\eta} \gtrsim 0.5$ is maintained.

4.2.1. Mesh generation with the Netgen software library

Fig. 4.9 shows discretizations of the three example microstructures from Fig. 3.16 (i) meshed with Netgen. To obtain as few elements as possible, the mesh granularity option in Netgen is chosen to be `very coarse` or `coarse`, depending which meshing process finished successfully. Additionally, mesh statistics featuring frequency distributions of the element shape factor η as well as the average element shape factor $\overline{\eta}$ are presented. All discretizations show an excellent average element shape factor. However, this factor, as a global measure on its own, is not sufficient for mesh validation, since already few badly shaped elements may ruin a proper finite element simulation in terms of ill-conditioned stiffness matrices or a very small required time increment. Due to inclusion-RVE intersections and their periodic continuations, unwanted volumetric shapes are unavoidable and thus, poorly shaped elements almost always occur. From the element shape factor frequency distributions of the different meshes it is deducible that the finer meshes lead to a decrease of the number of poor elements.

4.2.2. Mesh generation with the proposed algorithm

Fig. 4.10 depicts discretizations and mesh statistics of the three example microstructures from Fig. 3.16 (i) generated with the algorithm developed for this dissertation. Excellent average element shape factors are observed in combination with an increase in high quality elements for finer meshes. Additional distance queries and thresholds between inclusions and the RVE

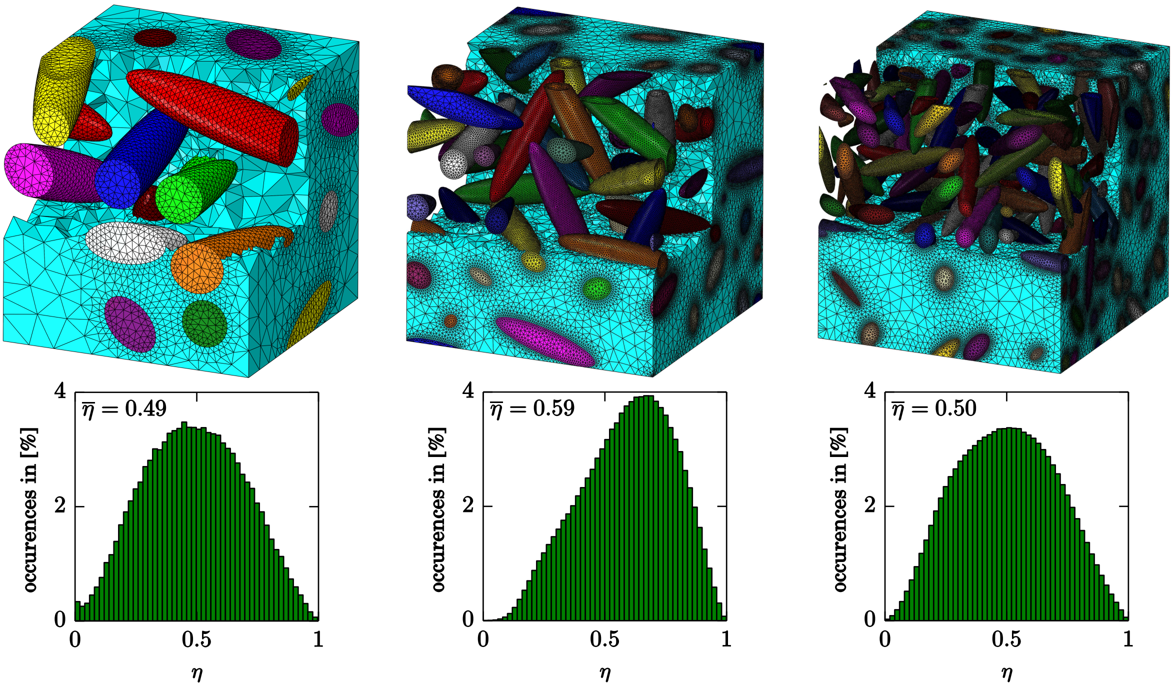

(a) (b) (c)

Figure 4.9.: Three example meshes of the microstructures from Fig. 3.16 (a) generated with NETGEN, featuring an inclusion volume fraction of approximately 20% together with mesh statistics featuring the average element shape factor $\overline{\eta}$: (a) 10 inclusions with 144214 elements (b) 50 inclusions with 1966106 elements and (c) 150 inclusions with 7314188 elements. The periodically continued parts of inclusions intersecting the RVE boundary exhibit identical colors. Fig. reproduced from [199] with permission from Elsevier.

boundary, as described in Sec. 3, support the formation of good-natured to be discretized volumes leading to a superb mesh quality.

4.2.3. Comparison

RVEs generated with NETGEN show noticeable mesh refinements at the inclusion interfaces. However, it is not possible to generate homogeneous meshes with NETGEN if anisotropic inclusions are present. It is suspected that this is due to the utilized advancing front meshing algorithm and its implementation concerning the rules of insertion of new triangles on regions of the ellipsoid surfaces that show increased curvatures, cf. [204]. RVEs generated with the above proposed algorithm reveal a more homogeneous element size distribution. Analyzing the presented discretizations in terms of mesh statistics, no significant differences between both approaches are observed. As depicted in Tab. 4.1, the average element shape factors and relative frequencies of $\eta \leq 10^{-4}$, as a quantitative measure of poor elements, are of similar size. The proposed algorithm reveals a slight benefit regarding microstructure approximation

Table 4.1.: Comparison of the approach developed herein to NETGEN for example microstructures with different number of inclusions and an inclusion volume fraction of $v_f = 0.2$.

	10 inclusions (Fig. 3.16 (a)(a))				50 inclusions (Fig. 3.16 (a)(b))				150 inclusions (Fig. 3.16 (a)(c))			
	$\overline{\eta}$	$\eta \leq$E-4	n_{el}	v_f	$\overline{\eta}$	$\eta \leq$E-4	n_{el}	v_f	$\overline{\eta}$	$\eta \leq$E-4	n_{el}	v_f
this work	0.53	2E-2 %	42211	0.192	0.50	2E-3 %	199955	0.192	0.52	0 %	732992	0.193
NETGEN	0.49	4E-2 %	144214	0.198	0.59	2E-4 %	1966106	0.199	0.50	4E-4 %	7314188	0.199

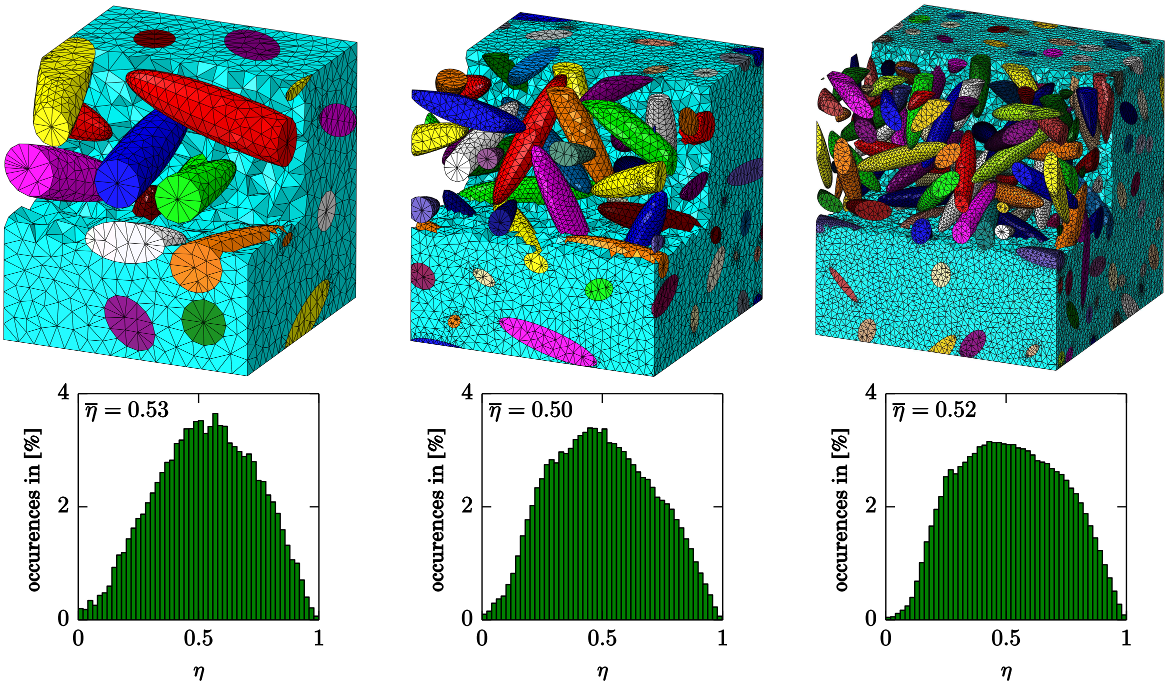

(a) (b) (c)

Figure 4.10.: Three example meshes generated with the algorithm depicted in Fig. 4.2. The underlying microstructures are taken from Fig. 3.16 (a) and possess an inclusion volume fraction of approximately 20% together. Additionally, the corresponding mesh statistics featuring the average element shape factor $\overline{\eta}$ are shown: (a) 10 inclusions with 42211 elements (b) 50 inclusions with 199955 elements and (c) 150 inclusions with 732992 elements. The periodically continued parts of inclusions intersecting the RVE boundary exhibit identical colors. Fig. reproduced from [199] with permission from Elsevier.

for sample (a) and (c) of Fig. 3.16 (i). However, the significant improvement concerns the total number of elements n_{el}. Already a visual inspection shows an increased amount of elements resulting in a very dense mesh of the NETGEN discretizations. Theses meshes have a very limited applicability w.r.t. finite element simulations in terms of a manageable computation time due to their enormous size. If many inclusions are needed in an RVE, it is almost impossible to conduct simulations with such a mesh. In contrast, the new meshing method reduces the total number of elements by a factor of up to 10, while still maintaining excellent mesh quality.

Another aspect worth mentioning concerns the approximate geometric representation of the microstructure through the mesh. Due to the curved nature of the inclusions, their boundaries cannot be described by tetrahedrons exactly. Additionally, the convexity of the considered inclusions always implicates a discretization featuring a reduced volume w.r.t. the intended one. As shown in Tab. 4.1, the actual volume fractions are slightly smaller than $v_f = 20\%$ for both approaches. Due to the larger number of elements of the NETGEN meshes, the inclusion volume fractions are closer to the intended ones. However, a minor adjustment in the described approach of Sec. 3, which is increasing the volume fraction v_f in accordance to the assumed lost amount due to meshing, resolves this problem.

5. Implementation of micromechanical boundary conditions[13]

This chapter focuses on the practical implementation of the microstructural boundary conditions introduced in Sec. 2.5.1. Besides the classical kinematic uniform boundary conditions (KUBC), static uniform boundary conditions (SUBC) and periodic boundary conditions (PBC), new approximate periodic boundary conditions (APBC) are suggested. The latter approach is an efficient way to apply periodic displacements and anti-periodic tractions on the boundary in an average sense, and, hence gives an alternative to relax the strong periodicity requirement. The feasibility and effectiveness of the proposed APBC is demonstrated on the example of a periodic microstructure featuring one inclusion.

With the microstructural information in form of an RVE (see Ch. 3) and a proper discretization (see Ch. 4) at hand, the next logical step to receive a micromechanical simulation model is the application of micromechanical boundary conditions (see Tab. 2.1). Beside the microstructural geometry and constitutive laws of the matrix and inclusions, the micromechanical boundary conditions are the governing factor of the gained results.

The TAYLOR- and SACHS-variants are trivial in the sense that no BVP needs to be solved. For TAYLOR conditions, the deformation gradient $\boldsymbol{F} = {}^{\mathrm{M}}\boldsymbol{F} \; \forall \; \vec{X} \in \mathcal{B}_0$ is prescribed in the entire domain. For a matrix-inclusion composite with only one inclusion constituent, denoted by the index (1), the desired averaged 1. PK stress becomes

$$ {}^{\mathrm{M}}\boldsymbol{P} = \frac{1}{V_{\mathrm{RVE}}} \int_{\mathcal{B}_0} \boldsymbol{P}\left({}^{\mathrm{M}}\boldsymbol{F}\right) dV_0 = v_f \boldsymbol{P}^{(1)}\left({}^{\mathrm{M}}\boldsymbol{F}\right) + [1 - v_f]\boldsymbol{P}^{(2)}\left({}^{\mathrm{M}}\boldsymbol{F}\right) \; . \tag{5.1} $$

Here $\boldsymbol{P}^{(1)}\left({}^{\mathrm{M}}\boldsymbol{F}\right)$ represents the constitutive law of the matrix and $\boldsymbol{P}^{(2)}\left({}^{\mathrm{M}}\boldsymbol{F}\right)$ represents the constitutive law of the inclusion. Contrary, the SACHS condition requires the inverse form of the material law, due to the prescribed stress $\boldsymbol{P} = {}^{\mathrm{M}}\boldsymbol{P} \; \forall \; \vec{X} \in \mathcal{B}_0$. The desired macroscopic deformation gradient then becomes

$$ {}^{\mathrm{M}}\boldsymbol{F} = \frac{1}{V_{\mathrm{RVE}}} \int_{\mathcal{B}_0} \boldsymbol{F}\left({}^{\mathrm{M}}\boldsymbol{P}\right) dV_0 = v_f \boldsymbol{F}^{(1)}\left({}^{\mathrm{M}}\boldsymbol{P}\right) + [1 - v_f]\boldsymbol{F}^{(2)}\left({}^{\mathrm{M}}\boldsymbol{P}\right) \; . \tag{5.2} $$

However, these two conditions are of no practical relevance. On the one hand, for non-linear, path dependent material laws it is not clear on which deformation path the final deformation state is reached. On the other hand, Eq. (5.2) requires inverse constitutive relations obtainable for very simple material laws only.

Therefore, the focus is put on KUBC, SUBC and PBC. In the framework of a deformation-driven FE formulation, typically only the first and last variants are utilized. These DIRICHLET boundary conditions are directly applied to degrees of freedom of boundary nodes of the FE mesh by prescribing displacements $\vec{u}$. Nevertheless, FE codes offer the possibility to apply traction boundary conditions, also known as NEUMANN boundary conditions, in form of nodal forces. Since pure NEUMANN problems cannot be solved due to the absence of a unique solution, a minimum set of DIRICHLET boundary conditions is necessary to prevent rigid

---

[13] This chapter is based on the publications: "FULLY PERIODIC RVES FOR TECHNOLOGICAL RELEVANT COMPOSITES: NOT WORTH THE EFFORT!" [200] and "Automatic generation and discretization of fully periodic representative volume elements of plain woven composites" [113].

body motions and a related singular tangential stiffness matrix.[14] Due to the deformation-driven character of the utilized FE formulation, these kind of analysis often entail additional iterations or unstable solution processes. Therefore, pure NEUMANN boundary conditions are only of subordinate relevance.

To demonstrate the practical implementation of the mentioned boundary conditions, Fig. 5 depicts an RVE with annotated RVE entities for referencing nodal sets to which the boundary conditions are applied. To prevent rigid body translations, the RVE is clamped at the corner $C_{x_0y_0z_0}$.[15] Furthermore, so-called reference nodes R_x, R_y and R_z are introduced. These nodes extend the global system of equations with additional translational degrees of freedom. By formulating kinematic constraints and the prescription of displacements or forces to the reference nodes eases the practical implementation of the boundary conditions.

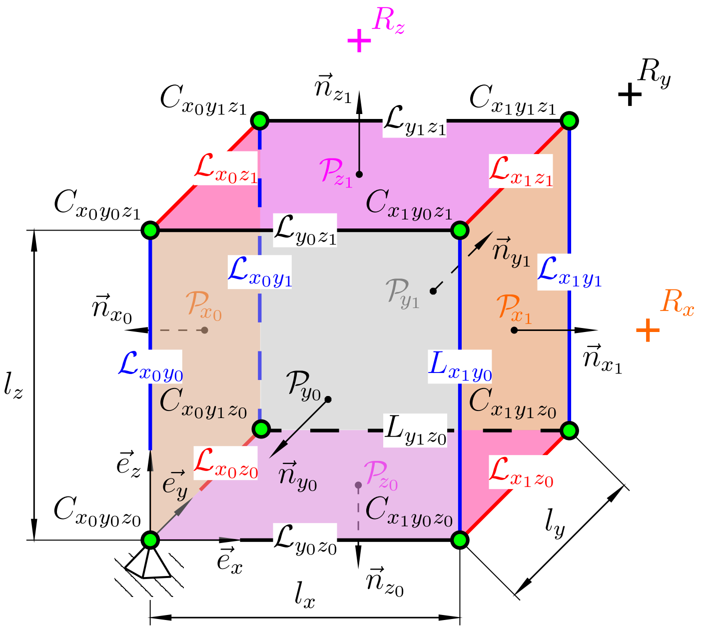

5.1. Kinematic uniform boundary conditions (KUBC)

KUBC are defined by Eq. (2.56). The macroscopic deformation gradient ${}^{\mathrm{M}}\boldsymbol{F}$ is input and ${}^{\mathrm{M}}\boldsymbol{P}$ output of the analysis. Rewriting Eq. (2.4) allows a formulation in terms of displacements by

$$\vec{u} = {}^{\mathrm{M}}\boldsymbol{H} \cdot \vec{X} \quad \forall \quad \vec{X} \in \partial\mathcal{B}_0 \ , \tag{5.3}$$

with the macroscopic displacement gradient ${}^{\mathrm{M}}\boldsymbol{H} = {}^{\mathrm{M}}\boldsymbol{F} - \mathbf{1}$. The RVE's nodal displacements at the boundary are prescribed such that the discretized version of Eq. (5.3) becomes

$$\vec{u}^{\,b} = {}^{\mathrm{M}}\boldsymbol{H} \cdot \vec{X}^b \qquad b = 1, \ldots, n_{\mathrm{b}} \ . \tag{5.4}$$

Here, $\vec{X}^b$ denotes the nodal locations on the RVE boundary with prescribed nodal displacements $\vec{u}^b$. The KUBC entail flat surfaces of the RVE justifying their name. These flat surfaces lead to compatible deformation modes in the sense that it is possible to tile space with the deformed RVEs. Rigid body rotations are intrinsically prevented by the clamped boundary.

Often, micromechanical simulations are intended to be compared with experiments. In this regard, uniaxial tensile or compressive loadings are of particular importance. They are characterized by a macroscopically one dimensional stress state. In a deformation-driven FE

---

[14] Superpositioned rigid body motions entail an infinite number of solutions to a pure NEUMANN problem. In this context, JAVILI et al. [112] introduce the term *semi-Dirichlet* boundary conditions.

[15] The prevention of rigid body motions in a deformation-driven FE formulation is crucial to circumvent singular stiffness matrices.

context, typically one of the macroscopic stretches ${}^{\mathrm{M}}\lambda_1, {}^{\mathrm{M}}\lambda_2$ or ${}^{\mathrm{M}}\lambda_3$ of ${}^{\mathrm{M}}\boldsymbol{H}$ is prescribed and, therefore, acts as the cause of such a stress state. As a consequence, not all nodal displacements on the RVE boundary can be prescribed a priori. The remaining tensor coordinates of the macroscopic displacement gradient are a result of the simulation. For anisotropic materials, they are non-zero. To ensure the required flatness of the RVE faces, the reference points are used. The applied placement boundary conditions then read

$$\begin{aligned} u_1^{\mathcal{P}_{x0}} &= 0 \ , \ u_1^{\mathcal{P}_{x1}} = u_1^{R_x} = \left[{}^{\mathrm{M}}\lambda_1 - 1\right] ||\Delta\vec{X}^x||_2 \\ u_2^{\mathcal{P}_{y0}} &= 0 \ , \ u_2^{\mathcal{P}_{y1}} = u_2^{R_y} = \left[{}^{\mathrm{M}}\lambda_2 - 1\right] ||\Delta\vec{X}^y||_2 \\ u_3^{\mathcal{P}_{z0}} &= 0 \ , \ u_3^{\mathcal{P}_{z1}} = u_3^{R_z} = \left[{}^{\mathrm{M}}\lambda_3 - 1\right] ||\Delta\vec{X}^z||_2 \end{aligned} \tag{5.5}$$

with $\Delta\vec{X}^x = \vec{X}^{\mathcal{P}_{x1}} - \vec{X}^{\mathcal{P}_{x0}}$, $\Delta\vec{X}^y = \vec{X}^{\mathcal{P}_{y1}} - \vec{X}^{\mathcal{P}_{y0}}$ and $\Delta\vec{X}^z = \vec{X}^{\mathcal{P}_{z1}} - \vec{X}^{\mathcal{P}_{z0}}$. These constraint equations between nodal degrees of freedom of RVE faces $\mathcal{P}_{x_1}, \mathcal{P}_{y_1}$ and $\mathcal{P}_{z_1}$ and corresponding reference nodes must be included in a simulation. Due to the zero displacement prescription of all nodes on the faces $\mathcal{P}_{x_0}, \mathcal{P}_{y_0}$ and $\mathcal{P}_{z_0}$, rigid body rotations are prevented such that the simulation setup is sound. The KUBC do not require any specific mesh topology, revealing them as operationally efficient to implement.

Solving the microstructural BVP yields the 1. PK stresses $\boldsymbol{P}(\vec{X}) \ \forall \ \vec{X} \in \mathcal{B}_0$. The desired macroscopic 1. PK stresses ${}^{\mathrm{M}}\boldsymbol{P}$ is computed by volume averaging or a surface averaging. In the scope of FE simulations, the continuous forms of these averages are discretized to

$$ {}^{\mathrm{M}}\boldsymbol{P} \approx \frac{1}{V_{\mathrm{RVE}}} \sum_{i=0}^{n_{\mathrm{el}}} \boldsymbol{P}_i \, V_{0_i}^{\mathrm{el}} \approx \frac{1}{V_{\mathrm{RVE}}} \sum_{i=0}^{n_{\mathrm{b}}} \vec{X}_i \otimes \vec{F}_i \ .^{16} \tag{5.6}$$

Here, $V_{0_i}^{\mathrm{el}}$ denotes the volume and $\boldsymbol{P}_i$ the 1. PK stress of element i. $\vec{F}_i$ represents the nodal force of node i in the current configuration. The discrete version of the surface integral is of particular interest, since its evaluation is much more efficient. No retrievement of element volumes or stresses at integration point level is necessary. Instead, only nodal information is required.

5.2. Static uniform boundary conditions (SUBC)

SUBC represent the counterpart to KUBC and are defined in Eq. (2.54). Input is the macroscopic 1. PK stress ${}^{\mathrm{M}}\boldsymbol{P}$ that defines the (to be prescribed) stress vectors $\vec{p}$ on the RVE boundary. Typically, FE packages offer the possibility to apply stress vector boundary conditions by means of distributed loads.[17] These tractions need to be modeled as so-called dead loads since $\vec{p}$ should not change in the course of deformation. As already mentioned, difficulties concerning the uniqueness of the solution emerge from the pure NEUMANN nature of the problem. By pinning the corner $C_{x_0y_0z_0}$, rigid body translations are prevented. Additionally, potential rotations of the RVE need to be suppressed to circumvent a singular tangential stiffness matrix of the FE system. The restriction of the following nodal degrees of freedom

$$ u_3^{C_{x_0y_1z_0}} = 0 \ , \ u_1^{C_{x_0y_0z_1}} = 0 \ , \ u_2^{C_{x_1y_0z_0}} = 0 \ . \tag{5.7}$$

reveals a possibility for linearized kinematics. They prevent rotations of the RVE around the x-axis, y-axis and z-axis. However, this choice is not unique and other corners or nodes could be constrained instead. Ideally, these boundary conditions should not invoke any reaction forces that alter the given boundary traction $\vec{p}$. This holds true in the small strain regime, since no distinction between the reference and current configuration is made. For large deformations, the situation is more complicated. Depending on the prescribed stress

---

[16] See App. A.3 for a detailed derivation.

[17] In `Abaqus` the option `DLOAD` is used.

vectors, non-zero displacement prescriptions of the corners might be necessary to accommodate a freely deforming RVE. To this end, Javili et al. [112, 193] suggest a procedure that iteratively adjusts the displacement prescriptions of Eq. (5.7) such that possible reaction forces vanish by augmenting the global system of equations. Due to the resulting mix of Dirichlet and Neumann boundary conditions, they introduce the term *semi*-Dirichlet boundary conditions. However, the method diminishes the practical relevance in the scope of commercial FE solvers since the global solution procedure must be modified. A viable alternative is given by substituting the prescribed zero displacement pinnings with linear elastic springs via

$$F_3^{C_{x_0 y_1 z_0}} = C u_3^{C_{x_0 y_1 z_0}} \quad , \quad F_1^{C_{x_0 y_0 z_1}} = C u_1^{C_{x_0 y_0 z_1}} \quad \text{and} \quad F_2^{C_{x_1 y_0 z_0}} = C u_2^{C_{x_1 y_0 z_0}} \ . \tag{5.8}$$

Here, C denotes the spring stiffness. To guarantee that C is not significantly altering the solution process

$$\frac{C}{l_i} \ll ||\mathbb{C}||_2 \tag{5.9}$$

must hold. Here, $\mathbb{C}$ denotes the tangential stiffness of the FE system and l_i the corresponding edge length of the RVE.[18] Similar to KUBC, SUBC do not have any requirements on the mesh.

The resulting macroscopic deformation gradient ${}^{\mathrm{M}}\boldsymbol{F}$, which is the output of a SUBC analysis, computes via volume averages or surface averages in a discretized way to

$$^{\mathrm{M}}\boldsymbol{F} \approx \frac{1}{V_{\mathrm{RVE}}} \sum_{i=0}^{n_{\mathrm{el}}} \boldsymbol{F}_i \, V_{0_i}^{\mathrm{el}} \approx \frac{1}{V_{\mathrm{RVE}}} \sum_{i=0}^{n_{\mathrm{b}}} \left[\vec{u}_i + \vec{X}_i \right] \otimes \vec{N}_i A_{0_i}^{\mathrm{el}\,19} \tag{5.10}$$

where $\boldsymbol{F}_i$ is the deformation gradient in element i. Since the element surface areas $A_{0\,i}^{\mathrm{el}}$ are required for evaluating the surface integral in its discrete version, the direct volume integral proves convenient.

5.3. Periodic boundary conditions (PBC)

PBC are an intermediate alternative to KUBC and SUBC. Contrary to KUBC, kinematic relations between boundary nodes are formulated instead of completely prescribing their displacement or loading. Starting with Eq. (2.59), the goal is to eliminate the displacement fluctuation $\vec{\tilde{u}}$. To this end, the difference of displacements of opposing RVE boundary sections ($\vec{u}^+$ and $\vec{u}^-$), corresponding to the subdivision of the RVE boundary into $\partial\mathcal{B}_0^+$ and $\partial\mathcal{B}_0^-$, see Eq. (2.57), yields

$$\vec{u}^+ - \vec{u}^- = {}^{\mathrm{M}}\boldsymbol{H} \cdot \left[\vec{X}^+ - \vec{X}^- \right] \ . \tag{5.11}$$

Eq. (5.11) represents the kinematic constraints between the nodal degrees of freedom of opposing RVE faces. Unfortunately, every nodal pair is required to possess the exact same planar position on the RVE faces. This fact entails the difficult demand of a periodic mesh topology addressed in the former chapter. For a better understanding, Tab. 5.1 lists the assignment of related positive and negative RVE boundaries with respect to the RVE faces. Since three opposing RVE faces are present, three variants of Eq. (5.11) exist. These variants are imposed via the three reference nodes R_x, R_y and R_z. To this end, the right hand side of

---

[18] Unfortunately, C cannot be chosen arbitrary small due to a resulting bad conditioned tangential stiffness matrix.

[19] See App. A.3 for a detailed derivation.

Table 5.1.: Assignment of the RVE faces w.r.t. the division of the RVE boundary according to Eq. (2.57).

$\partial\mathcal{B}_0$	x-direction	y-direction	z-direction
$-$	$\mathcal{P}_{x_0}$	$\mathcal{P}_{y_0}$	$\mathcal{P}_{z_0}$
$+$	$\mathcal{P}_{x_1}$	$\mathcal{P}_{y_1}$	$\mathcal{P}_{z_1}$

Eq. (5.11), which is known, is given in terms of $\vec{u}^{R_x}, \vec{u}^{R_y}$ and $\vec{u}^{R_z}$ via

$$\begin{aligned} x-\text{direction:}\quad \Delta\vec{X}^x &= \left[\vec{X}^+ - \vec{X}^-\right] = [l_x \; 0 \; 0]^{\mathrm{T}} \quad , \quad \vec{u}^{R_x} = {}^{\mathrm{M}}\boldsymbol{H}\cdot\Delta\vec{X}^x \\ y-\text{direction:}\quad \Delta\vec{X}^y &= \left[\vec{X}^+ - \vec{X}^-\right] = [0 \; l_y \; 0]^{\mathrm{T}} \quad , \quad \vec{u}^{R_y} = {}^{\mathrm{M}}\boldsymbol{H}\cdot\Delta\vec{X}^y \\ z-\text{direction:}\quad \Delta\vec{X}^z &= \left[\vec{X}^+ - \vec{X}^-\right] = [0 \; 0 \; l_z]^{\mathrm{T}} \quad , \quad \vec{u}^{R_z} = {}^{\mathrm{M}}\boldsymbol{H}\cdot\Delta\vec{X}^z \; . \end{aligned} \tag{5.12}$$

Then, the formulation of kinematic constraints ensuring Eq. (5.12) is given by

$$\vec{u}^{\mathcal{P}_{x_1}} - \vec{u}^{\mathcal{P}_{x_0}} = \vec{u}^{R_x} \quad , \quad \vec{u}^{\mathcal{P}_{y_1}} - \vec{u}^{\mathcal{P}_{y_0}} \quad = \vec{u}^{R_y} \quad \text{and} \quad \vec{u}^{\mathcal{P}_{z_1}} - \vec{u}^{\mathcal{P}_{z_0}} = \vec{u}^{R_z} \; . \tag{5.13}$$

Every equation in (5.13) condenses one set of nodal degrees of freedom. In analogy to the mesh generation procedure, degrees of freedom on the master faces remain in the set of unknowns. To prevent overconstraining, the nodal degrees of freedom on the edges need to be excluded from Eq. (5.13). For demonstrating this over-constraining, the situation of edges in z-direction ($\mathcal{L}_{x_0y_0}, \mathcal{L}_{x_1y_0}, \mathcal{L}_{x_1y_1}, \mathcal{L}_{x_0y_1}$) is elaborated in the following.

The nodal degrees of freedom on these edges need to simultaneously fulfill all possible versions of Eq. (5.11) featuring the x-direction and y-direction, such that

$$\begin{aligned} \vec{u}^{\mathcal{L}_{x_1y_0}} - \vec{u}^{\mathcal{L}_{x_0y_0}} &= \vec{u}^{R_x} \\ \vec{u}^{\mathcal{L}_{x_1y_1}} - \vec{u}^{\mathcal{L}_{x_0y_1}} &= \vec{u}^{R_x} \\ \vec{u}^{\mathcal{L}_{x_0y_1}} - \vec{u}^{\mathcal{L}_{x_0y_0}} &= \vec{u}^{R_y} \\ \vec{u}^{\mathcal{L}_{x_1y_1}} - \vec{u}^{\mathcal{L}_{x_1y_0}} &= \vec{u}^{R_y} \end{aligned} \tag{5.14}$$

must hold. The system of equations (5.14) can be cast into

$$\begin{bmatrix} 1 & 0 & 0 & -1 \\ 0 & 1 & -1 & -1 \\ 0 & 0 & 1 & -1 \\ -1 & 1 & 0 & 0 \end{bmatrix} \begin{bmatrix} \vec{u}^{\mathcal{L}_{x_1y_0}} \\ \vec{u}^{\mathcal{L}_{x_1y_1}} \\ \vec{u}^{\mathcal{L}_{x_0y_1}} \\ \vec{u}^{\mathcal{L}_{x_0y_0}} \end{bmatrix} = \begin{bmatrix} \vec{u}^{R_x} \\ \vec{u}^{R_x} \\ \vec{u}^{R_y} \\ \vec{u}^{R_y} \end{bmatrix} \; . \tag{5.15}$$

The coefficient matrix in Eq. (5.15) has rank= 3, and, hence possess rank deficiency. This rank deficiency indicates the overconstraining nature of the edge constraints. Therefore, one set of master degrees of freedom needs to remain in the set of unknowns on each edge. Accordingly, the master edge degrees of freedom $\vec{u}^{\mathcal{L}_{x_0y_0}}$ are chosen to remain in the simulation, such that the kinematic constraints for the edges in z-direction become

$$\begin{aligned} \vec{u}^{\mathcal{L}_{x_1y_0}} - \vec{u}^{\mathcal{L}_{x_0y_0}} &= \vec{u}^{R_x} \\ \vec{u}^{\mathcal{L}_{x_0y_1}} - \vec{u}^{\mathcal{L}_{x_0y_0}} &= \vec{u}^{R_y} \\ \vec{u}^{\mathcal{L}_{x_1y_1}} - \vec{u}^{\mathcal{L}_{x_0y_0}} &= \vec{u}^{R_x} + \vec{u}^{R_y} \end{aligned} \quad . \tag{5.16}$$

Similarly, relations of the remaining edges transform into

$$\begin{aligned} & x-\text{direction} && y-\text{direction} \\ & \vec{u}^{\mathcal{L}_{y_1z_0}} - \vec{u}^{\mathcal{L}_{y_0z_0}} = \vec{u}^{R_y} && \vec{u}^{\mathcal{L}_{x_1z_0}} - \vec{u}^{\mathcal{L}_{x_0z_0}} \quad = \vec{u}^{R_x} \\ & \vec{u}^{\mathcal{L}_{y_0z_1}} - \vec{u}^{\mathcal{L}_{y_0z_0}} = \vec{u}^{R_z} && \vec{u}^{\mathcal{L}_{x_0z_1}} - \vec{u}^{\mathcal{L}_{x_0z_0}} \quad = \vec{u}^{R_z} \\ & \vec{u}^{\mathcal{L}_{y_1z_1}} - \vec{u}^{\mathcal{L}_{y_0z_0}} = \vec{u}^{R_y} + \vec{u}^{R_z} && \vec{u}^{\mathcal{L}_{x_1z_1}} - \vec{u}^{\mathcal{L}_{x_0y_0}} \quad = \vec{u}^{R_x} + \vec{u}^{R_z} \end{aligned} \quad . \tag{5.17}$$

The master degrees of freedom sets are chosen to be $\vec{u}^{\mathcal{L}_{y_0z_0}}$ and $\vec{u}^{\mathcal{L}_{x_0z_0}}$. However, overconstraining for RVE corners must be prevented as well. Therefore, corners are excluded in Eq. (5.16) and (5.17). They are treated by exploiting Eq. (5.11) for every single corner in all three coordinate directions via

$$\begin{bmatrix} -1 & 1 & 0 & 0 & 0 & 0 & 0 & 0 \\ 0 & 0 & 1 & -1 & 0 & 0 & 0 & 0 \\ 0 & 0 & 0 & 0 & 0 & 0 & 1 & -1 \\ 0 & 0 & 0 & 0 & -1 & 1 & 0 & 0 \\ -1 & 0 & 0 & 1 & 0 & 0 & 0 & 0 \\ 0 & -1 & 1 & 0 & 0 & 0 & 0 & 0 \\ 0 & 0 & 0 & 0 & 0 & -1 & 1 & 0 \\ 0 & 0 & 0 & 0 & -1 & 0 & 0 & 1 \\ -1 & 0 & 0 & 0 & 1 & 0 & 0 & 0 \\ 0 & -1 & 0 & 0 & 0 & 1 & 0 & 0 \\ 0 & 0 & -1 & 0 & 0 & 0 & 1 & 0 \\ 0 & 0 & 0 & -1 & 0 & 0 & 0 & 1 \end{bmatrix} \begin{bmatrix} \vec{u}^{C_{x_0y_0z_0}} \\ \vec{u}^{C_{x_1y_0z_0}} \\ \vec{u}^{C_{x_1y_1z_0}} \\ \vec{u}^{C_{x_0y_1z_0}} \\ \vec{u}^{C_{x_0y_0z_1}} \\ \vec{u}^{C_{x_1y_0z_1}} \\ \vec{u}^{C_{x_1y_1z_1}} \\ \vec{u}^{C_{x_0y_1z_1}} \end{bmatrix} = \begin{bmatrix} \vec{u}^{R_x} \\ \vec{u}^{R_x} \\ \vec{u}^{R_x} \\ \vec{u}^{R_x} \\ \vec{u}^{R_y} \\ \vec{u}^{R_y} \\ \vec{u}^{R_y} \\ \vec{u}^{R_y} \\ \vec{u}^{R_z} \\ \vec{u}^{R_z} \\ \vec{u}^{R_z} \\ \vec{u}^{R_z} \end{bmatrix} . \tag{5.18}$$

Eq. (5.18) incorporates three conditions for all eight corners, leading to 12 unique equations. Again, the coefficient matrix possesses rank deficiency in having rank = 7. Therefore, only seven displacements can be eliminated from the global system of equations and $\vec{u}^{C_{x_0y_0z_0}}$ is chosen as the remaining master corner. Combining the equations of (5.18) eventually yields the desired relationship between all slave corner nodal degrees of freedom and the master nodal degrees of freedom by

$$\begin{aligned} \vec{u}^{C_{x_1y_0z_0}} - \vec{u}^{C_{x_0y_0z_0}} &= \vec{u}^{R_x} \\ \vec{u}^{C_{x_0y_1z_0}} - \vec{u}^{C_{x_0y_0z_0}} &= \vec{u}^{R_y} \\ \vec{u}^{C_{x_0y_0z_1}} - \vec{u}^{C_{x_0y_0z_0}} &= \vec{u}^{R_z} \\ \vec{u}^{C_{x_1y_1z_0}} - \vec{u}^{C_{x_0y_0z_0}} &= \vec{u}^{R_x} + \vec{u}^{R_y} \\ \vec{u}^{C_{x_0y_1z_1}} - \vec{u}^{C_{x_0y_0z_0}} &= \vec{u}^{R_y} + \vec{u}^{R_z} \\ \vec{u}^{C_{x_1y_0z_1}} - \vec{u}^{C_{x_0y_0z_0}} &= \vec{u}^{R_x} + \vec{u}^{R_z} \\ \vec{u}^{C_{x_1y_1z_1}} - \vec{u}^{C_{x_0y_0z_0}} &= \vec{u}^{R_x} + \vec{u}^{R_y} + \vec{u}^{R_z} \end{aligned} \quad . \tag{5.19}$$

To prevent rigid body translations, the displacement of the corner $C_{x_0y_0z_0}$ is pinned via

$$\vec{u}^{C_{x_0y_0z_0}} = \vec{0} \; . \tag{5.20}$$

By prescribing the remaining three displacements of the reference nodes $\vec{u}^{R_x}, \vec{u}^{R_y}$ and $\vec{u}^{R_z}$, the macroscopic deformation gradient, which is input to the analysis, reveals

$$\begin{aligned} {}^{\mathrm{M}}\boldsymbol{F} =& \frac{1}{||\Delta\vec{X}^{x}||_2} \left[\vec{u}^{R_x} + \Delta\vec{X}^{x}\right] \otimes \vec{N}^{x_1} \\ &+ \frac{1}{||\Delta\vec{X}^{y}||_2} \left[\vec{u}^{R_y} + \Delta\vec{X}^{y}\right] \otimes \vec{N}^{y_1} \\ &+ \frac{1}{||\Delta\vec{X}^{z}||_2} \left[\vec{u}^{R_z} + \Delta\vec{X}^{z}\right] \otimes \vec{N}^{z_1} \end{aligned} \tag{5.21}$$

with $\vec{N}^{x_1} = [1\ ,\ 0\ ,\ 0]^{\mathrm{T}}, \vec{N}^{y_1} = [0\ ,\ 1\ ,\ 0]^{\mathrm{T}}$ and $\vec{N}^{z_1} = [0\ ,\ 0\ ,\ 1]^{\mathrm{T}}$.[20]

Similar to the KUBC, uniaxial tensile tests might be of particular importance to compare micromechanical simulations with experiments. Again, an anisotropic material results in a fully occupied matrix of tensor components of the displacement gradient ${}^{\mathrm{M}}\boldsymbol{H}$ whereas only

---

[20] See App. A.3 for a detailed derivation.

one stretch is prescribed and the remaining tensor coordinates are outcome of the simulation. However, PBC are capable of incorporating the full anisotropic behavior. For demonstration purposes, uniaxial tension in x-direction is considered in the following. This tension is accommodated by prescribing

$$u_1^{R_x} = \left[{}^{\mathrm{M}}\lambda_1 - 1\right] ||\Delta\vec{X}^x||_2 \ . \tag{5.22}$$

To prevent rigid body rotations, ensuring a non-singular tangential stiffness matrix of the discretized system, *semi*-DIRICHLET boundary conditions need to be applied via augmenting the global system of equations or introducing negligible spring stiffnesses attached to the reference nodes. An important, frequently utilized assumption is a macroscopically orthotropic material. In that scenario, normal and shear components of the deformation decouple such that the macroscopic displacement gradient under uniaxial loading in the principal directions of the material simplifies to

$${}^{\mathrm{M}}\boldsymbol{H} = \begin{bmatrix} {}^{\mathrm{M}}\lambda_1 - 1 & 0 & 0 \\ 0 & {}^{\mathrm{M}}\lambda_2 - 1 & 0 \\ 0 & 0 & {}^{\mathrm{M}}\lambda_3 - 1 \end{bmatrix} \ . \tag{5.23}$$

Rigid body rotation about the z-axis, x-axis and y-axis are prevented by the constraints

$$u_2^{R_x} = 0 \quad , \quad u_3^{R_y} = 0 \ \text{ and } \ u_1^{R_z} = 0 \ . \tag{5.24}$$

The macroscopic 1. PK stress computes in analogy to Eq. (5.6). However, further simplifications are possible. As proven in App. A.3, a sum overall all reaction forces $\vec{F}^i$ at the boundary nodes i reduces to the external forces $\vec{F}^{R_x}$, $\vec{F}^{R_x}$ and $\vec{F}^{R_x}$ acting solely at the reference nodes and the macroscopic 1. PK is given by

$${}^{\mathrm{M}}\boldsymbol{P} = \frac{1}{V_{\mathrm{RVE}}} \left[\Delta\vec{X}^x \otimes \vec{F}^{R_x} \otimes + \Delta\vec{X}^y \otimes \vec{F}^{R_y} + \Delta\vec{X}^z \otimes \vec{F}^{R_z}\right] \ . \tag{5.25}$$

5.4. Approximate periodic boundary conditions (APBC)

The implementation of PBC, as described in the previous section, coercively requires a periodic mesh topology with node couples that show identical in-plane positions on opposing RVE faces. For a non-periodic mesh topology, it is not straightforward to apply PBC. The application of approximative periodic boundary conditions (APBC) represents a remedy. To this end, the enforcement of periodic displacement fluctuations on every point of opposing boundaries is substituted through the imposition of periodicity in an averaged sense. Hence, the dependence on matching meshes is circumvented.

LARSSON et al. [137] employ a mixed FE-formulation with an independent discretization of displacements inside the RVE and tractions on the boundary of the RVE by means of LAGRANGE multipliers. A parameterized transition between the exact PBC and SUBC eventually leads to weakly imposed boundary conditions independent of the mesh topology. NGUYEN et al. [166] pursue a different approach. They introduce polynomial interpolations to describe displacements on the RVE boundaries. The nodal degrees of freedom act as fulcrums to these interpolation functions. Eventually, the periodicity is enforced by formulating constraints between the interpolation functions of opposing sides not requiring any matching nodal pairs. However, the drawback of these two approaches lies in the fact that a seamless integration into commercial software is hardly possible.

A more practical approach represents the so-called mesh tieing. In general, commercial FE software packages offer possibilities to couple meshed surfaces, independent of their discretization granularity. YUAN et al. [251] or KASSEM [123] pursue this approach and formulate APBC by using the tieing capabilities in ABAQUS.[21] A similar, more manual approach, is

---

[21] In ABAQUS, coupling of meshed surfaces is conveniently established by utilizing the `*TIE` keyword.

suggested by Wippler et al. [246]. All of these approaches share the strategy of a node-wise coupling. Nodes from the designated master surface are projected onto the slave surface. These projections lie either on a corner, on an edge or inside an element face of the slave surface. By means of element shape functions, the deformation of the projected point is interpolated. Eventually, displacement constraints are formulated between the deformation of the projected node and its parent node to facilitate PBC. This form of coupling is also known as node-to-surface coupling or node-to-surface tieing. The major drawback, however, is a distinctive sensitivity to mesh density differences of master and slave surfaces. It is advised that master faces should always posses a finer mesh then corresponding slave surfaces, see [1, 251]. Furthermore, unwanted, artificial stress noise is observable in a node-to-surface coupling.

A better alternative is a surface-to-surface tieing. To this end, a more involved formulation, based on contact mechanics, is established to realize the coupling between surfaces by the costs of increased computational costs. However, this effort results in a significantly increased insensitivity w.r.t. varying surface mesh granularities as well as more accurate and smoother stress outputs. Therefore, the surface-to-surface approach justifies its choice over a node-to-surface approach. The following incorporation and algorithm implementation of a surface-to-surface tieing as well as a quantitative and qualitative comparison to the fully periodic reference solution represents a new contribution of this thesis.

For illustrating the practical implementation Fig. 5.1 depicts a non-periodic two-dimensional RVE. First, master faces $\mathcal{P}_{x_0}$ (red nodes) and $\mathcal{P}_{y_0}$ (green nodes) are introduced. These faces are copied and, for demonstration purposes, translated to their opposing counterparts, namely $\mathcal{P}_{x_1}$ (orange nodes) and $\mathcal{P}_{y_1}$ (blue nodes). The required constraints for PBC are then formulated between the degrees of freedom of the reference points (R_x and R_y), the copied slave faces and their parent master faces. Therefore, this approach solely uses nodal pairs with identical in-plane coordinates which are outlined by the red and violet area in Fig. 5.1. The actual RVE boundaries $\mathcal{P}_{x_1}$ and $\mathcal{P}_{y_1}$ are coupled to the copied faces via the described surface-to-surface coupling. This ensures an identical deformation of both surfaces. In the coupling procedure, $\mathcal{P}_{x_1}$ and $\mathcal{P}_{y_1}$ act as slave surfaces implying the condensation of degrees of freedom associated with theses surfaces.

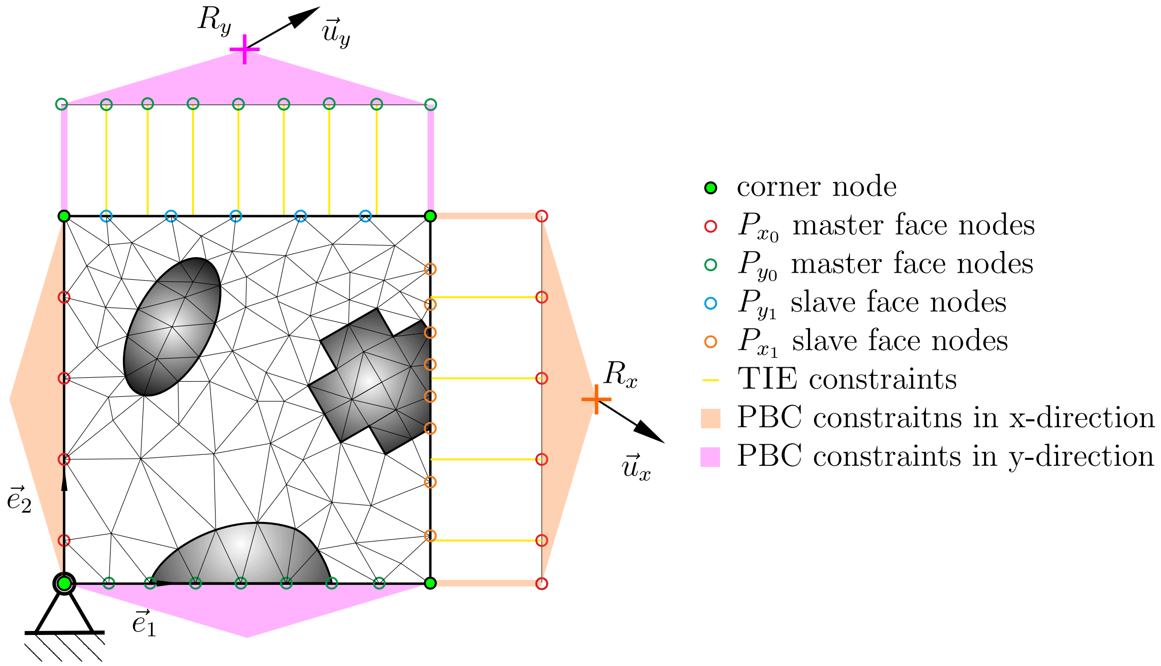

Figure 5.1.: Sketch of approximate PBC using surface-to-surface constraints.

To circumvent overconstraining for corners (black nodes) and edges (for three-dimensional RVEs), they must be excluded in the coupling process and individually constrained. In the three-dimensional case, three master edges ($\mathcal{L}_{x_0y_0}$, $\mathcal{L}_{y_0z_0}$, $\mathcal{L}_{x_0z_0}$) have to be introduced. These edges are copied and coupled to each slave edge individually (analog to the mentioned surfaces).[22] Since edges are one-dimensional, coupling solely relies on the nodes.[23] Eventually, the macroscopic deformation gradient is applied via reference points, see Sec. 5.3. Fig. 5.2 exemplarily depicts a three-dimensional non-periodic model subjected to uniaxial loading.

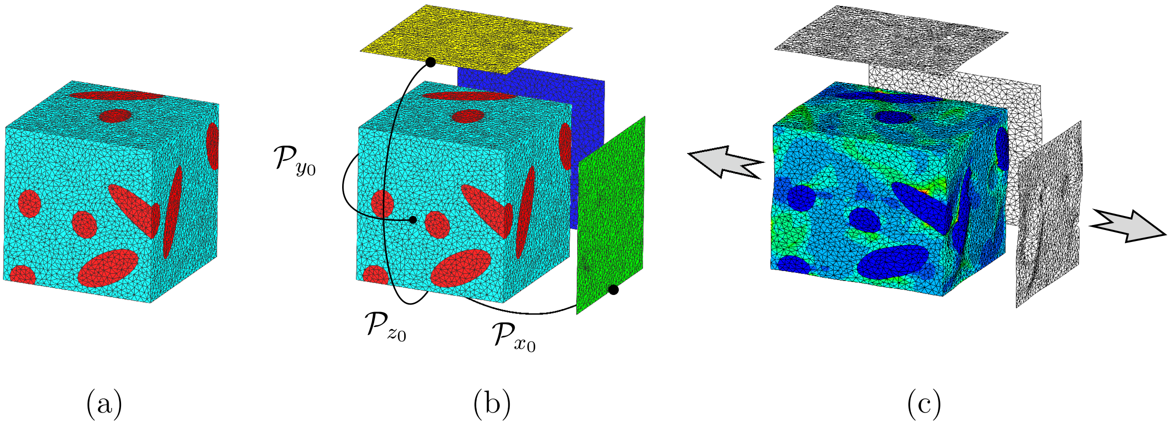

Figure 5.2.: Model setup of a three-dimensional non-periodic RVE employing the described methodology to setup APBC: (a) virgin mesh; (b) mesh tieing with copied master faces $\mathcal{P}_{x_0}, \mathcal{P}_{y_0}$ and $\mathcal{P}_{z_0}$ and (c) subjected tensile loading.

In the following, the APBC are validated w.r.t. their effectiveness and feasibility in the engineering practice. Inspired by the work of Miehe [160], three different RVEs representing the same material with a periodic inclusion arrangement but a non-periodic mesh topology, are investigated. Additionally, the fully periodic case is taken as a reference. Fig. 5.3 shows the geometric setup of the discretized RVEs: (a) fully periodic case with one inclusion at the RVE's center; (b) non-periodic mesh with one inclusion at the RVE's center; (c) non-periodic mesh with one eighth of the inclusion at each RVE corner and (d) non-periodic mesh with one inclusion close to the $\mathcal{P}^{x_0}$ side of the RVE. Due to the assumed periodic arrangement of the inclusions, all RVEs represent the same microstructure. The microstructural control parameter δ (see. Sec. 2.5), which is defined by the ratio of the RVE edge length $l_x = l_y = l_z = 1$ and the length of the ellipsoid of revolution $2c$, is taken as $\delta = 1.79$. The inclusion volume fraction of the single inclusion then computes to $v_f = 0.4\%$. The fully periodic reference setup is generated by the method described in Ch. 4. By utilizing an unstructured meshing technique for the remaining RVEs (b)-(d), non-periodic mesh topologies, predestinated for APBC, result. All RVEs feature approximately 25000 quadratic tetrahedral elements. A comparison of all three microstructures to the reference simulation, which ideally should yield the same effective material parameters, allows an evaluation of the capabilities of APBC.

To this end, the isotropic linear elastic material law of Eq. (2.37) is utilized for both constituents. For a profound investigation, the two opposing cases of a high and a low phase contrast ξ are considered. ξ denotes the ratio of material parameters of the constituents. In particular, a low phase contrast implies very soft inclusion that form voids in the limit case of $\xi \to 0$. The inverse scenario, with $\xi \to \infty$ denotes a very stiff inclusion which tend towards rigidity for the limit case. Tab. 5.3 lists the chosen material parameters, which relate to the example materials elaborated in Ch. 6.

To compute the effective Young's moduli ${}^{\mathrm{M}}E_{11}$ and the effective shear moduli ${}^{\mathrm{M}}G_{12}$, the RVEs are subjected to tensile and shear loadings in a small strain regime. Resulting macroscopic stress tensors are then directly utilized to compute the desired material parameters.[24]

---

[22] A master edge possesses three slave edges, and thus, three copies are necessary.

[23] In Abaqus, edge-coupling is realized by node-based surfaces tieing.

[24] In the small strain regime ${}^{\mathrm{M}}E_{11} = {}^{\mathrm{M}}\sigma_{11}/{}^{\mathrm{M}}\varepsilon_{11}$ and ${}^{\mathrm{M}}G_{12} = {}^{\mathrm{M}}\sigma_{12}/[2\,{}^{\mathrm{M}}\varepsilon_{12}]$ holds.

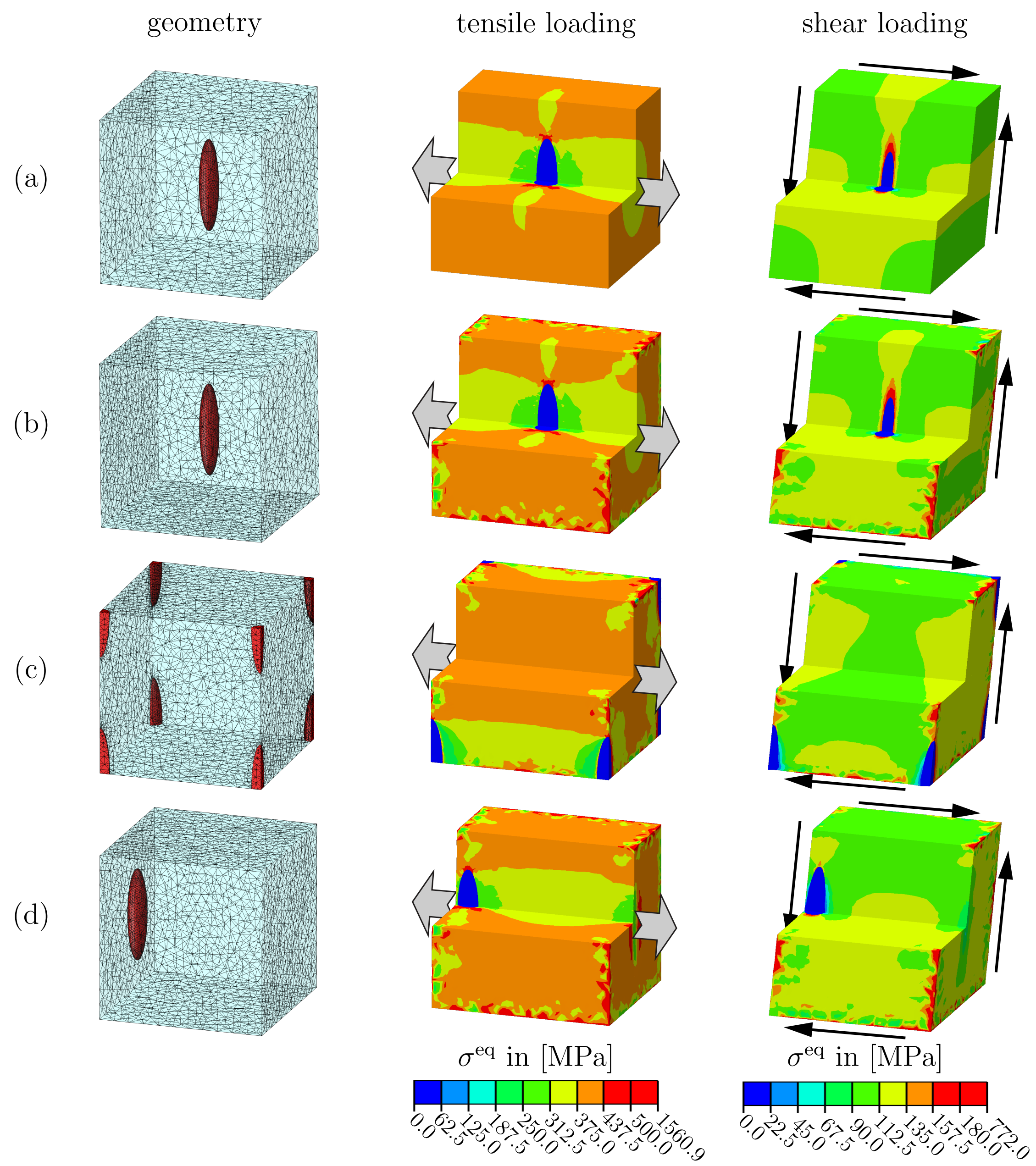

Figure 5.3.: Geometric setup and von Mises stress distributions σ^{eq} for tensile and shear loadings for a phase contrast of $\xi = \frac{1}{100}$ (soft inclusion): (a) fully periodic RVE with inclusion at the center; (b) APBC setup with inclusion at the RVE center; (b) APBC setup with the inclusion at the RVE corners and (d) APBC setup with the inclusion close to the boundary face $\mathcal{P}_{x_0}$.

All results are listed in Tab. 5.3.

Inspecting the discretization of the RVEs, it is of paramount importance to consider the resulting inclusion volume fractions. They are an influencing factor of first order regarding effective material parameters. Due to the meshing procedure, the true inclusion volume fraction varies from the intended one. This is reflected in the listed v_f values of Tab. 5.3, which are lower than the intended 0.4%. However, identical inclusion volume fractions are present such that macroscopic material parameters of the different model setups can be compared without losing generality.

This comparison reveals minor differences up to approximately 5% for all variants. These differences reflect the approximative character of APBC. It can be noticed that APBC tend to

Table 5.2.: Material properties for the RVE constituents.

E_{Matrix}	G_{Matrix}	$E_{\text{Inclusion}}$	$G_{\text{Inclusion}}$	ξ
3800	1300	38	13	$\frac{1}{100}$
3800	1300	38000	13000	100

Table 5.3.: Macroscopic material parameters for different single inclusion RVEs in a PBC and APBC setup.

phase contrast ratio	effective material parameters	inclusion positions / mesh setup			
		periodic	non-periodic		
		center	center	corner	side
$\xi = 1/100$	${}^{\text{M}}E_{11}$ [MPa]	3765.76	3783.91	3776.37	3784.63
	${}^{\text{M}}G_{12}$ [MPa]	1290.83	1296.30	1294.24	1296.65
$\xi = 100$	${}^{\text{M}}E_{11}$ [MPa]	3848.72	3866.48	3864.15	3868.43
	${}^{\text{M}}G_{12}$ [MPa]	1311.26	1316.83	1317.07	1317.11
v_f in [%]		0.395	0.395	0.395	0.395

give stiffer results than PBC. This fact is due to the increased constraints which are induced by the mesh tieing. Every node on a slave face is linked to multiple nodes on the copied master face. This increases the restrictions on the nodes' motion and subsequently the overall stiffness. In contrast, every node couple of the fully periodic model setup is connected to one reference point only, and, hence allowing a more flexible motion. However, the differences in the effective material parameters are negligible from an engineering point of view making APBC a viable alternative for homogenization.

To investigate the quality of the local character of the gained solution, Fig. 5.3 exemplarily depicts contour plots of the VON MISES stress distribution σ^{eq} for tensile and shear loadings for a phase contrast of $\xi = 1/100$ (soft inclusion). The stress distribution in the bulk region of the RVE reveals very similar patterns for all variants, which indicates the conformity of the simulations. However, some artificial stress peaks are observable for the APBC in the proximity of the RVE edges. These stress noises are due to the non-conformity of the meshes and the unavoidable node-to-node coupling of the RVE edges. The stress increases are another cause of the slightly increased overall stiffness of the APBC RVEs. Nevertheless, influences on the macroscopic properties are negligible demonstrating the highly effective applicability of APBC.

6. Model setups of matrix-inclusion composites and their influences[25]

In this chapter, various possibilities of setting up RVEs for computational micromechanical purposes under the light of the previous chapters are elaborated. The state-of-the-art, but cumbersome, approach to utilize a fully periodic model featuring a periodic microstructural geometry and a periodic mesh topology in combination with a high quality discretization with a large number of inclusions, is questioned. To this end, multiple methodologies of setting up FE models for homogenization purposes that extenuate these difficulties, are examined. Introduced approximations compare to the fully periodic reference solution which is obtainable by the methodologies introduced in the previous chapters. By means of a benchmark study featuring linear and non-linear material behavior for the matrix and inclusions with different phase contrasts, the most influential factors and viable approximations are highlighted. Eventually, the chapter concludes in giving guidelines to micromechanical model setups.

Setting up RVEs in computational micromechancis featuring a fully periodic geometry and a fully periodic mesh topology in combination with a high quality discretization is a cumbersome task and can significantly reduce the overall working efficiency. In the opinion of many researchers, a favorable FE model incorporates periodic RVEs with a large number of inhomogeneities as well as high quality discretizations suitable for the direct application of PBC [28–30, 79, 80, 87, 160, 179, 252]. By showing moderate boundary influences, PBC give a good compromise between the stiffer KUBC and the more compliant SUBC responses [94, 108, 120, 226]. Additionally, faster convergence towards the effective material parameters is observable when enlarging the RVE, qualifying PBC as state of the art. However, tremendous efforts are necessary to gather microstructural information and transfer it to a discretized model in that sense.

Generally, micromechanical analyses in engineering entail many approximations and uncertainties, e.g. material parameters, inclusion shapes etc.. In an efficient and meaningful model setup, all these inaccuracies should stay in the same order of influence. Therefore, it is questionable if it is worth to tolerate the accompanying labor of a fully periodic model setup for an engineering approach. To this end, various possibilities of relaxing the described strict requirements exist. Fig. 6.1 illustrates the here considered options.

First to mention is the RVE size, which is adjusted via the microstructural control parameter δ, see Eq. (2.39). The RVE size has a direct impact on all aspects of the model setup. Larger RVEs entail a computationally more challenging generation process of microstructural information [45]. The amount of inclusions also correlates to the discretization fineness, which is necessary to accurately resolve the microstructural geometry, and, hence correlates to the FE degree of freedom and therewith to the overall computational effort. Additionally, larger RVEs feature an enlarged boundary surface which increases the costs of setting up any kind of boundary conditions. However, the main advantage lies in the increased accuracy. Ideally, an RVE should be chosen infinitely large to yield the exact effective material response. In this regard, an increasing RVE size results in a vanishing surface-to-volume ratio such that boundary influences diminish. In practice, however, the computed results converge after a certain size is reached. Experimental findings, see Sec. 2.5, suggest to choose $\delta \in [5..60]$ depending on the considered material. Unfortunately, $\delta = 5$ in combination with an inclusion

---

[25] This chapter is based on the publication: "FULLY PERIODIC RVES FOR TECHNOLOGICAL RELEVANT COMPOSITES: NOT WORTH THE EFFORT!" [200]

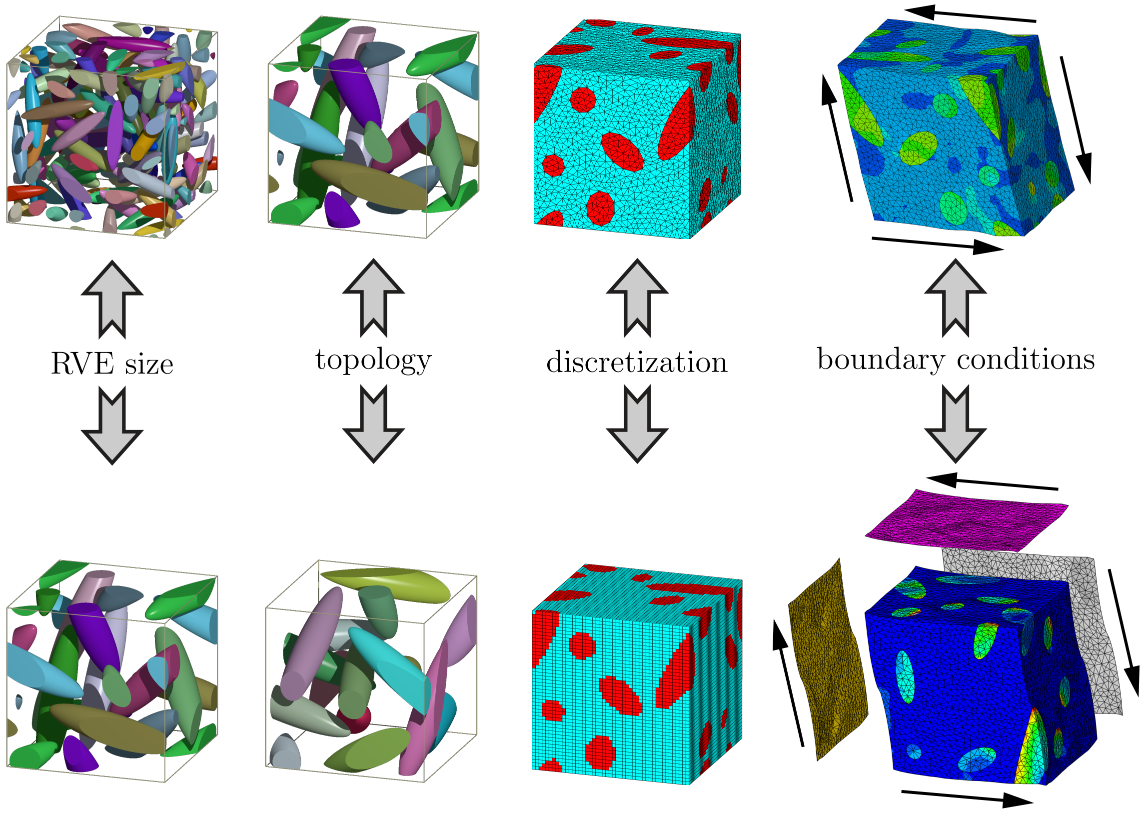

Figure 6.1.: Possibilities to relax the state-of-the-art model setup in computational micromechanics: reduction of the RVE size, detachment from periodicity in terms of microstructural morphology and discretization and application of APBC.

volume fraction of $v_f = 20\%$ is already a high value, resulting in RVEs with over 100 inclusions for ellipsoids of revolution with an aspect ratio of $\alpha = 5$, cf. Ch. 3. A remedy is given by the application of the ergodic hypothesis which assumes that averaging over many small samples (RVEs) gives the same result as averaging over one large sample. Unfortunately, the boundary influences on the macroscopic results reveal to be systematic errors. These errors are systematically larger for smaller RVEs then they are for larger ones, and hence qualifying the ergodic assumption as incorrect [83]. However, in the engineering practice, the introduced error is often tolerated and traded against reduced computational costs. The computational effort correlates with the degree of freedom n of the underlying FE system and numerical cost for many small RVEs is proportional to the amount of considered realizations. On the other hand, the direct (CHOLESKY decomposition) solution effort in linear FE problem correlates with $\mathcal{O}(n^3)$. Therefore, solving many microscopical BVP of small RVEs results in drastically reduced numerical expenses.

Another aspect concerns the microstructural topology, which ideally should be periodic. As elaborated in Ch. 3, this demand harshly restricts the generation of random microstructures, especially if high inclusion volume fractions are to be considered. In particular, the utilization of specific particle distributions can become cumbersome or even impossible to match for small RVEs. A withdrawal from periodicity is a simple solution to that dilemma, but with far-reaching consequences. On the one hand, requirements to the discretization drop. However, a non-periodic discretization does not allows to apply PBC, and hence violates the state-of-the-art approach.

The utilization of high quality meshes is also a vital factor to achieve trustworthy results. As demonstrated in Ch. 4, their (periodic) generation can become a very cumbersome and resource consuming task [30, 66, 199]. Discretizing geometrically complex microstructures (e.g., curved geometric features) is typically realized by employing tetrahedralizations. If inclusions in large quantity and of complex shape are to be considered, mesh automatization is hardly possible. Often manual adjustments that result in an increased modeling effort are necessary. The situation gets even worse if microstructural data is gained by experiments involving measurement noise causing tetrahedral meshing approaches to fails. The utilization of voxel discretizations resulting in regular grid-like meshes [80, 120] states a viable solution. Regular voxel meshes naturally feature a periodic mesh topology, allowing a straightforward application of PBC. However, the imprecise resolution of geometric features can deteriorate the simulations.

The last considered influence is related to the boundary conditions. As already stated, PBC always require a periodic mesh. As an alternative approach, APBC, KUBC or SUBC loosen this requirement, but result in overly stiff or underly compliant macroscopic responses.

The four detailed simplifications undoubtedly affect the overall results. However, from an engineering point of view, it is of paramount importance to quantify these influences for weighting advantages of more precise results against disadvantages of increased modeling efforts. To this end, a benchmark study that quantitatively compares alternative model setups with the fully periodic reference setup is presented in the following.

6.1. Benchmarking alternative model setups

All investigated RVEs are unit cubes and feature a target inclusion volume fraction of $v_f = 20\%$ with equally shaped, non-overlapping ellipsoids of revolution with an aspect ratio of $\alpha = 5$. Real materials that can be described by such a microstructural geometry are, e.g., so-called short fiber reinforced composites. They typically exist in two oppositional forms with very low phase contrasts ξ representing materials with soft inclusions and a stiffer matrix and very high phase contrasts ξ representing materials with stiff inclusions and a softer matrix. The phase contrast ξ is given by the ratio of the material properties of the constituents, e.g. the YOUNG's or shear modulus, via

$$\xi_E = \frac{E_{\text{Inclusion}}}{E_{\text{Matrix}}} \quad \text{or} \quad \xi_G = \frac{G_{\text{Inclusion}}}{G_{\text{Matrix}}} \; . \tag{6.1}$$

An example of the first material class are so-called rubber toughened polymers such as Acrylonitrile-Butadien-Styrene (ABS) [147, 159]. These materials feature soft rubbery inclusions that are intended to increase the fracture toughness of the thermoplastic Styrene-Acrylonitrile matrix material. In contrast, the glass-fibers or carbon-fibers in fiber reinforced composites are meant to improve the overall material stiffness, see [39, 175]. The stiffer inclusions serve as load-bearing components whose overall integrity is ensured by the matrix. To this end, Tab. 6.1 lists model material parameters of the linear elastic isotropic material behavior which is assumed for both constituents. It is worth noticing that there is a large discrepancy between the absolute difference of matrix and inclusion material parameters for both phase contrast variants: $\xi = 1/100$ correlates to $|E_{\text{Matrix}} - E_{\text{Inclusion}}| = |G_{\text{Matrix}} - G_{\text{Inclusion}}| = 3762\,\text{MPa}$ and $\xi = 100$ correlates to $|E_{\text{Matrix}} - E_{\text{Inclusion}}| = |G_{\text{Matrix}} - G_{\text{Inclusion}}| = 376200\,\text{MPa}$. Additionally, plasticity based on the standard VON MISES yield criterion is considered for the matrix material. A yield stress of $\sigma_y = 60\,\text{MPa}$ and a linear, isotropic hardening coefficient of 35 MPa are utilized to represent the deformation behavior of the matrix, cf. [207].

Table 6.1.: Material properties for the RVE constituents.

E_{Matrix} in [MPa]	G_{Matrix} in [MPa]	$E_{\text{Inclusion}}$ in [MPa]	$G_{\text{Inclusion}}$ in [MPa]	ξ
3800	1300	38	13	1/100
3800	1300	380000	130000	100

All RVEs are generated by the RSA method of Sec. 3.1 in a periodic and non-periodic way. The RVE size is varied by utilizing three different target inclusion numbers: 10, 50 and 100 inclusions. Here, the term target inclusion numbers refers to a periodic RVE that always exhibits the intended inclusion volume fraction. Non-periodic RVEs only approximately match the intended inclusion volume fraction due to the a priori unknown volumetric contributions of inclusions intersecting the RVE. Unfortunately, these contributions cannot be computed analytically which causes the approximative character. The actual microstructure generation process for the non-periodic case is terminated if the inclusion volume fraction deviates less than 1% from target volume fraction. Therefore, the inclusion volume fraction for non-periodic cases are only approximate and typically exhibit an increased inclusion number. The inclusion sizes and the microstructural control parameter δ depend on the RVE dimension, the intended inclusion number, the inclusion aspect ratio and the intended inclusion volume fraction. Tab. 6.2 lists the resulting δ.

Table 6.2.: RVE sizes

target inclusion number	10	50	100
δ	2.04	3.57	4.35

All RVEs are discretized by means of quadratic tetrahedral elements and voxel discretizations in a periodic or non-periodic way. In this context, tetrahedral elements are geometrically more versatile providing higher geometric accuracy. However, it is known that tetrahedral elements typically exhibit increased computational costs compared to hexahedral elements when aiming at the same accuracy, see [18, 32].

In total the described variants lead to five possible discretizations for one RVE size. Fig. 6.2 depicts these five variants on basis of a periodic and a non-periodic example RVE with $\delta = 2.04$. Additionally, the utilized microscopical boundary conditions are listed. Each RVE is subjected to KUBC, SUBC and PBC or APBC, depending on the underlying mesh topology. Discretizations are chosen such that the FE models exhibit a minimum element number of $n_{el} = 10^5$, see Eq. (4.4), allowing for a sufficient resolution of geometric features. However, due to the nature of the unstructured meshing process, it is impossible to determine the exact amount of elements a priori. In particular, slightly finer discretizations are generated in correspondence with sharper geometric features (increased curvatures) which occur for smaller inclusions. To ensure comparability, the meshes need to be isotropic in terms of the utilized element sizes to the greatest possible extent. All tetrahedral meshes are of high quality with an average element shape factor of $\eta \geq 0.5$ to ensure reliable results.

Another indispensable feature of discretizing is the deviation of the actual inclusion volume fractions from the intended one. Due to the meshing effect, i.e., tetrahedralized convex bodies always give smaller discretized volumes, all tetrahedralizations result in slightly decreased inclusion volume fractions. To this end, Fig. 6.3 shows the averaged inclusion volume fractions of all discretized variants. Voxel meshes naturally reach the intended inclusion volume fraction of 20% more precisely. This behavior is related to the staircaselike discretization of the inclusions. Alternately, too much or too little volume is assigned to the inclusion constituent and positive and negative effects cancel out. The highest deviation from the intended inclusion volume fraction occurs for RVEs featuring a non-periodic topology in combination with a non-periodic tetrahedralization. They are in the range of 1%. Since the inclusion volume fraction is an influencing factor of first order, it is crucial to minimize these effects for comparability in the envisaged benchmark study. To this end, all inclusions of the voxelized RVEs are isotropically shrinked to match the inclusion volume fraction of their tetrahedralized counterparts. As confirmed by Fig. 6.4, occurring differences between tetrahedralized and voxelized RVEs are eliminated eventually.

For each RVE, 20 randomized realizations are subjected to uniaxial tension and simple shear

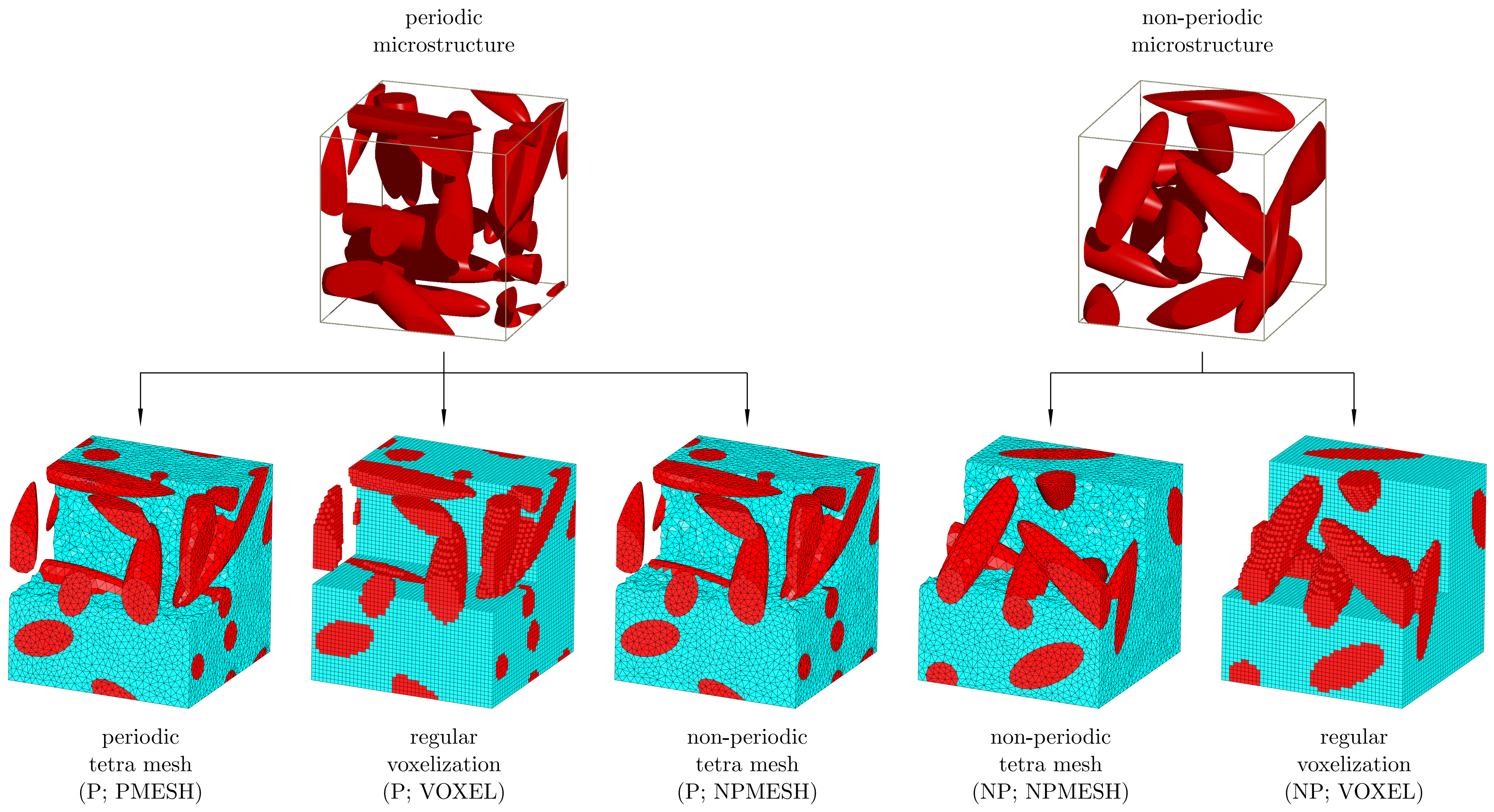

	(P; PMESH)	(P; VOXEL)	(P; NPMESH)	(NP; NPMESH)	(NP; VOXEL)
KUBC	●	●	●	●	●
PBC	●	●			
APBC			●	●	●
SUBC	●	●	●	●	●

Figure 6.2.: Periodic and non-periodic model setups and the boundary conditions considered in the benchmark study, exemplarily demonstrated on the example of an RVE featuring a non-dimensional control parameter $\delta = 2.04$.

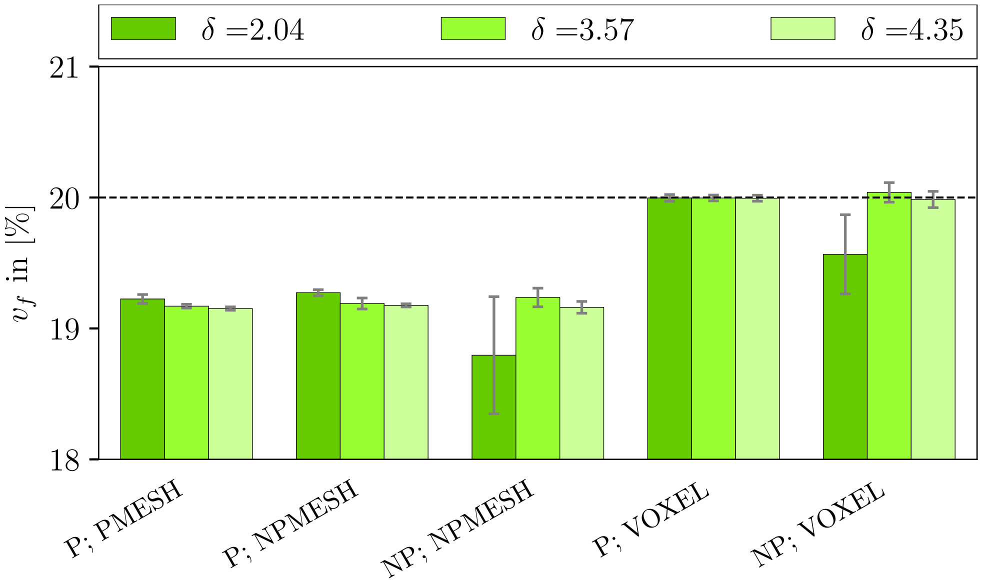

Figure 6.3.: Actual inclusion volume fractions of the discretized RVEs. Abbreviations: P - periodic topology; NP - non-periodic topology; PMESH - periodic tetra mesh; VOXEL - voxel mesh; NPMESH - non-periodic tetra mesh.

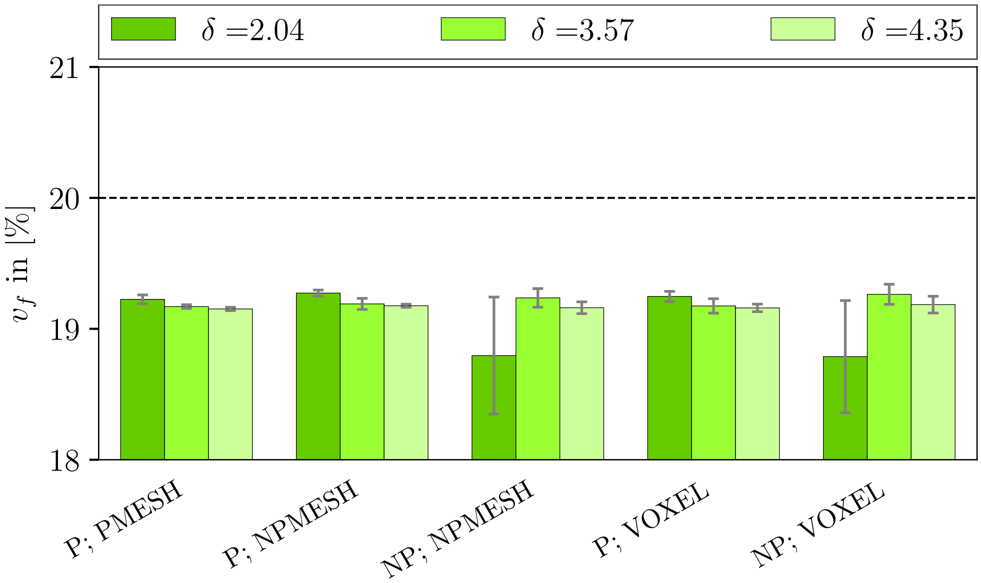

Figure 6.4.: Actual inclusion volume fractions of the discretized RVEs with adjusted inclusion size for the voxelized discretizations. Abbreviations: P - periodic topology; NP - non-periodic topology; PMESH - periodic tetra mesh; VOXEL - voxel mesh; NPMESH - non-periodic tetra mesh.

in the small strain context. A statistical study is given to support the results and extenuate atrifacts due to the randomness of the RVE generation process. Eventually, macroscopic YOUNG's moduli ${}^{\mathrm{M}}E$ and shear moduli ${}^{\mathrm{M}}G$ serve as criterion for the comparison of the simulations. All results are normalized to the numerical reference solution obtained by the fully periodic case (periodic topology, periodic mesh and PBC) with 100 inclusions. To this end, a total of 3600 simulations are conducted for this study.[26]

---

[26] 3 RVE sizes times 2 periodic and 3 non-periodic topologies and discretizations times 3 types of boundary conditions times 2 loading cases times 2 phase contrasts times 20 realizations result in 3600 simulations.

6.1.1. Results and Discussion

As a first step, the fully periodic reference solution is examined to verify its referential character. To this end, Tab. 6.3 documents the gained averaged macroscopic Young's and shear moduli, their 95% confidence intervals and the analytical Voigt and Reuss bounds.

Table 6.3.: Averaged effective material parameters of the reference solution and Voigt and Reuss bounds.

δ		2.04	3.57	4.35	Voigt	Reuss
$\xi = 1/100$	$^{\mathrm{M}}E_{11}$ [MPa]	2563.3 ± 35.9	2539.9 ± 12.9	2559.1 ± 8.6	3047.6	182.7
	$^{\mathrm{M}}G_{12}$ [MPa]	900.8 ± 5.4	903.2 ± 2.2	908.3 ± 1.6	1042.6	62.5
$\xi = 100$	$^{\mathrm{M}}E_{11}$ [MPa]	7118.5 ± 289.3	6900.9 ± 104.1	7028.1 ± 72.1	79040.0	4738.2
	$^{\mathrm{M}}G_{12}$ [MPa]	2335.2 ± 64.6	2349.1 ± 30.8	2405.3 ± 23.7	27040.0	1620.9

All computed macroscopic moduli lie within their bounds. The averaged moduli associated with one phase contrast vary only in the range of a few percent. Confidence intervals of all considered setups quickly decrease when enlarging the RVE size. Due to the large absolute difference for the matrix and inclusion material parameters of setups with $\xi = 100$, the largest confidence intervals ranging from 4% to 1%, can be found for the Young's modulus. These small deviations and the quick descent of the confidence intervals qualifies the fully periodic RVEs with 100 inclusions as a converged solution. Notably, variants featuring a high phase contrast show increased fluctuations of the moduli and increased confidence intervals. This effect can be addressed to the large absolute difference of the material parameters between the two constituents.

To evaluate the non-linear material behavior, Fig. 6.5 shows the macroscopic stress-strain path of, respectively, one realization of the fully periodic setup. The two load cases of all three

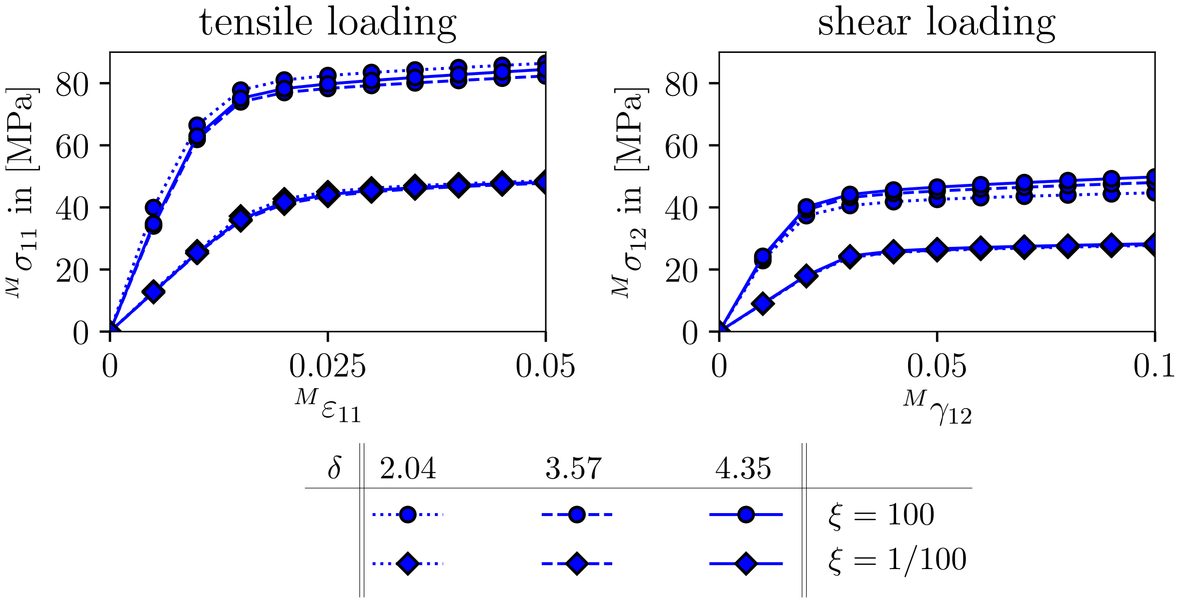

Figure 6.5.: Macroscopic stress-strain path of one reference solution RVE featuring 100 inclusions, a periodic topology, a periodic discretization and PBC for tensile and simple shear loading. For PBC or APBC the approriate boundary conditions are applied where possible. In the case of a periodic mesh PBC and APBC give identical results.

considered RVE sizes are shown. The course of deformation of the composite commences with the linear-elastic regime. At a strain of approximately 1% a transfer into the plastic deformation regime follows. The final stage with ${}^{\mathrm{M}}\varepsilon_{11} = 0.05$ or ${}^{\mathrm{M}}\gamma_{12} = 2\,{}^{\mathrm{M}}\varepsilon_{12} = 0.1$ shows a pronounced plastic deformation. Due to the utilized von Mises plasticity that relies on the shape modification hypothesis, tensile loadings are capable to withstand higher macroscopic stresses than shear loadings. However, for both loading cases, the sets of stress-strain paths linked to one phase contrasts show only minor spreads w.r.t. varying RVE sizes. Consequently, the largest RVE in the fully periodic setup is considered converged.

Fig. 6.6 summarizes the results of all considered model setups by showing the normalized elastic and plastic responses. Detailed results are given in Appendix A.4.

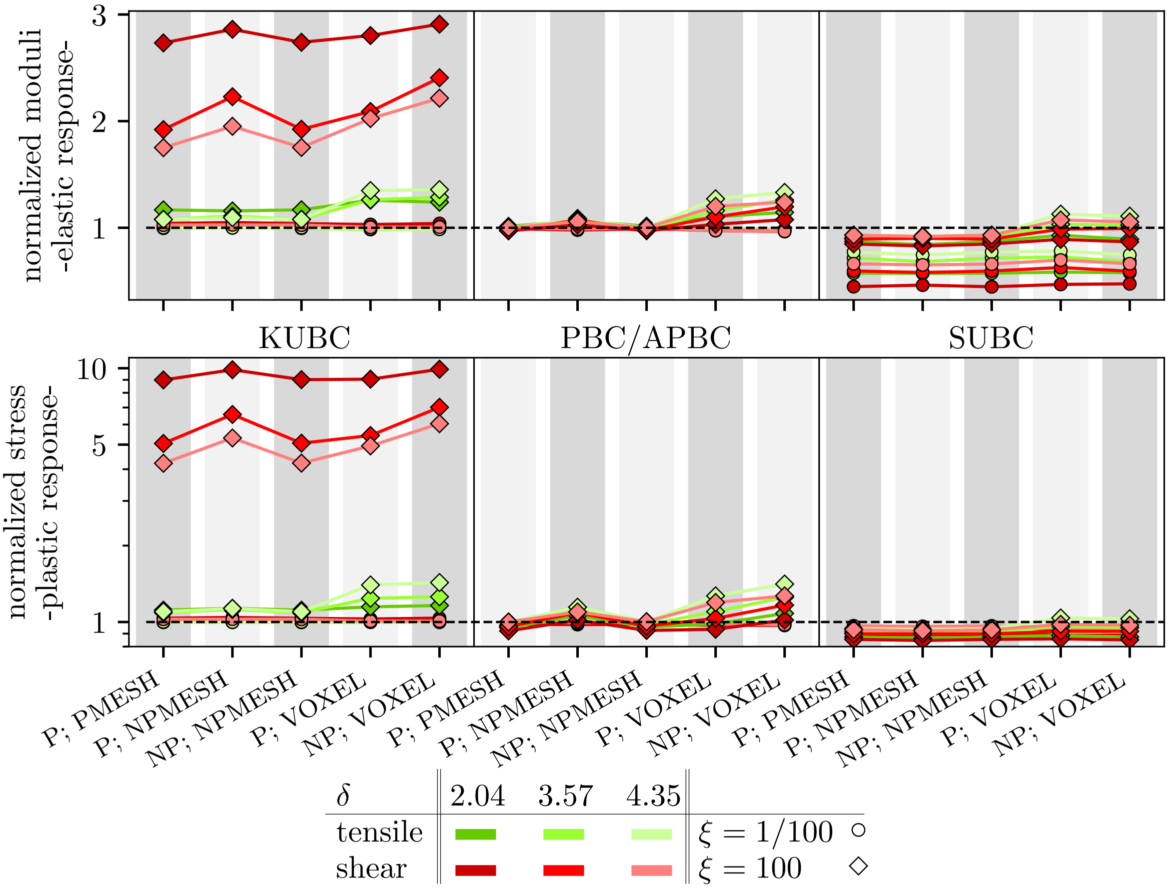

Figure 6.6.: To the periodic reference solution normalized effective Young's and shear moduli and to the periodic reference solution normalized macroscopic stress responses (tensile ${}^{\mathrm{M}}\sigma_{11}$, shear ${}^{\mathrm{M}}\sigma_{12}$) at ${}^{\mathrm{M}}\varepsilon_{11} = 0.05$ and ${}^{\mathrm{M}}\varepsilon_{12} = 0.05$ where a pronounced plastic deformation is present for all model variants, RVE sizes and phase contrasts. For PBC or APBC the approriate boundary conditions are applied where possible. In the case of a periodic mesh PBC and APBC give identical results. Abbreviations: P - periodic topology; NP - non-periodic topology; PMESH - periodic tetra mesh; VOXEL - voxel mesh; NPMESH - non-periodic tetra mesh.

Influences of topology

The effective macroscopic responses are seemingly largely independent of the chosen combinations of periodic and non-periodic topologies respectively meshes. Fig. 6.6 clearly demonstrates that. W.r.t. the results, the RVE setups can be divided into two main classes w.r.t. the employed discretization technique: tetrahedral meshes and voxel meshes. For both cases the three or respectively two combinations predict a very similar material behavior: the markers in each group indicate the same normalized response, independent of the topology combination. Fig. 6.7 exemplarily shows contour plots of the VON MISES stress of a non-periodic RVE realization subjected to APBC and discretized with tetrahedral elements at ${}^{\mathrm{M}}\varepsilon_{11} = {}^{\mathrm{M}}\varepsilon_{12} = 0.05$. Occurring artificial stress peaks and dips are highlighted. These stress disturbances are associated with the enforced kinematic compatibility on the one hand and the non-periodic morphology on the other hand. Inclusions intersecting the RVE boundary are missing their periodic counter parts, and hence introduce stress noises on the opposing boundary. However, these stress artifacts on the RVE boundary, induced by the non-periodicity, entail minor effects only. They do not dominate the visible stress contours, and thus are not influencing the overall macroscopic response in a significant way.

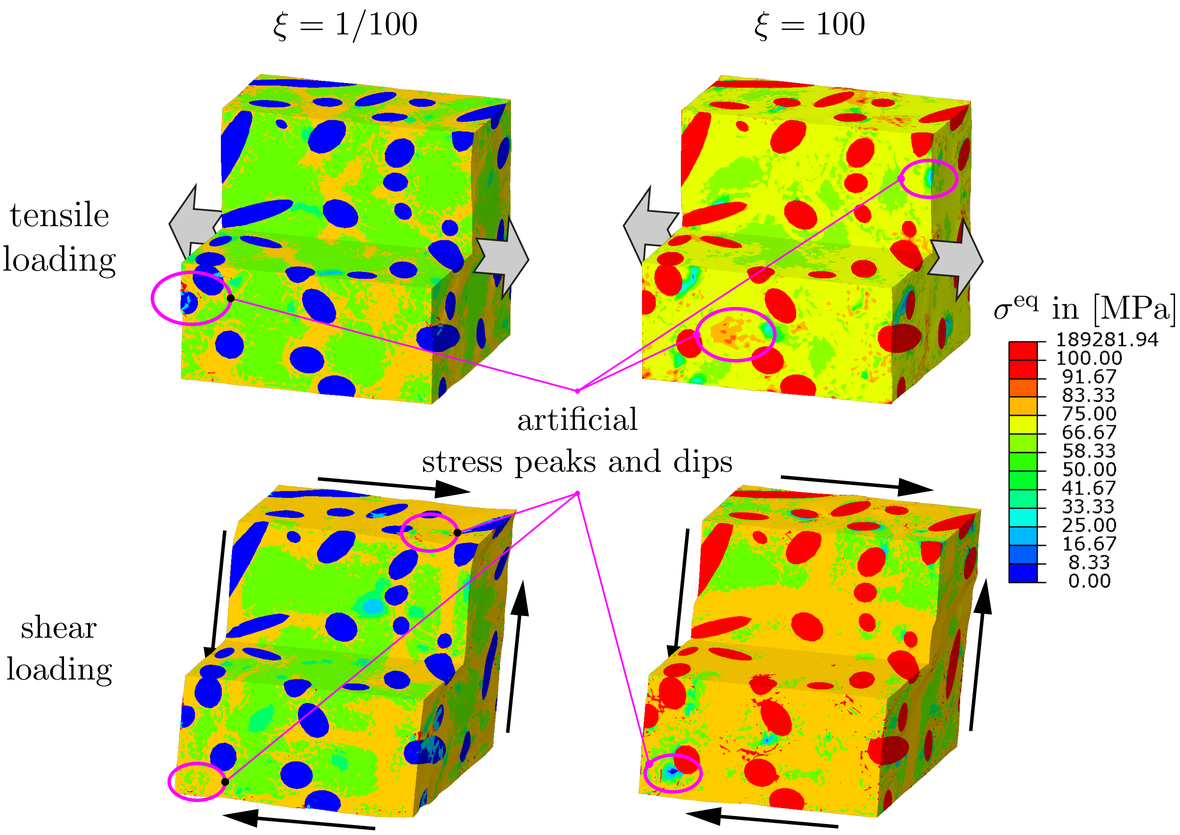

Figure 6.7.: Contour plots of the VON MISES stress of a non-periodic RVE realization with $\delta = 3.57$ and applied APBC at ${}^{\mathrm{M}}\varepsilon_{11} = {}^{\mathrm{M}}\varepsilon_{12} = 0.05$. Artificial stress peaks due to the non-periodicity in combination with the enforced APBC are highlighted.

Deviations from the reference solution in the macroscopic responses of non-periodic RVEs can be addressed to the varying actual inclusion volume fractions. The effect is pronouncedly observable for $\xi = 1/100$ due to the increased absolute difference between the matrix and inclusion material parameters. However, it is not addressable to topological influences but rather to the microstructure generation process.

All this is true for the elastic as well as the plastic material behavior, tensile respectively shear loading, both stiffness ratios, all three RVE sizes and the various applied boundary conditions. The effort of the RVE construction strongly differs between the analyzed combinations whereas simulation times are in similar ranges. Consequently, the high effort of constructing a fully periodic RVE, with a periodic topology as well as a periodic mesh, does not pay off and simpler approaches should be used.

Influence of the discretization

Voxelized meshes show positive or negative deviations from the reference solution depending on the phase contrast. In particular, for model setups with a high phase contrast ($\xi = 100$), the voxelized RVEs give a stiffer macroscopic response compared to their tetrahedralized counterparts, while the opposite is true for model setups featuring $\xi = {}^{1}/_{100}$. To this end, Fig. 6.8 depicts the obtained results in the light of the different phase contrasts. Due to the high absolute difference of the material parameters for $\xi = 100$ the shortcoming of the voxel RVEs are more pronounced. Fig. 6.9 exemplarily depicts contour plots of the von Mises stress of one fully periodic RVE with $\delta = 3.57$ discretized with tetrahedral and hexahedral elements for the two considered loading cases. The inclusions of the voxelized RVEs show higher stresses, and hence explaining the stiffer macroscopic response. These increased stresses emanate from the introduced stress concentration of the staircase like character of the grid-like mesh, and hence the stress artifacts can be addressed to the poorly approximated geometry. Increasing the RVE size while keeping the discretization fineness constant amplifies this effect. Furthermore, the linear character of the hexahedral elements does not allow to resolve stress gradients as precisely as the tetrahedral counterpart. All this leads to deviations of up to 25% for tensile loadings, which may not be acceptable.

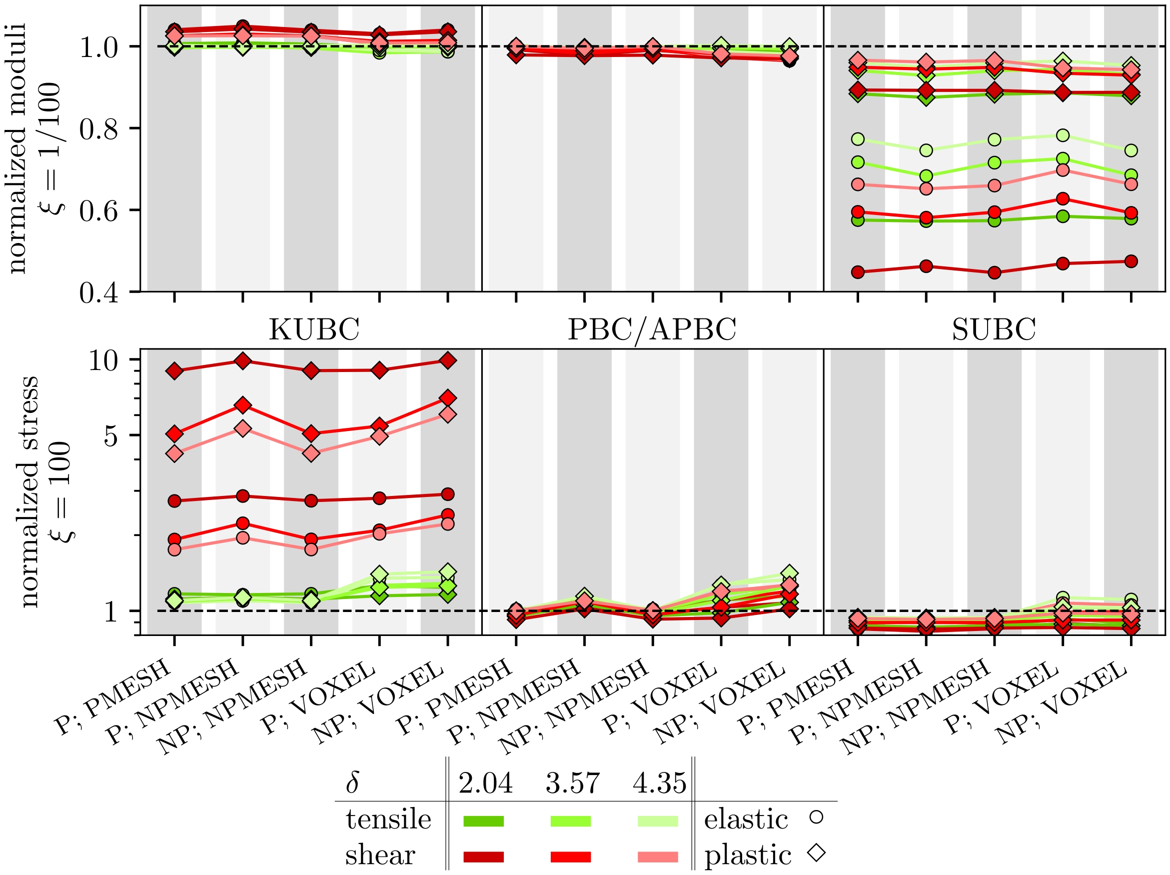

Figure 6.8.: Normalized responses - effective Young's and shear moduli and macroscopic stress responses (tensile ${}^{\mathrm{M}}\sigma_{11}$, shear ${}^{\mathrm{M}}\sigma_{12}$) at a state of deformation (${}^{\mathrm{M}}\varepsilon_{11} = {}^{\mathrm{M}}\varepsilon_{12} = 0.05$) featuring a pronounced plastic deformation for all model variants - for all model variants in the light of different phase contrasts ξ. For PBC or APBC the approriate boundary conditions are applied where possible. In the case of a periodic mesh PBC and APBC give identical results. Abbreviations: P - periodic topology; NP - non-periodic topology; PMESH - periodic tetra mesh; VOXEL - voxel mesh; NPMESH - non-periodic tetra mesh.

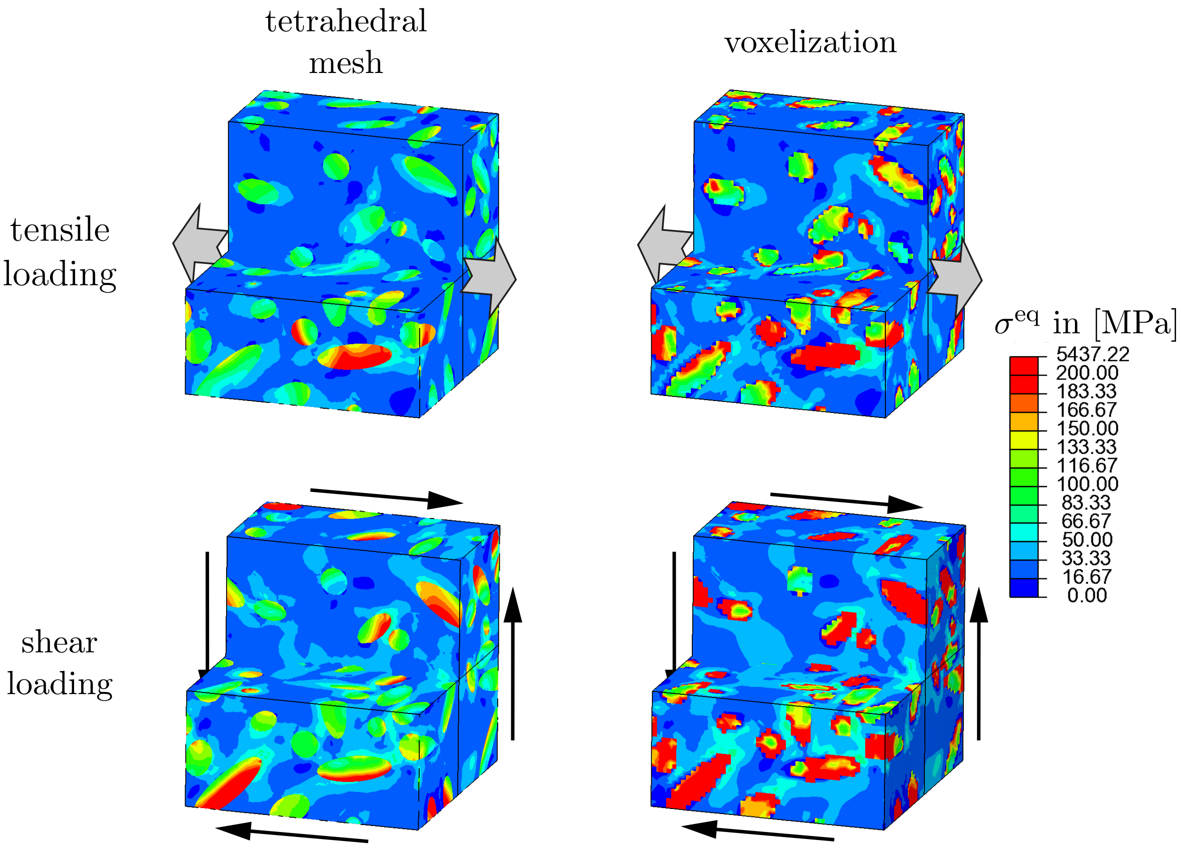

Figure 6.9.: Contour plots of the von Mises stress of a fully periodic RVE realization with $\delta = 3.57$ and applied PBC at ${}^{\mathrm{M}}\varepsilon_{11} = {}^{\mathrm{M}}\varepsilon_{12} = 0.005$ discretized by a periodic tetrahedralization and a regular voxelization for a phase contrast of $\xi = 1/100$.

However, a low phase contrast results in minor deviations in the range of a few percent, cf. App. A.4. Therefore, the employed meshing technique has to be chosen carefully depending on the phase contrast.

Influence of boundary conditions

W.r.t. elastic and plastic material behavior, topology combinations, RVE size and load cases, the obtained differences are negligible. However, w.r.t. the phase contrast ξ, the choice of boundary conditions may influence the results' quality to a large extent. In case of a low phase contrast $\xi = 1/100$ (stiff matrix and soft inclusions), KUBC and PBC predict very similar effective properties. Contrary, SUBC reveal large discrepancies of 22.7% up to 55.3% for elastic material behavior respectively 18.0% up to 40.4% for von Mises plasticity, and hence are unacceptable.

If the composite under consideration possesses a high phase contrast, the situation drastically changes. In this case, the SUBC performance enhances and results are within the range of PBC. Now, KUBC clearly overestimate the effective material properties to an unacceptable degree. In particular, these boundary conditions overestimate the reference solution by several hundred percent in the case of simple shear loadings due to the high restriction of the system's degree of freedom. The more relaxed setting of tensile loadings mitigate this behavior, probably to an acceptable extend for tetrahedral discretizations.

Conclusion

As discussed above, a fully periodic topology-mesh-RVE might not be worth the construction effort and thus non-periodic counterparts are strongly recommended. In this case, truly PBC have to be substituted by APBC. Advantageously, they are easily set up and their performance is by no means inferior to the truly PBC. Disadvantageously, they necessitate slightly longer computational times.

As reported in the literature, KUBC are a more problematic choice in homogenization leading to overly stiff responses whereas SUBC show a softer response. The benchmark study shows that KUBC and SUBC are very sensitive w.r.t. the phase contrast. Special caution is necessary with combinations of KUBC and voxelized RVEs. However, depending on the phase contrast, actual differences to PBC might be in the range of tolerable approximations. If the FE model is set up for one particular material or for a set of materials with similar phase contrasts, either all high or all low, a short investigation of the different uniform boundary conditions might be well worth the effort to circumvent the fully periodic setup. If the model is set up for materials with a strong deviation in the phase contrasts, one needs to invest the effort of setting up PBC or APBC in order to obtain meaningful numerical results for all simulations. In particular the presented APBC ease the model generation effort.

7. Application to nanoparticulate composites

The conglomerate of the introduced methodologies of the previous chapters is applied to a nanoparticulate composite consisting of ultra-stiff ceramic nanoparticles embedded in a polymeric matrix. The aim is to calibrate the model setup against experimental data and investigate the complex deformation mechanisms which are not accessible via experiments. Physically meaningful material models are utilized for the inclusions and the matrix. Special emphasis is placed on the polymeric matrix material model to capture the full deformation from the initial entropic-elasticity up to the transition into the energy-elastic limit. Failure is modeled by a matrix-inclusion-interface debonding in the form of cohesive damage, justified by the high surface to volume ratio of the particles in the compound. In contrast to previous chapters, strong emphasis is layed on the local behavior of the composite to gain new insights of the interplay between the constituents. Eventually, simulations of experimental unfeasible load cases give a deeper insight of the composites micromechanics.

The typical struggle in materials design to manufacture macroscopic materials of high strength and stiffness in combination with a high fracture toughness shows promising advance by utilizing nanocomposites. These composites are a relatively new class of materials [15, 25, 106, 237, 245]. Naturally occurring nanocomposites are shells, teeth or bones. They show superior mechanical properties, such as extreme stiffness to density ratios, very high material strength and a very high fracture toughness. GAO et al. [71] relate these properties to a combination of various micromechanical mechanisms operating on different length scales. Exemplarily, the micromechanical hierarchy of a tooth can be divided into three scales: (1) nanofibers, (2) rods that consist of many nanofibers and (3) decussating bundles of rods that form the tooth [197]. Besides the overall composite character, the most important feature is known to be the smallest length scale: the nanoscale. Nanoscaled objects are assumed to be almost free of any defects or cracks, and, hence flawless and extremely resilient. Load bearing is solely maintained by interatomic covalent bonds entailing an exceptional macroscopic stiffnesses [9]. However, the pure (particulate) materials are typically very brittle. Their inherent fracture energy is by several orders of magnitude lower than the fracture energy of the fully heterogeneous material. Only in the composite arrangement fracture toughness increases to an acceptable level for engineering applications.[27]

For the already mentioned natural materials the nanoscaled objects are outlined in the following. Teeth are build out of needle-like crystals that posses a thickness of 15-20 nm and are embedded in a softer matrix material. Bones show mineral crystal like platelets of a few nm thickness inside a soft collagen matrix. Nacre is formed by a brick and mortar like structure with layers that are a few hundred nanometers in thickness. For all these composites, the macroscopic loading is accommodated by complex load transferring mechanisms over several hierarchy levels. Due to the nanoscaled nature of these elementary building components, artificial reproduction of an entire multiscale composite of this kind is extremely difficult and up to date an unsolved problem.

Nevertheless, many efforts have been made to mimic these materials which will be discussed in the following. Here, the key idea is not to reproduce the entire micromechanical hierarchy, but to solely consider the lowest scale by utilizing nanometer-sized inclusions. Although, only

---

[27] Monolithic $CaCo_3$, which forms the basis of nacre, possess a fracture energy 3000 times less then nacre itself, cf. [71].

one length scale is considered, these synthesized nanoparticulate composites already show promising properties, similar to the mechanical behavior of their natural role models. The dominating effect in composites of that type is an extremely high ratio of inclusion surface area to inclusion volume. Due to the large inclusion surface area, high loads can be transfered. GAO et. al [71] conclude that this load transfer must be sustained by large tensile stress bearing inclusions. Due to the flawless nature of the inclusions, tensile stresses are supported by strong covalent or ionic bonds of the particulate material. The load transfer between particles is sustained by the matrix material. Since the much softer matrix is not capable of resisting high tensile loads, the deformation behavior must be shear dominated. To this end, the matrix must tolerate a high shear deformation without fracture. Due to the high inclusion surface area, the load transfer between the inclusions and the matrix is smooth. Stress concentrations are kept at a level, tolerable for the matrix material. For maintaining the composite's overall stiffness must the matrix material ideally show isochoric characteristics.

A promising class of nanoparticulate materials in that sense are polymeric nanocomposites (PNCs), see VAIA et. al [237] or WINEY et. al [245]. Distinctive to this material class is the polymeric matrix in which the nanosized fillers are embedded. Polymers consist of macromolecules that are linked together to form a three-dimensional network of connected polymer chains. These links are entanglements of the chains or covalent or ionic bonds. The polymeric deformation behavior is initially dominated by the resistence of undulated polymer chains against straightening also known as entropic-elasticity. In their bulky appearance low ($E = 0.1 - 10\,\mathrm{MPa}$ for rubber) to moderate ($E = 1000 - 3000\,\mathrm{MPa}$ for polycarbonate) YOUNG's moduli and a low ($\sigma_y = 5{-}10\,\mathrm{MPa}$) to moderate tensile strength ($\sigma_y \approx 55{-}70\,\mathrm{MPa}$), depending on the grade of cross-linking, is observable. To fulfill the requirements of a high shear resistance, the polymers in nanocomposites must be highly cross-linked. An additional fact that enhances mechanical properties of the matrix material, in a way suitable for their application in nanocomposites, is a largely reduced molecular weight. The reduced molecular weight emanates from the confined absolute space between the nanoparticles. Since nanofillers show dimensions of only a few nm, the gaps between particles are in the same order of magnitude. Therefore, the characteristic length of the interspaces between the particles, to be filled with polymer chains, is very small. It is assumed that the polymeric network in a nanocomposite possesses much shorter polymer chains, and hence a to the bulky equivalent decreased mesh size is present [182]. Another problem concerns a mechanically sound adhesive bond between the nanoparticles and the matrix. Fortunately, polymers offer the possibility to be combined with various kinds of chemical structures that can be utilized to form adhesive bonds (i.e. functional end-groups that form covalent bonds, ionic bonds, hydrogen bonds) [138]. In combination with their good processability, polymers qualify as an excellent matrix material in nanocomposites.

However, the manufacturing of a mechanically stable PNC, ready for engineering applications, still remains a major challenge. The most straightforward way of manufacturing this kind of composite is accomplished by a layer by layer strategy with clay platelet-like inclusions. These platelet-like inclusions possess extreme aspect ratios of $\alpha \approx 50 - 1000$ [241], and smoothly transfer tensile loads to the matrix. TANG et. al [225] manufacture such PNCs by forming alternating layers of montmorillonite clay platelets and polyelectrolytes. The specimens show a promising YOUNG's modulus of 11 GPa. However, only very thin composite layers of a few μm in thickness can be produced with the suggested method. LIAQAT et. al [142] introduce a multilayered nanocomposite consisting of TiO_2 platelets with 3-hydroxytyramine substituted polymers in-between. The composite shows a YOUNG's modulus of 17.5 GPa. Here, the authors identify a strong adhesion between the polymers and the nanofillers as a key feature for the composite's integrity. Similarly, PODSIADLO et. al [182] manufacture a PNC film. They utilize a polyvinyl alcohol polymer and montmorillonite clays. Different manufacturing processes lead to an outstanding YOUNG's modulus of up to 106 GPa.

However, the disadvantage of the mentioned approaches are the very thin resulting specimens. Additionally, due to the layered structure, an intrinsic anisotropy is introduced into the material. All specified macroscopic material parameters and benefits of the composite are restricted to this thin layer which results in only a minor importance for engineering applications.

A more recent strategy that circumvents these difficulties represents the utilization of spherical nanoinclusions. Due to the isotropic inclusions which are uniformly distributed in the matrix, the composite does not have a predominant direction. CHO et. al [38] show that, although the load bearing mechanisms of spherical inclusions are different to composites with nanoplatelets, it is possible to enhance the mechanical properties of composites by utilizing nanoscaled particles of aspect ratios $\alpha \approx 1$. To this end, the authors embed glass bead particles and aluminum dioxide particles of varying diameters from 0.5 mm to 15 nm in vinyl ester. By utilizing an inclusion volume fraction of $v_f = 3\%$, they report an increasing YOUNG's modulus with decreasing particle size for the nanometer range. In particular, the composite's YOUNG's modulus shows an increase of 15% w.r.t. the stiffness of the vinyl ester ($E_{\text{vinyl ester}} = 3.5\,\text{GPa}$). The manufactured specimens are in the dimension of several mm. However, due to difficulties in the preparation process that lead to cluster formation of the particles, a decrease of the tensile strength is reported. Furthermore, the effects of the nanofillers to the overall mechanical properties are insignificantly small due to the low inclusion volume fraction.

The more recent work of GEORGOPANOS et al. [74] overcomes these difficulties. As can be seen in Fig. 7.2 (a), the authors are able to produce a PNC in the dimensions of a few mm with much a higher inclusion volume fraction of $v_f = 60\%$ by employing a sophisticated manufacturing process. The composite consists of ceramic iron oxide particles embedded in a polybutadien (rubbery) matrix. Microcompression and microbending tests yield YOUNG's moduli in the range of $12 - 20\,\text{GPa}$. If the typical YOUNG's modulus of rubber ($E_{\text{rub}} = 0.3\,\text{MPa}$) is taken as reference, the nanofillers lead to an enormous increase of the YOUNG's modulus by a factor of $66 \cdot 10^3$ w.r.t. the matrix stiffness underlining the promising potential of this particular PNC.

However, the large scatter in the obtained stress-strain curves raise unanswered questions. Experimentally, the composite is only subjected to compressive and bending loadings, leaving the tensile behavior unknown. Furthermore, it is unclear what kind of microscopic deformation mechanisms involving the interplay between the matrix and the inclusions lead to the macroscopic behavior. In the following, these questions are investigated by continuum mechanics based micromechanical simulations, demonstrating thereby the application potential of the methods developed in the previous sections of this thesis. However, it has to be stated that the following considerations are very close to the limit of continuum mechanics due to the nanoscaled nature of the composite's microstructure. Continuum mechanics, being a phenomenological field theory, is based on smearing out the discrete nature of matter which only makes sense if the number of discrete entities is large enough. However, continuum mechanics often is a useful tool to yield acceptable qualitative statements even in these limits. Following several continuum mechanical based works listed in the review article of BERNARDO et al. [20], it is assumed here that the micromechanical mechanisms are still possible to be described via such an approach.

7.1. Model setup

Fig. 7.1 depicts the microstructure of the examined PNC composite on the nanoscale. The stiff ceramic inclusions consist of iron oxide Fe_3O_4. As reported in [74], the particles' radius and the composite's inclusion volume fraction are given by

$$d_{\text{incl}} = 11\,\text{nm} \text{ and } v_f = 60\% \ . \tag{7.1}$$

The micrograph of Fig. 7.2 reveals an amorphous arrangement of monodispersed particles. All particles are surrounded by the polymeric matrix. Since the inclusion volume fraction is near

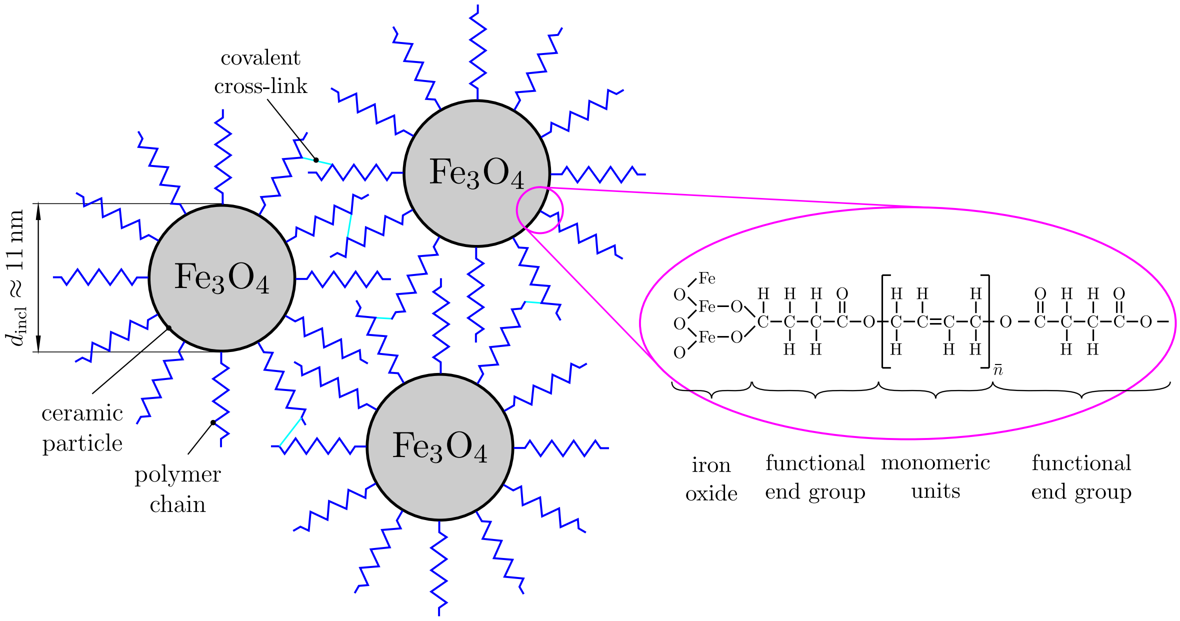

Figure 7.1.: Microstructure of the nanoparticulate composite.

the random jamming limit, a perfect FCC arrangement of the particles can help to estimate the average particle distance as 0.8 nm. The largest gap between particles in an idealized FCC arrangement is 17.9 nm. These values give an estimation of the confined space to be filled with the polymeric matrix. The polymeric chains of the matrix are attached to all particles via their functionalized end-groups. These functionalized end-groups are of particular importance since they form the link between the polymeric matrix and the ceramic inclusions. To this end, the mechanically sound bonding is established by covalent bonds between the carbon atoms of the end-groups and oxygen atoms of the ceramic inclusions. GEORGOPANOS et al. [74] use the industrially widely applied polymer polybutadien, also known as rubber, for the matrix material. Its monomeric building unit is 1-3-butadiene. This monomeric unit is repeated $\bar{n}$ times to form a polymer chain. Each monomer holds a double bond between two carbon atoms in its non-cross-linked state. The cross-linking takes place through pressurizing the specimens at a certain temperature. The temperature in combination with the pressure breaks the double bonds apart and covalent bonds to neighboring chains are formed. Because of the applied temperature, pressure and ample cross-linking agents in combination with the confined available space, the polybutadien is highly cross-linked. Due to the covalent nature of the cross-links, the polymer gains its final characteristics, making it suitable for the stable formation of the PNC.

The micromechanical geometry is a key factor for the pursued simulations. BERNARDO et al. [20] give a comprehensive summary of advancements in the recent years on that topic for PNCs. By far the most widely utilized RVEs are repeating unit cells incorporating only a small amount of inclusions that make statistical statements impossible. The highest considered inclusion volume fractions are approximately $v_f = 20\%$. Some contributions consider randomized RVEs generated with RSA algorithms which are not applicable to the PNC of interest. Furthermore, BERNARDO et al. [20] report only few studies incorporating the matrix, the particles and the interfacial regions. However, they conclude the indispensability to model the matrix-particle interface for realistic results. These facts motivate the setup of a randomized RVE explicitly incorporating the matrix, the particle and the interfacial region.

According to experimental micrographs depicted in Fig. 3 (a), the LUBACHEVSKY-STILLINGER-algorithm, see Sec. 3.2, is chosen for RVE generation. Every RVE holds 25, 50 or 100 inclusions. To get a statistical statement, 10 realization are generated per RVE setting. Fig. 7.2 (b) exemplarily depicts an example RVE with 25 inclusions. Exploiting Eq. (2.39), this

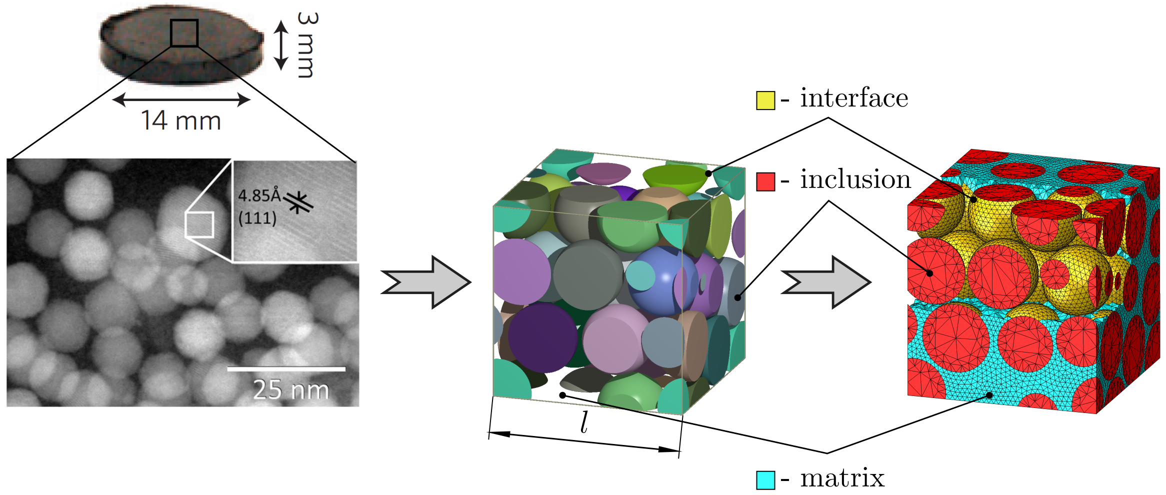

(a) (b) (c)

Figure 7.2.: Modeling approach: experimental micrographs (a), RVE (b), periodic FE discretization featuring 157051 linear tetrahedral elements (c). Experimental images taken from [47] and [74].

gives the following microstructural control parameters

$$\delta = \frac{l}{L} = \frac{\sqrt[3]{V_{\text{RVE}}}}{2r_{\text{incl}}} = \sqrt[3]{\frac{\frac{n_{\text{incl}} v_{\text{incl}}}{v_f}}{\frac{3}{4}\frac{1}{\pi} v_{\text{incl}}}} = \sqrt[3]{\frac{\frac{n_{\text{incl}}}{v_f}}{\frac{3}{4}\frac{1}{\pi}}} = \{2.8, 5.6, 11.2\} \tag{7.2}$$

with the inclusion radius r_{incl}, the volume of a single inclusion v_{incl} and the total number of inclusions n_{incl}. All RVEs are periodically discretized by approximately $1.5 \cdot 10^5, 2.8 \cdot 10^5$ or $3.5 \cdot 10^5$ linear tetrahedral elements depending on the number of inclusions n_{incl}, see Fig. 7.2 (c). To account for interfacial effects, the mesh is densified at the particle shells, resulting in an inhomogeneous discretization. In particular, all particles are meshed such that each surface shell possesses at least 1000 triangles. Cohesive behavior between the inclusion and the particles is taken into account by utilizing zero thickness cohesive interfaces. The automatic insertion of zero thickness cohesive interfaces into an existing mesh is not a trivial task. An algorithm that automatically conducts this task is developed in App. A.6. All RVEs are subjected to compressive and tensile loadings in the scope of PBC. The commercial finite element software ABAQUS is used to conduct all simulations.

7.2. Material modeling

The experimental findings of the compression tests in [74] show macroscopic strains up to 6% accompanied by macroscopic stresses of 300 − 900 MPa. Due to the extremely high stiffness ratio of the inclusions w.r.t. the matrix material in combination with the high inclusion volume fraction, it is assumed that the gross of the macroscopic deformation must be maintained by locally large deformations of the matrix, which motivates a finite deformation setting. However, the stiff inclusions are sufficiently describable by the linear-elastic limit case of any non-linear constitutive law. Hyperelasticity is assumed for either material, see Eq. (2.33). To that end, ABAQUS offers the UHYPER subroutine interface, to formulate user defined materials. If the dependence of the free energy $\varrho_0\psi$ on the second invariant is omitted and an additive split into an isochoric and volumetric part is assumed, the following quantities must be specified in the subroutine:

$$\varrho_0\psi(I_{\bar{b}}, J), \frac{\partial \varrho_0\psi}{\partial I_{\bar{b}}}, \frac{\partial^2 \varrho_0\psi}{\partial I_{\bar{b}}^2}, \frac{\partial \varrho_0\psi}{\partial J}, \frac{\partial^2 \varrho_0\psi}{\partial J^2}, \frac{\partial^3 \varrho_0\psi}{\partial J^3} \ . \tag{7.3}$$

7.2.1. Nanoparticles

The Neo-Hookean form of the specific free energy is chosen to describe the deformation behavior of the nanoparticles via

$$\varrho_0\psi(I_{\bar{b}}, J) = \frac{\mu_0^{\text{incl}}}{2}[I_{\bar{b}} - 3] + \frac{K_0^{\text{incl}}}{2}\left[\frac{J^2-1}{2} - \ln(J)\right] \tag{7.4}$$

which leads to

$$\begin{aligned} \frac{\partial \varrho_0\psi}{\partial I_{\bar{b}}} &= \frac{\mu_0^{\text{incl}}}{2} \ , \\ \frac{\partial^2 \varrho_0\psi}{\partial I_{\bar{b}}^2} &= 0 \ , \\ \frac{\partial \varrho_0\psi}{\partial J} &= \frac{K_0^{\text{incl}}}{2}\left[J - \frac{1}{J}\right] \ , \\ \frac{\partial^2 \varrho_0\psi}{\partial J^2} &= \frac{K_0^{\text{incl}}}{2}\left[1 + \frac{1}{J^2}\right] \ , \\ \frac{\partial^3 \varrho_0\psi}{\partial J^3} &= -\frac{K_0^{\text{incl}}}{J^3} \ . \end{aligned} \tag{7.5}$$

μ_0^{incl} represents the initial shear modulus and K_0^{incl} the initial bulk modulus. Since experiments of iron-oxide in the nanoscaled state are not available in the literature, the linear-elastic material parameters of its bulky state are taken and listed in Tab. 7.1. The utilization of the Neo-Hookean form is motivated by the extreme phase contrast between particles and matrix. In the composite deformation, the particles can be regarded as almost rigid. Therefore, only the linear-elastic deformation behavior in form of the small-strain limit of any non-linear material law, is of importance.

Table 7.1.: Material parameters for the inclusion material taken from Georgopanos et. al [74].

E^{incl} in [MPa]	ν^{incl}	μ_0^{incl} in [GPa]	K_0^{incl} in [GPa]
163	0.3	62.7	135.8

7.2.2. Polymeric matrix

Structural (statistical) constitutive formulations of polymeric materials often focus on the of deformation of a single polymer chain. The approach is based on the assumption that the free energy incorporates the change in configurational entropy of monomeric building units of the polymer chain during deformation, see Fig. 7.3 (a) and Rubinstein [191]. The simplest model to describe these configurations in a statistical manner is the freely-jointed chain model. It is assumed that a polymer chain consists of rigid subunits that are joined by perfectly flexible hinges making them orientationally independent from each other, see Fig. 7.3 (b). Due to the nature of the atomic bonds between monomers, which entail bond angles and certain bond stiffnesses, the segment length L_K of these subunits is larger than a monomeric building unit. Therefore, a chain is constructible of N_{K} effective repeating units each of length L_K. Here,

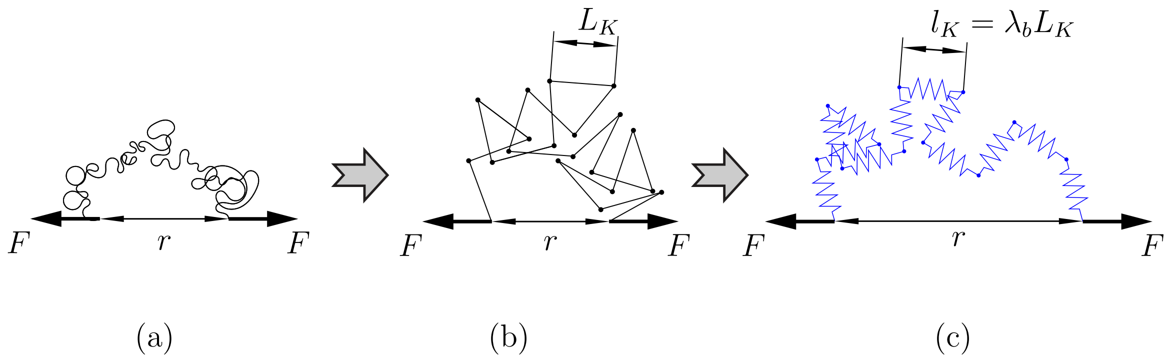

Figure 7.3.: Modeling of polymer chains: (a) original chain, (b) freely jointed chain model and (c) extension of MAO et al. [155].

L_{K} is the KUHN length and gives a measure of the statistical segment length. The contour length $r_{\max}$ of the entire chain is then given by

$$r_{\max} = N_K L_K \; . \tag{7.6}$$

For polybutadien RUBINSTEIN et al. [191] or FETTERS et al. [60] report a KUHN length of $L_{\mathrm{K}} \in [0.83\,\mathrm{nm}..0.96\,\mathrm{nm}]$. Considering the confined available space between the particles, this gives a N_K in the range from 1 to 18. Typically, N_K is much larger to allow statistical derivations of the free energy. In the following, it is assumed that N_K is still large enough to fulfill the requirements of statistical considerations.

To establish a relation between the chain force F and the end-to-end distance r, a free energy ψ_{ch} must be formulated. The desired relation between the chain force F and the end-to-end distance r is then given by

$$F(r) = \frac{\partial \psi_{\mathrm{ch}}(r)}{\partial r} \; . \tag{7.7}$$

Various suggestions on how to choose ψ_{ch} exist in the literature [191]. These models may rely on the mentioned freely-jointed chain model in combination with GAUSSIAN or non-GAUSSIAN statistics [135] or extend to the consideration of bond stiffnesses and valence angles. In the present study, it is of particular importance to model the chain-behavior up to the limit of a fully stretched chain. Due to the rigidity of the KUHN segments, a pronounced chain stretching must go along with a progressive stiffening. A sophisticated model, especially suitable for highly stretched and stiff polymers, is the Worm-Like-Chain (WLC). This model can be understood as an extension to the freely-jointed chain model incorporating the bond stiffness between segments. A widely used interpolative approximation to the WLC model is the suggestion by MARKO et al. [157] via

$$\begin{aligned} \psi_{\mathrm{ch}} &= \frac{k_B T r_{\max}}{4 L_P}\left[2\lambda_r^2 - \frac{1}{1-\lambda_r} - \lambda_r\right] + \psi_{\mathrm{ch}_0} \text{ and} \\ F &= \frac{\partial \psi_{\mathrm{ch}}}{\partial r} = \frac{k_B T}{4 L_P}\left[4\lambda_r + \frac{1}{[1-\lambda_r]^2} - 1\right] \; . \end{aligned} \tag{7.8}$$

Here the relative chain stretch $\lambda_r = \frac{r}{r_{\max}}$, the BOLTZMANN constant k_B, the absolute temperature T, the persistence length L_P and initial energy ψ_{ch_0} are introduced. ψ_{ch_0} is a constant to ensure $\psi_{\mathrm{ch}}(\lambda_r = 0) = 0$. L_P is a length over which tangent vectors of the chain become decorrelated.[28] For an ideal chain (non-interacting segments) the persistence length is half the KUHN length such that

$$L_p = \frac{1}{2} L_K \; . \tag{7.9}$$

---

[28] The persistence length is often used to describe semi-flexible polymers and incorporates rotational-isomeric-states, stiffnesses of the links, helicity as well as the fact that real chains can never fold back onto itself.

Eq. (7.8) shows a distinctive singularity as $\lambda_r \to 1$, which reflects the limited extensibility of the chain. With the help of statistical arguments it can be shown (random walk statistics) that the undeformed root-mean-square end-to-end distance r_0 of a freely jointed chain evaluates to

$$r_0 = \frac{r_{\max}}{\sqrt{N_K}} \ . \tag{7.10}$$

Then the relative chain stretch λ_r is expressible via

$$\lambda_r = \frac{r}{r_{\max}} = \frac{r}{r_0}\frac{1}{\sqrt{N_K}} = \frac{\lambda_{\text{ch}}}{\lambda_L} \ . \tag{7.11}$$

For the sake of simplicity, the limit stretch $\lambda_L = \sqrt{N_K}$ is introduced in the former equation. λ_{ch} denotes the overall chain stretch and relates the actual end-to-end distance r to the root-mean-square end-to-end distance of the undeformed chain.

It is important to point out that only for $\lambda_r = 0$ Eq. (7.8) gives a vanishing chain force. However, OGDEN et al. [168] state that $\lambda_r \in [1/\sqrt{N_K}..1]$. This restriction leads to a non-vanishing chain force in the initial state, where the end-to-end distance takes the length of the undeformed root-mean-square r_0. These two viewpoints are somewhat contradictory and state a conceptual problem. On the one hand, $F(\lambda_r = 0) = 0$ goes along with a mathematical sound formulation that gives zero forces for zero deformation. From an engineering perspective, this is the desired behavior. On the other hand, the non-vanishing initial force in the initial state for $F(\lambda_r = 1/\sqrt{N_K}) \neq 0$ is explainable by the random motion of the chain segments due to an associated thermal energy fluctuation of the polymer chain at finite temperatures. From a statistical physics point of view, the latter argument is more appealing. Only for very large N_K the initial force approaches zero and both viewpoints merge. This fact eases the discrepancy and makes the introduced error of a non-vanishing but small initial chain force acceptable.

Up to this point, only entropic contributions are considered. However, if the chain is highly stretched up to its contour length $R_{\max}$, energetic contributions emanating form bond deformations dominate the mechanical chain response, see LAKE et al. [136]. To incorporate an energy-elastic part into the free energy, MAO et al. [155] suggest to introduce flexible KUHN segments. Fig. 7.3 (c) depicts this idea. The rigid links are substituted by spring-like elements. The length of every segment in the deformed state follows the kinematic relation

$$l_K = \lambda_b L_K \ . \tag{7.12}$$

Here, L_K denotes the initial length of the KUHN segment, l_K denotes the current length of the KUHN segment and λ_b represents the bond stretch. This assumption assumes that all segments stretch in the same manner, resulting in a single λ_b valid for all chain segments. To this end, the limit stretch λ_L in Eq. (7.11) is substituted by $\lambda_L \lambda_b$ such that

$$\lambda_r = \frac{\lambda_{\text{ch}}}{\lambda_L \lambda_b} \ . \tag{7.13}$$

Consequently, the locking chain stretch changes in the course of deformation. The energetic contribution of a single KUHN segment is then chosen to depend quadratically on the logarithmic bond strain $\varepsilon_b = \ln(\lambda_b)$ via

$$\psi_{\text{K}}^{\text{en}} = \frac{1}{2} E_{\text{ch}}^b \varepsilon_b^2 = \frac{1}{2} E_{\text{ch}}^b \ln(\lambda_b)^2 \ . \tag{7.14}$$

Here, E_{ch}^b is a material parameter of dimension energy that represents the stiffness of the bonds. With $L_P = \frac{1}{2} L_K = \frac{1}{2}\frac{r_{\max}}{N_K}$ the free energy of the entire chain is given by

$$\psi_{\text{ch}} = \psi_{\text{ch}}^{\text{en}} + \psi_{\text{ch}}^{\text{ent}} = \lambda_L^2 \frac{1}{2} E_{\text{ch}}^b \ln(\lambda_b)^2 + \frac{k_B T}{2}\lambda_L^2 \left[2\lambda_r^2 - \frac{1}{1-\lambda_r} - \lambda_r \right] + \psi_{\text{ch}_0} \ . \tag{7.15}$$

Utilizing the principle of minimum energy, to ensures extremality of the free energy, gives the implicit equation

$$\frac{\partial \psi_{\mathrm{ch}}}{\partial \lambda_b} = 0 \tag{7.16}$$

to determine the internal variable λ_b.

To embed the described single chain model in a continuum mechanical framework, a transition from the single chain deformation to a continuous deformation must be established. Advanced methods assume the existence of representative network structures [26]. Fig. 7.4 (a) depicts the network structure of one of the most successful models in the initial state, the eight-chain Arruda-Boyce-model [6]. Corners of an infinitesimal volume element with edge length dl are connected by eight chains of length $\frac{\sqrt{3}}{2}dl$. All chains link together at the cube center. In the deformed state, see Fig. 7.4 (b), all chains stretch to a length of $\frac{\sqrt{\bar{\lambda}_1^2+\bar{\lambda}_2^2+\bar{\lambda}_3^2}}{2}dl$, where $\bar{\lambda}_1, \bar{\lambda}_2$ and $\bar{\lambda}_3$ are the principle stretches of the isochoric deformation gradient. Then, the chain stretch is

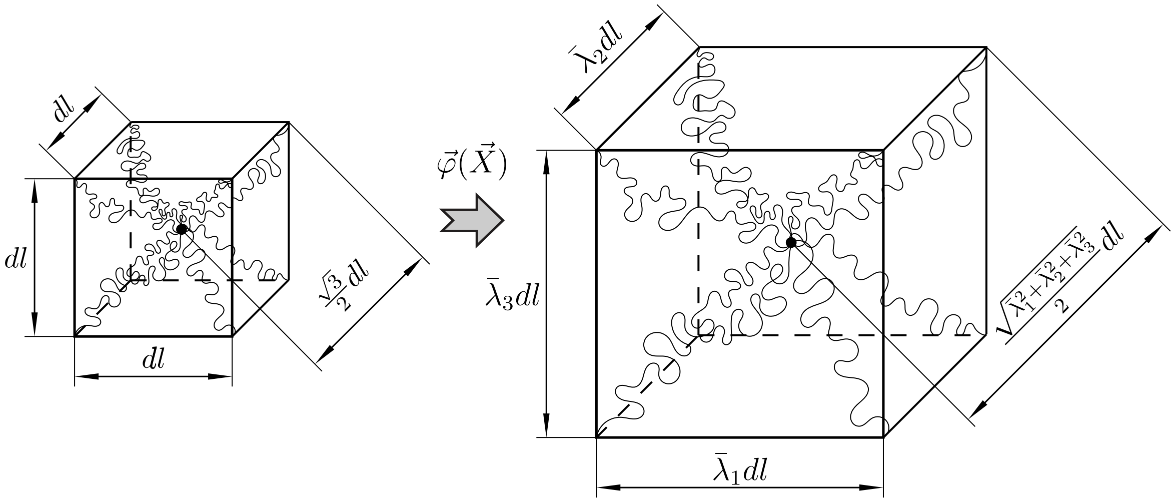

(a) (b)

Figure 7.4.: Eight chain Arruda-Boyce model [6]: Deformation from the initial state of an infinitesimal volume element (a) to the deformed state (b).

$$\lambda_{\mathrm{ch}} = \frac{\frac{\sqrt{\bar{\lambda}_1^2+\bar{\lambda}_2^2+\bar{\lambda}_3^2}}{2}dl}{\frac{\sqrt{3}}{2}dl} = \sqrt{\frac{\bar{\lambda}_1^2+\bar{\lambda}_2^2+\bar{\lambda}_3^2}{3}} = \sqrt{\frac{I_{\bar{b}}}{3}} \ . \tag{7.17}$$

As a first step towards the continuum mechanical formulation of the free energy, λ_{ch} is substituted in Eq. (7.13). In addition, the free energy ψ_{ch} of a single chain has to be transfered to an energy density by a multiplication with the amount of polymer chains per reference volume N_{ch}. The free energy density then reads

$$\varrho_0 \psi = N_{\mathrm{ch}} \psi_{\mathrm{ch}} = \lambda_L^2 \frac{1}{2} N_{\mathrm{ch}} E_{\mathrm{ch}}^b \ln(\lambda_b)^2 + N_{\mathrm{ch}} \frac{k_B T}{2} \lambda_L^2 \left[2\lambda_r^2 - \frac{1}{1-\lambda_r} - \lambda_r \right] + \varrho_0 \psi_0 \ . \tag{7.18}$$

ψ_0 is a constant to ensure a vanishing free energy in the undeformed state. An extension with a standard volumetric free energy contribution that accounts for volume changes of the bulk material, brings

$$\begin{aligned}\varrho_0\psi =&\frac{1}{2}E^b\lambda_L^2\left[\ln(\lambda_b)^2-\ln(\lambda_b^{\text{ini}})^2\right]+\mu\lambda_L^2\left[B(\lambda_r)-B(\lambda_r^{\text{ini}})\right]\\&+\frac{K_0^{\text{Matrix}}}{2}\left[\frac{J^2-1}{2}-\ln(J)\right]\,,\\B(\lambda_r)=&2\lambda_r^2-\frac{1}{1-\lambda_r}-\lambda_r\quad\text{and}\\\lambda_r=&\frac{\lambda_{\text{ch}}}{\lambda_L\lambda_b}\,.\end{aligned}\tag{7.19}$$

Here, the abbreviation $\mu = N_{\text{ch}}\frac{k_BT}{2}$, $E^b = N_{\text{ch}}E_b$ and the function $B(\lambda_r)$ are introduced for convenience.[29] $\varrho_0\psi_0$ is replaced by terms involving the initial bond stretch λ_b^{ini} and the initial relative stretch $\lambda_r^{\text{ini}} = \frac{1}{\lambda_L\lambda_b^{\text{ini}}}$ to ensure vanishing free energy density at the undeformed initial state. These quantities must be computed a priori.

To obtain the required derivatives of Eq. (7.3) the solution of Eq. (7.16) and computation of λ_b^{ini} is necessary. Following the detailed derivations of App. A.5 brings

$$\begin{aligned}\frac{\partial\varrho_0\psi}{\partial I_{\bar b}}&=\frac{\mu}{6}\lambda_L^2\lambda_{\text{ch}}^{-2}\lambda_rB'(\lambda_r)\\\frac{\partial^2\varrho_0\psi}{\partial I_{\bar b}^2}&=\frac{1}{2}\left[\frac{\mu}{3}\lambda_L^2\left[B'(\lambda_r)+\lambda_rB''(\lambda_r)\right]\frac{\partial\lambda_r}{\partial\lambda_{\text{ch}}}-\frac{2}{3}\mu\lambda_L^2\lambda_{\text{ch}}^{-3}\lambda_rB'(\lambda_r)\right]\frac{1}{6}\frac{1}{\lambda_{\text{ch}}}\\\frac{\partial\varrho_0\psi}{\partial J}&=\frac{K_0^{\text{Matrix}}}{2}\left[J-\frac{1}{J}\right]\\\frac{\partial^2\varrho_0\psi}{\partial J^2}&=\frac{K_0^{\text{Matrix}}}{2}\left[1+\frac{1}{J^2}\right]\\\frac{\partial^3\varrho_0\psi}{\partial J^3}&=-\frac{K_0^{\text{Matrix}}}{J^3}\end{aligned}\tag{7.20}$$

with

$$B'(\lambda_r)=4\lambda_r+\frac{1}{\left[1-\lambda_r\right]^2}-1\quad\text{and}\quad B''(\lambda_r)=4+\frac{2}{\left[1-\lambda_r\right]^3}\,.\tag{7.21}$$

μ and the term $\frac{\partial\lambda_r}{\partial\lambda_{\text{ch}}}$ are numerically computed in the course of the non-linear equation solution process.

Material parameters

To complete the formulation of the matrix material the material parameters μ_0^{Matrix}, K_0^{Matrix}, N_K and E^b must be specified. Retrieving these parameters is not a trivial task since the matrix material experiences a condition not comparable to its bulky state. The confined, nanometer scaled space between the nanofillers results in an entropic parameter N_K which differs from its macroscopic version. It is unclear how strong the chains are linked, whether or not chain entanglements are comparable to the ones found in the microstructure when the material is produced at macroscopic quantities or if chain segments can still be treated as ideal (no interaction phenomena between the segments). At the moment, no experimental findings are available that offer material data of polybutadiene in a such nanoscale condition. However, the monomeric building units are identical for a nanoscaled material sample or the bulk material. Therefore, it is reasonable to assume that the deformation mechanisms

---

[29] The free energy density of Eq. (7.19) can be written in a more general form by using the function $B(\lambda_r)$. If $B(\lambda_r) = 3\lambda_r^2 - 3$, the free energy simplifies to the NEO-HOOKEAN form. For $B(\lambda_r) = \lambda_r\beta + \ln\left(\frac{\beta}{\sinh(\beta)}\right)$ the free energy density turns into the suggestion of KUHN et al. [135]. Here, $\beta = \mathcal{L}^{-1}(\lambda_r)$ denotes the inverse LANGEVIN function with $\mathcal{L}(\lambda_r) = \coth(\lambda_r) - \lambda_r^{-1}$.

are similar for both material states allowing their derivation from the ones associated with macroscopic rubber specimens.

Initially, most engineering materials deform in a linear-elastic way. This deformation behavior is characterizable via linear elastic material parameters. For industrial rubber, the initial shear modulus is reported as $\mu_0^{\text{Matrix}} = 0.3\,\text{MPa}$, see [7, 86].

The entropic chain entanglement is characterized via N_K. BOYCE et al. [26] or KROON [134] give valuable insights in the interpretation and adaptation of this parameter in the light of macroscopic experiments.[30] However, this value cannot be taken directly for the nanoscaled matrix material. As reported by GEORGOPANOS et al. [74], the utilized polybutadien shows a tremendous reduction in the molecular weight and a reduced density compared to its bulky counterpart. This goes along with much shorter effective polymer chains and, hence, a reduced mesh size of the polymeric network. Therefore, the effective chain length L_{eff} must be retrieved by microscopic considerations.

In a polymeric network L_{eff} is understood as the free contour length between two entanglement or cross-link points of the polymer chains. This length is available for entropic straightening and identical to $r_{\max}$ such that

$$L_{\text{eff}} = N_K L_K \ . \tag{7.22}$$

To estimate L_{eff} the eight-chain ARRUDA-BOYCE network structure of Fig. 7.4 is assumed. Then, the polymer density ϱ_{PB} can be computed via the mass m_{RVE} of the cubical network structure RVE and the cubical volume V_{RVE} of a network structure RVE by

$$\varrho_{\text{PB}} = \frac{m_{\text{RVE}}}{V_{\text{RVE}}} = \frac{8L_{\text{AB}}\varrho_{\text{L}}}{L_{\text{cube}}^3} = \frac{3\sqrt{3}\varrho_{\text{L}}}{L_{\text{AB}}^2} \tag{7.23}$$

where ϱ_{L} is the length-related mass of the polymer chain, L_{AB} is the effective contour length of the eight-chain ARRUDA-BOYCE network structure model and L_{cube} the edge length of the cubical network structure RVE. ϱ_{L} is given by

$$\varrho_{\text{L}} = \frac{m_{\text{mono}}}{L_{\text{mono}}} \tag{7.24}$$

with the mass of a monomeric unit m_{mono} and the length of a monomeric unit L_{mono}. LECHNER et al. [138] report the formula

$$\text{Headgroup}-(\text{CH}_2-\text{CH}=\text{CH}-\text{CH}_2)_{\bar{n}}-\text{Headgroup}$$

as the basic structure of polybutadien. Therefore, a monomer consists of one carbon double bond of length L_{double} and three carbon single bonds of length L_{single} such that $L_{\text{mono}} = 3L_{\text{single}} + L_{\text{double}} = 0.59\,\text{nm}$, see [93]. With the mass of a carbon atom m_C and the mass of a hydrogen atom m_H the monomeric mass evaluates to $m_{\text{mono}} = 4m_C + 6m_H = 8.98 \cdot 10^{-23}$ g and subsequently $\varrho_{\text{L}} = 1.51 \cdot 10^{-13}\,\text{g/m}$. With the polymer density $\varrho_{\text{PB}} = 9 \cdot 10^5\,\text{g/m}^2$, taken from GEORGOPANOS et al. [74], and $L_K \approx 0.9\,\text{nm}$, L_{BC} can be computed. However, the actual effective length L_{eff} is assumed to be related to L_{BC} via a fitting parameter c to account for approximative shortcomings of the eight-chain ARRUDA-BOYCE network structure. These shortcomings are non-ideal chain entanglements and cross-linking points or to few assumed chains per network structure RVE. Here, c is chosen to be 0.97 and $N_K = 1.01$ after extensive numerical efforts.

The bond-stiffness parameter of the network is defined by $E^b = N_{\text{ch}} E_{\text{ch}}^b$, whereas E_{ch}^b is related to the bond energy of the chain segments. MAO et al. [155] report a value of

---

[30] It has to be mentioned that the free energy derived by KUHN et al. [135] is utilized here. However, their free energy form is very similar to the WLC since a singularity for $\lambda_r \to 1$ is present. This allows drawing analogies between both model variants. They report $N_K = 26.5$ for industrial rubber which is retrieved vie curve fitting from macroscopic experiments.

$E^b_{\text{ch}} = 60\,\text{eV}$ for a C-C bond at $T = 300\,\text{K}$, gained by ab-initio simulations. Via

$$\frac{E^b}{\mu} = \frac{N_{\text{ch}} E^b_{\text{ch}}}{\frac{N_{\text{ch}} k_b T}{2}} \tag{7.25}$$

they compute values in the range of $E^b = 500\,\text{MPa}$ for a given μ. However, μ corresponds to the macroscopical initial shear modulus in their consideration, which is far too large for rubbery materials. This makes the interpretation of E^b_{ch} and its associated conclusions questionable. In this work, E^b is considered a fitting parameter and chosen as $E^b = 1000\,\text{MPa}$ after several comparative computational simulations.

The remaining material parameter K_0^{Matrix} denotes the bulk modulus. Typically, polymeric materials are modeled as incompressible, since the resistance to volumetric deformations is much higher then to shear deformations. Nevertheless, a finite K_0^{Matrix} is considered here, because the polymer matrix is deformed above the entropic limit. Energy elastic materials, e.g. metals, are known to posses a bulk modulus in the range of their shear response. Therefore,

$$K_0^{\text{Matrix}} = 10 E^b = 10000\,\text{MPa} \tag{7.26}$$

is assumed.

For completeness Tab. 7.2 summarizes all material parameters for the polymer matrix. Fig. 7.5 depicts the stress-strain relation of uniaxial tension. Clearly visible is the non-linear, entropic deformation in the beginning which smoothly transfers to a linear response relatable to the energy-elastic regime.

Table 7.2.: Material parameters for the matrix material.

μ_0^{matrix} in [MPa]	K_0^{matrix} in [MPa]	$N_K = \lambda_L^2$	E^b in [MPa]
0.3	10000	1.01	1000

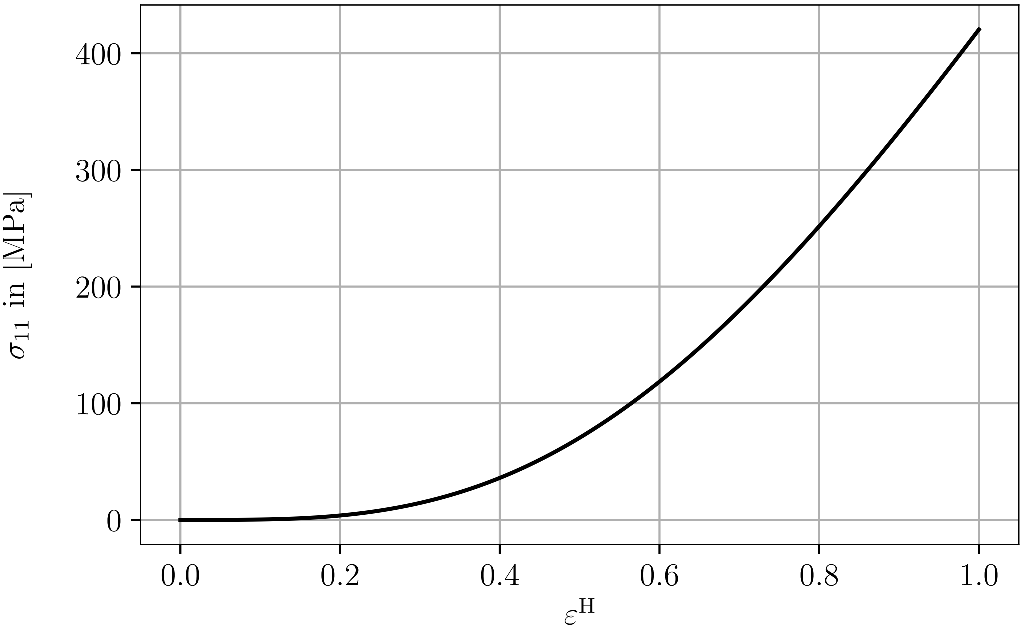

Figure 7.5.: Stress-strain curve of the matrix-material model.

7.2.3. Matrix-inclusion-interface

Following the arguments of DREYER et al. [47], carboxylate bonds between the nanoparticles and the matrix are weaker then the covalent C-C bonds in the polymer chain and failure occurs at the matrix-inclusion interface much more likely. Hence, this debonding dominates the composite's failure.

A general way of describing the interaction between the matrix interface and the inclusion interface is the formulation of a cohesive zone model in form of a traction separation law, see e.g. the summarizing article of SCHEIDER [196]. This law establishes a relationship between the surface traction $\vec{t}$ in the interface and the interface separation $\vec{\delta}$. The simplest form is given by

$$\begin{aligned} \bar{\vec{t}} &= \boldsymbol{K} \cdot \vec{\delta} \\ [\bar{t}_n \; \bar{t}_s \; \bar{t}_t]^{\mathrm{T}} &= \operatorname{diag}(K_n, K_s, K_t) \cdot [\delta_n \; \delta_s \; \delta_t]^{\mathrm{T}} \end{aligned} \tag{7.27}$$

with the elastic normal traction $\bar{t}_n$, the first and second elastic shear tractions $\bar{t}_s$ and $\bar{t}_t$ as well as the respective normal and shear separations δ_n, δ_s and δ_t. Here, $\overline{(\dots)}$ denotes elastic predictions computed by the elastic traction-separation behavior for the current separations without damage. $\boldsymbol{K}$ is the uncoupled, elastic stiffness tensor including the normal and tangential stiffnesses K_n, K_s and K_t. In the following, isotropic cohesive behavior is assumed such that $K_n = K_s = K_t = K_{\mathrm{coh}}$. Inspired by continuum damage models, a damage variable $D \in [0..1]$ is introduced to model degradation. In particular, D is utilized to describe the degradation of the cohesive stiffness. To this end, the tractions are substituted by

$$\begin{aligned} t_n &= \begin{cases} [1-D]\bar{t}_n & \bar{t}_n \geq 0 \\ \bar{t}_n & \text{else} \end{cases} , \\ t_s &= [1-D]\bar{t}_s \ , \\ t_t &= [1-D]\bar{t}_t \ . \end{aligned} \tag{7.28}$$

The altered normal traction t_n is formulated in a way such that degradation does not occur for compressive loadings. Damage initiates if the maximum traction ratio reaches a value of one. This criteria is modeled via

$$1 \geq \max\left(\frac{< t_n >}{t_n^{\max}}, \frac{t_s}{t_s^{\max}}, \frac{t_t}{t_t^{\max}}\right) \tag{7.29}$$

with the maximum normal and maximum shear tractions $t_n^{\max}, t_s^{\max}$ and $t_t^{\max}$. Here, $< \cdots >$ denotes the MACAULAY brackets. Due to the assumed isotropy

$$t_n^{\max} = t_s^{\max} = t_t^{\max} \tag{7.30}$$

must hold. Damage evolution is described via the effective traction $t_m = \sqrt{< t_n >^2 + t_s^2 + t_t^2}$ and the effective separation $\delta_m = \sqrt{< \delta_n >^2 + \delta_s^2 + \delta_t^2}$ to establish a multilinear mean traction-separation course, as depicted in Fig. 7.6. This functional course is specified by the maximum mean separation $t_m^{\max}$, the critical mean separation δ_m^c, the reduced maximum mean separation $\alpha t_m^{\max}$ and a corresponding mean separation $\delta_m^{f_1}$ and $\delta_m^{f_2}$. δ_m^c is defined through the linear-elastic limit and computes to

$$\delta_m^c = \frac{t_m^{\max}}{K_{\mathrm{coh}}} \tag{7.31}$$

utilizing the maximum mean traction $t_m^{\max}$. The first descending branch relates to the separation energy Γ_c. Γ_c represents the amount of dissipated energy after failure and is interpretable as the triangle between the points $(0,0)$, $(\delta_m^c, t_m^{\max})$ and $(\delta_m^f, 0)$. To ensure numerical stability in form of a non-vanishing traction, a change in the degradation slope is introduced at $\delta_m^{f_1}$, which corresponds to a traction level $\alpha t_m^{\max}$. The final separation $\delta_m^{f_2}$ specifies the point of total fracture where $D = 1$ and the present traction vanishes. For $\max\left(\frac{<t_n>}{t_n^{\max}}, \frac{t_s}{t_s^{\max}}, \frac{t_t}{t_t^{\max}}\right) = 1$, the

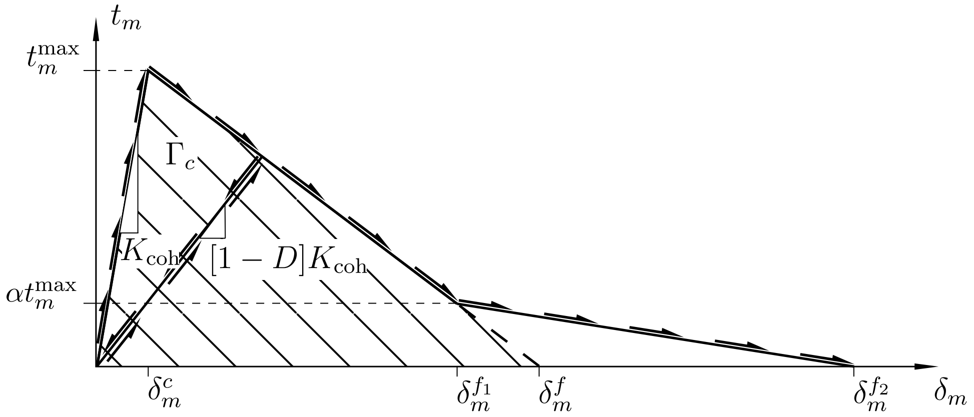

Figure 7.6.: Employed multilinear traction-separation law.

evolution of the damage variable in dependence of the mean separation can be given explicitly by

$$D = \begin{cases} \frac{\delta_m^f[\delta_m - \delta_m^c]}{\delta_m[\delta_m^f - \delta_m^c]} & \delta_m \leq \delta_m^{f_1} \\ \frac{\delta_m[\delta_m^f - \delta_m^c][\delta_m^{f_2} - \delta_m^{f_1}] - \delta_m^c[\delta_m^f - \delta_m^{f_1}][\delta_m^{f_2} - \delta_m]}{\delta_m[\delta_m^f - \delta_m^c][\delta_m^{f_2} - \delta_m^{f_1}]} & \text{else} \end{cases} \tag{7.32}$$

with $\delta_m^f = \frac{\Gamma_c}{2t_m^{\max}}$, $\delta_m^c = \frac{t_m^{\max}}{K}$, $\delta_m^{f_2} = \beta\delta_m^{f_1}$ and $\delta_m^{f_1} = \delta_m^f - \alpha[\delta_m^f - \delta_m^c]$. Due to the simplicity of the model, no evolution equations needs to be numerically integrated. In all simulations $\alpha = \frac{1}{100}$ to reduce the remaining traction after the gross of damage. Furthermore, $\beta = 1000$ to ensure a numerically stable degradation to the fully separated state.

The described cohesive zone model is implemented via a surface based cohesive formulation within the simulation software package Abaqus. In comparison to more versatile cohesive elements, cohesive surfaces show increased numerical stability. Here, the traction separation law is evaluated in an integral manner. Furthermore, it has to be mentioned that a degrading material response is very likely to suffer from convergence difficulties due to a decreasing material stiffness. Emerging singular stiffness matrices in the context of FE simulations is a common problem. To ensure numerical stability, viscous regularization techniques can be beneficially employed [150]. Here, an artificial damping is introduced by replacing D with a viscous damage D^v that is defined by

$$\dot{D}^v = \frac{1}{\eta}[D - D^v] \tag{7.33}$$

with the damping factor or stabilization variable η. Eq. (7.33) is a generalization of the well-known Duvaut–Lions viscoplasticity regularization. The introduced damping provokes more compliant regions that show an increased damage evolution in terms of a locally higher strain rate or damage rate to behave much stiffer. A quality criterion for negligible artificial effects is a negligible viscous damage energy in comparison to the internal energy of the model. Throughout all simulations the choice of $\eta = 10^{-3}\,\text{s}$ proved useful.

Material parameters

The cohesive interface introduces a specific length scale in the modeling process that enters via the critical separation δ_m^c. In contrast to the other employed lengths (RVE edge length, characteristic inclusion dimension), δ_m^c is not a relative quantity. Therefore all parameters of the cohesive zone model must comply with the employed units of the model, namely: [MPa] for stresses and [LU] for length. Here, one LU is the edge length of the RVE.

To specify the critical separation, it is constructive to investigate covalent atomic bonds. Typical, length of covalent atomic bonds lie in the range of Å [93]. Here, it is assumed that the critical separation is 1/10 of the bond length or 1/100 of the particle diameter such that

$$\delta_m^c = \frac{1}{1000} d_{\text{incl}} = 0.011\text{nm} = 0.011 \cdot 10^{-6}\,\text{mm} \ . \tag{7.34}$$

This value correlates with the one in BOCKO et al. [24].

The separation energies Γ_0 of the considered nanoparticulate materials are not available from experiments. However, [96] HECKEL et al. conduct density functional theory simulations for nanoparticulate materials with similar constituents (they investigate a titanium oxide - carboxyl bond). They report separation energies in the range of $\Gamma_0 = 50\frac{\text{meV}}{Å^2}$ to $\Gamma_0 = 200\frac{\text{meV}}{Å^2}$ which roughly relates to $\Gamma_0 = 1.6\frac{\text{J}}{\text{m}^2}$. This separation energy applies to a cohesive surface which is perfectly covered by bonded carboxyl groups. Such a perfect coverage is not realistic since the manufacturing process will never be ideal. DREYER et al. [47] report that the area density of the polymeric material on the particle surface is reduced due to desorption. In accordance with their results, Γ_0 is reduced by the factor 1/10 such that

$$\Gamma_0 = 0.16\frac{\text{J}}{\text{m}^2} = 1.6 \cdot 10^{-4}\text{MPa}\,\text{mm} \tag{7.35}$$

is taken here.

No experimental data is available for the maximum traction. According to MA et al. [151], $t^{\max}$ is in the range of some 100 MPa. Supported by numerical simulations and a comparison with the experimental results (see. Fig. 7.7)

$$t_n^{\max} = t_s^{\max} = t_t^{\max} = 500\,\text{MPa} \tag{7.36}$$

is chosen here.

Eventually, the cohesive stiffnesses K_{coh} is given by

$$K_{\text{coh}} = \frac{t^{\max}}{\delta_c^m} = 4.5454 \cdot 10^{10}\,\frac{\text{MPa}}{\text{mm}}\ .^{31} \tag{7.37}$$

Eventually, all length dependent quantities need to be adjusted to the considered RVE size to comply with the RVE dimensions (edge length of 1 LU). To this end, the relation

$$1\text{LU} = \frac{d_{\text{incl}}}{2}\left[\frac{3}{4}\frac{1}{\pi}\frac{v_f}{n_{\text{incl}}}\right]^{-\frac{1}{3}} \tag{7.38}$$

must hold and Tab. 7.3 summarizes the resulting material parameters

Table 7.3.: Utilized material parameters for the cohesive zone model.

n_{incl}	25	50	100
$t_n^{\max} = t_s^{\max} = t_t^{\max}$ in [MPa]	500	500	500
δ_m^c in [LU]$\cdot 10^{-4}$	3.25	2.58	2.05
LU in [mm]$\cdot 10^{-5}$	3.07	3.87	4.87
Γ_0 in [MPa]$\cdot$[LU]	5.21	4.13	3.28
K_{coh} in [MPa]$\cdot$[LU] $\cdot 10^6$	1.39	1.76	2.22

---

[30] Due to the relatively small critical separation K_{coh} evaluates very stiff. This high stiffness proves convenient since the overall model stiffness is not influenced significantly.

7.3. Results and discussion

7.3.1. Uniaxial compression

Fig. 7.7 depicts the experimental data adopted from GEORGOPANOS et al. [74] together with the numerically obtained macroscopic stress-strain behavior for uniaxial compression. First to notice is the relatively wide spread of the experimental curves. The determined YOUNG's modulus varies from 9.1 GPa to 23.7 GPa. Analogous, the total strength of the composite varies in the from 270 MPa to 850 MPa at maximal strains from 3% to 5.5%. Characteristic to the stress-strain curves is a linear regime in the beginning of the deformation up to $\varepsilon = 2\%$. Thereafter follows a smooth transition into the non-linear stress-strain regime which is assumed to be accompanied by interface degradation. Total failure occurs very sudden.

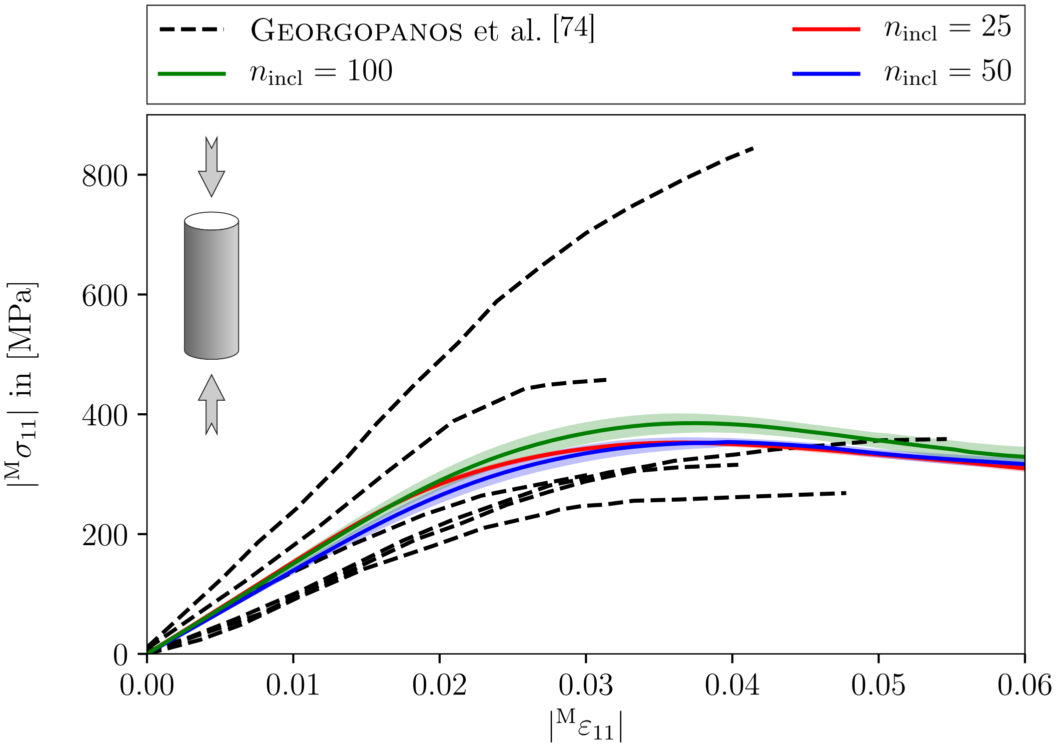

Figure 7.7.: Experimentally and numerically obtained macroscopic stress-strain curves for uniaxial compression. The solid lines represent mean values and shaded areas represent the standard deviation. The experimental data is adopted form GEORGOPANOS et al. [74].

With regard to the computationally determined curves, a qualitatively good agreement with the experiments can be observed. Tab. 7.4 lists the averaged macroscopic initial YOUNG'S moduli and their standard deviations w.r.t. the different RVE sizes. They are well within the range of the experimentally determined ones. In accordance with the data from GEORGOPANOS et al. [74], stress degradation initiates at roughly $|{}^{\mathrm{M}}\varepsilon_{11}| \approx 2\%$. All RVE variants exhibit a stress maximum from 340 MPa to 380 MPa at a macroscopic strain of $|{}^{\mathrm{M}}\varepsilon_{11}| \approx 3.6\%$.

Table 7.4.: Macroscopic initial YOUNG'S moduli and standard deviation for compression.

n_{incl}	25	50	100
${}^{\mathrm{M}}E_{11}$ in [GPa]	15.43 ± 0.33	13.98 ± 0.65	15.14 ± 0.78

Since no failure mechanisms are considered for the matrix material, no total failure of the entire RVE is observable. In accordance to the experiments only macroscopic strains up to 6% are considered. It can be stated that the RVE setting and employed material parameters are able to match the experiments to a satisfactory extend. Minor differences between the mean responses w.r.t. the different RVE sizes are observable. However, the standard deviation increases with the utilized number of inclusions per RVE. This effect is explainable by the increased randomness of the particle arrangement for increasing RVE sizes. Depending on the individual distances and relative particle positions damage initiates and evolves more differently.

To study the local behavior, Fig. 7.8 depicts contour plots of the VON MISES stress σ^{eq}, the bond strain $\varepsilon_b = \ln(\lambda_b)$ and the interface damage D of one example realization per investigated RVE size in the deformed state at $|^{\text{M}}\varepsilon_{11}| = 6\%$. Due to the high stiffness of the nanoparticles, the highest stresses are observable at material points of the inclusions. However, more important for the composites strength are the stresses the polymer has to withstand. Here, peaks occur in the vicinity of particles that are closest together. These stresses reach values up to 400 MPa to 500 MPa independent of the RVE size and are correlated to the maximum traction t_{max}.

The deformation behavior under tension is characterized by the formation of debonded particles that show cavities lateral to the loading direction. These cavities emerge in a distributed manner depending on the interplay of locally different distances between particles and their relative arrangement. The contour plots of the bond strain ε_b reveals shear bands that are inclined by approximately 45° w.r.t. the loading direction. Within these shear bands maximum bond strains up to 30% are observable. The shear bands provoke the particles to slide off each other which in turn accommodates the macroscopic compression. Inspecting the interface damage confirms the shear dominated local deformation behavior. The gross of interface damage can be identified along the former mentioned shear bands. The peculiarity of the shear deformation mode increases with the RVE size.

The shown results have been obtained by fitting the parameters $t_n^{\max}$, δ_m^{c}, E^b and N_k. In the future these parameters should be computed via further simulations such as ab initio, density functional theory simulations or molecular dynamics such that a more sound coupling between microscopic phenomena to the continuum mechanical material laws is established.

7.3.2. Uniaxial tension

Fig.7.9 depicts the macroscopic-strain curves for uniaxial tension. The linear elastic response transitions to a non-linear stress-strain course at $^{\text{M}}\varepsilon_{11} \approx 1\%$. For $^{\text{M}}\varepsilon_{11} \approx 3\%$ the composite's strength is reached. Maximal bearable macroscopic tensile stresses range from 200 MPa to 230 MPa. Analogous to the compressive loading cases, no total failure of the RVE is observable since no damage in the interconnected matrix is considered. Tab. 7.5 lists the averaged initial YOUNG'S moduli and their standard deviations. In comparison to the moduli obtained from the compression test a slight stiffness decrease of approximately 1.5 GPA can be determined, whereas standard deviation broaden for increased RVE sizes.

Table 7.5.: Macroscopic initial YOUNG'S moduli and standard deviation for uniaxial tension.

n_{incl}	25	50	100
$^{\text{M}}E_{11}$ in [GPa]	13.64 ± 0.21	12.44 ± 0.58	13.53 ± 0.55

To study the local behavior under tensile loading Fig. 7.10 depicts contour plots of the VON MISES stress σ^{eq}, the bond strain $\varepsilon_b = \ln(\lambda_b)$ and the interface damage D of one example realization per investigated RVE size in the deformed state at $^{\text{M}}\varepsilon_{11} = 6\%$. Again, the maximum stresses arise in material points of the nanoparticles. Similarly to compression, stresses

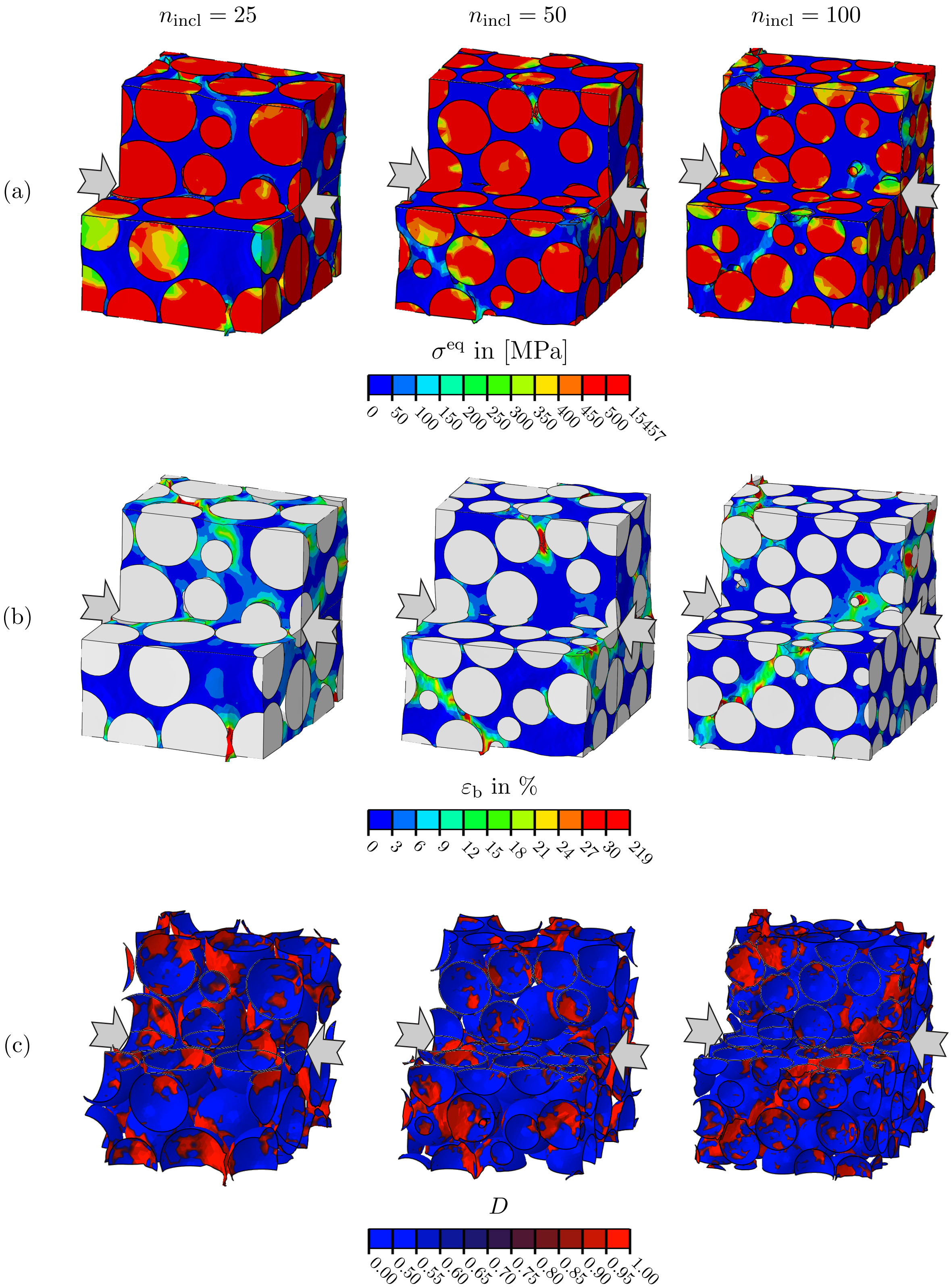

Figure 7.8.: Different contour plots for one RVE realization per RVE size subjected to compressive loading at a macroscopic strain of ${}^{\mathrm{M}}\varepsilon = 6\%$: (a) VON MISES stress σ^{eq}, (b) bond strain $\varepsilon_b = \ln(\lambda_b)$ and (c) cohesive damage D on cohesive surfaces.

in the matrix reach their maximum in the vicinity of two adjacent particles. These stresses range from 400 MPa to 500 MPa. However, the stress maxima in the matrix are locally more concentrated in comparison to compression. The RVE size is not influencing maximal stresses

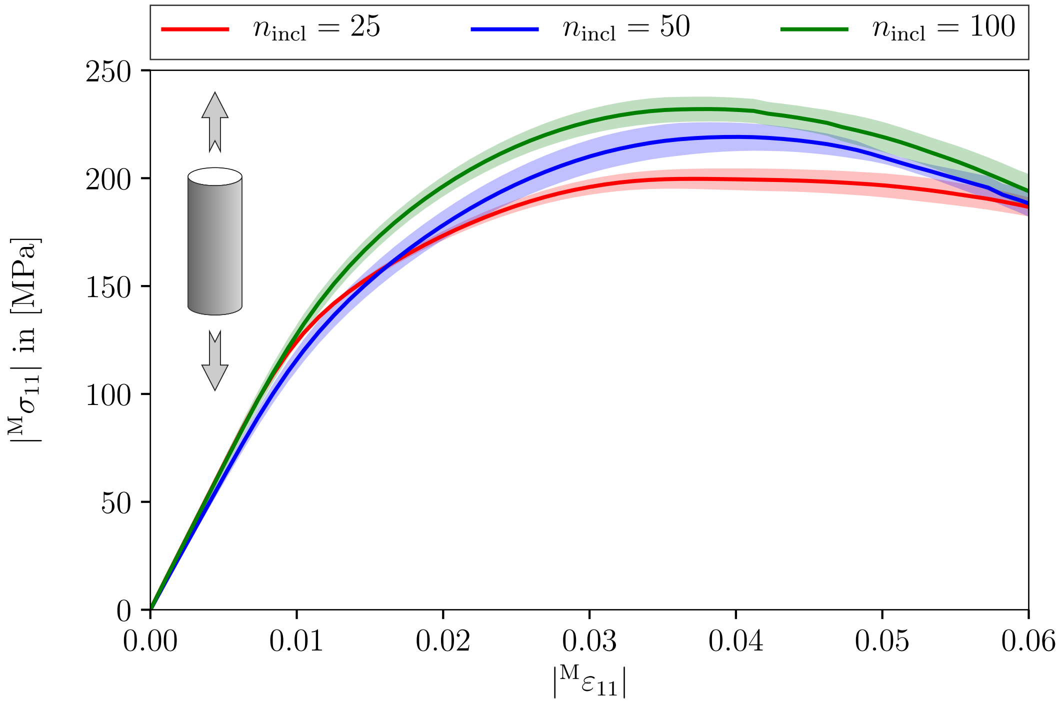

Figure 7.9.: Macroscopic stress-strain curves for uniaxial tension. The solid lines represent mean values and shaded areas represent the standard deviation.

in a significant way.

The deformation patterns are dominated by debonded particles with cavities in the loading direction. Depending on the RVE size, locally distributed maxima of bond strains up to 20% are observable in the vicinity of adjacent particles. The strain pattern between these particles can also be identified as shear bands. However, for small RVEs with $n_{\text{incl}} = 25$, the localized shear strains occur only between adjacent particle pairs. Such pairs are distributed over the RVE. Larger RVEs entail a pronounced linkage of these particle strain pairs up to a continuously evolving failure path. This path is inclined by 45° to the loading directions and eventually separates the RVE (see Fig. 7.10 (b) $n_{\text{incl}} = 100$). The interface damage distribution also reflects this behavior. For smaller RVEs interface damage is distributed more uniformly over the RVE whereas the large RVEs show a clear concentration of interface damage along the failure path.

7.3.3. Discussion

In summary, it can be stated that the presented model is capable of qualitatively representing the experimental findings related to composites consisting of a polymer matrix and ceramic nanoparticles, cf. [74]. Different deformation mechanisms can be identified by the simulations for tensile and compressive loadings. As a result, a slight tension-compression asymmetry of the initial YOUNG'S modulus can be confirmed by the simulations, cf. [74]. A pile-up effect such that the stiff nanoparticles support each other bear the applied load results in stiffer response under uniaxial compression. In combination with the shear dominated material behavior of the polymeric matrix, the pile up effect leads to a tendency for the nanoparticles to slide off each other. Due to the deformation of particles towards each other and a resulting interface debonding lateral to the loading direction, the composite shows a higher material strength under compression. For tension the particles do not support each other and scattered debonding takes place in a much earlier stage of macroscopic deformation. Therefore, the total strength decreases.

Another finding of the simulations is the necessity for relatively large RVEs. Although the

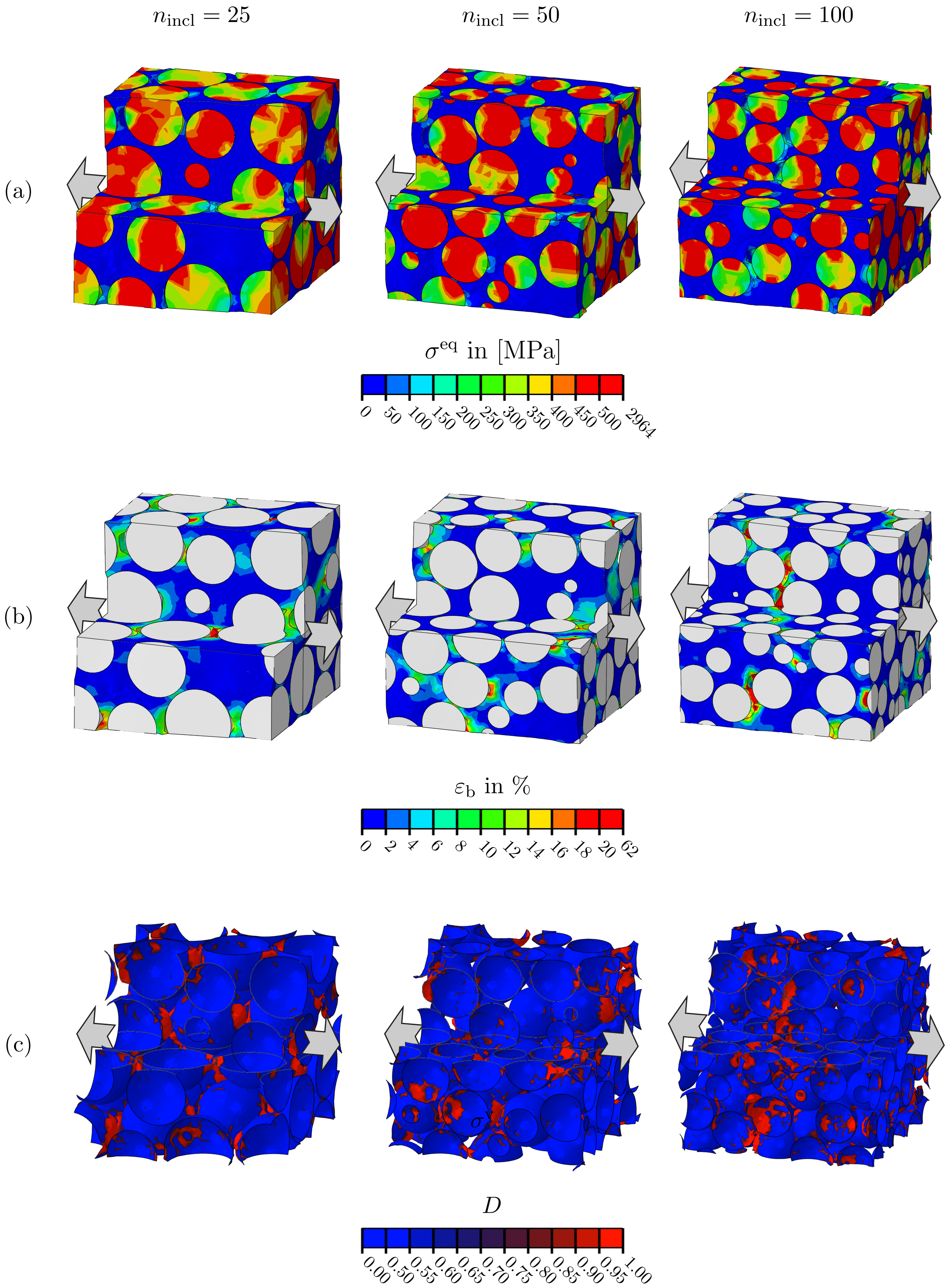

Figure 7.10.: Different contour plots for one RVE realization per RVE size subjected to tensile loading at a macroscopic strain of ${}^{\text{M}}\varepsilon = 6\%$: (a) von Mises stress σ^{eq}, (b) bond strain $\varepsilon_b = \ln(\lambda_b)$ and (c) cohesive damage D on cohesive surfaces.

linear-elastic material behavior is captured equally well by either RVE size, this is not the case for the interface failure patterns. Here, the localized failure patterns observable for the RVEs with $n_{\text{incl}} = 100$ are much more realistic. The formation of a single connecting path of debonded particle pairs can be interpreted as a macroscopic crack. This effect is amplified in the tensile loading scenario. Furthermore, it is observable that the increased randomness of the nanoparticle arrangement for large RVEs correlates with a broader deviation of the macroscopic stress-strain behavior. This increased randomness might be interpretable as imperfect particle rearrangements that trigger damage initiation. Nanoparticles that possess distances smaller than the idealized FCC arrangement are more exposed to stress concentrations and interface debonding initiates in an earlier stage of the macroscopic deformation. However, the larger scatter of the experimental results cannot be reproduced by the simulations. Probably more profound imperfections exist in the real material. Nanoparticles may be partly or totally detached from the matrix material, and, hence possess an imperfect bonding.

8. Summary and outlook

8.1. Conclusion

This thesis studies the computational modeling of randomized matrix-inclusions composites using representative volume elements, shows ways to improve the integration into engineering practice of this approach and eventually applies these methods to a polymer nanocomposite. Here, the goal is to study and predict the macroscopic and microscopic mechanical deformation behavior of the composite, that is, homogenization and localization. All developed methods are highly automizable and can be seamlessly integrated into engineering practice.

The well-known controversy in the preprocessing of FE analysis to fulfill the desired conditions of a fully periodic state-of-the-art RVE and simultaneously generate random RVEs with a large number of complex (non-spherical) inclusions with acceptable effort, is tackled. As a first step in the preprocessing, random placement procedures for ellipsoids, cylinders, capsules, spheres and convex polyhedra are recapitulated. Here, the focus lies on the non-trivial distance computation between the inclusion to ensure non-overlapping in a periodic and non-periodic RVE setting. Suggested improvements to existing algorithms allow the fast and reliable generation of microstructures featuring more than 100 inclusions, aspect ratios up to $\alpha = 20$ and inclusion volume fractions of up to $v_f = 20\%$ by means of RSA algorithms. The attainable inclusion volume fractions are limited due to the simplistic nature of RSA procedures. Extensions are highlighted by molecular dynamics inspired generation methods or collective rearrangement methods. Comparing all generation methods via statistical properties of the RVEs such as orientation distributions and two-point correlation functions identifies weaknesses and strengths of the employed methods.

The second stage in preprocessing is discretizing. Often identified as the bottle neck in setting up an analysis, periodic meshing represents a major obstacle. This work proposes an algorithm that is capable of automatically meshing three-dimensional, random, non-overlapping matrix-inclusion RVEs by means of tetrahedral elements. The ensured periodicity of the discretization allows a direct application of PBC. Key feature of the meshing process is a hierarchical discretization approach starting from points, over line meshes and face meshes to the final tetrahedralization. By differentiating between master and slave inclusions in combination with a successive processing of the geometric data, the algorithm proves very effective and stable. Due its generality, modifications to all types of inclusions without any restrictions are straightforward. The proposed algorithm is efficient, robust and automized. It produces high quality meshes while keeping the total number of elements significantly lower then comparable softwares like NETGEN, and hence, at a manageable minimum under computational viewpoints.

The gained fully periodic RVEs comply with the state-of-the-art approach and act as a reference solution for the subsequently conducted benchmark study. This benchmark study quantitatively evaluates the questions: how important is the utilization of the cumbersome state-of-the-art approach and what kind of inaccuracies entail from relaxations of that model setup. A comparison of RVEs with different stiffness ratios of matrix and inclusions, non-periodic and periodic microstructural topologies, periodic and non-periodic tetrahedral meshes as well as structured voxel discretizations, KUBC and SUBC, APBC and PBC offers precise insights in the mechanisms of computational micromechancis. Thereby also an improved way of imposing APBC to non-periodic meshes in a practicable way, introduced. Exemplarily, the gained RVEs are subjected to macroscopic uniaxial tensile and simple shear loadings employing linear elastic and non-linear elastic-plastic material behavior. Confirming the effects documented in the literature, it is found that KUBC are a potentially problematic choice in homogenization leading to overly stiff responses whereas SUBC show a softer response. KUBC and SUBC may, however, be simple and viable alternatives for specific phase contrast between the matrix and the inclusions. On the one hand KUBC show superior performance at low stiffness ratios, whereas SUBC are more suitable for high stiffness ratios. The novelty of the results unfolds in the analysis of the behavior of non-periodic and periodic RVEs. It reveals that no significant differences are observable between both variants such that the benefit of applying a periodic topology is highly questionable. Finally, it is found that APBC represent a veritable way of applying PBC to non-periodic RVEs in a fashion very accessible to engineering practice.

Eventually, applicability of the methods is demonstrated in the analysis of a novel polymer nanocomposites consisting of randomly distributed monodispersed, spherical, ceramic iron oxide particles which are embedded in a polybutadiene matrix. To represent the superior properties of this composite, such as a high stiffness and a high strength in combination with a low weight, emanating from the microstructure, a sophisticated model is developed. In particular, the material model suggested in [155, 223] is adopted to capture the entropy-elastic and energy-elastic deformation regime of the polymer. Detailed numerical analyses of the employed material model allows a fast and stable solution of the arising non-linear equations. Furthermore, the incorporation of the particle-matrix interface failure via a cohesive damage model reveals as a necessary condition to match experimental results of compression tests. By using physically meaningful material parameters, which are calibrated against experimental findings of compression tests, the local behavior is analyzed. It is found that the macroscopic deformation behavior results from the formation of local shear bands between a single layer of inclusions whereas debonding occurs equally likely in the entire RVE. These characteristic deformation patterns reveal valuable insights in the composite's micromechanics.

8.2. Outlook

The numerical investigation of matrix-inclusion composites is a vital element of modern engineering. Due to the constant development of new material classes, with polymer nanocomposites as one of the more recent examples, there is a pressing need to understand the micromechanical behavior of these materials. To this end, the generation of RVEs and subsequent micromechanical analyses are an important component.

In order to analyze more realistic microstructures, it is possible to extend the generation methods introduced in Ch. 3 to arbitrary non-convex inclusions and feed the RSA approaches by random distributions gained from experimental data. However, the distance or contact computation of arbitrary shapes requires a discretization of the particles and/or complex contact simulations [249], which are not yet suitable to be seamlessly incorporated in the engineering practice. One of the major challenges remains the truly random generation of RVEs in combination with a high inclusion volume fraction. To this end, the proven methods need to be extended by more versatile shapes than spheres. Exemplarily, GOHESSEIN et al. [77] alter the original LUBACHEVSKY-STILLINGER-algorithm by utilizing ellipsoids. The developed methods of this thesis to compute distances between cylinders is a viable option to be likewisely utilized in the LUBACHEVSKY-STILLINGER-algorithm for the generation of high inclusion volume fraction RVEs with cylindrical inclusions.

To further increase the feasibility of randomized RVEs in the scope of FE analyses, (periodic) mesh generation of non-convex shapes needs to be considered as well. Although, very recent contributions, see e.g. [141], offer ways of generating conforming and non-conforming meshes of arbitrary shapes in an automated manner, the problem of an excessive number of elements remains. The application of the Alg. 4.2 to non-convex particle shapes should be straightforward and represents a remedy to the inconveniently large mesh sizes of [141]. In addition it is worth mentioning that a parallelized implementation of the hierarchical meshing procedure is straightforward and capable of generating a considerable speed-up in the case of very large RVEs with more than 100 inclusions.

Such large RVEs might be an unavoidable choice for the investigated polymer nanocomposite of Ch. 7. As an extension to the current state of modeling, the incorporation of imperfections seems to be a necessary condition to capture the large spread of the experimentally documented deformation behavior. Assuming scattered non-perfect particles, with already debonded interfaces, could explain the diverse stiffnesses and material strengths observed in microcompression and microbending tests. To this end, RVEs with a large number of inclusions are required. A promising option to capture non-ideal characteristics of the microstructure seems the removal of individual particles, while keeping the total, experimentally verified, inclusions volume fraction constant. Subsequent statistical analyses over a variety of RVEs should then represent a good tool to evaluate and explain the large spread. Considering continuum damage for the polymeric matrix can be beneficial to describe the entire degradation of the composite up to total failure. Existing, physically motivated damage models for polymeric materials, see e.g. [223], promise to give valuable insights into the formation of local failure and deformation patterns. To further understand the micromechanical characteristics of these polymer nanocomposite, it is worth investigating the interplay of the competing mechanisms of debonding and continuum damage.

In conclusion, it can be stated that the provided methods and models form a sophisticated base to investigate matrix inclusion composites in a systematic and automated manner, complying with and extending the state of the art. In particular, the investigation of one of the most promising material classes of the presence, PNCs, shows high relevance and can act as a starting point to further understand, improve and optimize this composite on a microscopic level.

A. Appendix

A.1. Linearization of hyperelasticity

Isotropic hyperelastic material models are formulated by postulating the free energy density $\varrho_0\psi$ via the three tensor invariants of the right or left CAUCHY-GREEN stretch tensors $\boldsymbol{C}$ or $\boldsymbol{b}$. For a sophisticated material law, the stress-strain relation must coincide with the linear-elastic HOOKE's law $\boldsymbol{\sigma} = \mathbb{C} : \boldsymbol{\varepsilon}$ in the limit of infinitesimal kinematics. To this end, a derivation of this limit case for identifying initial material parameters, accessible via experiments, is given in the following. Assuming

$$\varrho_0\psi = \varrho_0\psi^{\mathrm{iso}}(I_{\bar{b}}) + \varrho_0\psi^{\mathrm{vol}}(J) \tag{A.1}$$

leads to

$$\boldsymbol{\sigma} = 2J^{-1}\frac{\partial\varrho_0\psi^{\mathrm{iso}}(I_{\bar{b}})}{\partial I_{\bar{b}}}\bar{\boldsymbol{b}}' + \frac{\partial\varrho_0\psi}{\partial J}\mathbf{1} \ . \tag{A.2}$$

$\varrho_0\psi$ is a non-linear function and therefore entails a non-linear stress-deformation behavior. Consequences are deformation dependent tangent bulk and shear moduli, c.f. [161, 206]. To encircle consistency and a relation of the utilized (non-linear) material parameters with the linear-elastic ones follows by inspecting the linearized version of Eq. (A.2). A linear TAYLOR-series expansion of Eq. (A.2) at the initial configuration $\boldsymbol{F} = \mathbf{1}$ results in

$$\boldsymbol{\sigma} = \boldsymbol{\sigma}\big|_{\boldsymbol{b}=\mathbf{1}} + \left.\frac{\partial\boldsymbol{\sigma}}{\partial\boldsymbol{b}}\right|_{\boldsymbol{b}=\mathbf{1}} : [\boldsymbol{b} - \mathbf{1}] + \mathcal{O}(\boldsymbol{b}^2) = \boldsymbol{\sigma}\big|_{\boldsymbol{b}=\mathbf{1}} + 2\left.\frac{\partial\boldsymbol{\sigma}}{\partial\boldsymbol{b}}\right|_{\boldsymbol{b}=\mathbf{1}} : \boldsymbol{\varepsilon} + \mathcal{O}(\boldsymbol{b}^2) \ . \tag{A.3}$$

The infinitesimal strain tensor $\boldsymbol{\varepsilon}$ relates to $\boldsymbol{b}$ via

$$\boldsymbol{b} = \mathbf{1} + \vec{\nabla}(\vec{u}) + \vec{\nabla}(\vec{u})^T + \vec{\nabla}(\vec{u}) \cdot \vec{\nabla}(\vec{u})^T = \mathbf{1} + 2\boldsymbol{\varepsilon} + \vec{\nabla}(\vec{u}) \cdot \vec{\nabla}(\vec{u})^T \ . \tag{A.4}$$

The derivative in Eq. (A.3) computes to

$$\begin{aligned}\frac{\partial\boldsymbol{\sigma}}{\partial\boldsymbol{b}} =& \frac{\partial^2\varrho_0\psi}{\partial J^2}\frac{J}{2}\mathbf{1}\otimes\boldsymbol{b}^{-1} \\ &+ 4J^{-1}\frac{\partial\varrho_0\psi}{\partial I_{\bar{b}}}\left[\mathbb{1}^{\mathrm{S}} - \frac{1}{3}\mathbf{1}\otimes\mathbf{1}\right]\left[J^{-2/3}\mathbb{1}^{\mathrm{S}} - \frac{1}{3}\bar{\boldsymbol{b}}\otimes\boldsymbol{b}^{-1}\right] \\ &+ 4J^{-1}\frac{\partial^2\varrho_0\psi}{\partial I_{\bar{b}}^2}\bar{\boldsymbol{b}}'\otimes[J^{-2/3}\mathbf{1} - \frac{1}{3}I_{\bar{b}}\boldsymbol{b}^{-1}] \\ &- 2J^{-1}\frac{\partial\varrho_0\psi}{\partial I_{\bar{b}}}\bar{\boldsymbol{b}}'\otimes\boldsymbol{b}^{-1}\end{aligned} \tag{A.5}$$

with

$$\frac{\partial J}{\partial\boldsymbol{b}} = \frac{J}{2}\boldsymbol{b}^{-1} \quad , \quad \frac{\partial I_{\bar{b}}}{\partial\bar{\boldsymbol{b}}} = \mathbf{1} \quad , \quad \frac{\partial\bar{\boldsymbol{b}}'}{\partial\bar{\boldsymbol{b}}} = \mathbb{1}^{\mathrm{S}} - \frac{1}{3}\bar{\mathbf{1}}\otimes\mathbf{1} \quad \text{and} \quad \frac{\partial\bar{\boldsymbol{b}}}{\partial\boldsymbol{b}} = J^{-2/3}\mathbb{1}^{\mathrm{S}} - \frac{1}{3}\bar{\boldsymbol{b}}\otimes\boldsymbol{b}^{-1} \ . \tag{A.6}$$

For the initial configuration, which is chosen to be stress free,

$$\boldsymbol{\sigma}\big|_{\boldsymbol{b}=\mathbf{1}} = \mathbf{0} \tag{A.7}$$

must hold. Furthermore, the first order term in Eq. (A.3) becomes

$$2\left.\frac{\partial\boldsymbol{\sigma}}{\partial\boldsymbol{b}}\right|_{\boldsymbol{b}=\mathbf{1}} = \left.\frac{\partial^2\varrho_0\psi}{\partial J^2}\right|_{\boldsymbol{b}=\mathbf{1}}\mathbf{1}\otimes\mathbf{1} + 4\left.\frac{\partial\varrho_0\psi}{\partial I_{\bar{b}}}\right|_{\boldsymbol{b}=\mathbf{1}}\left[\mathbb{1}^{\mathrm{S}} - \frac{1}{3}\mathbf{1}\otimes\mathbf{1}\right] \tag{A.8}$$

since $\bar{\boldsymbol{b}}' = \boldsymbol{0}$, $J = 1$ and $\bar{\boldsymbol{b}} = \boldsymbol{1}$ such that the elastic material law reads

$$\boldsymbol{\sigma} = \left[\left. \frac{\partial^2 \varrho_0 \psi}{\partial J^2} \right|_{\boldsymbol{b}=\boldsymbol{1}} \boldsymbol{1} \otimes \boldsymbol{1} + 4 \left. \frac{\partial \varrho_0 \psi}{\partial I_{\bar{b}}} \right|_{\boldsymbol{b}=\boldsymbol{1}} \left[\mathbb{1}^{\mathrm{S}} - \frac{1}{3} \boldsymbol{1} \otimes \boldsymbol{1} \right] \right] : \boldsymbol{\varepsilon} = \mathbb{C} : \boldsymbol{\varepsilon} \ . \tag{A.9}$$

Comparison with the elasticity tensor for isotropic materials $\mathbb{C} = K_0 \boldsymbol{1} \otimes \boldsymbol{1} + 2\mu_0 \left[\mathbb{1}^{\mathrm{S}} - \frac{1}{3} \boldsymbol{1} \otimes \boldsymbol{1} \right]$ brings the desired initial (for $\boldsymbol{F} = \boldsymbol{1}$) or tangent moduli

$$K_0 = \left. \frac{\partial^2 \varrho_0 \psi}{\partial J^2} \right|_{\boldsymbol{b}=\boldsymbol{1}} \quad \text{and} \quad \mu_0 = 2 \left. \frac{\partial \varrho_0 \psi}{\partial I_{\bar{b}}} \right|_{\boldsymbol{b}=\boldsymbol{1}} \ . \tag{A.10}$$

A specific choice of the free energy may then be calibrated against these initial moduli which are often measured in experiments.

A.2. Computation of the two-point correlation function by FOURIER transforms

The two-point correlation function of phase i for statistically homogeneous media under the assumption of ergodicity is given by

$$S_2^{(i)}(\vec{r}) = \lim_{\mathcal{B}_0 \to \infty} \frac{1}{V_0} \int_{\mathcal{B}_0} I^{(i)}(\vec{X}) I^{(i)}(\vec{X} + \vec{r}) dV. \tag{A.11}$$

Eq. (A.11) is quite similar to a convolutional integral, except for the sign of the second indicator function. The convolution theorem states that the FOURIER transform of a convolution of two functions is the pointwise product of their FOURIER transforms. Inspired by this fact, a derivation of the relation between the FOURIER transforms of the indicator function and the two-point correlation function is given in the following. To assign integration variables to their associated infinitesimal volume elements, the following indexed notation is utilized:

$$\vec{X}, \vec{Y}, \vec{Z}, \vec{r}, \vec{\omega} \to dV_X, dV_Y, dV_Z, dV_r, dV_\omega \ . \tag{A.12}$$

The FOURIER transform of a function $h(\vec{X})$ and its inverse transformation are given via

$$\begin{aligned} \mathcal{F}(h)(\omega) = \mathcal{H}(\vec{\omega}) &= \lim_{\mathcal{B}_0 \to \infty} \int_{\mathcal{B}_0} h(\vec{X}) e^{-i2\pi\vec{\omega}\cdot\vec{X}} dV_X \qquad \text{and} \\ h(\vec{X}) = \mathcal{F}^{-1}(\mathcal{H})(\vec{X}) &= \lim_{\mathcal{B}_\omega \to \infty} \int_{\mathcal{B}_\omega} \mathcal{H}(\vec{\omega}) e^{i2\pi\vec{\omega}\cdot\vec{X}} dV_\omega \end{aligned} \tag{A.13}$$

where $\mathcal{B}_\omega$ is the domain in the FOURIER space. Since the indicator function $I^{(i)}$ is a real valued function, Eq. (A.11) is expressible via $I^{(i)}$ and its complex conjugated version $I^{(i)^*}$ such that

$$S_2^{(i)}(\vec{r}) = \lim_{\mathcal{B}_0 \to \infty} \frac{1}{V_0} \int_{\mathcal{B}_0} I^{(i)^*}(\vec{X}) I^{(i)}(\vec{X} + \vec{r}) dV_X \ . \tag{A.14}$$

The variable substitution $\vec{X} = \vec{Y} - \vec{r}$ and $dV_X = dV_Y$ yields

$$S_2^{(i)}(\vec{r}) = \lim_{\mathcal{B}_0 \to \infty} \frac{1}{V_0} \int_{\mathcal{B}_0} I^{(i)^*}(\vec{Y} - \vec{r}) I^{(i)}(\vec{Y}) dV_Y \tag{A.15}$$

which is subjected to a FOURIER transform such that

$$\mathcal{F}\left(S_2^{(i)}\right)(\vec{\omega}) = \lim_{\mathcal{B}_0 \to \infty} \int_{\mathcal{B}_0} \frac{1}{V_0} \int_{\mathcal{B}_0} I^{(i)^*}(\vec{Y} - \vec{r}) I^{(i)}(\vec{Y}) e^{-i2\pi\vec{\omega}\cdot\vec{r}} dV_Y dV_r \ . \tag{A.16}$$

Substituting $\vec{r} = \vec{Z} + \vec{Y}$ and $dV_r = dV_Z$ followed by a rearrangement of the integrals leads to

$$\begin{aligned}\mathcal{F}\left(S_2^{(i)}\right)(\vec{\omega}) &= \lim_{\mathcal{B}_0\to\infty} \frac{1}{V_0}\int_{\mathcal{B}_0}\int_{\mathcal{B}_0} I^{(i)^*}(-\vec{Z}) I^{(i)}(\vec{Y}) e^{-i2\pi\vec{\omega}\cdot\vec{Z}} e^{-i2\pi\vec{\omega}\cdot\vec{Y}} dV_Y dV_Z \\ &= \lim_{\mathcal{B}_0\to\infty}\frac{1}{V_0}\int_{\mathcal{B}_0} I^{(i)^*}(-\vec{Z}) e^{-i2\pi\vec{\omega}\cdot\vec{Z}} dV_Z \underbrace{\lim_{\mathcal{B}_0\to\infty}\int_{\mathcal{B}_0} I^{(i)}(\vec{Y}) e^{-i2\pi\vec{\omega}\cdot\vec{Y}} dV_Y}_{\mathcal{F}(I^{(i)})(\vec{\omega})} \ . \end{aligned} \tag{A.17}$$

The first term in Eq. (A.17) can be simplified by the substitution $\vec{X} = -\vec{Z}$ and $dV_X = -dV_Z$ such that

$$\mathcal{F}\left(S_2^{(i)}\right)(\vec{\omega}) = \left(\lim_{\mathcal{B}_0\to\infty}\frac{1}{V_0}\int_{\mathcal{B}_0} I^{(i)^*}(\vec{X}) e^{i2\pi\vec{\omega}\cdot\vec{X}} dV_X\right)\mathcal{F}(I^{(i)})(\vec{\omega}) \ . \tag{A.18}$$

Due to the fact that the integration limits must also be subjected to this variable change and the relation

$$\begin{aligned}\lim_{\mathcal{B}_0\to\infty}\int_{\mathcal{B}_0} f(\vec{X}) dV_X &= \int_{-\infty}^{\infty}\int_{-\infty}^{\infty}\int_{-\infty}^{\infty} f(\vec{X}) dX_1 dX_2 dX_3 \\ &= -\int_{\infty}^{-\infty}\int_{\infty}^{-\infty}\int_{\infty}^{-\infty} f(\vec{X}) dV_X \ , \end{aligned} \tag{A.19}$$

the negative sign in $dV_X = -dV_Z$ cancels out by transforming back the integration limits. For complex conjugated numbers $a^* b = (ab^*)^*$ and $(e^{i\varphi})^* = e^{-i\varphi}$ must hold. Therefore, the final form of the FOURIER transform of the two-point correlation function is given by

$$\begin{aligned}\mathcal{F}\left(S_2^{(i)}\right)(\vec{\omega}) &= \lim_{\mathcal{B}_0\to\infty}\frac{1}{V_0}\underbrace{\left(\lim_{\mathcal{B}_0\to\infty}\int_{\mathcal{B}_0} I^{(i)}(\vec{X}) e^{-i2\pi\vec{\omega}\cdot\vec{X}} dV_X\right)^*}_{\mathcal{F}^*(I^{(i)})(\omega)}\mathcal{F}(I^{(i)})(\vec{\omega}) \\ &= \lim_{\mathcal{B}_0\to\infty}\frac{1}{V_0}\mathcal{F}(I^{(i)})^*(\vec{\omega})\mathcal{F}(I^{(i)})(\vec{\omega}) \ . \end{aligned} \tag{A.20}$$

The FOURIER transform of the two-point correlation function can be computed by the point-wise product of the FOURIER transform of the indicator function and its complex conjugate version. This product is also called power spectral density. The inverse FOURIER transformation gives the requried two-point correlation function via

$$S_2^{(i)}(\vec{r}) = \lim_{\mathcal{B}_0\to\infty}\frac{1}{V_0}\mathcal{F}^{-1}\left(\mathcal{F}(I^{(i)})^*(\vec{\omega})\mathcal{F}(I^{(i)})(\vec{\omega})\right)(\vec{r}) \ . \tag{A.21}$$

If the indicator function is periodic, e.g. in the case of a periodic RVE, it is sufficient to conduct the integrals over this periodic region only such that

$$S_2^{(i)}(\vec{r}) = \frac{1}{V_{\text{RVE}}}\mathcal{F}^{-1}\left(\mathcal{F}(I^{(i)})^*(\vec{\omega})\mathcal{F}(I^{(i)})(\vec{\omega})\right)(\vec{r}) \tag{A.22}$$

holds.

A.3. Kinematic and kinetic conclusions from averaging volume integrals over the RVE domain

In micromechanics it is often beneficial to substitute a volume integral over the entire RVE domain $\mathcal{B}_0$ by a surface integral over the entire RVE boundary $\partial\mathcal{B}_0$. The macroscopic deformation gradient ${}^{\mathrm{M}}\boldsymbol{F}$ is defined via

$${}^{\mathrm{M}}\boldsymbol{F} = \frac{1}{V_{\text{RVE}}}\int_{\mathcal{B}_0}\boldsymbol{F}\, dV_0 = \frac{1}{V_{\text{RVE}}}\int_{\mathcal{B}_0}\vec{\nabla}_X(\vec{x})\, dV_0 \ . \tag{A.23}$$

By employing Gauss's integral theorem, the gradient operator is eliminated such that

$$ {}^{\mathrm{M}}\boldsymbol{F} = \frac{1}{V_{\mathrm{RVE}}} \int_{\partial\mathcal{B}_0} \vec{x} \otimes \vec{N} \, dA_0 \; . \tag{A.24} $$

Similarly, the macroscopic 1. PK stress defined by

$$ {}^{\mathrm{M}}\boldsymbol{P} = \frac{1}{V_{\mathrm{RVE}}} \int_{\mathcal{B}_0} \boldsymbol{P} \, dV_0 \tag{A.25} $$

can be evaluated in terms of a surface integral. To this end, the following manipulations are conducted:

$$ \begin{aligned} {}^{\mathrm{M}}\boldsymbol{P} &= \frac{1}{V_{\mathrm{RVE}}} \int_{\mathcal{B}_0} \left[\boldsymbol{P}^{\mathrm{T}} \cdot \boldsymbol{1}\right]^{\mathrm{T}} dV_0 = \frac{1}{V_{\mathrm{RVE}}} \int_{\mathcal{B}_0} \left[\boldsymbol{P}^{\mathrm{T}} \cdot \vec{\nabla}_X(\vec{X})\right]^{\mathrm{T}} dV_0 \\ &= \frac{1}{V_{\mathrm{RVE}}} \int_{\mathcal{B}_0} \left[-\vec{\nabla}_X \cdot \boldsymbol{P}^{\mathrm{T}} \otimes \vec{X} + \vec{\nabla}_X \cdot \left[\boldsymbol{P}^{\mathrm{T}} \otimes \vec{X}\right]\right]^{\mathrm{T}} dV_0 \; . \end{aligned} \tag{A.26} $$

Since the microscopic balance of momentum $\vec{\nabla}_X \cdot \boldsymbol{P}^{\mathrm{T}} = \vec{0}$ holds, the integral theorem of Gauss is applicable and

$$ {}^{\mathrm{M}}\boldsymbol{P} = \frac{1}{V_{\mathrm{RVE}}} \int_{\partial\mathcal{B}_0} \vec{X} \otimes \boldsymbol{P}^{T} \cdot \vec{N} \, dA_0 = \frac{1}{V_{\mathrm{RVE}}} \int_{\partial\mathcal{B}_0} \vec{X} \otimes \vec{p} \, dA_0 \; . \tag{A.27} $$

In FE simulations, the continuous integrals need to be substituted by sums of discrete nodal or element related values. For the macroscopic deformation gradient, this yields

$$ \begin{aligned} {}^{\mathrm{M}}\boldsymbol{F} &= \frac{1}{V_{\mathrm{RVE}}} \int_{\mathcal{B}_0} \boldsymbol{F} \, dV_0 &&= \frac{1}{V_{\mathrm{RVE}}} \int_{\partial\mathcal{B}_0} \vec{x} \otimes \vec{N} \, dA_0 \\ &= \frac{1}{V_{\mathrm{RVE}}} \sum_i^{\infty} \lim_{\Delta V_{0i} \to 0} \boldsymbol{F} \, \Delta V_{0_i}^{\mathrm{el}} &&= \frac{1}{V_{\mathrm{RVE}}} \sum_i^{\infty} \lim_{\Delta A_{0i} \to 0} \left[\vec{u}_i + \vec{X}_i\right] \otimes \vec{N}_i \, \Delta A_{0i} \\ &\approx \frac{1}{V_{\mathrm{RVE}}} \sum_i^{n_{\mathrm{el}}} \boldsymbol{F}_i \, V_{0_i}^{\mathrm{el}} &&\approx \frac{1}{V_{\mathrm{RVE}}} \sum_i^{n_{\mathrm{b}}} \left[\vec{u}_i + \vec{X}_i\right] \otimes \vec{N}_i A_{0_i}^{\mathrm{el}} \end{aligned} \tag{A.28} $$

with the intial volume $V_{0_i}^{\mathrm{el}}$ of element i, the element surface $A_{0_i}^{\mathrm{el}}$ associated to node i at the RVE boundary and the total amount of elements n_{el}. The volume integral can be evaluated directly conducting a sum over all elements. Contrary, the surface integral requires a summation over all n_{b} nodes on the boundary whereas associated element surface areas $A_{0_i}^{\mathrm{el}}$ can be cumbersome to obtain.

Similarly, the macroscopic 1. PK stress can be evaluated via

$$ \begin{aligned} {}^{\mathrm{M}}\boldsymbol{P} &= \frac{1}{V_{\mathrm{RVE}}} \int_{\mathcal{B}_0} \boldsymbol{P} \, dV_0 &&= \frac{1}{V_{\mathrm{RVE}}} \int_{\partial\mathcal{B}_0} \vec{X} \otimes \vec{p} \, dA_0 \\ &= \frac{1}{V_{\mathrm{RVE}}} \sum_i^{\infty} \lim_{\Delta V_{0i} \to 0} \boldsymbol{P} \, \Delta V_{0i} &&= \frac{1}{V_{\mathrm{RVE}}} \sum_i^{\infty} \lim_{\Delta A_{0i} \to 0} \vec{X}_i \otimes \vec{p}_i \, \Delta A_{0i} \\ &\approx \frac{1}{V_{\mathrm{RVE}}} \sum_i^{n_{\mathrm{el}}} \boldsymbol{P}_i \, V_{0_i}^{\mathrm{el}} &&= \frac{1}{V_{\mathrm{RVE}}} \sum_i^{\infty} \vec{X}_i \otimes \lim_{\Delta A_{0i} \to 0} \frac{\Delta \vec{F}_i}{\Delta A_{0i}} \, \Delta A_{0i} \approx \frac{1}{V_{\mathrm{RVE}}} \sum_i^{n_{\mathrm{b}}} \vec{X}_i \otimes \vec{F}_i \end{aligned} \tag{A.29} $$

with $\vec{F}_i$ being the nodal force of node i at position $\vec{X}_i$ on the RVE boundary. Here, the surface integral formulation is of particular advantage since solely a summation of the outer product of nodal coordinates and nodal forces is required. These quantities are a direct outcome of the simulation.

However, for PBC the sum over all boundary nodes can be further simplified by taking advantage of the kinematic constraints and associated constraint forces. For demonstration

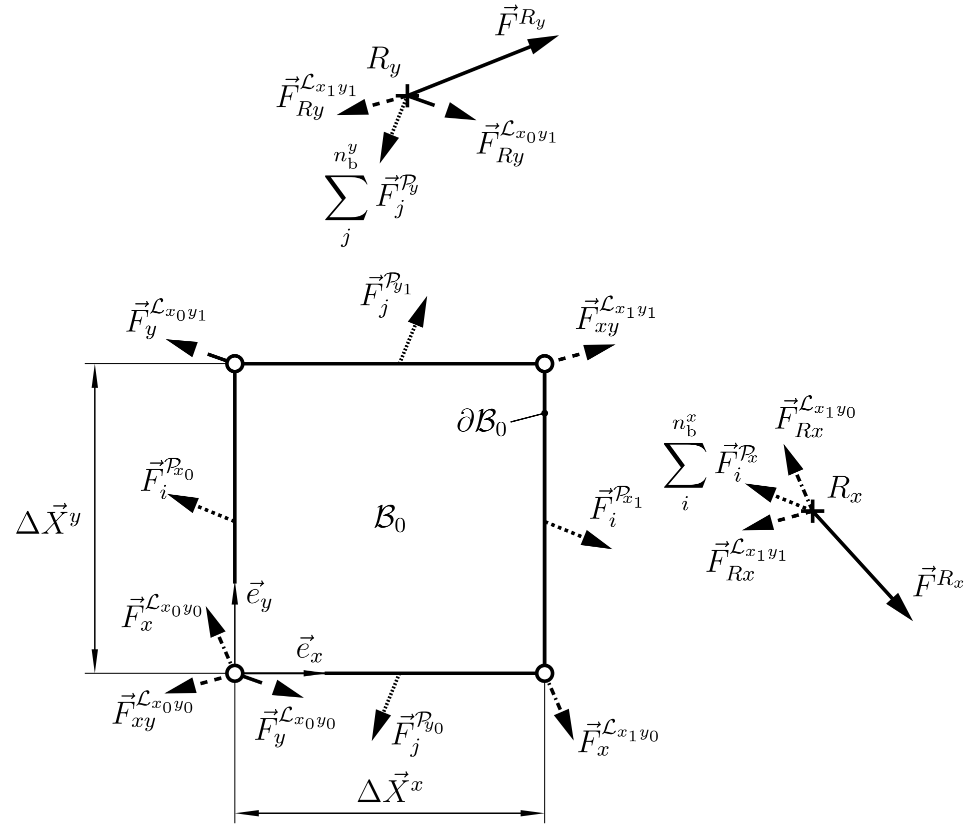

Figure A.1.: Free body diagram of a two-dimensional square-shaped RVE and the reference nodes R_x and R_y. All constraint forces and external forces are visible.

purposes, the two-dimensional case is elaborated in the following. Fig. A.1 depicts a schematic representation of a free body diagram of a square RVE and the reference nodes R_x and R_y. The forces $\vec{F}^{R_x}$ and $\vec{F}^{R_y}$ are reaction forces emerging from prescribed displacements $\vec{u}^{R_x}$ and $\vec{u}^{R_y}$ at the reference nodes to accommodate ${}^{\mathrm{M}}\boldsymbol{F}$. The remaining forces are correlated to the kinematic constraints, described in the following.

In analogy to the three-dimensional case, see Sec. 5.3, kinematic constraints are formulated for nodes on the RVE boundary. These constraint and correlated constraint forces are listed in the following:

$$\vec{u}^{\mathcal{P}_{x_1}} - \vec{u}^{\mathcal{P}_{x_0}} = \vec{u}^{R_x} \qquad \leftrightarrow \vec{F}^{\mathcal{P}_{x_1}}_i \,,\ \vec{F}^{\mathcal{P}_{x_0}}_i \,,\ \vec{F}^{\mathcal{P}_x}_i \tag{A.30a}$$

$$\vec{u}^{\mathcal{P}_{y_1}} - \vec{u}^{\mathcal{P}_{y_0}} = \vec{u}^{R_y} \qquad \leftrightarrow \vec{F}^{\mathcal{P}_{y_1}}_j \,,\ \vec{F}^{\mathcal{P}_{y_0}}_j \,,\ \vec{F}^{\mathcal{P}_y}_j \tag{A.30b}$$

$$\vec{u}^{\mathcal{L}_{x_1 y_0}} - \vec{u}^{\mathcal{L}_{x_0 y_0}} = \vec{u}^{R_x} \qquad \leftrightarrow \vec{F}^{\mathcal{L}_{x_1 y_0}}_x \,,\ \vec{F}^{\mathcal{L}_{x_0 y_0}}_x \,,\ \vec{F}^{\mathcal{L}_{x_1 y_0}}_{R_x} \tag{A.30c}$$

$$\vec{u}^{\mathcal{L}_{x_0 y_1}} - \vec{u}^{\mathcal{L}_{x_0 y_0}} = \vec{u}^{R_y} \qquad \leftrightarrow \vec{F}^{\mathcal{L}_{x_0 y_1}}_y \,,\ \vec{F}^{\mathcal{L}_{x_0 y_0}}_y \,,\ \vec{F}^{\mathcal{L}_{x_0 y_1}}_{R_y} \tag{A.30d}$$

$$\vec{u}^{\mathcal{L}_{x_1 y_1}} - \vec{u}^{\mathcal{L}_{x_0 y_0}} = \vec{u}^{R_x} + \vec{u}^{R_y} \qquad \leftrightarrow \vec{F}^{\mathcal{L}_{x_1 y_1}}_{xy} \,,\ \vec{F}^{\mathcal{L}_{x_0 y_0}}_{xy} \,,\ \vec{F}^{\mathcal{L}_{x_1 y_1}}_{R_x} \,,\ \vec{F}^{\mathcal{L}_{x_1 y_1}}_{R_y} \tag{A.30e}$$

Every kinematical quantity $\vec{u}$ in Eq. (A.30) entails a corresponding reaction force, acting at the position of the constraining degree of freedom, namely somewhere on the RVE boundary or the two referential nodes.

To simplify Eq. (A.28), the summation over all boundary nodes is divided in a sum over opposing boundaries such that

$$\begin{aligned} {}^{\mathrm{M}}\boldsymbol{F} = \frac{1}{V_{\mathrm{RVE}}} \Bigg[& \sum_{i}^{n_{\mathrm{b}}^{x}} \left[\vec{u}_i^{\mathcal{P}_{x_1}} + \vec{X}_i^{x_1}\right] \otimes \vec{N}_i^{x_1} A_{0_i}^{\mathrm{el}} + \sum_{i}^{n_{\mathrm{b}}^{x}} \left[\vec{u}_i^{\mathcal{P}_{x_0}} + \vec{X}_i^{x_0}\right] \otimes \vec{N}_i^{x_0} A_{0_i}^{\mathrm{el}} \\ & + \sum_{j}^{n_{\mathrm{b}}^{y}} \left[\vec{u}_i^{\mathcal{P}_{y_1}} + \vec{X}_i^{y_1}\right] \otimes \vec{N}_i^{y_1} A_{0_i}^{\mathrm{el}} + \sum_{j}^{n_{\mathrm{b}}^{y}} \left[\vec{u}_i^{\mathcal{P}_{y_0}} + \vec{X}_i^{y_0}\right] \otimes \vec{N}_i^{y_0} A_{0_i}^{\mathrm{el}} \Bigg] \end{aligned} \tag{A.31}$$

holds. Since the corner nodes have a vanishing associated boundary surface, terms including corners do not appear in (A.31). By means of of the kinematic constraints (A.30a) and (A.30b) and the anti-periodicity conditions of opposing normal vectors, see Eq. (2.58), a further simplification yields

$$\begin{aligned} {}^{\mathrm{M}}\boldsymbol{F} &= \frac{1}{V_{\mathrm{RVE}}} \Bigg[\sum_{i}^{n_{\mathrm{b}}^{x}} \left[\vec{u}_i^{\mathcal{P}_{x_1}} - \vec{u}_i^{\mathcal{P}_{x_0}} + \vec{X}_i^{x_1} - \vec{X}_i^{x_0}\right] \otimes \vec{N}_i^{x_1} A_{0_i}^{\mathrm{el}} \\ &\qquad + \sum_{j}^{n_{\mathrm{b}}^{y}} \left[\vec{u}_i^{\mathcal{P}_{y_1}} - \vec{u}_i^{\mathcal{P}_{y_0}} + \vec{X}_j^{y_1} - \vec{X}_j^{y_0}\right] \otimes \vec{N}_j^{y_1} A_{0_i}^{\mathrm{el}} \Bigg] \\ &= \frac{1}{V_{\mathrm{RVE}}} \Bigg[\sum_{i}^{n_{\mathrm{b}}^{x}} A_{0_i}^{\mathrm{el}} \left[\vec{u}^{R_x} + \Delta\vec{X}^{x}\right] \otimes \vec{N}^{x_1} + \sum_{j}^{n_{\mathrm{b}}^{y}} A_{0_j}^{\mathrm{el}} \left[\vec{u}^{R_y} + \Delta\vec{X}^{y}\right] \otimes \vec{N}^{y_1} \Bigg] . \end{aligned} \tag{A.32}$$

Here, the relations $\Delta\vec{X}^x = \vec{X}_i^{x_1} - \vec{X}_i^{x_0}$ and $\Delta\vec{X}^y = \vec{X}_i^{y_1} - \vec{X}_i^{y_0}$ are introduced. Since the normal vector $\vec{N}$ is constant on each side of the RVE, the normal vector of the $\mathcal{P}_{x_1}$-side is given by $\vec{N}^{x_1} = \vec{N}_i^{x_1} = -\vec{N}_i^{x_0}$ and the normal vector of the $\mathcal{P}_{y_1}$-side is given by $\vec{N}^{y_1} = \vec{N}_i^{y_1} = -\vec{N}_j^{y_0}$. Furthermore, the summation over all elements surfaces A_0^{el} are expressible via

$$\sum_{i}^{n_{\mathrm{b}}^{x}} A_{0_i}^{\mathrm{el}} = ||\Delta\vec{X}^y||_2 \quad \text{and} \quad \sum_{j}^{n_{\mathrm{b}}^{y}} A_{0_j}^{\mathrm{el}} = ||\Delta\vec{X}^x||_2 \; . \tag{A.33}$$

With $V_{\mathrm{RVE}} = ||\Delta\vec{X}^x||_2 ||\Delta\vec{X}^y||_2$, Eq. (A.32) eventually reduces and the macroscopic deformation gradient is given by

$${}^{\mathrm{M}}\boldsymbol{F} = \frac{1}{||\Delta\vec{X}^x||_2}[\vec{u}^{R_x} + \Delta\vec{X}^x] \otimes \vec{N}^{x_1} + \frac{1}{||\Delta\vec{X}^y||_2}[\vec{u}^{R_y} + \Delta\vec{X}^y] \otimes \vec{N}^{y_1} \tag{A.34}$$

which is straightforward to extend to the three-dimensional case for a cuboidal RVE:

$$\begin{aligned} {}^{\mathrm{M}}\boldsymbol{F} = & \frac{1}{||\Delta\vec{X}^x||_2} \left[\vec{u}^{R_x} + \Delta\vec{X}^x\right] \otimes \vec{N}^{x_1} \\ + & \frac{1}{||\Delta\vec{X}^y||_2} \left[\vec{u}^{R_y} + \Delta\vec{X}^y\right] \otimes \vec{N}^{y_1} \quad . \\ + & \frac{1}{||\Delta\vec{X}^z||_2} \left[\vec{u}^{R_z} + \Delta\vec{X}^z\right] \otimes \vec{N}^{z_1} \end{aligned} \tag{A.35}$$

The situation turns out to be more difficult for the macroscopic 1. PK stress. To simplify its definition, given in Eq. (A.29), the constraint forces need to be investigated. Therefore, the equilibrium of forces at the reference points is considered via

$$\begin{aligned} \vec{0} &= \sum_{i}^{n_b^x} \vec{F}_i^{\mathcal{P}_x} + \vec{F}_{R_x}^{\mathcal{L}_{x_1 y_0}} + \vec{F}_{R_x}^{\mathcal{L}_{x_1 y_1}} + \vec{F}_{R_x} \\ & \qquad\qquad\qquad\qquad\qquad\qquad . \\ \vec{0} &= \sum_{j}^{n_b^y} \vec{F}_i^{\mathcal{P}_y} + \vec{F}_{R_y}^{\mathcal{L}_{x_0 y_1}} + \vec{F}_{R_y}^{\mathcal{L}_{x_1 y_1}} + \vec{F}_{R_y} \end{aligned} \tag{A.36}$$

In addition to the equilibrium equations, the principle of virtual work must be satisfied. The principle of virtual work states that a group of forces, correlated to one kinematic constraint, is not contributing to the external work and therefore entails a vanishing virtual work contribution $\delta W = 0$.[32] This principle is used to establish a relation between the reaction forces and corresponding virtual displacements $\delta\vec{u}$ that are compatible with the constraints. Exemplarily, an observation of the kinematic constraint (A.30a), which links nodes on the faces $\mathcal{P}_{x_1}$ and $\mathcal{P}_{x_0}$, brings

$$\delta W_i = 0 = \vec{F}_i^{\mathcal{P}_{x_1}} \cdot \delta\vec{u}_i^{\mathcal{P}_{x_1}} + \vec{F}_i^{\mathcal{P}_{x_0}} \cdot \delta\vec{u}_i^{\mathcal{P}_{x_0}} + \vec{F}_i^{\mathcal{P}_x} \cdot \delta\vec{u}_i^{R_x} \tag{A.37}$$

for the i^{th} node. The variation of (A.30a)

$$\delta\vec{u}^{\mathcal{P}_{x_1}} - \delta\vec{u}^{\mathcal{P}_{x_0}} = \delta\vec{u}^{R_x} \tag{A.38}$$

allows the substitution of $\delta\vec{u}_i^{\mathcal{P}_{x_1}}$ in Eq. (A.37), which yields

$$\delta W_i = 0 = \left[\vec{F}_i^{\mathcal{P}_{x_1}} + \vec{F}_i^{\mathcal{P}_{x_0}}\right] \cdot \delta\vec{u}^{\mathcal{P}_{x_0}} + \left[\vec{F}_i^{\mathcal{P}_{x_1}} + \vec{F}_i^{\mathcal{P}_x}\right] \cdot \delta\vec{u}_i^{R_x} \ . \tag{A.39}$$

Since the non-vanishing variations $\delta\vec{u}^{\mathcal{P}_{x_0}}$ and $\delta\vec{u}_i^{R_x}$ are independent of each other,

$$\vec{F}_i^{\mathcal{P}_{x_1}} = -\vec{F}_i^{\mathcal{P}_{x_0}} = -\vec{F}_i^{\mathcal{P}_x} \tag{A.40}$$

must hold. An analogous treatment of the remaining constraints in (A.30) yields

$$\begin{aligned}
\vec{F}_j^{\mathcal{P}_{y_1}} &= -\vec{F}_j^{\mathcal{P}_{y_0}} = -\vec{F}_j^{\mathcal{P}_y} \\
\vec{F}_x^{\mathcal{L}_{x_1y_0}} &= -\vec{F}_x^{\mathcal{L}_{x_0y_0}} = -\vec{F}_{R_x}^{\mathcal{L}_{x_1y_0}} \\
\vec{F}_y^{\mathcal{L}_{x_0y_1}} &= -\vec{F}_y^{\mathcal{L}_{x_0y_0}} = -\vec{F}_{R_y}^{\mathcal{L}_{x_0y_1}} \\
\vec{F}_{xy}^{\mathcal{L}_{x_1y_1}} &= -\vec{F}_{xy}^{\mathcal{L}_{x_0y_0}} = -\vec{F}_{R_x}^{\mathcal{L}_{x_1y_1}} = -\vec{F}_{R_y}^{\mathcal{L}_{x_1y_1}}
\end{aligned} \ . \tag{A.41}$$

The Eq. (A.40) and (A.41) are the desired relations between the constraint forces. It is worth noticing that the anti-periodic traction constraint (2.62) is exactly recovered in its discrete version. Utilizing the relations between the constraint forces allows a further simplification of (A.29).

First, the summation over all boundary nodes n_{b} is split up into a sum over n_{b}^x point pairs of the opposing RVE faces $\mathcal{P}_{x_1}$ and $\mathcal{P}_{x_0}$ and n_{b}^y point pairs of the opposing RVE faces $\mathcal{P}_{y_1}$ and $\mathcal{P}_{y_0}$ as well as the corner nodes such that

$$\begin{aligned}
{}^{\text{M}}\boldsymbol{P} &= \frac{1}{V_{\text{RVE}}} \sum_k^{n_{\text{b}}} \vec{X}_k \otimes \vec{F}_k \\
&= \frac{1}{V_{\text{RVE}}} \left[\sum_i^{n_{\text{b}}^x} \vec{X}_i^{x_1} \otimes \vec{F}_i^{\mathcal{P}_{x_1}} + \sum_k^{n_b^x} \vec{X}_i^{x_0} \otimes \vec{F}_i^{\mathcal{P}_{x_0}} \right. \\
&\quad + \sum_j^{n_{\text{b}}^y} \vec{X}_j^{y_1} \otimes \vec{F}_j^{\mathcal{P}_{y_1}} + \sum_j^{n_b^y} \vec{X}_j^{y_0} \otimes \vec{F}_j^{\mathcal{P}_{y_0}} \\
&\quad + \vec{X}^{x_1y_0} \otimes \vec{F}_x^{\mathcal{L}_{x_1y_0}} + \vec{X}^{x_0y_1} \otimes \vec{F}_y^{\mathcal{L}_{x_0y_1}} + \vec{X}^{x_1y_1} \otimes \vec{F}_{xy}^{\mathcal{L}_{x_1y_1}} \\
&\quad \left. + \vec{X}^{x_0y_0} \otimes \left[\vec{F}_x^{\mathcal{L}_{x_0y_1}} + \vec{F}_x^{\mathcal{L}_{x_1y_0}} + \vec{F}_{xy}^{\mathcal{L}_{x_0y_0}}\right] \right] \ .
\end{aligned} \tag{A.42}$$

---

[32] A more geometrical interpretation of the principle of virtual work is given by the fact that the constraint forces need to be perpendicular to the hypersurface defined through the constraints. This requirement is equivalent to the condition that a supervector, containing all constraint forces, is parallel to the gradient of the constraint.

Here $\vec{X}_i^{x_0}$ and $\vec{X}_i^{x_1}$ correspond to points on the RVE faces $\mathcal{P}_{x_0}$ and $\mathcal{P}_{x_1}$, $\vec{X}_j^{y_0}$ and $\vec{X}_j^{y_1}$ correspond to points on the RVE faces $\mathcal{P}_{y_0}$ and $\mathcal{P}_{y_1}$ and $\vec{X}^{x_0y_0}$, $\vec{X}^{x_1y_0}$, $\vec{X}^{x_0y_1}$ and $\vec{X}^{x_1y_1}$ correspond to the RVE corner positions. Substituting all occurring forces in Eq. (A.42) by the constraint forces acting at the reference nodes and respecting the relation $\vec{X}^{x_1y_1} = \vec{X}^{x_1y_0} + \vec{X}^{x_0y_1}$ yields

$$\begin{aligned}{}^{\mathrm{M}}\boldsymbol{P} = \frac{1}{V_{\mathrm{RVE}}}\Bigg[& -\sum_i^{n_b^x}\left[\vec{X}_i^{x_1} - \vec{X}_i^{x_0}\right] \otimes \vec{F}_i^{\mathcal{P}_x} - \left[\vec{X}^{x_1y_0} - \vec{X}^{x_0y_0}\right] \otimes \vec{F}_{R_x}^{\mathcal{L}_{x_1y_0}} - \left[\vec{X}^{x_1y_0} - \vec{X}^{x_0y_0}\right] \otimes \vec{F}_{R_x}^{\mathcal{L}_{x_1y_1}} \\ & -\sum_i^{n_b^y}\left[\vec{X}_i^{y_1} - \vec{X}_i^{y_0}\right] \otimes \vec{F}_i^{\mathcal{P}_y} - \left[\vec{X}^{x_0y_1} - \vec{X}^{x_0y_0}\right] \otimes \vec{F}_{R_y}^{\mathcal{L}_{x_0y_1}} - \left[\vec{X}^{x_0y_1} - \vec{X}^{x_0y_0}\right] \otimes \vec{F}_{R_y}^{\mathcal{L}_{x_1y_1}}\Bigg] .\end{aligned}$$

Since

$$\begin{aligned}\Delta\vec{X}^x &= \vec{X}_i^{x_1} - \vec{X}_i^{x_0} = \vec{X}^{x_1y_0} - \vec{X}^{x_0y_0} \\ \Delta\vec{X}^y &= \vec{X}_i^{y_1} - \vec{X}_i^{y_0} = \vec{X}^{x_0y_1} - \vec{X}^{x_0y_0} \ ,\end{aligned} \tag{A.43}$$

a further simplification results in

$$\begin{aligned}{}^{\mathrm{M}}\boldsymbol{P} = \frac{1}{V_{\mathrm{RVE}}}\Bigg[& -\Delta\vec{X}^x \otimes \left[\sum_i^{n_b^x} \vec{F}_i^{\mathcal{P}_x} + \vec{F}_{R_x}^{\mathcal{L}_{x_1y_0}} + \vec{F}_{R_x}^{\mathcal{L}_{x_1y_1}}\right] \\ & -\Delta\vec{X}^y \otimes \left[\sum_i^{n_b^y} \vec{F}_i^{\mathcal{P}_y} + \vec{F}_{R_y}^{\mathcal{L}_{x_0y_1}} + \vec{F}_{R_y}^{\mathcal{L}_{x_1y_1}}\right]\Bigg] .\end{aligned} \tag{A.44}$$

With the force equilibrium (A.36), the bracket terms in (A.44) are substituted by the reaction forces of the reference points such that

$${}^{\mathrm{M}}\boldsymbol{P} = \frac{1}{V_{\mathrm{RVE}}}\left[\Delta\vec{X}^x \otimes \vec{F}^{R_x} + \Delta\vec{X}^y \otimes \vec{F}^{R_y}\right] . \tag{A.45}$$

Eventually, the sum over all boundary points of the RVE is reduced to the sum over the reference points. An extension to the three-dimensional case is straightforward, leading to

$${}^{\mathrm{M}}\boldsymbol{P} = \frac{1}{V_{\mathrm{RVE}}}\left[\Delta\vec{X}^x \otimes \vec{F}^{R_x} + \Delta\vec{X}^y \otimes \vec{F}^{R_y} + \Delta\vec{X}^z \otimes \vec{F}^{R_z}\right] . \tag{A.46}$$

A.4. Diagrams of the Benchmark study

This section lists the detailed results of the benchmark study of Ch. 6. All diagrams feature the averaged normalized macroscopic entities, whereas the normalization is conducted w.r.t. the largest considered RVE in a fully periodic model setup. Besides the averaged values, confidence intervals are shown in terms of gray error bars.

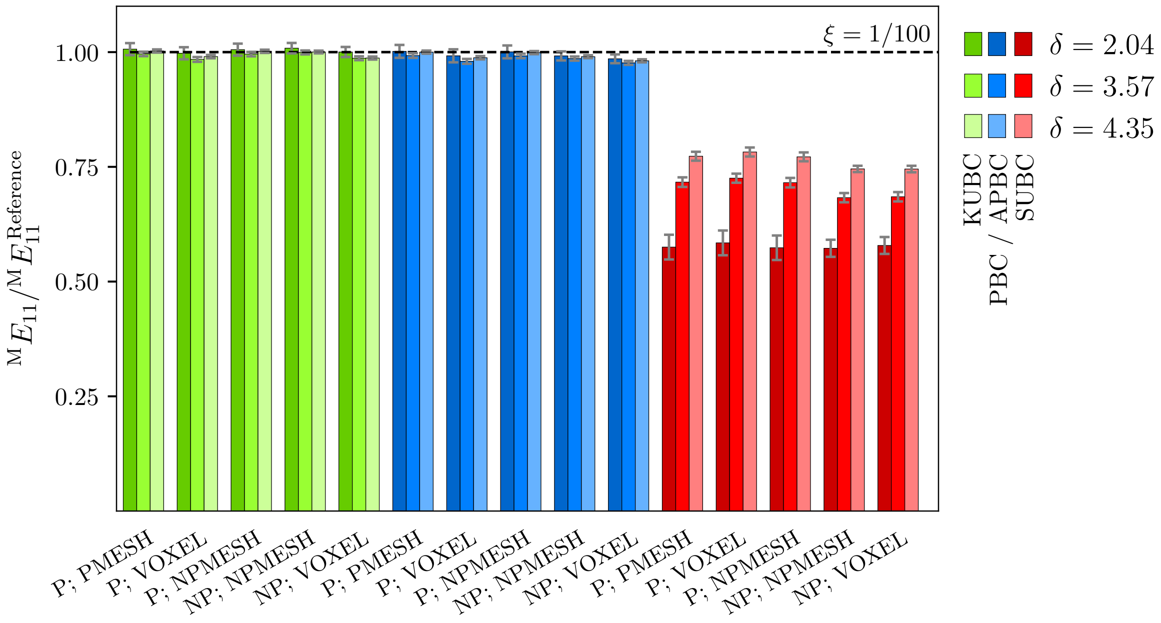

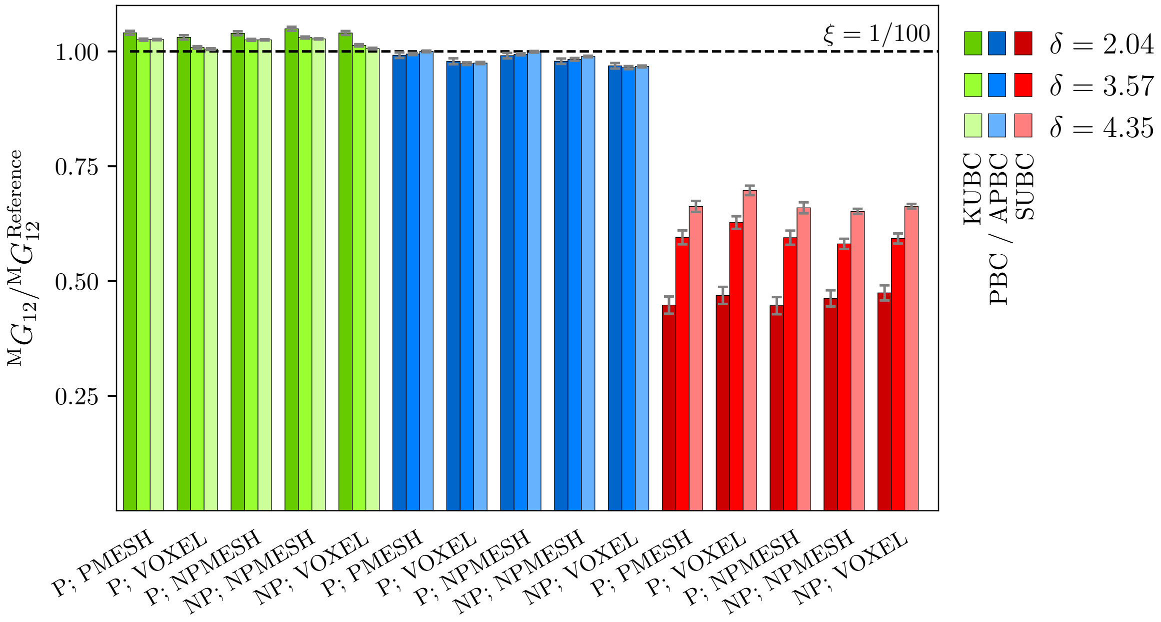

Figure A.2.: Normalized responses - macroscopic YOUNG's and shear moduli for a phase contrast of $\xi = 1/100$.

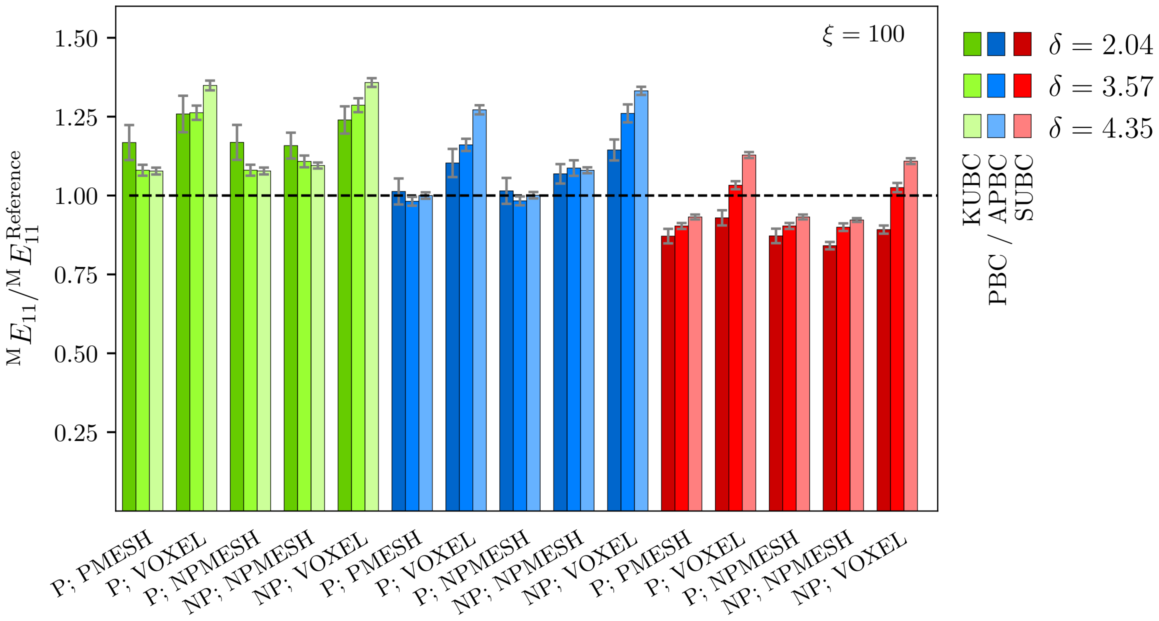

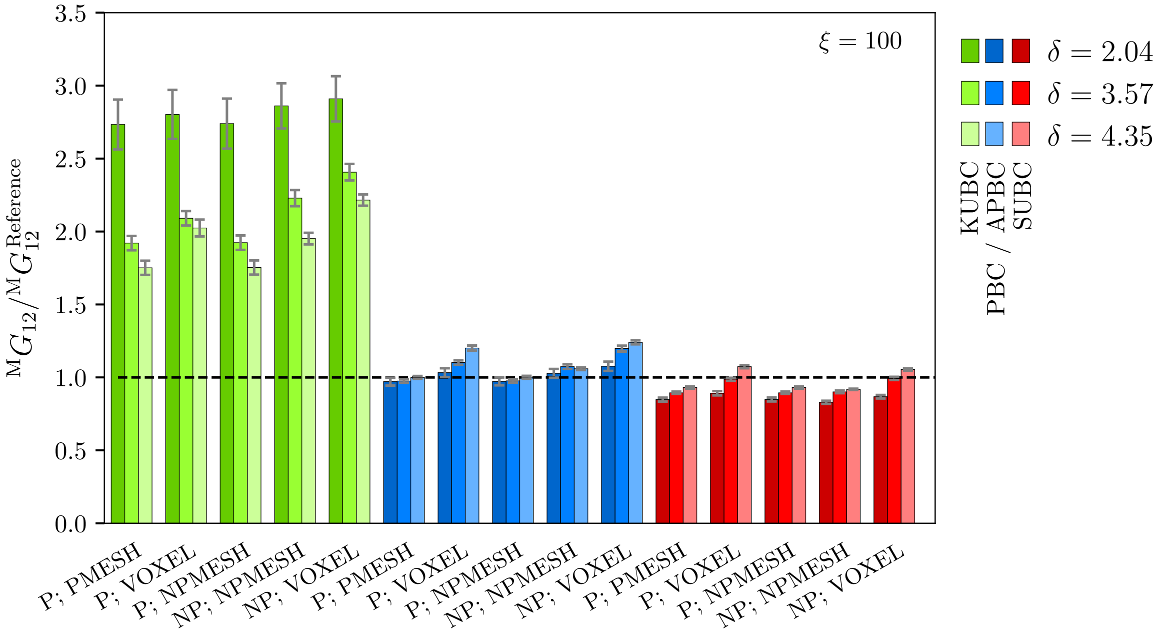

Figure A.3.: Normalized responses - macroscopic YOUNG's and shear moduli for a phase contrast of $\xi = 100$.

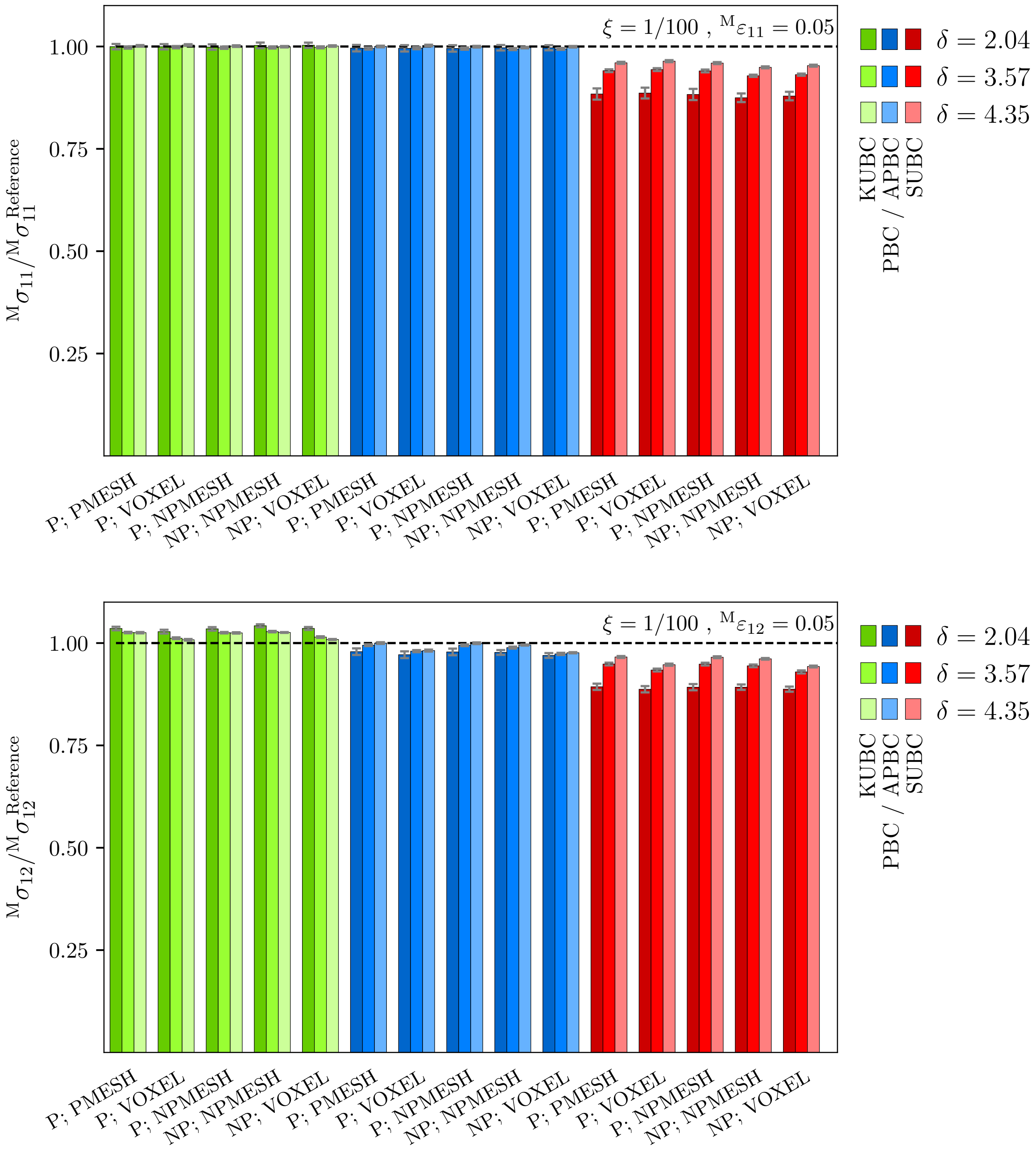

Figure A.4.: Normalized responses - macroscopic tensile and shear responses for a phase contrast of $\xi = 1/100$ at a state of deformation with a pronounced plastic deformation.

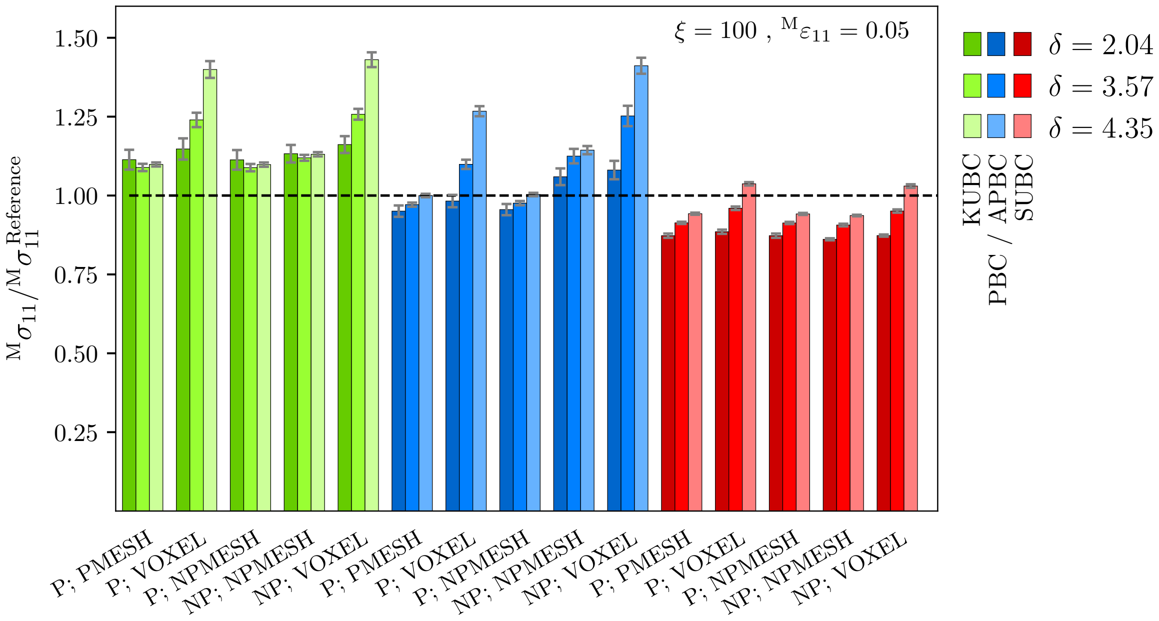

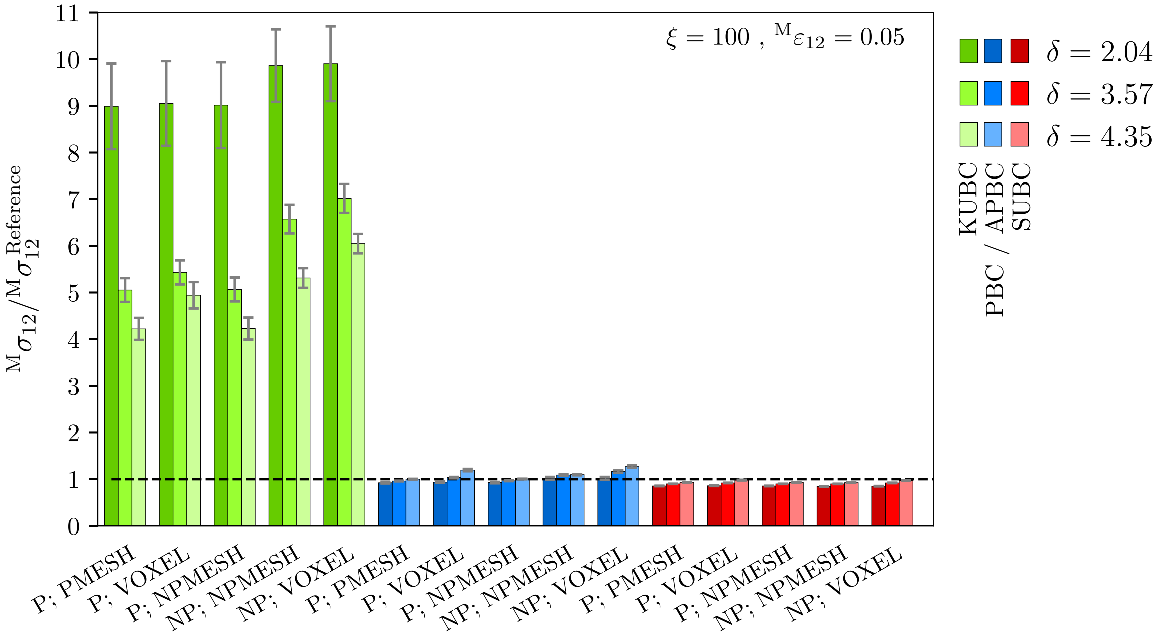

Figure A.5.: Normalized responses - macroscopic tensile and shear responses for a phase contrast of $\xi = 100$ at a state of deformation with a pronounced plastic deformation.

A.5. Numerical treatment of the polymeric matrix material law

Computing the quantities of Eq. (7.3) for the material law introduced in 7.2.2 requires the solution of the implicit Eq. (7.16) at any given deformation state characterized by $I_{\bar{b}}$ and J. To this end, the internal variable λ_b is obtained by finding the roots of the residuum

$$r(\lambda_b) = \frac{\partial \varrho_0 \psi}{\partial \lambda_b} = E^b \lambda_L^2 \frac{\ln(\lambda_b)}{\lambda_b} - \mu \lambda_L^2 B'(\lambda_r) \frac{\lambda_r}{\lambda_b} \overset{!}{=} 0 \tag{A.47}$$

with

$$B'(\lambda_r) = 4\lambda_r + \frac{1}{[1-\lambda_r]^2} - 1 \; . \tag{A.48}$$

Applying standard numerical techniques to solve the non-linear Eq. (A.47) is not straightforward since numerical difficulties arise for $\lambda_r \to 1$. In this region $B'(\lambda_r)$ exhibits a singularity. For more clarity, Fig. A.6 exemplarily depicts the residuum for $I_{\bar{b}} = 3.3$ ($\lambda_{\text{ch}} = 1.0488$ based on Eq. (7.17)).[33] Three roots exist of which only the largest one, with $\lambda_b^* = 1.0445$ (red circle), complies with the physical meaningful restriction $\lambda_r < 1$. The remaining roots (blue circles) generate unphysical results with $\lambda_r > 1$. Numerical solution techniques of non-linear equations, like the Newton-Raphson procedure, heavily depend on the initial values and only give one root. If the initial values are not chosen close enough to the desired solution, either an unphysical root is found or the algorithm diverges.

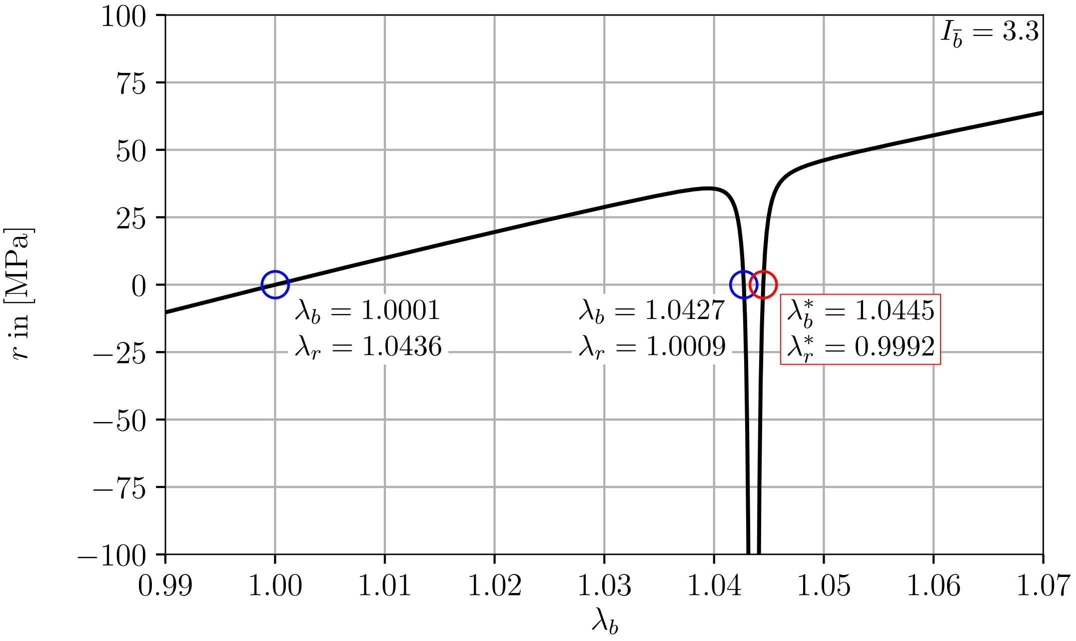

Figure A.6.: Residuum $r(\lambda_b)$ to compute the bond stretch λ_b.

To overcome this difficulty, Eq. (A.47) is multiplied with $\frac{\lambda_b}{\lambda_L^2}$ and the unknown variable λ_b is substituted by λ_r via Eq. (7.13). The new residuum r_1 then reads

$$r_1(\lambda_r) = E^b \left[\ln\left(\frac{\lambda_{ch}}{\lambda_L}\right) - \ln(\lambda_r) \right] - \mu B'(\lambda_r) \lambda_r \; . \tag{A.49}$$

Fig. A.7 shows the graph of r_1. It is observable that r_1 appears quite similar to r. Three roots exist and an approximately linear functional form at locations in sufficient distance from the singularity is observable. Due to the linear-like behavior gradient based methods converge to wrong solutions ($\lambda_r = 1.0436$) easily if the initial values are not close enough to the physical

---

[33] The later motivated material parameters of the examined PNC, listed in Tab. 7.2, are chosen here.

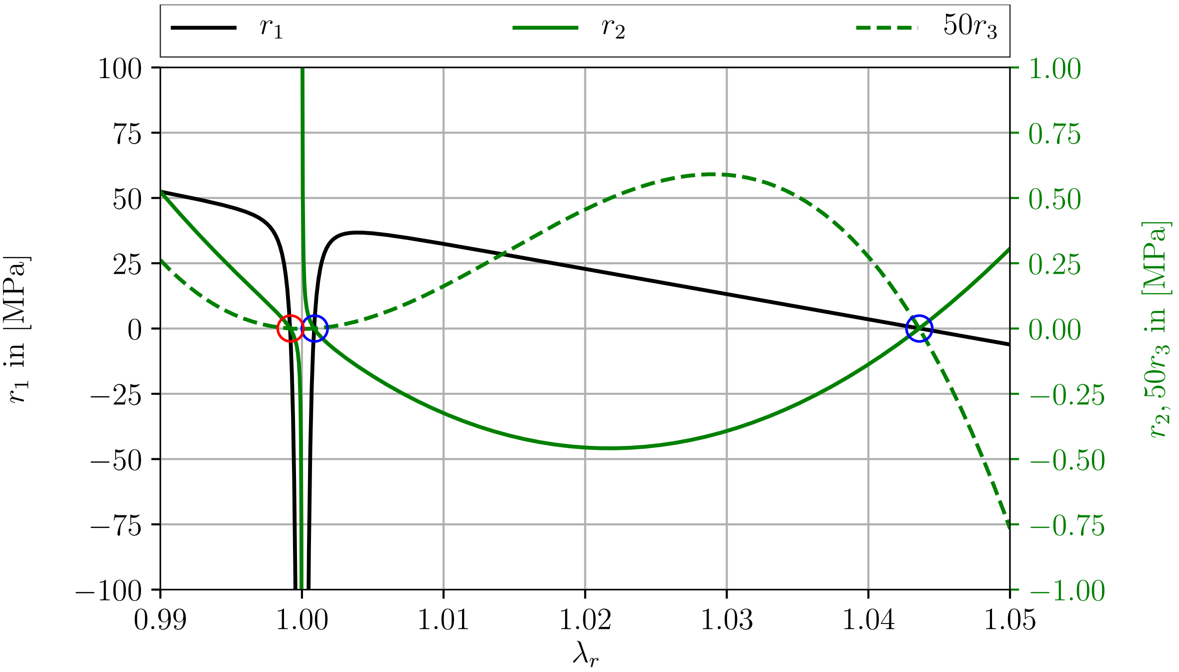

Figure A.7.: Different derived residua of Eq. (A.47) with the desired solution marked by a red circle.

meaningful solution. Therefore, r_1 proves equally unsuitable for the application of numerical root finding techniques. A further enhancement is achieved by multiplying Eq. (A.49) with $1 - \lambda_r$ or $[1 - \lambda_r]^2$ to weaken or remove the singularity. The resulting residua r_2 and r_3 are given by

$$r_2 = \left[E^b \left[\ln\left(\frac{\lambda_{ch}}{\lambda_L}\right) - \ln(\lambda_r)\right] - \mu B'(\lambda_r)\lambda_r\right][1 - \lambda_r] \tag{A.50}$$

and

$$r_3 = \left[E^b \left[\ln\left(\frac{\lambda_{ch}}{\lambda_L}\right) - \ln(\lambda_r)\right] - \mu B'(\lambda_r)\lambda_r\right][1 - \lambda_r]^2 \tag{A.51}$$

$$= E^b(1-\lambda_r)^2 \ln\left(\frac{\lambda_{ch}}{\lambda_L}\right) - E^b(1-\lambda_r)^2\ln(\lambda_r) - 4\lambda_r^2\mu\left(\lambda_r^2 - \frac{9}{4}\lambda_r + \frac{3}{2}\right) \; . \tag{A.52}$$

As can be seen in Fig. A.7, the singularity is completely removed for r_3. Unfortunately, r_3 is not very well suited for finding the desired λ_r^* either. Causative for this circumstance is a second (unphysical) root very close to λ_r^*. Due to the finite precision of computers, it is likely that the iteration process of a NEWTON-RAPHSON scheme converges to a $\lambda_r > 1$. However, r_3 shows similarity to a quartic function and is used to compute initial guesses. By utilizing the TAYLOR series expansion of the logarithm

$$\ln(\lambda_r) \approx \lambda_r - 1 - \frac{1}{2}(\lambda_r - 1)^2 \; , \tag{A.53}$$

which is valid for $\lambda_r \to 1$, Eq. (A.52) becomes

$$\begin{aligned} qr_3(\lambda_r) = & \left(\frac{1}{2}E - 4\mu\right)\lambda_r^4 \\ & + (-3E + 9\mu)\,\lambda_r^3 \\ & + \left(E\ln\left(\frac{\lambda_{ch}}{\lambda_L}\right) + 6(E-\mu)\right)\lambda_r^2 \\ & + \left(-2E\ln\left(\frac{\lambda_{ch}}{\lambda_L}\right) - 5E\right)\lambda_r \\ & + E\left(\ln\left(\frac{\lambda_{ch}}{\lambda_L}\right) + \frac{3}{2}\right) . \end{aligned} \tag{A.54}$$

This is a quartic polynomial approximation to Eq. (A.52). The closed form formula [114] gives all roots of $qr_3(\lambda_r)$. Eventually, the initial guess $\lambda_r^{\nu_0}$ is taken as the smallest value of the roots of $qr_3(\lambda_r)$. With $\lambda_r^{\nu_0}$ at hand, a Newton-Raphson scheme, applied to r_2, quickly converges to the desired λ_r^*. The Jacobian is given by

$$\begin{aligned} \frac{\partial r_2}{\partial \lambda_r} = & [1-\lambda_r]\left[-\frac{E^b}{\lambda_r} - \mu\left[B'(\lambda_r) + B''(\lambda_r)\lambda_r\right]\right] \\ & - \lambda_r\left[E^b\left[\ln\left(\frac{\lambda_{ch}}{\sqrt{n}}\right) - \ln(\lambda_r)\right] - \mu\lambda_L^2 B'(\lambda_r)\lambda_r\right] . \end{aligned} \tag{A.55}$$

Here,

$$B''(\lambda_r) = 4 + \frac{2}{[1-\lambda_r]^3} \tag{A.56}$$

denotes the second derivative of $B(\lambda_r)$. Due to the superb initial guess, the desired λ_r^* (red circle in Fig. A.7) often requires only two iterations.

As mentioned earlier, the undeformed initial state ($I_{\bar{b}} = 3$, $\lambda_{\text{ch}} = 1$) goes along with a non-vanishing, thermally induced force. Consequently, the initial bond stretch $\lambda_b^{\text{ini}} \neq 1$ respectively $\lambda_r^{\text{ini}} \neq 1$ must be determined a priori. Additionally, the initial shear modulus μ_0^{Matrix}, accessible via experiments, does not coincide with the introduced μ of Eq. (7.19). Contrary to Mao et al. [155], who chose $\mu = \mu_0$, here μ is determined a priori as well. This allows to operate with a meaningful material parameter in terms of μ_0^{Matrix}. With the relation

$$\begin{aligned} \frac{\partial \varrho_0\psi}{\partial I_{\bar{b}}} & = \left[\underbrace{\frac{\partial\varrho_0\psi}{\partial\lambda_b}}_{=0}\frac{\partial\lambda_b}{\partial\lambda_{\text{ch}}} + \frac{\partial\varrho_0\psi}{\partial\lambda_r}\frac{\partial\lambda_r}{\partial\lambda_{\text{ch}}}\right]\frac{\partial\lambda_{\text{ch}}}{\partial I_{\bar{b}}} \\ & = \mu\lambda_L^2 B'(\lambda_r)\frac{1}{\lambda_b\lambda_L}\frac{1}{6}\sqrt{\frac{3}{I_{\bar{b}}}} \\ & = \frac{\mu}{6}\lambda_L^2 B'(\lambda_r)\frac{1}{\lambda_b\lambda_L}\frac{1}{\lambda_{\text{ch}}} = \frac{\mu}{6}\frac{1}{\lambda_b^2}\frac{B'(\lambda_r)}{\lambda_r} = \frac{\mu}{6}\frac{\lambda_L^2}{\lambda_{\text{ch}}^2}\lambda_r B'(\lambda_r) \end{aligned} \tag{A.57}$$

the root of the residuum vector function

$$\underline{\bar{r}}\left(\underline{\bar{x}} = [\mu, \lambda_r]^{\text{T}}\right) = \begin{bmatrix} 2\frac{\partial\varrho_0\psi}{\partial I_{\bar{b}}} - \mu_0^{\text{Matrix}} \\ \frac{\partial\varrho_0\psi}{\partial\lambda_b}[1-\lambda_r] \end{bmatrix} = \begin{bmatrix} \frac{\mu}{3}\lambda_{\text{ch}}^{-2}\lambda_L^2\lambda_r B'(\lambda_r) - \mu_0^{\text{Matrix}} \\ r_2(\lambda_r) \end{bmatrix} = \underline{0} \tag{A.58}$$

must be obtained numerically. The first row of the residuum vector $\underline{\bar{r}}$ corresponds to the definition of the initial shear modulus derived in App. A.1. For a Newton-Raphson scheme, the Jacobian matrix, which reads

$$\underline{\underline{J}} = \begin{bmatrix} \frac{\partial\bar{r}_1}{\partial\mu} & \frac{\partial\bar{r}_1}{\partial\lambda_r} \\ \frac{\partial\bar{r}_2}{\partial\mu} & \frac{\partial\bar{r}_2}{\partial\lambda_r} \end{bmatrix} = \begin{bmatrix} \frac{\mu}{3}\lambda_{\text{ch}}^{-2}\lambda_L^2\lambda_r B'(\lambda_r) & \frac{\mu}{3}\lambda_{\text{ch}}^{-2}\lambda_L^2\left[B'(\lambda_r) + \lambda_r B''(\lambda_r)\right] \\ -B'(\lambda_r)\lambda_r & -\frac{E}{\lambda_r} - \mu\left[B'(\lambda_r) + \lambda_r B''(\lambda_r)\right] \end{bmatrix} , \tag{A.59}$$

is required to iterate for μ and λ_r^{ini}. Again, the initial guess essentially influences the convergence behavior of the iterative scheme. Since, initially the chain network is only deformed mildly, it is reasonable to assume $\lambda_b^{\nu_0} = 1$. This assumption justifies the initial values

$$\mu^{\nu_0} = \frac{\mu_0^{\text{Matrix}}}{\frac{1}{3}\lambda_{\text{ch}}^2 \lambda_L^{-2} B'(\lambda_r)\lambda_r} \quad \text{and} \quad \lambda_r^{\nu_0} = \frac{1}{\lambda_L} \ , \tag{A.60}$$

whereas μ^{ν_0} is derived from Eq. (A.57) and Eq. (A.10). Due to the good initial guess, only few iterations are necessary to obtain μ, λ_r^{ini} or respectively λ_b^{ini}.[34]

With the model parameters μ, λ_b^{ini} and λ_r^{ini} determined and a robust solution procedure for the internal variable λ_b at hand, the derivatives of Eq. (7.3) can be computed. As already derived in Eq. (A.57)

$$\frac{\partial \varrho_0 \psi}{\partial I_{\bar{b}}} = \frac{\mu}{6}\lambda_L^2 \lambda_{\text{ch}}^{-2} \lambda_r B'(\lambda_r) = \frac{\mu_T}{2} \tag{A.61}$$

with μ_T being the tangent shear modulus. The determination of second derivative $\frac{\partial^2 \varrho_0 \psi}{\partial I_{\bar{b}}^2}$ is more involved due to the dependency of λ_r on λ_{ch} and subsequently $I_{\bar{b}}$. In general

$$\begin{aligned} \frac{\partial^2 \varrho_0 \psi}{\partial I_{\bar{b}}^2} &= \frac{1}{2}\left[\frac{\partial \mu_T}{\partial \lambda_r}\frac{\partial \lambda_r}{\partial \lambda_{\text{ch}}} + \frac{\partial \mu_T}{\partial \lambda_{\text{ch}}}\right]\frac{\partial \lambda_{\text{ch}}}{\partial I_{\bar{b}}} \\ &= \frac{1}{2}\left[\frac{\mu}{3}\lambda_L^2 \left[B'(\lambda_r) + \lambda_r B''(\lambda_r)\right]\frac{\partial \lambda_r}{\partial \lambda_{\text{ch}}} - \frac{2}{3}\mu \lambda_L^2 \lambda_{\text{ch}}^{-3} \lambda_r B'(\lambda_r)\right]\frac{1}{6}\frac{1}{\lambda_{\text{ch}}} \end{aligned} \tag{A.62}$$

holds. However, $\frac{\partial \lambda_r}{\partial \lambda_{\text{ch}}}$ can only be obtained by exploiting the residuum $r_1(\lambda_{\text{ch}}, \lambda_r)$ defined in Eq. (A.49). For any iterated λ_r, $r_1 = 0$ holds, which makes the application of the implicit function theorem possible. In particular, the total derivative of r_1 can be written as

$$dr_1(\lambda_r, \lambda_{\text{ch}}) = \frac{\partial r_1}{\partial \lambda_r} d\lambda_r + \frac{\partial r_1}{\partial \lambda_{\text{ch}}} d\lambda_{\text{ch}} = 0 \tag{A.63}$$

which in turn leads to the desired expression

$$\frac{\partial \lambda_r}{\partial \lambda_{\text{ch}}} = -\left[\frac{\partial r_1}{\partial \lambda_r}\right]^{-1} \frac{\partial r_1}{\partial \lambda_{\text{ch}}} \ . \tag{A.64}$$

To evaluate Eq. (A.64), the derivatives of the residuum r_1

$$\begin{aligned} \frac{\partial r_1}{\partial \lambda_r} &= -\frac{E^b}{\lambda_r} - \mu\left[B'(\lambda_r) + B''(\lambda_r)\lambda_r\right] \ , \\ \frac{\partial r_1}{\partial \lambda_{\text{ch}}} &= \frac{E^b}{\lambda_{\text{ch}}} \end{aligned} \tag{A.65}$$

are necessary and Eq. (A.62) is fully determined.[35]

A.6. Insertion of cohesive interfaces

To consider cohesive material behavior in a FE analysis, it is necessary to insert zero thickness cohesive interfaces like cohesive elements or cohesive surfaces along material interfaces. Different materials are typically referenced by different element sets and form the basis of the following algorithm. Fig. A.8 depicts the basic steps of the insertion procedure. A FE discretization featuring two elements of which one element belongs to element set 0 and one

---

[34] For the later motivated material parameters, listed in Tab. 7.2, $\mu = 3.066 \cdot 10^{-5}\,\text{MPa}$, $\lambda_r^{\text{ini}} = 0.9942$ and $\lambda_b^{\text{ini}} = 1.0001$.

[35] The term of Eq. (A.62) is also referred to as algorithmic tangent.

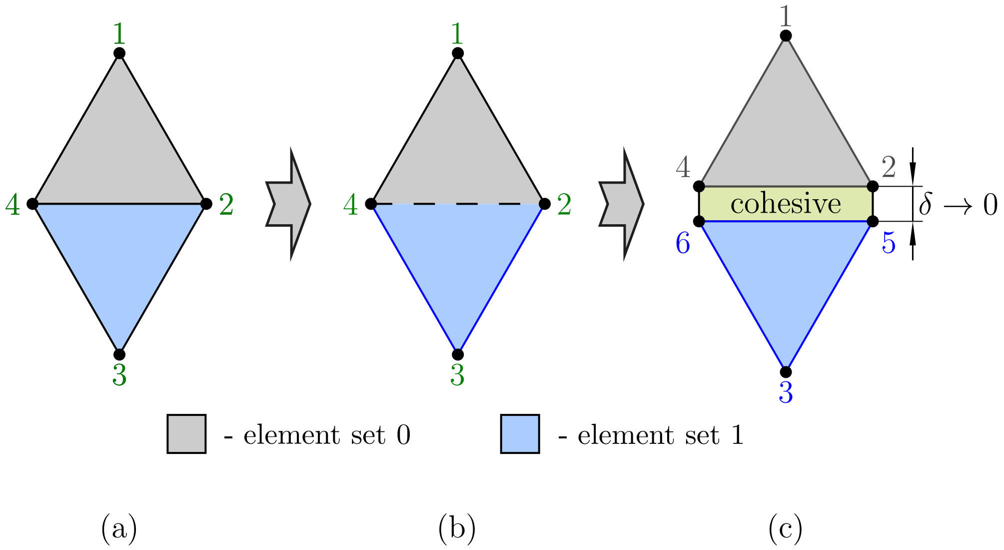

Figure A.8.: Principle of cohesive interfaces insertion on the example of a two element discretization: (a) original mesh with element sets and element node connectivity information, (b) identification of boundary objects (nodes and element faces) between element sets and (c) insertion of cohesive interfaces by duplicating boundary nodes, introducing cohesive features and reconnecting the original elements.

element to element set 1 is considered. The material interface is formed by the element faces between node 2 and 4. First, the material interfaces are detected by identifying nodes and elements that form these interfaces. Next, the mesh is separated at the material interfaces by duplicating the interfacing nodes and reconnecting the involved nodes to the elements of the different sets. The parent nodes and the duplicated nodes are eventually utilized to form the cohesive interface.[36]

Nguyen [167] introduced an algorithm to execute the described procedure. The suggested algorithm solely relies on the information of interface-nodes. These nodes are attained by searching the element array for interface connectivities. Nodes which are connected to two different element sets and at the same time belong to one element are duplicated. Thereafter, the algorithm reconnects elements to the new nodes and inserts cohesive interfaces. Unfortunately, this algorithm has three drawbacks.

First, the original algorithm does not cover the correct insertion of cohesive interfaces for points, where three or more material interfaces connect, see Fig. A.9 (a). Although a workaround is proposed in [167], the described solution requires the generation of an array that contains the information of the neighbors of all elements. The subsequent modification of the connectivities of the cohesive interface features results in a very complex and computationally expensive overall procedure. Secondly, thin material layers, consisting only of one element in thickness direction, will lead to erroneous results. Since no look-up of whether the element boundary is also a material interface or not is done, cohesive features might be wrongly inserted. In the example of Fig. A.9 (b), a cohesive feature would be wrongly inserted between the nodes 1 and 2 by Nguyens algorithm. A final point of criticism is the fact that cohesive features are inserted without any distinction of the material interfaces. If, for example, a model with three material sets, 0, 1 and 2, is considered, the algorithm allows the definition of only one cohesive property.

These circumstances motivate the development of a new strategy to automatically insert zero thickness cohesive features. Fig. A.10 depicts the flowchart of the suggested algorithm. Input is the initial mesh with the `nds` array that contains the nodal coordinates $[n_x^i, n_y^i, \dots]$ of node i, the element connectivity array `ele` that contains the node identification numbers

---

[36] For demonstration purposes the cohesive interfaces are displayed with a finite thickness δ.

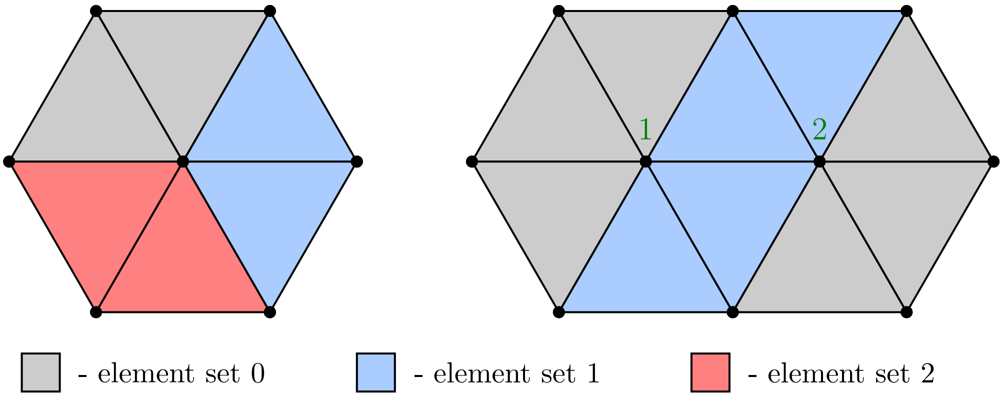

(a) (b)

Figure A.9.: Special test cases for the cohesive feature insertion algorithm: (a) multi-material set points and (b) one element layers of material sets.

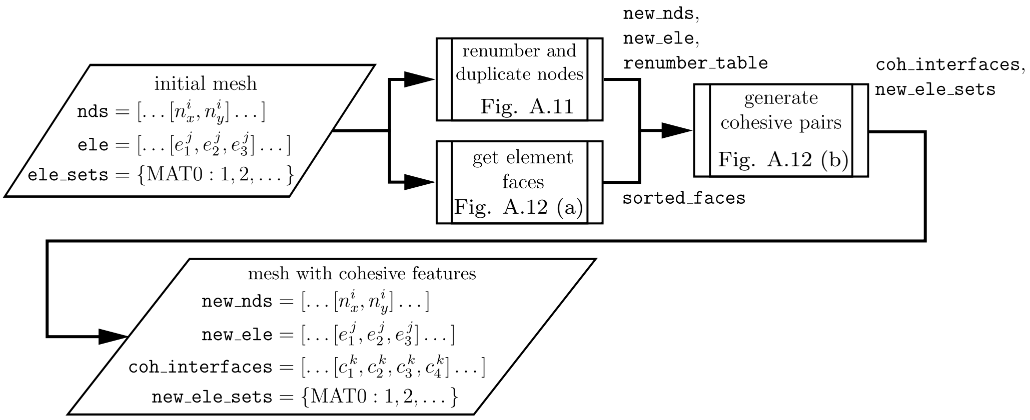

Figure A.10.: Flowchart of the algorithm to automatically insert cohesive features between element sets.

(ids) $[e_1^j, e_2^j, e_3^j, \ldots]$ of element j and the `ele_sets` array that contains element ids of the different element sets.

The entire procedure is demonstrated on basis of an example highlighted in Fig. A.11 (a). In the first step, nodes on the interfaces are duplicated and element faces are obtained. Key feature of the nodes duplication is the two-dimensional integer array `renumber_table`. Its rows correlate to the element sets and its columns correlate to the node ids of the mesh. Initially this array is filled with the value -1. By looping over all element sets, the `renumber_table` is filled row-wise by positive integers in ascending order. Each integer corresponds to the newly assigned node ids of the current element set. It is evident that columns in the fully processed `renumber_table` that possess more than one non -1 entry, indicate nodes that need to be duplicated, see Fig. A.11 (b). Therefore a `new_nds` array containing the initial nodes and the newly duplicated nodes is generated. Additionally, the element connectivity array needs renumbering in accordance to the new node counting, which results to the `new_ele` array. As shown in Fig. A.11 (c), the new mesh is split apart at the cohesive interfaces.[37]

Simultaneously, the algorithm retrieves the relevant element faces, at which cohesive interfaces are to be inserted. In the example of Fig. A.11 (a) no cohesive features need to be

---

[37] It is worth noticing that the separation of nodes makes it possible to correlate each node to a single element set. In that sense, nodes that share the same coordinates in a zero thickness cohesive interface setting can be clearly distinguished. This fact is particularly useful when applying PBC where nodal pairs on the RVE boundary need to searched based on their coordinates.

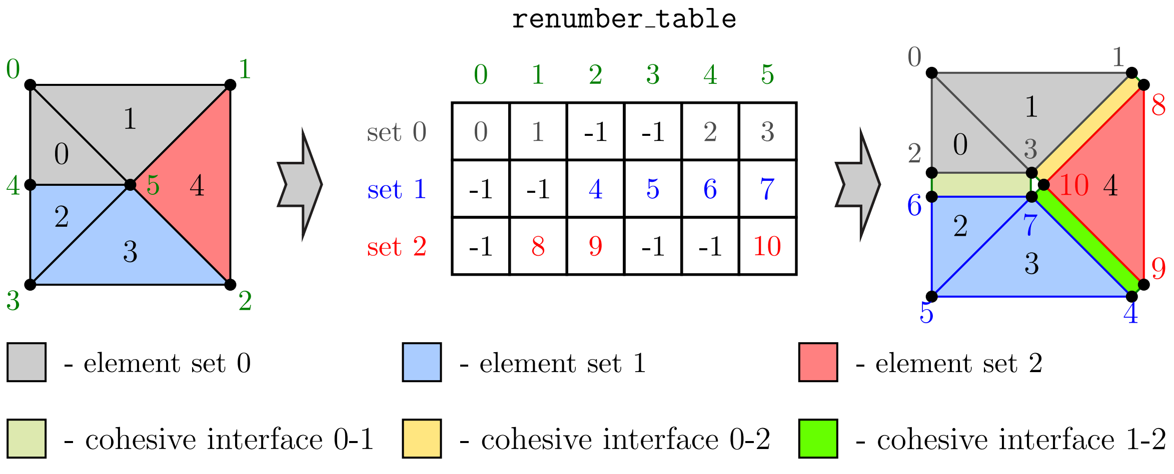

(a) (b) (c)

Figure A.11.: Insertion of cohesive features: (a) initial mesh with 5 elements, 6 nodes and 3 different element sets, (b) generation of the `renumber_table` array and (c) duplicated, renumbered nodes and reconnected elements with cohesive pairs.

inserted between the element face formed by node 0 and 5 as well as the element face formed by node 3 and 5 of the initial mesh. To eliminate these element faces the `unsorted_faces` array is generated by use of the mapping from the element connectivity to the element faces, see Fig. A.12 (a). The first column of `unsorted_faces` represents the element set, the face is connected to. The remaining columns refer to the node ids located at the vertices of the element boundaries (in 2D the boundaries are lines resulting in two node ids per element face). A row-wise sorting of the node ids transforms the `unsorted_faces` into the `sorted_faces`. By applying a row-wise unification that is deleting all multiple occurring rows, element set internal element faces are deleted. The key idea is to include the first column of `sorted_faces` in the unification operation. This prevents the deletion of element faces that later form the cohesive interfaces.

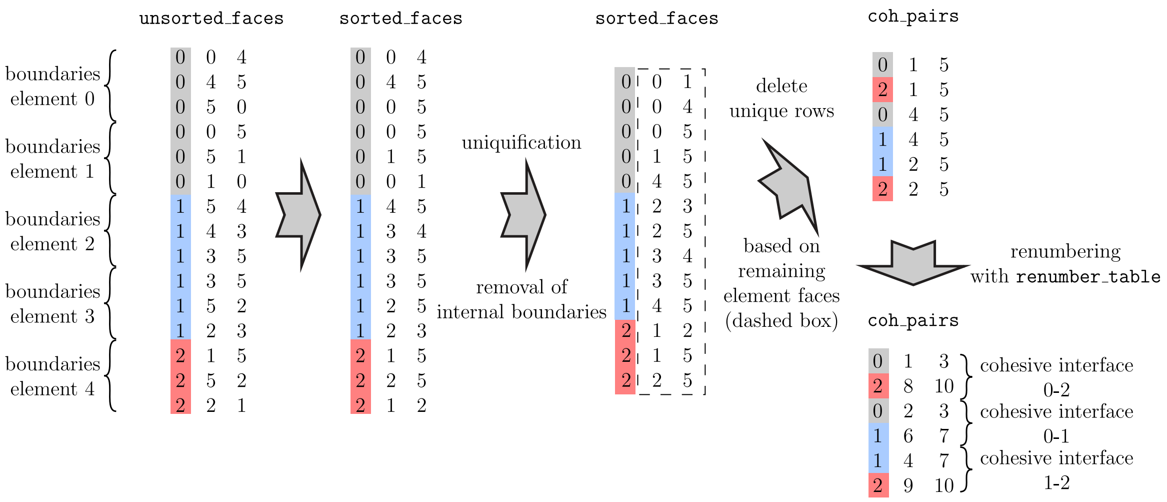

(a) (b)

Figure A.12.: Finding element faces (a) and subsequent generation of cohesive pairs (b).

Fig. A.12 (b) outlines the final procedure of the algorithm, which is the generation of cohesive pairs. Indicated by the dashed box, only the node ids in `sorted_faces` are considered. The set information of the first column are kept but excluded for the subsequent array manipulations. Based on the unique row ids of the dashed box, corresponding rows of `sorted_faces` are removed to form the `coh_pairs` array. This operation eliminates all boundary element faces such that solely element faces connected to cohesive interfaces are kept. A column wise sorting based on the node id containing columns (column 2 and 3) yields a sorted `coh_pairs` array. This sorting entails that cohesive pairs attached to two different set occur successively. This can be seen by the rows that contain identical node ids but different element set ids. Since the element set information is still current, a renumbering of the node ids based on the `renumber_table` array is straightforward. With the information of the cohesive pairs the `coh_interfaces` array is formed. Every element of this array consists of the nodes ids $[c_1^k, c_2^k, c_3^k, c_4^k, \ldots]$ of the cohesive interface k. To refer to the newly generated cohesive interfaces the `ele_sets` array is extended to `new_ele_sets` including the newly generated cohesive interfaces. Fig. A.11 (c) depicts the final result. It is noticeable that the algorithm introduces a hole at the junction point of the material sets (node 5 of the initial mesh). This violation of the mesh's compactness is unavoidable and a side effect of the fact that cohesive features are attached to faces and not vertices.

The presented algorithm is extremely fast and efficient due to the excessive use of array slicing and indexing. Only small loops over all element sets are necessary in the generation of the `renumber_table`. The utilization of sophisticated search functions benefits the overall computational costs.[38] All special test cases are intrinsically considered.

---

[38] In particular the `Python` library `numpy` with its functions `unique,lexsort` and `where` is used in the algorithm.

Bibliography

[1] Abaqus 6.14. Online documentation, 2014.

[2] J. Aboudi, S. M. Arnold, and B. A. Bednarcyk. Micromechanics of Composite Materials. Elsevier, 2013.

[3] S. Agarwal, R. A. Srivatsan, and S. Bandyopadhyay. Analytical Determination of the Proximity of Two Right-Circular Cylinders in Space. Journal of Mechanisms and Robotics, 8(4):041010, 2016.

[4] B. J. Alder and T. E. Wainwright. Studies in Molecular Dynamics. II. Behavior of a Small Number of Elastic Spheres. The Journal of Chemical Physics, 33(5): 1439–1451, 1960.

[5] H. A. Almohamad and S. Z. Selim. An algorithm for computing the distance between two circular disks. Applied Mathematical Modelling, 27(2):115–124, 2003.

[6] E. M. Arruda and M. C. Boyce. A three-dimensional constitutive model for the large stretch behavior of rubber elastic materials. Journal of the Mechanics and Physics of Solids, 41(2):389–412, 1993.

[7] M. F. Ashby and D. R. H. Jones. Engineering Materials 1. Elsevier Science, 2011.

[8] M. F. Ashby, S. F. Bush, N. Swindells, R. Bullough, G. Ellison, Y. Lindblom, R. W. Cahn, and J. F. Barnes. Technology of the 1990s: Advanced Materials and Predictive Design [and Discussion]. Philosophical Transactions of the Royal Society A: Mathematical, Physical and Engineering Sciences, 322(1567):393–407, 1987.

[9] M. F. Ashby, H. Shercliff, and D. Cebon. Materials. Elsevier LTD, Oxford, 2013.

[10] F. Aurenhammer. Voronoi diagrams—a survey of a fundamental geometric data structure. ACM Computing Surveys, 23(3):345–405, 1991.

[11] M. Bailakanavar, Y. Liu, J. Fish, and Y. Zheng. Automated modeling of random inclusion composites. Engineering with Computers, 30(4):609–625, 2014.

[12] T. J. Baker. Mesh generation: Art or science? Progress in Aerospace Sciences, 41(1):29–63, 2005.

[13] C. B. Barber, D. P. Dobkin, and H. Huhdanpaa. The quickhull algorithm for convex hulls. ACM Transactions on Mathematical Software, 22(4):469–483, 1996.

[14] S. Bargmann, B. Klusemann, J. Markmann, J. E. Schnabel, K. Schneider, C. Soyarslan, and J. Wilmers. Generation of 3D representative volume elements for heterogeneous materials: A review. Progress in Materials Science, 96:322–384, 2018.

[15] F. Barthelat, Z. Yin, and M. J. Buehler. Structure and mechanics of interfaces in biological materials. Nature Reviews Materials, 1(4), 2016.

[16] T. Belytschko, W. K. Liu, B. Moran, and K. Elkhodary. Nonlinear finite elements for continua and structures. John Wiley & Sons, 2013.

[17] A. Benabbou, H. Borouchaki, P. Laug, and J. Lu. Geometrical modeling of granular structures in two and three dimensions. Application to nanostructures. International Journal for Numerical Methods in Engineering, 80(4):425–454, 2009.

[18] S. E. Benzley, E. Perry, K. Merkley, B. Clark, and G. Sjaardama. A comparison of all hexagonal and all tetrahedral finite element meshes for elastic and elasto-plastic analysis. In Proceedings, 4th international meshing roundtable, volume 17, pages 179–191. Sandia National Laboratories Albuquerque, NM, 1995.

[19] H. Berger, S. Kari, U. Gabbert, R. R. Ramos, J. B. Castillero, and R. G. Díaz. Evaluation of effective material properties of randomly distributed short cylindrical fiber composites using a numerical homogenization technique. Journal of Mechanics of Materials and Structures, 2(8):1561–1570, 2007.

[20] L. F. A. Bernardo, A. P. B. M. Amaro, D. G. Pinto, and S. M. R. Lopes. Modeling and simulation techniques for polymer nanoparticle composites - A review. Computational Materials Science, 118:32–46, 2016.

[21] J. G. Berryman. Random close packing of hard spheres and disks. Physical Review A, 27(2):1053–1061, 1983.

[22] J. Besson. Continuum Models of Ductile Fracture: A Review. International Journal of Damage Mechanics, 19(1):3–52, 2009.

[23] D. Biermann, R. Joliet, and T. Michelitsch. Fast distance computation between cylinders for the design of mold temperature control systems. Technical report, Technical University of Dortmund, 2008.

[24] J. Bocko and P. Lengvarský. Application of Finite Element Method for Analysis of Nanostructures. Acta Mechanica et Automatica, 11(2):116–120, 2017.

[25] F. Bouville, E. Maire, S. Meille, B. V. de Moortèle, A. J. Stevenson, and S. Deville. Strong, tough and stiff bioinspired ceramics from brittle constituents. Nature Materials, 13(5):508–514, 2014.

[26] M. C. Boyce and E. M. Arruda. Constitutive Models of Rubber Elasticity: A Review. Rubber Chemistry and Technology, 73(3):504–523, 2000.

[27] L. Brassart, I. Doghri, and L. Delannay. Homogenization of elasto-plastic composites coupled with a nonlinear finite element analysis of the equivalent inclusion problem. International Journal of Solids and Structures, 47(5):716–729, 2010.

[28] H. Böhm. A short introduction to continuum micromechanics. Technical report, Vienna University of Technology, 2018.

[29] H. J. Böhm and W. Han. Comparisons between three-dimensional and two-dimensional multi-particle unit cell models for particle reinforced metal matrix composites. Modelling and Simulation in Materials Science and Engineering, 9(2):47–65, 2001.

[30] H. J. Böhm, A. Eckschlager, and W. Han. Multi-inclusion unit cell models for metal matrix composites with randomly oriented discontinuous reinforcements. Computational Materials Science, 25(1-2):42–53, 2002.

[31] F. C. Campbell. Structural Composite Materials. ASM International, 2010.

[32] J. Carl, D. Müller-Hoeppe, and M. Meadows. Comparison of tetrahedral and brick elements for linear elastic analysis. University of Colorado Boulder, Boulder, USA, 2006.

[33] G. Catalanotti. On the generation of RVE-based models of composites reinforced with long fibres or spherical particles. COMPOSITE STRUCTURES, 138:84–95, 2016.

[34] N. Chawla, R. S. Sidhu, and V. V. Ganesh. Three-dimensional visualization and microstructure-based modeling of deformation in particle-reinforced composites. ACTA MATERIALIA, 54(6):1541–1548, 2006.

[35] X.-D. Chen, J.-H. Yong, G.-Q. Zheng, J.-C. Paul, and J.-G. Sun. Computing minimum distance between two implicit algebraic surfaces. COMPUTER-AIDED DESIGN, 38(10): 1053–1061, 2006.

[36] X. Cheng, S. C. Tjong, and R. K. Y. Li. Synthesis and optical properties of cadmium sulfide/polymer nanocomposite particles. In PHYSICAL PROPERTIES AND APPLICATIONS OF POLYMER NANOCOMPOSITES, pages 3–30. Elsevier, 2010.

[37] R. G. Chittawadigi and S. K. Saha. An analytical method to detect collision between cylinders using dual number algebra. In 2013 IEEE/RSJ INTERNATIONAL CONFERENCE ON INTELLIGENT ROBOTS AND SYSTEMS. IEEE, 2013.

[38] J. Cho, M. S. Joshi, and C. T. Sun. Effect of inclusion size on mechanical properties of polymeric composites with micro and nano particles. COMPOSITES SCIENCE AND TECHNOLOGY, 66(13):1941–1952, 2006.

[39] D. D. L. Chung. CARBON FIBER COMPOSITES. ELSEVIER, 1994.

[40] J. H. Conway and N. J. A. Sloane. SPHERE PACKINGS, LATTICES AND GROUPS. Springer, 1999.

[41] D. W. Cooper. Random-sequential-packing simulations in three dimensions for spheres. PHYSICAL REVIEW A, 38(1):522–524, 1988.

[42] P. A. Cundall and O. D. L. Strack. A discrete numerical model for granular assemblies. GÉOTECHNIQUE, 29(1):47–65, 1979.

[43] F. de Francqueville, P. Gilormini, and J. Diani. Representative volume elements for the simulation of isotropic composites highly filled with monosized spheres. INTERNATIONAL JOURNAL OF SOLIDS AND STRUCTURES, 2018.

[44] E. A. de Souza Neto, D. Peri, and D. R. J. Owen. COMPUTATIONAL METHODS FOR PLASTICITY. John Wiley & Sons, 2008.

[45] J. Dirrenberger, S. Forest, and D. Jeulin. Towards gigantic RVE sizes for 3D stochastic fibrous networks. INTERNATIONAL JOURNAL OF SOLIDS AND STRUCTURES, 51(2): 359–376, 2014.

[46] A. Donev, S. Torquato, F. H. Stillinger, and R. Connelly. Jamming in hard sphere and disk packings. JOURNAL OF APPLIED PHYSICS, 95(3):989–999, 2004.

[47] A. Dreyer, A. Feld, A. Kornowski, E. D. Yilmaz, H. Noei, A. Meyer, T. Krekeler, C. Jiao, A. Stierle, V. Abetz, H. Weller, and G. A. Schneider. Organically linked iron oxide nanoparticle supercrystals with exceptional isotropic mechanical properties. NATURE MATERIALS, 15(5):522–528, 2016.

[48] W. J. Drugan and J. R. Willis. A micromechanics-based nonlocal constitutive equation and estimates of representative volume element size for elastic composites. JOURNAL OF THE MECHANICS AND PHYSICS OF SOLIDS, 44(4):497–524, 1996.

[49] Q. Du, V. Faber, and M. Gunzburger. Centroidal Voronoi Tessellations: Applications and Algorithms. SIAM REVIEW, 41(4):637–676, 1999.

[50] P. Eaton and P. West. ATOMIC FORCE MICROSCOPY. Oxford University Press, 2010.

[51] D. Eberly. Intersection of ellipsoids. Technical report, Magic Software, 2017.

[52] D. Eberly. Distance between two line segments in 3D. GEOMETRIC TOOLS, INC, 2018.

[53] D. H. Eberly. 3D GAME ENGINE DESIGN. Taylor & Francis Ltd., 2006.

[54] A. E. Efimov, A. G. Tonevitsky, M. Dittrich, and N. B. Matsko. Atomic force microscope (AFM) combined with the ultramicrotome: a novel device for the serial section tomography and AFM/TEM complementary structural analysis of biological and polymer samples. JOURNAL OF MICROSCOPY, 226(3):207–216, 2007.

[55] M. J. Emerson, K. M. Jespersen, A. B. Dahl, K. Conradsen, and L. P. Mikkelsen. Individual fibre segmentation from 3D X-ray computed tomography for characterising the fibre orientation in unidirectional composite materials. COMPOSITES PART A: APPLIED SCIENCE AND MANUFACTURING, 97:83–92, 2017.

[56] K. E. Evans and A. G. Gibson. Prediction of the maximum packing fraction achievable in randomly oriented short-fibre composites. COMPOSITES SCIENCE AND TECHNOLOGY, 25(2):149–162, 1986.

[57] P. Evesque. Fluctuations, Correlation and Representative Elementary Volume (REV) in Granular Materials. 2000.

[58] J. Feder. Random sequential adsorption. JOURNAL OF THEORETICAL BIOLOGY, 87 (2):237–254, 1980.

[59] Y. T. Feng, K. Han, and D. R. J. Owen. Filling domains with disks: an advancing front approach. INTERNATIONAL JOURNAL FOR NUMERICAL METHODS IN ENGINEERING, 56(5):699–713, 2003.

[60] L. J. Fetters, D. J. Lohse, and R. H. Colby. Chain Dimensions and Entanglement Spacings. In PHYSICAL PROPERTIES OF POLYMERS HANDBOOK, pages 447–454. Springer New York, 2007.

[61] F. Feyel. A multilevel finite element method (FE2) to describe the response of highly non-linear structures using generalized continua. COMPUTER METHODS IN APPLIED MECHANICS AND ENGINEERING, 192(28-30):3233–3244, 2003.

[62] J. Fish. PRACTICAL MULTISCALING. John Wiley & Sons, 2013.

[63] P. J. Frey and P.-L. George. MESH GENERATION. John Wiley & Sons, 2008.

[64] F. Fritzen. MICROSTRUCTURAL MODELING AND COMPUTATIONAL HOMOGENIZATION OF THE PHYSICALLY LINEAR AND NONLINEAR CONSTITUTIVE BEHAVIOR OF MICRO-HETEROGENEOUS MATERIALS. PhD thesis, Karlsruher Institut für Technologie, 2011.

[65] F. Fritzen and T. Böhlke. Periodic three-dimensional mesh generation for particle reinforced composites with application to metal matrix composites. INTERNATIONAL JOURNAL OF SOLIDS AND STRUCTURES, 48(5):706–718, 2011.

[66] F. Fritzen, T. Böhlke, and E. Schnack. Periodic three-dimensional mesh generation for crystalline aggregates based on Voronoi tessellations. COMPUTATIONAL MECHANICS, 43(5):701–713, 2009.

[67] G. Gaiselmann, D. Froning, C. Tötzke, C. Quick, I. Manke, W. Lehnert, and V. Schmidt. Stochastic 3D modeling of non-woven materials with wet-proofing agent. INTERNATIONAL JOURNAL OF HYDROGEN ENERGY, 38(20):8448–8460, 2013.

[68] G. Gaiselmann, C. Tötzke, I. Manke, W. Lehnert, and V. Schmidt. 3D microstructure modeling of compressed fiber-based materials. JOURNAL OF POWER SOURCES, 257: 52–64, 2014.

[69] M. Galli, J. Botsis, and J. Janczak-Rusch. An elastoplastic three-dimensional homogenization model for particle reinforced composites. COMPUTATIONAL MATERIALS SCIENCE, 41(3):312–321, 2008.

[70] U. Galvanetto and M. H. F. Aliabadi. MULTISCALE MODELING IN SOLID MECHANICS. Imperial Collega Press, 2009.

[71] H. Gao, B. Ji, I. L. Jager, E. Arzt, and P. Fratzl. Materials become insensitive to flaws at nanoscale: Lessons from nature. PROCEEDINGS OF THE NATIONAL ACADEMY OF SCIENCES, 100(10):5597–5600, 2003.

[72] D. Gay, S. V. Hoa, and S. W. Tsai. COMPOSITE MATERIALS: DESIGN AND APPLICATIONS, SECOND EDITION. CRC Press, 2007.

[73] M. G. D. Geers, V. G. Kouznetsova, and W. A. M. Brekelmans. Multi-scale computational homogenization: Trends and challenges. JOURNAL OF COMPUTATIONAL AND APPLIED MATHEMATICS, 234(7):2175–2182, 2010.

[74] P. Georgopanos, G. A. Schneider, A. Dreyer, U. A. Handge, V. Filiz, A. Feld, E. D. Yilmaz, T. Krekeler, M. Ritter, H. Weller, and V. Abetz. Exceptionally strong, stiff and hard hybrid material based on an elastomer and isotropically shaped ceramic nanoparticles. SCIENTIFIC REPORTS, 7(1), 2017.

[75] S. Ghosh, K. Lee, and S. Moorthy. Two scale analysis of heterogeneous elastic-plastic materials with asymptotic homogenization and Voronoi cell finite element model. COMPUTER METHODS IN APPLIED MECHANICS AND ENGINEERING, 132(1-2):63–116, 1996.

[76] E. Ghossein and M. Lévesque. A fully automated numerical tool for a comprehensive validation of homogenization models and its application to spherical particles reinforced composites. INTERNATIONAL JOURNAL OF SOLIDS AND STRUCTURES, 49(11-12):1387–1398, 2012.

[77] E. Ghossein and M. Lévesque. Random generation of periodic hard ellipsoids based on molecular dynamics: A computationally-efficient algorithm. JOURNAL OF COMPUTATIONAL PHYSICS, 253:471–490, 2013.

[78] R. F. Gibson. A review of recent research on mechanics of multifunctional composite materials and structures. COMPOSITE STRUCTURES, 92(12):2793–2810, 2010.

[79] I. M. Gitman, H. Askes, and L. J. Sluys. Representative volume: Existence and size determination. ENGINEERING FRACTURE MECHANICS, 74(16):2518–2534, 2007.

[80] R. Gluege. Generalized boundary conditions on representative volume elements and their use in determining the effective material properties. COMPUTATIONAL MATERIALS SCIENCE, 79:408–416, 2013.

[81] R. Gluege and M. Weber. Numerical properties of spherical and cubical representative volume elements with different boundary conditions. TECHNISCHE MECHANIK, 33(2): 97–103, 2013.

[82] R. Gluege, M. Weber, and A. Bertram. Comparison of spherical and cubical statistical volume elements with respect to convergence, anisotropy, and localization behavior. COMPUTATIONAL MATERIALS SCIENCE, 63:91–104, 2012.

[83] R. Glüge. BEITRÄGE ZUR ANALYTISCHEN UND NUMERISCHEN HOMOGENISIERUNG IN DER MATERIALMODELLIERUNG. PhD thesis, Otto-von-Guericke-Universität Magdeburg, 2016.

[84] R. Greve. KONTINUUMSMECHANIK. Springer, 2003.

[85] D. Gross and T. Seelig. FRACTURE MECHANICS. Springer International Publishing, 2018.

[86] K.-H. Grote and J. Feldhusen, editors. DUBBEL. Springer Berlin Heidelberg, 2014.

[87] A. A. Gusev. Representative volume element size for elastic composites: A numerical study. JOURNAL OF THE MECHANICS AND PHYSICS OF SOLIDS, 45(9):1449–1459, 1997.

[88] A. A. Gusev, P. J. Hine, and I. M. Ward. Fiber packing and elastic properties of a transversely random unidirectional glass/epoxy composite. COMPOSITES SCIENCE AND TECHNOLOGY, 60(4):535–541, 2000.

[89] T. Hales. A proof of the Kepler conjecture. ANNALS OF MATHEMATICS, 162(3):1065–1185, 2005.

[90] K. Han, Y. T. Feng, and D. R. J. Owen. Sphere packing with a geometric based compression algorithm. POWDER TECHNOLOGY, 155(1):33–41, 2005.

[91] L. T. Harper, C. C. Qian, R. Luchoo, and N. A. Warrior. 3D geometric modelling of discontinuous fibre composites using a force-directed algorithm. JOURNAL OF COMPOSITE MATERIALS, 51(17):2389–2406, 2016.

[92] Z. Hashin. Analysis of Composite Materials - A Survey. JOURNAL OF APPLIED MECHANICS, 50(3):481, 1983.

[93] W. M. Haynes, editor. CRC HANDBOOK OF CHEMISTRY AND PHYSICS. Taylor & Francis, 2016.

[94] S. Hazanov and C. Huet. Order relationships for boundary conditions effect in heterogeneous bodies smaller than the representative volume. JOURNAL OF THE MECHANICS AND PHYSICS OF SOLIDS, 42(12):1995–2011, 1994.

[95] D. He, N. N. Ekere, and L. Cai. Computer simulation of random packing of unequal particles. PHYSICAL REVIEW E, 60(6):7098–7104, 1999.

[96] W. Heckel, T. Würger, S. Müller, and G. Feldbauer. Van der Waals Interaction Really Matters: Energetics of Benzoic Acid on TiO2 Rutile Surfaces. THE JOURNAL OF PHYSICAL CHEMISTRY C, 121(32):17207–17214, 2017.

[97] C. T. Herakovich. Mechanics of composites: A historical review. MECHANICS RESEARCH COMMUNICATIONS, 41:1–20, 2012.

[98] R. Hill. Elastic properties of reinforced solids: Some theoretical principles. JOURNAL OF THE MECHANICS AND PHYSICS OF SOLIDS, 11(5):357–372, 1963.

[99] R. Hill. On constitutive inequalities for simple materials-I. JOURNAL OF THE MECHANICS AND PHYSICS OF SOLIDS, 16(4):229–242, 1968.

[100] E. L. Hinrichsen, J. Feder, and T. Jøssang. Geometry of random sequential adsorption. JOURNAL OF STATISTICAL PHYSICS, 44(5-6):793–827, 1986.

[101] K. Hitti, P. Laure, T. Coupez, L. Silva, and M. Bernacki. Precise generation of complex statistical Representative Volume Elements (RVEs) in a finite element context. COMPUTATIONAL MATERIALS SCIENCE, 61:224–238, 2012.

[102] K. Ho-Le. Finite element mesh generation methods: a review and classification. COMPUTER-AIDED DESIGN, 20(1):27–38, 1988.

[103] G. A. Holzapfel. NONLINEAR SOLID MECHANICS. John Wiley & Sons, 2000.

[104] M. Hori and S. Nemat-Nasser. On two micromechanics theories for determining micro–macro relations in heterogeneous solids. MECHANICS OF MATERIALS, 31(10):667–682, 1999.

[105] M. F. Horstemeyer. Multiscale Modeling: A Review. In PRACTICAL ASPECTS OF COMPUTATIONAL CHEMISTRY, pages 87–135. Springer Netherlands, 2009.

[106] H. Hu, L. Onyebueke, and A. Abatan. Characterizing and Modeling Mechanical Properties of Nanocomposites-Review and Evaluation. JOURNAL OF MINERALS AND MATERIALS CHARACTERIZATION AND ENGINEERING, 09(04):275–319, 2010.

[107] M. Huang and Y.-m. Li. X-ray tomography image-based reconstruction of microstructural finite element mesh models for heterogeneous materials. COMPUTATIONAL MATERIALS SCIENCE, 67:63–72, 2013.

[108] C. Huet. Application of variational concepts to size effects in elastic heterogeneous bodies. JOURNAL OF THE MECHANICS AND PHYSICS OF SOLIDS, 38(6):813–841, 1990.

[109] H. Imai, M. Iri, and K. Murota. Voronoi Diagram in the Laguerre Geometry and Its Applications. SIAM JOURNAL ON COMPUTING, 14(1):93–105, 1985.

[110] M. Islam, G. J. Tudryn, and C. R. Picu. Microstructure modeling of random composites with cylindrical inclusions having high volume fraction and broad aspect ratio distribution. COMPUTATIONAL MATERIALS SCIENCE, 125:309–318, 2016.

[111] H. M. Jaeger and S. R. Nagel. Physics of the Granular State. SCIENCE, 255(5051): 1523–1531, 1992.

[112] A. Javili, S. Saeb, and P. Steinmann. Aspects of implementing constant traction boundary conditions in computational homogenization via semi-Dirichlet boundary conditions. COMPUTATIONAL MECHANICS, 59(1):21–35, 2016.

[113] N. Jendrysik, K. Schneider, and S. Bargmann. Automatic generation and discretization of fully periodic representative volume elements of plain woven composites. JOURNAL OF COMPOSITE MATERIALS, 52(29):4061–4073, 2018.

[114] Y. B. Jia. Roots of Polynomials. Com S 477/577 Notes, 2016.

[115] B. D. Jones and J. R. Williams. Fast computation of accurate sphere-cube intersection volume. ENGINEERING COMPUTATIONS, 34(4):1204–1216, 2017.

[116] E. Jones, T. Oliphant, and P. Peterson. {SciPy}: open source scientific tools for {Python}, 2014.

[117] R. Jullien and P. Meakin. Random sequential adsorption with restructuring in two dimensions. JOURNAL OF PHYSICS A: MATHEMATICAL AND GENERAL, 25(4):L189–L194, 1992.

[118] J. M. Jung, J. H. Yoo, H. J. Jeong, S. Lee, and H. S. Kim. Three-Dimensional Characterization of SiC Particle-Reinforced Al Composites Using Serial Sectioning Tomography and Thermo-mechanical Finite Element Simulation. METALLURGICAL AND MATERIALS TRANSACTIONS A, 45(12):5679–5690, 2014.

[119] W. Kahan. How futile are mindless assessments of roundoff in floating-point computation? RETRIEVED OCTOBER, 13:2017, 2006.

[120] T. Kanit, S. Forest, I. Galliet, V. Mounoury, and D. Jeulin. Determination of the size of the representative volume element for random composites: statistical and numerical approach. INTERNATIONAL JOURNAL OF SOLIDS AND STRUCTURES, 40(13-14):3647–3679, 2003.

[121] S. Kari, H. Berger, and U. Gabbert. Numerical evaluation of effective material properties of randomly distributed short cylindrical fibre composites. COMPUTATIONAL MATERIALS SCIENCE, 39(1):198–204, 2007.

[122] S. Kari, H. Berger, R. Rodriguez-Ramos, and U. Gabbert. Computational evaluation of effective material properties of composites reinforced by randomly distributed spherical particles. COMPOSITE STRUCTURES, 77(2):223–231, 2007.

[123] G. A. Kassem. MICROMECHANICAL MATERIAL MODELS FOR POLYMER COMPOSITES THROUGH ADVANCED NUMERICAL SIMULATION TECHNIQUES. PhD thesis, RWTH Aachen University, 2009.

[124] J. S. Ketchel and P. M. Larochelle. Line Based Collision Detection of Cylindrical Rigid Bodies. In VOLUME 2: 28TH BIENNIAL MECHANISMS AND ROBOTICS CONFERENCE, PARTS A AND B. ASME, 2004.

[125] J. S. Ketchel and P. M. Larochelle. Collision Detection of Cylindrical Rigid Bodies Using Line Geometry. In VOLUME 7: 29TH MECHANISMS AND ROBOTICS CONFERENCE, PARTS A AND B. ASME, 2005.

[126] Z. F. Khisaeva and M. Ostoja-Starzewski. On the Size of RVE in Finite Elasticity of Random Composites. JOURNAL OF ELASTICITY, 85(2):153–173, 2006.

[127] B. Klusemann and B. Svendsen. Homogenization methods for multi-phase elastic composites: Comparisons and benchmarks. TECHNISCHE MECHANIK, 30(4):374–386, 2010.

[128] M. Kodam, R. Bharadwaj, J. Curtis, B. Hancock, and C. Wassgren. Cylindrical object contact detection for use in discrete element method simulations. Part I - Contact detection algorithms. CHEMICAL ENGINEERING SCIENCE, 65(22):5852–5862, 2010.

[129] B. Koohbor, S. Ravindran, and A. Kidane. Experimental determination of Representative Volume Element (RVE) size in woven composites. OPTICS AND LASERS IN ENGINEERING, 90:59–71, 2017.

[130] V. Kouznetsova, W. A. M. Brekelmans, and F. P. T. Baaijens. An approach to micro-macro modeling of heterogeneous materials. COMPUTATIONAL MECHANICS, 27(1):37–48, 2001.

[131] V. G. Kouznetsova, M. G. D. Geers, and W. A. M. Brekelmans. Multi-scale second-order computational homogenization of multi-phase materials: a nested finite element solution strategy. COMPUTER METHODS IN APPLIED MECHANICS AND ENGINEERING, 193(48-51):5525–5550, 2004.

[132] V. G. Kouznetsova, M. G. D. Geers, and W. A. M. Brekelmans. COMPUTATIONAL HOMOGENISATION FOR NON-LINEAR HETEROGENEOUS SOLIDS. In COMPUTATIONAL AND EXPERIMENTAL METHODS IN STRUCTURES, pages 1–42. Imperial College Press, 2009.

[133] M. Krause, J. M. Hausherr, B. Burgeth, C. Herrmann, and W. Krenkel. Determination of the fibre orientation in composites using the structure tensor and local X-ray transform. JOURNAL OF MATERIALS SCIENCE, 45(4):888–896, 2010.

[134] M. Kroon. A constitutive model for strain-crystallising Rubber-like materials. MECHANICS OF MATERIALS, 42(9):873–885, 2010.

[135] W. Kuhn and F. Grün. Beziehungen zwischen elastischen Konstanten und Dehnungsdoppelbrechung hochelastischer Stoffe. KOLLOID-ZEITSCHRIFT, 101(3):248–271, 1942.

[136] G. J. Lake and A. G. Thomas. The strength of highly elastic materials. PROCEEDINGS OF THE ROYAL SOCIETY OF LONDON. SERIES A. MATHEMATICAL AND PHYSICAL SCIENCES, 300(1460):108–119, 1967.

[137] F. Larsson, K. Runesson, S. Saroukhani, and R. Vafadari. Computational homogenization based on a weak format of micro-periodicity for RVE-problems. COMPUTER METHODS IN APPLIED MECHANICS AND ENGINEERING, 200(1-4):11–26, 2011.

[138] M. D. Lechner, K. Gehrke, and E. H. Nordmeier. MAKROMOLEKULARE CHEMIE. Springer, 2014.

[139] C. Lennerz and E. Schomer. Efficient distance computation for quadratic curves and surfaces. In GEOMETRIC MODELING AND PROCESSING. THEORY AND APPLICATIONS. GMP 2002. IEEE Comput. Soc, 2002.

[140] Y. Li and S. Ji. A geometric algorithm based on the advancing front approach for sequential sphere packing. GRANULAR MATTER, 20(4), 2018.

[141] B. Liang, A. Nagarajan, and S. Soghrati. Scalable parallel implementation of CISAMR: a non-iterative mesh generation algorithm. COMPUTATIONAL MECHANICS, 64(1):173–195, 2018.

[142] F. Liaqat, M. N. Tahir, E. Schechtel, M. Kappl, G. K. Auernhammer, K. Char, R. Zentel, H.-J. Butt, and W. Tremel. High-Performance TiO2Nanoparticle/DOPA-Polymer Composites. MACROMOLECULAR RAPID COMMUNICATIONS, 36(11):1129–1137, 2015.

[143] A. Lin and S.-P. Han. On the Distance between Two Ellipsoids. SIAM JOURNAL ON OPTIMIZATION, 13(1):298–308, 2002.

[144] C. Liu. On the minimum size of representative volume element: An experimental investigation. EXPERIMENTAL MECHANICS, 45(3):238–243, 2005.

[145] J. LLorca, C. Gonzalez, J. M. Molina-Aldareguia, J. Segurado, R. Seltzer, F. Sket, M. Rodriguez, S. Sádaba, R. Munoz, and L. P. Canal. Multiscale Modeling of Composite Materials: a Roadmap Towards Virtual Testing. ADVANCED MATERIALS, 23(44):5130–5147, 2011.

[146] D. S. H. Lo. FINITE ELEMENT MESH GENERATION. CRC Press, 2015.

[147] B. S. Lombardo, H. Keskkula, and D. R. Paul. Influence of ABS type on morphology and mechanical properties of PC/ABS blends. JOURNAL OF APPLIED POLYMER SCIENCE, 54(11):1697–1720, 1994.

[148] B. D. Lubachevsky and F. H. Stillinger. Geometric properties of random disk packings. JOURNAL OF STATISTICAL PHYSICS, 60(5-6):561–583, 1990.

[149] V. J. Lumelsky. On fast computation of distance between line segments. INFORMATION PROCESSING LETTERS, 21(2):55–61, 1985.

[150] S. Ma, I. Scheider, and S. Bargmann. Continuum damage modeling and simulation of hierarchical dental enamel. MODELLING AND SIMULATION IN MATERIALS SCIENCE AND ENGINEERING, 24(4):045014, 2016.

[151] S. Ma, I. Scheider, and S. Bargmann. Ultrastrong nanocomposites with interphases: Nonlocal deformation and damage behavior. EUROPEAN JOURNAL OF MECHANICS - A/SOLIDS, 75:93–108, 2019.

[152] A. Madra, P. Breitkopf, A. Rassineux, and F. Trochu. Image-based model reconstruction and meshing of woven reinforcements in composites. INTERNATIONAL JOURNAL FOR NUMERICAL METHODS IN ENGINEERING, 112(9):1235–1252, 2017.

[153] F. Maggi, S. Stafford, T. L. Jackson, and J. Buckmaster. Nature of packs used in propellant modeling. PHYSICAL REVIEW E, 77(4), 2008.

[154] E. Maire, J. Y. Buffière, L. Salvo, J. J. Blandin, W. Ludwig, and J. M. Létang. On the Application of X-ray Microtomography in the Field of Materials Science. ADVANCED ENGINEERING MATERIALS, 3(8):539, 2001.

[155] Y. Mao, B. Talamini, and L. Anand. Rupture of polymers by chain scission. EXTREME MECHANICS LETTERS, 13:17–24, 2017.

[156] L. I. Mao-hua, Y. A. N. G. Yan-qing, B. HUANG, L. U. O. Xian, W. ZHANG, H. A. N. Ming, and R. U. Ji-gang. Development of advanced electron tomography in materials science based on TEM and STEM. TRANSACTIONS OF NONFERROUS METALS SOCIETY OF CHINA, 24(10):3031–3050, 2014.

[157] J. F. Marko and E. D. Siggia. Stretching DNA. MACROMOLECULES, 28(26):8759–8770, 1995.

[158] P. K. Mehta and P. J. M. Monteiro. CONCRETE: MICROSTRUCTURE, PROPERTIES, AND MATERIALS. McGraw-Hill Education Ltd, 2013.

[159] G. H. Michler. KUNSTSTOFF-MIKROMECHANIK: MORPHOLOGIE, DEFORMATIONS- UND BRUCHMECHANISMEN. C. Hanser, 1992.

[160] C. Miehe. Strain-driven homogenization of inelastic microstructures and composites based on an incremental variational formulation. INTERNATIONAL JOURNAL FOR NUMERICAL METHODS IN ENGINEERING, 55(11):1285–1322, 2002.

[161] L. A. Mihai and A. Goriely. How to characterize a nonlinear elastic material? A review on nonlinear constitutive parameters in isotropic finite elasticity. PROCEEDINGS OF THE ROYAL SOCIETY A: MATHEMATICAL, PHYSICAL AND ENGINEERING SCIENCE, 473(2207), 2017.

[162] J. Mościński, M. Bargieł, Z. A. Rycerz, and P. W. M. Jacobs. The Force-Biased Algorithm for the Irregular Close Packing of Equal Hard Spheres. MOLECULAR SIMULATION, 3(4):201–212, 1989.

[163] F. Naddeo, N. Cappetti, and A. Naddeo. Automatic versatile parametric procedure for a complete FEM structural analysis of composites having cylinder-shaped reinforcing fibres. COMPUTATIONAL MATERIALS SCIENCE, 81:239–245, 2014.

[164] M. Nardin, E. Papirer, and J. Schultz. Contribution a l'etude des empilements au hasard de fibres et/ou de particules spheriques. Powder Technology, 44(2):131–140, 1985.

[165] V. Nguyen, M. Stroeven, and L. J. Sluys. MULTISCALE CONTINUOUS AND DISCONTINUOUS MODELING OF HETEROGENEOUS MATERIALS: A REVIEW ON RECENT DEVELOPMENTS. Journal of Multiscale Modelling, 03(04):229–270, 2011.

[166] V.-D. Nguyen, E. Béchet, C. Geuzaine, and L. Noels. Imposing periodic boundary condition on arbitrary meshes by polynomial interpolation. Computational Materials Science, 55:390–406, 2012.

[167] V. P. Nguyen. An open source program to generate zero-thickness cohesive interface elements. Advances in Engineering Software, 74:27–39, 2014.

[168] R. W. Ogden, G. Saccomandi, and I. Sgura. On worm-like chain models within the three-dimensional continuum mechanics framework. Proceedings of the Royal Society A: Mathematical, Physical and Engineering Sciences, 462(2067): 749–768, 2005.

[169] A. Okabe, B. Boots, K. Sugihara, and S. N. Chiu. Spatial Tessellations. Wiley John + Sons, 2000.

[170] S. Oller. Numerical Simulation of Mechanical Behavior of Composite Materials. Springer, 2014.

[171] M. Ostoja-Starzewski. Material spatial randomness: From statistical to representative volume element. Probabilistic Engineering Mechanics, 21(2):112–132, 2006.

[172] F. Otero, S. Oller, and X. Martinez. Multiscale Computational Homogenization: Review and Proposal of a New Enhanced-First-Order Method. Archives of Computational Methods in Engineering, 25(2):479–505, 2016.

[173] Y. Pan, L. Iorga, and A. A. Pelegri. Numerical generation of a random chopped fiber composite RVE and its elastic properties. Composites Science and Technology, 68(13):2792–2798, 2008.

[174] Y. Pan, L. Iorga, and A. A. Pelegri. Analysis of 3D random chopped fiber reinforced composites using FEM and random sequential adsorption. Computational Materials Science, 43(3):450–461, 2008.

[175] L. C. Pardini and L. G. B. Manhani. Influence of the Testing Gage Length on the Strength, Youngs Modulus and Weibull Modulus of Carbon Fibres and Glass Fibres. Materials Research, 5(4):411–420, 2002.

[176] J. G. Parkhouse and A. Kelly. The Random Packing of Fibres in Three Dimensions. Proceedings of the Royal Society A: Mathematical, Physical and Engineering Sciences, 451(1943):737–746, 1995.

[177] M. V. Pathan, V. L. Tagarielli, S. Patsias, and P. M. Baiz-Villafranca. A new algorithm to generate representative volume elements of composites with cylindrical or spherical fillers. Composites Part B: Engineering, 110:267–278, 2017.

[178] C. Pelissou, J. Baccou, Y. Monerie, and F. Perales. Determination of the size of the representative volume element for random quasi-brittle composites. International Journal of Solids and Structures, 46(14-15):2842–2855, 2009.

[179] D. Perić, E. A. de Souza Neto, R. A. Feijóo, M. Partovi, and A. J. C. Molina. On micro-to-macro transitions for multi-scale analysis of non-linear heterogeneous materials: unified variational basis and finite element implementation. INTERNATIONAL JOURNAL FOR NUMERICAL METHODS IN ENGINEERING, 87(1-5):149–170, 2010.

[180] A. P. Philipse. The Random Contact Equation and Its Implications for (Colloidal) Rods in Packings, Suspensions, and Anisotropic Powders. LANGMUIR, 12(5):1127–1133, 1996.

[181] O. Pierard, C. González, J. Segurado, J. LLorca, and I. Doghri. Micromechanics of elasto-plastic materials reinforced with ellipsoidal inclusions. INTERNATIONAL JOURNAL OF SOLIDS AND STRUCTURES, 44(21):6945–6962, 2007.

[182] P. Podsiadlo, A. K. Kaushik, E. M. Arruda, A. M. Waas, B. S. Shim, J. Xu, H. Nandivada, B. G. Pumplin, J. Lahann, A. Ramamoorthy, and N. A. Kotov. Ultrastrong and Stiff Layered Polymer Nanocomposites. SCIENCE, 318(5847):80–83, 2007.

[183] F. P. Preparata and M. I. Shamos. COMPUTATIONAL GEOMETRY. Springer New York, 1985.

[184] W. H. Press, S. A. Teukolsky, W. T. Vetterling, and B. P. Flannery. NUMERICAL RECIPES. Cambridge University Pr., 2007.

[185] R. Quey, P. R. Dawson, and F. Barbe. Large-scale 3D random polycrystals for the finite element method: Generation, meshing and remeshing. COMPUTER METHODS IN APPLIED MECHANICS AND ENGINEERING, 200(17-20):1729–1745, 2011.

[186] S. Ravindran, B. Koohbor, and A. Kidane. Experimental characterization of meso-scale deformation mechanisms and the RVE size in plastically deformed carbon steel. STRAIN, 53(1):e12217, 2016.

[187] H. Richter. Mote3D: an open-source toolbox for modelling periodic random particulate microstructures. MODELLING AND SIMULATION IN MATERIALS SCIENCE AND ENGINEERING, 25(3):035011, 2017.

[188] M. D. Rintoul and S. Torquato. Reconstruction of the Structure of Dispersions. JOURNAL OF COLLOID AND INTERFACE SCIENCE, 186(2):467–476, 1997.

[189] P. Romero and E. Masad. Relationship between the Representative Volume Element and Mechanical Properties of Asphalt Concrete. JOURNAL OF MATERIALS IN CIVIL ENGINEERING, 13(1):77–84, 2001.

[190] F. Roters, P. Eisenlohr, L. Hantcherli, D. D. Tjahjanto, T. R. Bieler, and D. Raabe. Overview of constitutive laws, kinematics, homogenization and multiscale methods in crystal plasticity finite-element modeling: Theory, experiments, applications. ACTA MATERIALIA, 58(4):1152–1211, 2010.

[191] M. Rubinstein and R. H. Colby. POLYMER PHYSICS, volume 23. Oxford University Press New York, 2003.

[192] C. Rycroft. Voro++: a three-dimensional Voronoi cell library in C++. Technical report, Lawrence Berkeley National Lab., 2009.

[193] S. Saeb, P. Steinmann, and A. Javili. Aspects of Computational Homogenization at Finite Deformations: A Unifying Review From Reuss to Voigts Bound. APPLIED MECHANICS REVIEWS, 68(5):050801, 2016.

[194] V. Salnikov, D. Choï, and P. Karamian-Surville. On efficient and reliable stochastic generation of RVEs for analysis of composites within the framework of homogenization. COMPUTATIONAL MECHANICS, 55:127–144, 2015.

[195] T. Sawada and T. Kusaka. Strength predictions by applied effective volume theory in short-glass-fibre-reinforced plastics. Polymer Testing, 62:143–153, 2017.

[196] I. Scheider. Numerical Simulation of Material Separation Using Cohesive Zone Models. In Handbook of Mechanics of Materials, pages 1–42. Springer Singapore, 2018.

[197] I. Scheider, T. Xiao, E. Yilmaz, G. A. Schneider, N. Huber, and S. Bargmann. Damage modeling of small-scale experiments on dental enamel with hierarchical microstructure. Acta Biomaterialia, 15:244–253, 2015.

[198] C. F. Schmid, L. H. Switzer, and D. J. Klingenberg. Simulations of fiber flocculation: Effects of fiber properties and interfiber friction. Journal of Rheology, 44(4):781–809, 2000.

[199] K. Schneider, B. Klusemann, and S. Bargmann. Automatic three-dimensional geometry and mesh generation of periodic representative volume elements for matrix-inclusion composites. Advances in Engineering Software, 99:177–188, 2016.

[200] K. Schneider, B. Klusemann, and S. Bargmann. Fully periodic RVEs for technological relevant composites: not worth the effort! Journal of Mechanics of Materials and Structures, 12(4):471–484, 2017.

[201] M. Schneider. The sequential addition and migration method to generate representative volume elements for the homogenization of short fiber reinforced plastics. Computational Mechanics, 59(2):247–263, 2016.

[202] P. J. Schneider and D. H. Eberly. Geometric Tools for Computer Graphics. Elsevier, 2003.

[203] J. Schröder and K. Hackl. Plasticity and Beyond. Springer, 2014.

[204] J. Schöberl. NETGEN An advancing front 2D/3D-mesh generator based on abstract rules. Computing and Visualization in Science, 1(1):41–52, 1997.

[205] T. Schüler, R. Jänicke, and H. Steeb. Nonlinear modeling and computational homogenization of asphalt concrete on the basis of XRCT scans. Construction and Building Materials, 109:96–108, 2016.

[206] N. H. Scott. The Incremental Bulk Modulus, Young's Modulus and Poisson's Ratio in Nonlinear Isotropic Elasticity: Physically Reasonable Response. Mathematics and Mechanics of Solids, 12(5):526–542, 2007.

[207] T. Seelig and E. V. der Giessen. A cell model study of crazing and matrix plasticity in rubber-toughened glassy polymers. Computational Materials Science, 45(3): 725–728, 2009.

[208] B. R. Seth. Generalized strain measure with applications to physical problems. Technical report, Mathematics Research Center, United States Army, University of Wisconsin, 1961.

[209] Z. Shan and A. M. Gokhale. Representative volume element for non-uniform microstructure. Computational Materials Science, 24(3):361–379, 2002.

[210] A. Sheidaei, M. Baniassadi, M. Banu, P. Askeland, M. Pahlavanpour, N. Kuuttila, F. Pourboghrat, L. T. Drzal, and H. Garmestani. 3-D microstructure reconstruction of polymer nano-composite using FIB-SEM and statistical correlation function. Composites Science and Technology, 80:47–54, 2013.

[211] P. Sheng, J. Zhang, and Z. Ji. An advanced 3D modeling method for concrete-like particle-reinforced composites with high volume fraction of randomly distributed particles. COMPOSITES SCIENCE AND TECHNOLOGY, 134:26–35, 2016.

[212] J. Shewchuk. What Is a Good Linear Finite Element? Interpolation, Conditioning, Anisotropy, and Quality Measures. UNIVERSITY OF CALIFORNIA AT BERKELEY, 73: 137, 2002.

[213] J. R. Shewchuk. Triangle: Engineering a 2D quality mesh generator and Delaunay triangulator. In APPLIED COMPUTATIONAL GEOMETRY TOWARDS GEOMETRIC ENGINEERING, pages 203–222. Springer, 1996.

[214] H. Si. Tetgen A quality tetrahedral mesh generator and three-dimensional delaunay triangulator. WEIERSTRASS INSTITUTE FOR APPLIED ANALYSIS AND STOCHASTIC, BERLIN, GERMANY, page 81, 2006.

[215] H. Si. TetGen, a Delaunay-Based Quality Tetrahedral Mesh Generator. ACM TRANSACTIONS ON MATHEMATICAL SOFTWARE, 41(2):1–36, 2015.

[216] D. Sohn, J. Y. Park, Y.-S. Cho, J. H. Lim, and H. Lee. Periodic Mesh Generation for Composite Structures using Polyhedral Finite Elements. JOURNAL OF THE COMPUTATIONAL STRUCTURAL ENGINEERING INSTITUTE OF KOREA, 27(4):239–245, 2014.

[217] K.-A. Sohn, B. Juttler, M.-S. Kim, and W. Wang. Computing distances between surfaces using line geometry. In 10TH PACIFIC CONFERENCE ON COMPUTER GRAPHICS AND APPLICATIONS, 2002. PROCEEDINGS. IEEE Comput. Soc, 2002.

[218] J. E. Spowart, H. E. Mullens, and B. T. Puchala. Collecting and analyzing microstructures in three dimensions: A fully automated approach. JOM, 55(10):35–37, 2003.

[219] R. A. Srivatsan and S. Bandyopadhyay. An analytical formulation for finding the proximity of two arbitrary cylinders in space. In PROCEEDINGS OF CONFERENCE ON ADVANCES IN ROBOTICS - AIR 2013. ACM Press, 2013.

[220] D. Stoyan. Simulation and Characterization of Random Systems of Hard Particles. IMAGE ANALYSIS & STEREOLOGY, 21(4):41, 2002.

[221] M. Stroeven, H. Askes, and L. J. Sluys. Numerical determination of representative volumes for granular materials. COMPUTER METHODS IN APPLIED MECHANICS AND ENGINEERING, 193(30-32):3221–3238, 2004.

[222] P. M. Suquet. ELEMENTS OF HOMOGENIZATION FOR INELASTIC SOLID MECHANICS. Springer, 1985.

[223] B. Talamini, Y. Mao, and L. Anand. Progressive damage and rupture in polymers. JOURNAL OF THE MECHANICS AND PHYSICS OF SOLIDS, 111:434–457, 2018.

[224] R. Talreja and C. V. Singh. DAMAGE AND FAILURE OF COMPOSITE MATERIALS. Cambridge University Press, 2012.

[225] Z. Tang, N. A. Kotov, S. Magonov, and B. Ozturk. Nanostructured artificial nacre. NATURE MATERIALS, 2(6):413–418, 2003.

[226] K. Terada, M. Hori, T. Kyoya, and N. Kikuchi. Simulation of the multi-scale convergence in computational homogenization approaches. INTERNATIONAL JOURNAL OF SOLIDS AND STRUCTURES, 37(16):2285–2311, 2000.

[227] M. Thomas, N. Boyard, L. Perez, Y. Jarny, and D. Delaunay. Representative volume element of anisotropic unidirectional carbon-epoxy composite with high-fibre volume fraction. COMPOSITES SCIENCE AND TECHNOLOGY, 68(15-16):3184–3192, 2008.

[228] W. Tian, L. Qi, J. Zhou, J. Liang, and Y. Ma. Representative volume element for composites reinforced by spatially randomly distributed discontinuous fibers and its applications. COMPOSITE STRUCTURES, 131:366–373, 2015.

[229] S. Torquato. RANDOM HETEROGENEOUS MATERIALS. Springer, 2002.

[230] S. Torquato, T. M. Truskett, and P. G. Debenedetti. Is Random Close Packing of Spheres Well Defined? PHYSICAL REVIEW LETTERS, 84(10):2064–2067, 2000.

[231] D. Trias, J. Costa, J. A. Mayugo, and J. E. Hurtado. Random models versus periodic models for fibre reinforced composites. COMPUTATIONAL MATERIALS SCIENCE, 38(2): 316–324, 2006.

[232] D. Trias, J. Costa, A. Turon, and J. Hurtado. Determination of the critical size of a statistical representative volume element (SRVE) for carbon reinforced polymers. ACTA MATERIALIA, 54(13):3471–3484, 2006.

[233] A. Trueman, S. Knight, J. Colwell, T. Hashimoto, J. Carr, P. Skeldon, and G. Thompson. 3-D tomography by automated in situ block face ultramicrotome imaging using an FEG-SEM to study complex corrosion protective paint coatings. CORROSION SCIENCE, 75:376–385, 2013.

[234] P. Trusov and I. Keller. The theory of constitutive relations. PART I. PERM: PERM STATE TECHNICAL UNIVERSITY, 1997.

[235] S.-T. Tu, W.-Z. Cai, Y. Yin, and X. Ling. Numerical Simulation of Saturation Behavior of Physical Properties in Composites with Randomly Distributed Second-phase. JOURNAL OF COMPOSITE MATERIALS, 39(7):617–631, 2005.

[236] M. D. Uchic, M. A. Groeber, and A. D. Rollett. Automated serial sectioning methods for rapid collection of 3-D microstructure data. JOM, 63(3):25–29, 2011.

[237] R. A. Vaia and H. D. Wagner. Framework for nanocomposites. MATERIALS TODAY, 7 (11):32–37, 2004.

[238] J. G. M. van Mier. FRACTURE PROCESSES OF CONCRETE. CRC press, 2017.

[239] W. M. Visscher and M. Bolsterli. Random Packing of Equal and Unequal Spheres in Two and Three Dimensions. NATURE, 239(5374):504–507, 1972.

[240] D. Vranek. Fast and Accurate Circle-Circle and Circle-Line 3D Distance Computation. JOURNAL OF GRAPHICS TOOLS, 7(1):23–31, 2002.

[241] A. Walther, I. Bjurhager, J.-M. Malho, J. Pere, J. Ruokolainen, L. A. Berglund, and O. Ikkala. Large-Area, Lightweight and Thick Biomimetic Composites with Superior Material Properties via Fast, Economic, and Green Pathways. NANO LETTERS, 10(8): 2742–2748, 2010.

[242] B. Widom. Random Sequential Addition of Hard Spheres to a Volume. THE JOURNAL OF CHEMICAL PHYSICS, 44(10):3888–3894, 1966.

[243] G. Wildes, H. Keskkula, and D. R. Paul. Fracture characterization of PC/ABS blends: effect of reactive compatibilization, ABS type and rubber concentration. POLYMER, 40 (25):7089–7107, 1999.

[244] S. R. Williams and A. P. Philipse. Random packings of spheres and spherocylinders simulated by mechanical contraction. PHYSICAL REVIEW E, 67(5), 2003.

[245] K. I. Winey and R. A. Vaia. Polymer Nanocomposites. MRS BULLETIN, 32(04):314–322, 2007.

[246] J. Wippler, S. Fünfschilling, F. Fritzen, T. Böhlke, and M. J. Hoffmann. Homogenization of the thermoelastic properties of silicon nitride. ACTA MATERIALIA, 59(15):6029–6038, 2011.

[247] P. Wriggers. NONLINEAR FINITE ELEMENT METHODS. Springer, 2008.

[248] S. Yamamoto and T. Matsuoka. Dynamic simulation of microstructure and rheology of fiber suspensions. POLYMER ENGINEERING & SCIENCE, 36(19):2396–2403, 1996.

[249] M. Yang, A. Nagarajan, B. Liang, and S. Soghrati. New algorithms for virtual reconstruction of heterogeneous microstructures. COMPUTER METHODS IN APPLIED MECHANICS AND ENGINEERING, 338:275–298, 2018.

[250] Y. Yu, J. Cui, and F. Han. An effective computer generation method for the composites with random distribution of large numbers of heterogeneous grains. COMPOSITES SCIENCE AND TECHNOLOGY, 68(12):2543–2550, 2008.

[251] Z. Yuan and J. Fish. Toward realization of computational homogenization in practice. INTERNATIONAL JOURNAL FOR NUMERICAL METHODS IN ENGINEERING, 73(3):361–380, 2007.

[252] X. Yue and E. Weinan. The local microscale problem in the multiscale modeling of strongly heterogeneous media: Effects of boundary conditions and cell size. JOURNAL OF COMPUTATIONAL PHYSICS, 222(2):556–572, 2007.

[253] A. Zankel, J. Wagner, and P. Poelt. Serial sectioning methods for 3D investigations in materials science. MICRON, 62:66–78, 2014.

[254] J. Zeman and M. Šejnoha. From random microstructures to representative volume elements. MODELLING AND SIMULATION IN MATERIALS SCIENCE AND ENGINEERING, 15(4):S325–S335, 2007.

[255] J. Zhou, L. Qi, and A. M. Gokhale. Generation of Three-Dimensional Microstructure Model for Discontinuously Reinforced Composite by Modified Random Sequential Absorption Method. JOURNAL OF ENGINEERING MATERIALS AND TECHNOLOGY, 138 (2):021001, 2016.